CYRIC

ANNUAL REPORT

2000

(January 2000 - December 2000)

CYCLOTRON AND RADIOISOTOPE CENTER
TOHOKU UNIVERSITY
http://www.cyric.tohoku.ac.jp/

PREFACE

In this twenty-first issue of the CYRIC Annual Report, we summarize the activities for research and development and results of training for radioisotope safe-treatment at Cyclotron and Radioisotope Center (CYRIC), Tohoku University during the calendar year 2000.

In order to realize the motto of Tohoku University, the principle of CYRIC, as a research and education institute to open it's facilities for common-use over university members, is to maintain K=12-MeV and 110-MeVAVF cyclotrons and related facilities, including positron emission tomography (PET) systems, as an important scientific infrastructure, and to carry out the role of the center of our university for safe-handling of radiation and radioisotopes. As such, we aim to support development of fundamental but promising researches and interdisciplinary ones together with promotion of the leaders in the fields of the nuclear science so as to answer the social demands.

The accelerator and related facilities together with building including radiation shields was inspected by the Nuclear Safety Division, Science and Technology Bureau, MEXT on 30 June, 2000. Then, official performance test of the new K=110MeV, 930 AVF cyclotron with beam acceleration has been carried out successfully. The research program committee has accepted new proposals, and scheduled the beam time over the coming three months in 2001.

Studies with PIXE (Particle Induced X-ray Emission) technique have been continuously performed by using electrostatic accelerator, installed at FNL (Fast Neutron Laboratory) in Graduate School of Technology, Tohoku University, under the scientific tie-up between CYRIC and FNL. Indeed, more than six groups are running under this project using a total of its 240 hours beam-time.

Synthesis of radiopharmaceuticals for clinical research with PET (Positron Emission Tomography) and other applications have been continuously carried out. The small size AVF cyclotron HM-12, installed under scientific and technical tie-up among IDAC, CYRIC and Sumitomo Heavy Industry Co. Ltd, has steadily been operated. Positron emitting radio-nuclides was provided with 300 hours exposure by 12-MeV proton beams, while those by 6-MeV deuteron beams were done with 264 hrs exposure. With a number of radiopharmaceuticals thus produced, 54 research programs are running covering almost all clinical research fields together with works for basic medical research with volunteers.

During 2000 school year, 539 of staff members and students of Tohoku University were trained at this Center in the beginner's course of safe handling of radiation and

radioisotopes, while 279 staff members and students in the "x-ray course". In addition, 60 of staff members and students were trained in the course of safe handling of radiation from a SOR (Synchrotron Orbital Radiation).

On November 10 and 11, 2000, a workshop was held to discuss the proposal presented for the studies with the new K=110 AVF cyclotron and related facilities. Followings are the program. We are indebted to the speakers.

*An advanced stage of nuclear medicine by PET with newly developed heavier positron emitting nuclide: by R. Iwata and K. Yamaguchi (CYRIC)

*Mechanism of high-energy ion atom collision and it's application: by K. Ishii (Graduate School of Technology)

*Assessment of atomic reactor materials, and development of maintenance and integrity techniques for them: by A. Hasegawa (Graduate School of Technology)

*Development of neutron fields and measurement of neutron cross sections: by M. Baba (CYRIC)

*Nuclear physics by proton-rich unstable nuclear-beams: Search for the ground state of ^{10}N by the p(^{10}C,n)^{10}N reaction: by H. Ohtsu (Graduate School of Science)

*Production of high-energy gamma-ray and π- and η-mesons by coherent nucleons-nucleons collision; by J. Kasagi (Graduate School of Science)

*Study of nuclear structure and astro-nuclear physics by means of gamma-ray spectroscopy: by Y. Gono (Kyushu University)

*Production of polarized nuclei and measurement of electromagnetic moments of unstable nuclei by RI-beam: by M. Tanigaki (Kyoto University) and S. Ohya (Niigata University)

*Development of low-energy polarized RI-beam production: by K. Asahi (RIKEN)

*Nuclear chemistry of super-heavy nuclei: H. Kudo (Niigata University)

*Study of spin-isospin excitation in nuclei and nucleon-nucleus optical-potential in <100MeV region: by A. Terakawa and H. Orihara (CYRIC)

*Synthesis of heavy elements and their decay and chemical properties: T. Ohstuki ((Graduate School of Science)

We are very grateful to Tohoku University and to the Ministry of Education, Sports, Culture, Science and Technology for their continuous support.

January, 2001

Hikonojo ORIHARA
Director
Cyclotron and Radioisotope Center, Tohoku University

EDITORS:

Hikonojo	*ORIHARA*
Tatsuo	*IDO*
Masatoshi	*ITOH*
Mamoru	*BABA*
Tsutomu	*SHINOZUKA*

WORD PROCESSED BY

Yu-ko YAMASHITA

CONTENTS

I. PHYSICS AND TECHNOLOGY

II. CHEMISTRY

III. MEDICINE AND BIOLOGY (Basic)

IV. MEDICINE AND BIOLOGY (Clinical)

V. RADIATION PROTECTION AND TRAINING OF SAFE HANDLING

I. PHYSICS AND TECHNOLOGY

I. 1. Method of Determination for Gamow-Teller Matrix-elements in Light Nuclei by (p,n) Cross-section at E_p=35 MeV

Orihara H., Terakawa A., Itoh K., Suzuki H., Kumagai K., Kikuchi Y., Jon G. C., Ishii K.**, Niizeki T.***, and Ohnuma H.*****

Cyclotron and Radioisotope Center, Tohoku University
*Institute of Physics, Academia Sinica Nankang Taipei, Taiwan 11529**
*Department of Quantum Science and Energy Engineering, Graduate School of Technology, Tohoku University***
*Faculty of Home Economics, Tokyo Kasei University, Itabashi, Tokyo173-8602, Japan****
*Department of Physics, Chiba Institute of Technology, Narashino-shi, Chiba 275-0023, Japan*****

INTRODUCTION

A Gamow-Teller (GT) matrix element with ΔT=1 and ΔS=1 nuclear response carrys significant information of spin-isospin excitation in nuclei including that for wave functions. Historically, the GT-matrix element has been determined through the β-decay rate, while a number of studies have been carried out to calibrate the (p,n) cross sections to the corresponding GT-matrix element[1]. The latter has a great advantage to reach a transition which is inaccessible by β -decay experiments, including such a transition exciting the giant Gamow-Teller resonance.

With intermediate energy protons at IUCF[2,3], for example, one can selectively excite the spin-flip components in the (p,n) reaction due to strong spin-isospin effective interaction ($V_{\sigma\tau}$). Moreover, the experimental condition in which one is able to reach q≈0 at θ_{lab} = 0°. makes it reliable to determine a GT-matrix element. In low energy (p,n) reaction with 35-MeV protons at CYRIC, it has been found possible to obtain basically the same information as that at intermediate energies if careful analysis including exchange terms is carried out. Various problems associated with the distorted-wave (DW) analysis of low-energy (p,n) data were discussed in detail by Ohnuma et al[4].

One of the advantages of the low energy (p,n) experiment is its high-resolution, enabling us to observe separately an important GT-transition. In this report, we discuss the reliability to calibrate the 35-MeV (p,n) cross sections to a corresponding GT-matrix element by observing the (p,n) reactions on nine light N=Z+2 nuclei, which are members of T_z =-1, 0 and 1 isobar triplets, and strong β decay rates are well known[5]. They are ^{10}Be-^{10}B-^{10}C, ^{14}C-^{14}N-^{14}O, ^{18}O-^{18}F-^{18}Ne, ^{22}Ne-^{22}Na-^{22}Mg, ^{26}Mg-^{26}Al-^{26}Si, ^{30}Si-^{30}P-^{30}S, ^{34}S-^{34}Cl-^{34}Ar, and ^{42}Ca-^{42}Sc-^{42}Ti. Among them, (p,n) reactions on ^{14}C, ^{18}O and ^{34}S have been published in our previous papers[6-8]. Beyond the nuclei heavier than A=48, no such simple nuclear structure appear. Except the case of the ^{10}Be, ^{10}B and ^{10}C triplet, where target materials are

not available in an ordinary manner, others all GT- and F-transitions among triplets may be explored by the (p,n) reaction. An example of T_z =-1, 0 and 1 isobar triplets is illustrated schematically in Fig. 1 for the case of the ^{26}Mg-^{26}Al-^{26}Si triplet[9].

EXPERIMENT

The experiment was performed at the Cyclotron and Radioisotope Center, Tohoku University, with a 35-MeV proton beam from an AVF-cyclotron and a beam swinger system. The details of the experimental setup have been described previously[10,11]. Neutron energies were measured by the time-of-flight technique (TOF), where neutrons were detected by a detector array located at 44.3 m from the target. The detectors, 23.2 litters in a total sensitive volume, were filled with organic liquid scintillator NE213. The absolute efficiencies of the detectors were obtained from the ^{7}Li(p,n)^{7}Be activation analyses with an error less than 6%. Errors in the absolute magnitude of (p,n) cross sections were estimated to be less than 12%. All the targets were enriched isotopes with enrichments higher than 95%.

Figure 2 shows an excitation energy neutron spectrum measured for the ^{26}Mg(p,n)^{26}Al reaction at 25-degrees. Prominent isolated peaks of neutrons leading to the 1.058- and 1.851-MeV, 1^+ states are seen to be excited, together with those to the first excited 0^+, IAS at 0.228MeV.

RESULTS AND DISCUSSION

Sample of experimental results are shown in Figs. 2 through 5 for angular distributions of neutrons leading to the previously mentioned 0^+ and 1^+ states in ^{26}Al. The $0^+ \rightarrow 0^+$, IAS (p,n) transition (see Fig. 2) is analog to the Fermi β -decay from 0^+, T=1 ground state of ^{26}Si to the 0^+, T=1 0.2282-MeV state in ^{26}Al, as shown in Fig. 1, while the $0^+ \rightarrow 1^+$ transitions (see Figs. 3-5) correspond to the Gamow-Teller β -decay from 0^+, T=1 ground state of ^{26}Si to the 1^+, T=0 states in ^{26}Al, in which the most prominent one leading to the 1.0577-MeV state is used for the main purpose of the present work. As seen in these figure, the angular distributions are similar to each other so long as these in angular region larger than ~20 degree. It should be noted that the IAS Fermi-type (p,n) reaction proceeds through L = 0 transfer. As such, dominant fraction for these GT-type transition may be L = 0 transfer as discussed in detail in Ref. [8].

Due to reaction dynamics for the present experimental conditions of incident proton-energy at 35MeV and of target mass in 14 ≤A ≤70, an L=0 transition's angular distribution steadily has a bell-shape peaked at θ_{lab}~25°, where the linear momentum transfer q is no longer close to zero value. On the other hand, a 0-degree cross section is changes rapidly along with increase of the target mass, etc. Therefor, to find a proportional relationship between the (p,n) cross section and GT matrix element at low-energies is not so straightforward as in intermediate energies where an L = 0 transition exhibits the 0-degree

peaked angular distribution and the $q \sim 0$ condition, being same situation with β-decays, is achievable. Nevertheless, we know empirically that stronger β -decay yields larger (p,n) cross section leading to the same residual state. The log ft value from ^{26}Si to the 1.0577- and 1.835-MeV states in ^{26}Al are, respectively, 3.55 and 3.86 giving a factor of 2.04 as seen in Fig. 1, while the ratio of peak height of neutrons from the ^{26}Mg(p,n)^{26}Al reaction leading to the 1.0577- and 1.835-MeV states in ^{26}Al is almost 2.0 as seen in Figs. 4 and 5. In order to find more realistic proportional relationship spreading over a wide range of light nuclei, systematic (p,n) studies at 35MeV have been carried with a series of targets as described before. Angular distribution measurement and distorted wave (DW) analysis for all targets have been carried out to be sure that the reaction occurs indeed through $L = 0$ transition and to find a reasonable peak cross section around $\theta_{lab} = 25°$. The data are compared with the microscopic DW results calculated by the computer code DWBA-70[12], which includes knock-on exchange effects in an exact manner. Optical potential parameters of Becchetti and Greenlees[13] are used for the entrance channel. Those for the exit channel were self-consistent potential parameters derived by Carlson et al[14]. The effective nucleon-nucleon interactions used in the present DW analysis are those by Bertsch et al. (M3Y)[15]. Sensitivity of such calculations to the optical-potential parameters is elaborated in Ref.[4]. One body transition densities (OBTD) for microscopic DWBA calculation have been obtained by shell-model computer code OXBASH[16].

Table 1 summarizes the present results. Data for β -decay were taken from recent review by Singh et al[5]. We translate the experimental logft values into B_β(GT), assuming the free values for vector and axial-vector coupling constants as $(g_A/g_A)^2 = (1.251)^2$. The GT-matrix elements, thus obtained, are distributed over 1.1 to 3.2 giving a good place to investigate the proportionality relationship. We discuss about the peak cross sections of the (p,n) reactions obtained by DW fitting curves around θ~25 degree. In order to eliminate many possible ambiguities, the $0^+ \rightarrow 1^+$ cross sections are normalized to those of $0^+ \rightarrow 0^+$ ones. We define a factor N as;

$$N = \frac{B_\beta(\mathrm{GT})}{(d\sigma/d\Omega)_{0^+\rightarrow 1^+,\,\mathrm{peak}}/(d\sigma/d\Omega)_{\mathrm{IAS,\,peak}}}$$

In the case that charge symmetry of the nuclear force is valid and proportionality relationship between β-decay matrix element B_β(GT) and (p,n) cross section exists, N may converge to a constant value. The N values listed in Table 1 lay indeed around $\langle N \rangle_{\mathrm{average}} = 1.96$ with the standard deviation of 5.6% for eight samples. The same results are illustrated in Fig. 7 showing the linear relationship with the gradient of 1.96 ± 0.11. The last column of Table 1 lists the presently obtained $B_{p,n}$(GT), comparison with B_β(GT) in the third column being satisfactory.

In order to test the feasibility of the present method to extract a GT matrix element from the low-energy (p,n) cross sections, we compare $B_{p,n}$(GT) by the ^{26}Mg(p,n)^{26}Al reaction

at E_p = 35 MeV with those by an intermediate energy (p,n) work at E_p = 135 MeV reported by Madey et al.[3] based on the data in Fig. 5 for the GT-type transition leading to the 1.851-MeV state in ^{26}Al. They have reported the $B_{p,n}$ (GT:q = 0.05fm^{-1}) to be 0.50, while our result extracted through the present procedure is 0.53 ± 0.03. Note that B_β(GT) from log ft value of 3.86 in Fig. 1 is 0.544. These three values coincide within the error. Now we are able to estimate the $B_{p,n}$(GT) for the transition to the 5.019-MeV state, being energetically inaccessible by β-decay. As depicted in Fig. 6 the peak cross section is 0.227 mb/sr, thus we obtain a value of 0.24 ± 0.02, log ft being 4.22.

SUMMARY

In summary, experimental results for prominent GT-type $0^+ \rightarrow 1^+$ transitions observed in the (p,n) reactions on ^{14}C, ^{18}O, ^{22}Ne, ^{26}Mg, ^{30}Si, ^{34}S, ^{38}Ar and ^{42}Ca were discussed by comparing their cross sections with analog Gamow-Teller β-decay strengths in order to find a proportionality relationship. A reasonable method has been found to calibrate a $0^+ \rightarrow 1^+$ (p,n) cross section to the corresponding GT matrix element by the aid of that for IAS transition. The obtained GT-matrix element was successfully compared with that at intermediate energy. Also given were a GT-matrix element for which β -decay experiment was energetically inaccessible.

This method is valid for (p,n) reactions at low-energy with target mass in 14≤ A≤42. Beyond this region for fp-shell nuclei, this method may be applicable so long as both GT- and F-type transitions show a similar pattern for their angular distribution of differential cross sections.

This work is supported by grant in aid for scientific research of Ministry of Education, Culture, Sports, and Science and Technology No.13640257.

References

1) Taddeucci T. N. et al, Nucl. Phys. **A469** (1987) 125.
2) Goodman C. D. et al., Phys. Lett. **107B** (1981) 406.
3) Madey R. et al., Phys. Rev. C **35** (1987) 2011.
4) Ohnuma H. et al., Nucl. Phys. **A467**, 61(1987).
5) Singh B.et al., Nuclear Data Sheets **84** (1998) 487.
6) Kabasawa M. et al., Phys. Rev. C**45** (1992) 1220.
7) Oura M.et al., Nucl Phys. **A586** (1995) 20.
8) Furukawa K. et al., Phys. Rev. C**36** (1987) 1686.
9) Table of Isotope Eigh Edition (1996), ed. by Firestone R. B. et al.
10) Orihara H. and Murakami T., Nucl. Instrum. Methods 181, 15(1981).
11) Orihara H. et al., Methods **A257** (1987) 189.
12) Schaeffer R. and Raynal J., the computer program DWBA70 (unpublished).
13) Becchetti F. D. and Greenlees G. W., Phys. Rev. **182** (1969) 1190.
14) Bertsch G., et al., Nucl. Phys. **A284** (1977) 399.
15) Carlson J. D., Zafiratos C. D. and Lind D. A., Nucl. Phys. **A249** (1975) 29
16) The shell model code OXBASH, Echegoyen A. E. et al., National Superconducting Cyclotron Laboratory Report No. 524 (1984).

Table 1. Comparison of GT matrix elements obtained by the (p,n) reaction with those by super-allowed β-decay.

β-decay				(p,n)Reaction				
decay	E_x (MeV)	log *ft*	B_β(GT)[#1]	Reaction	Cross Section (mb/sr) $(d\sigma/d\Omega)_{peak}$ $0^+\rightarrow1^+$ trans.	Cross Section (mb/sr) $(d\sigma/d\Omega)_{peak}$ IAS trans.	N[#2]	B_{pn} (GT)[#3]
$^{14}O(0^+)\rightarrow{}^{14}N(1^+)$	3.9478	3.13	2.922	^{14}C (p,n) $^{14}N(1^+)$	4.01	2.51	1.83	3.13±0.17
$^{18}Ne(0^+)\rightarrow{}^{18}F(1^+)$	0.0	3.09	3.204	^{18}O (p,n) $^{18}F(1^+)$	3.06	1.72	1.80	3.49±0.19
$^{22}Mg(0^+)\rightarrow{}^{22}Na(1^+)$	1.9362	3.44	1.431	$^{22}Ne(p,n)^{22}Na(1^+)$	1.32	1.82	1.97	1.42±0.08
$^{26}Si(0^+)\rightarrow{}^{26}Al(1^+)$	1.0577	3.55	1.111	$^{26}Mg(p,n)^{26}Al(1^+)$	1.01	1.85	2.04	1.07±0.06
$^{30}S(0^+)\rightarrow{}^{30}P(1^+)$	3.0194	3.56	1.086	$^{30}Si(p,n)^{30}P(1^+)$	0.803	1.52	2.06	1.04±0.06
$^{34}Ar(0^+)\rightarrow{}^{34}Cl(1^+)$	3.1291	3.45	1.399	^{34}S (p,n) $^{34}Cl(1^+)$	0.816	1.23	2.11	1.30±0.07
$^{38}Ca(0^+)\rightarrow{}^{38}K(1^+)$	1.6983	3.40	1.570	$^{38}Al(p,n)^{38}K(1^+)$	0.912	1.10	1.89	1.63±0.09
$^{42}Ti(0^+)\rightarrow{}^{42}Sc(1^+)$	0.6111	3.17	2.665	$^{42}Ca(p,n)^{42}Sc(1^+)$	1.52	1.13	1.98	2.64±0.15

$\langle N\rangle = 1.96 \pm 0.11$

[#1] derived from log *ft* through the relation:

$$B_\beta(\mathrm{GT}) = \frac{6170}{\left(\frac{g_A}{g_V}\right)^2 f\,t}$$

[#2] N is defined as:

$$N = \frac{B_\beta(\mathrm{GT})}{(d\sigma/d\Omega)_{0^+\rightarrow1^+,\,\mathrm{peak}}/(d\sigma/d\Omega)_{\mathrm{IAS,\,peak}}}$$

[#3] B_{pn} (GT) is extracted as:

$$B_{pn}(\mathrm{GT}) = \langle N\rangle (d\sigma/d\Omega)_{0^+\rightarrow1^+,\,\mathrm{peak}}/(d\sigma/d\Omega)_{\mathrm{IAS,\,peak}}$$

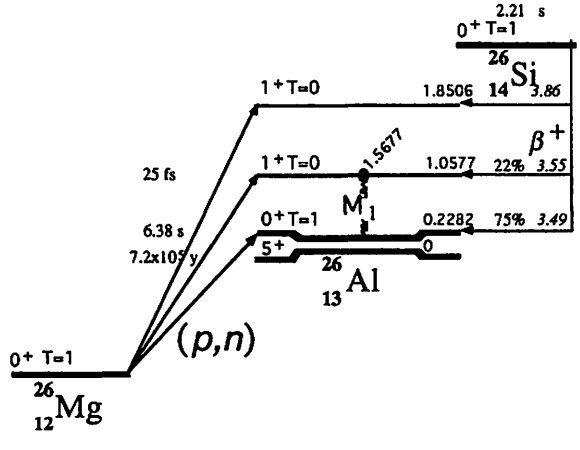

Fig. 1. Level diagram of the A=26 isobar triplet ^{26}Mg – ^{26}Al – ^{26}Si.

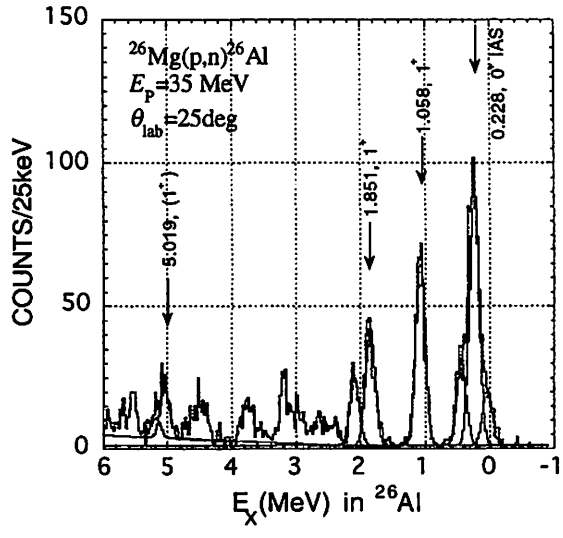

Fig. 2. A sample energy spectrum for the ^{26}Mg(p,n) ^{26}Al reaction at 25° with a flight path of 44.3 m. Energy per channel is 25 keV.

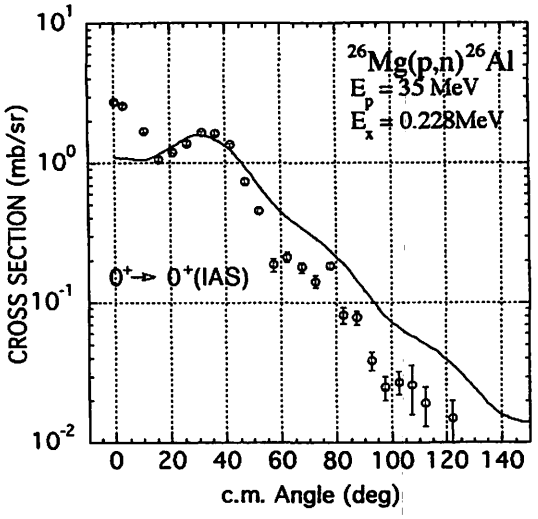

Fig. 3. Differential cross sections for neutrons leading to the 0.228-MeV 0^+ states in ^{26}Al. The curves are DWBA results described in the text.

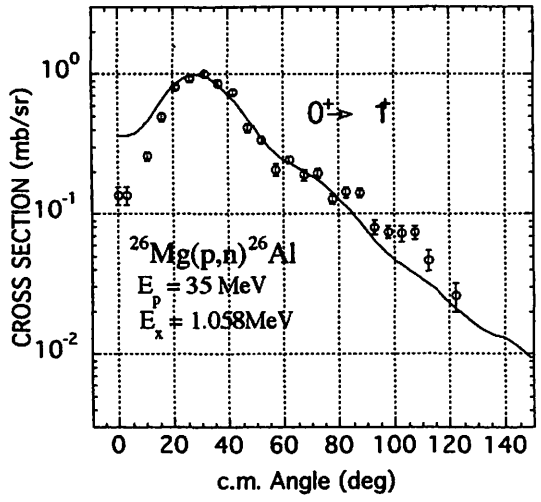

Fig. 4. Differential cross sections for neutrons leading to the 1.058 1^+ states in ^{26}Al. The curves are DWBA results described in the text.

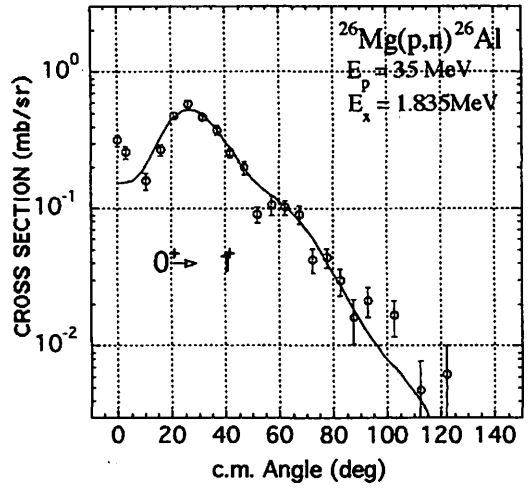

Fig. 5. Differential cross sections for neutrons leading to the 1.835 1^+ state in ^{26}Al. The curves are DWBA results described in the text.

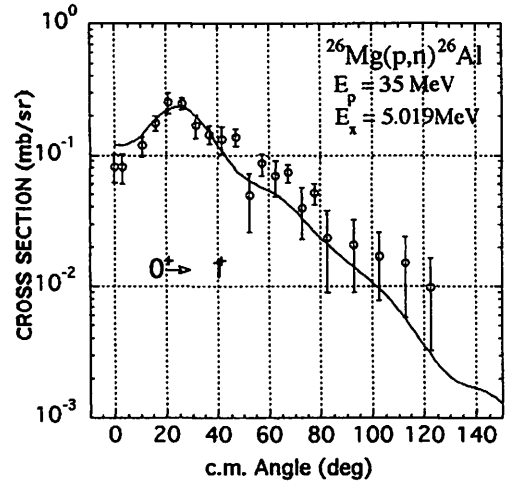

Fig. 6. Differential cross sections for neutrons leading to the 5.019 1^+ state in ^{26}Al. The curves are DWBA results described in the text.

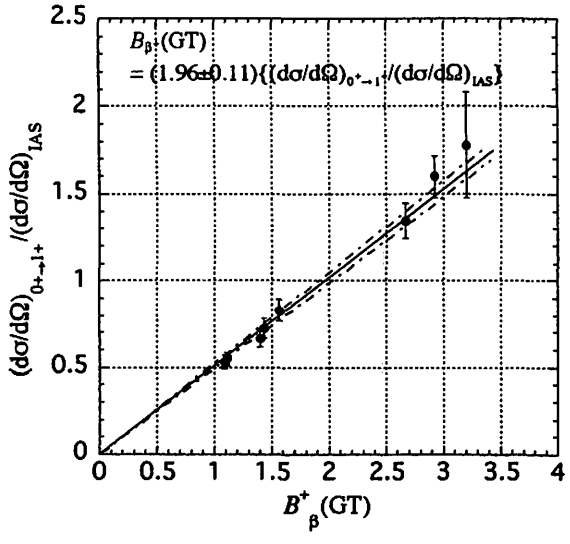

Fig. 7. Proportionality relationship between B_β(GT) values and GT-type $0^+ \rightarrow 1^+$ (p,n) cross sections.

I. 2. Level Scheme of ^{141}Nd

*Gono Y., Kashiyama O., Fukuchi T., Shinozuka T. *, Fujita M. *, Yamazaki A. *, and Sonoda T. **

Department of Physics, Kyushu University
*Cyclotron and Radioisotope Center, Tohoku University**

The excited states of ^{141}Nd was studied by using a ^{140}Ce(α, 3n)^{141}Nd reaction. An α-beam of 37 MeV was used and was delivered by Cyric. The $\gamma\gamma$-coincidence data was taken by two Ge detectors of relative efficiencies of 40 and 50%. Coincidences were made in 4-dimension parameters of E_γ- E_γ -T_γ-$T_{\gamma RF}$. A number of events collected was 2.1×10^7 in 12 hours.

A level scheme of ^{141}Nd was reported up to a level of (25/2) at 5271 keV[1] and discussed using weak and intermediate couplings. However in a coincidence spectrum obtained in the present experiment and gated on a 130 keV transition, 336 and 1024 keV γ-rays appeared clearly as shown in Fig.1. They were placed in parallel to a 130 keV transition in Ref.1. These three transitions turned out to be in cascade. And only three transitions of 248, 348 and1782 keV were seen in an off-beam spectrum which is shown in Fig.2. They are found to be in cascade relation each other. These three transitions were also seen in a delayed spectrum gated on a 1294 keV γ-ray and a post prompt part of T_γ spectrum. These facts proved that an excited state at 3135 keV is an isomer. However a life-time of this isomer could not be extracted in the present experiment.

Based on these results, a new level scheme of ^{141}Nd is proposed as shown in Fig.3. When one compares the resulted level scheme with those of neighboring isotopes, i.e. ^{143,144}Sm, a newly found isomer in ^{141}Nd may be interpreted to be of a coupling of an $h_{11/2}$ neutron hole to a 6^+ state in ^{142}Nd.

Reference

1) J. Ludziejewski et al., Z. Phys. **A 281** (1977) 287.

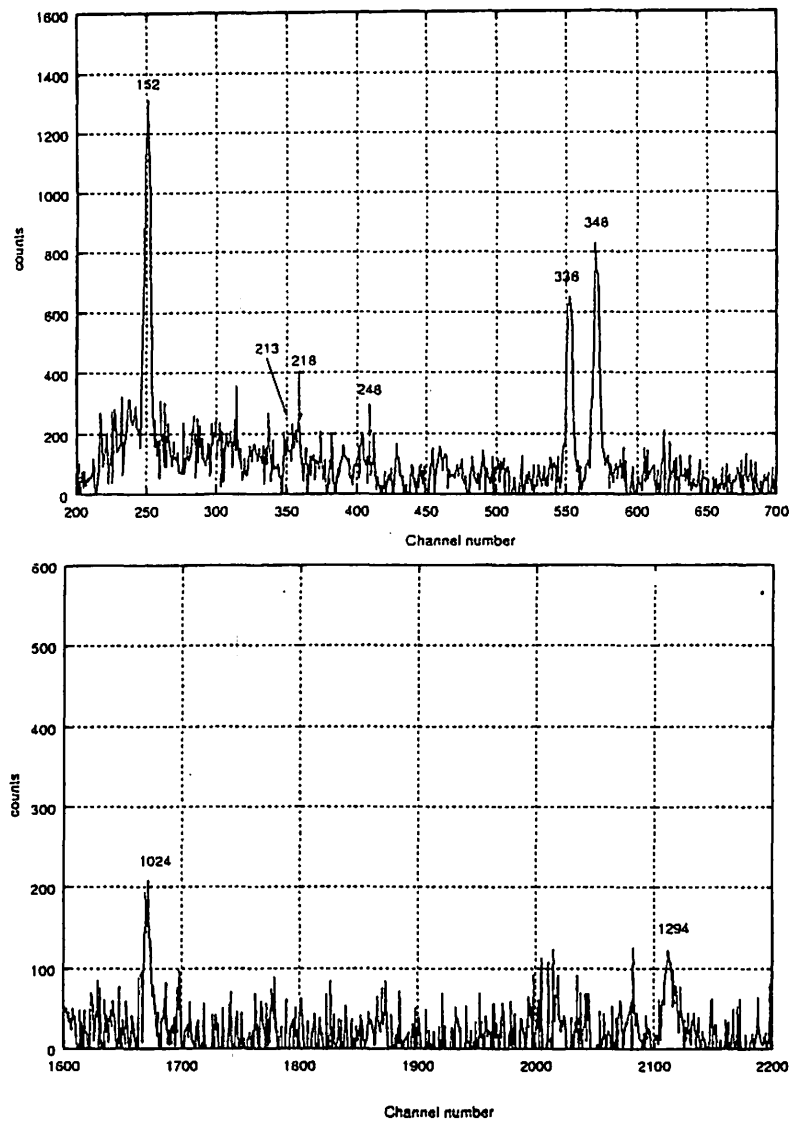

Fig. 1. Prompt coincidence spectrum obtained by gating on a 130 keV gamma-ray.

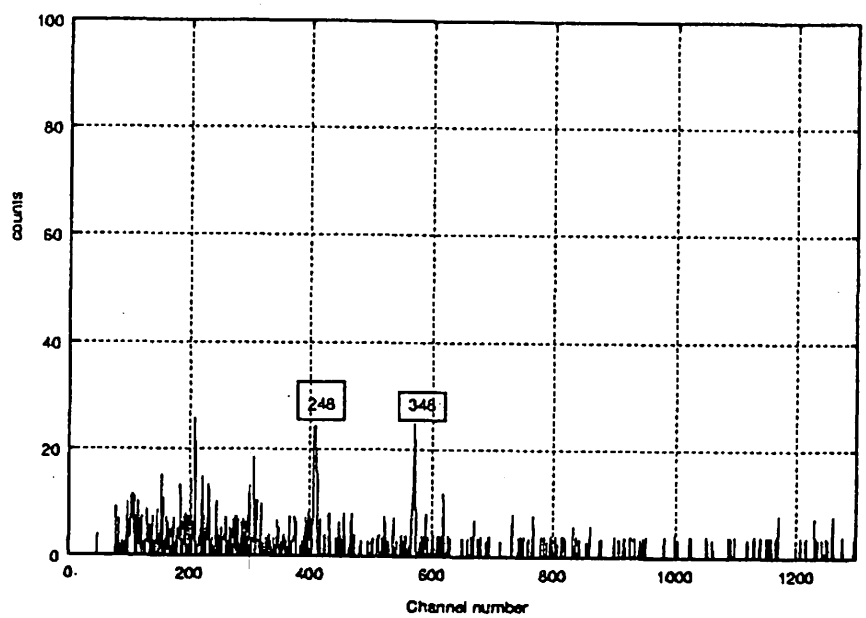

Fig. 2. Off-beam coincidence spectrum obtained gating on off-beam part of $T_{\gamma\text{-}RF}$ spectrum and a 1782 keV gamma-ray.

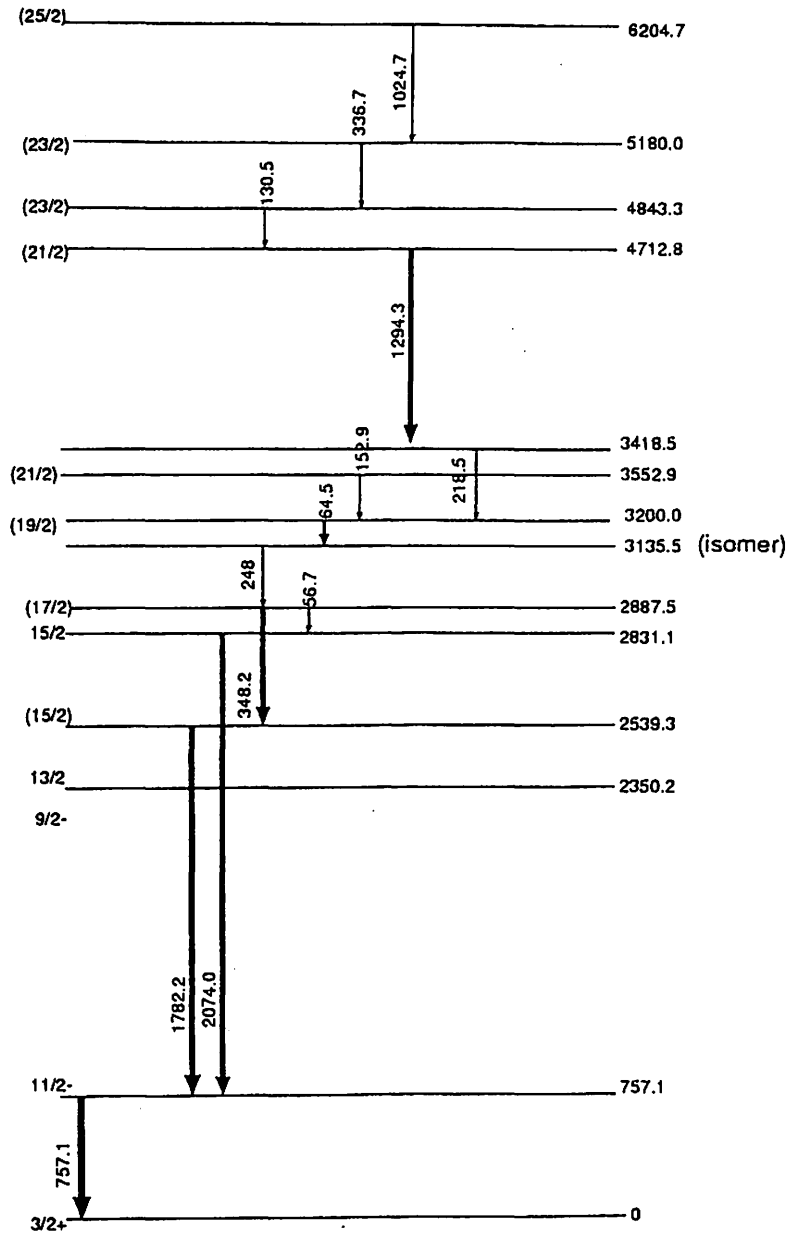

Fig. 3. A proposed level scheme of ^{141}Nd.

I. 3. Development of Low Energy Hyperpolarized Radioactive Isotope Beams

Miyoshi H., Ueno H.*, Asahi K.*,**, Ogawa H.*, Kameda D.*, Kaihara J.*, Sato W.**, Watanabe H.**, and Shinozuka T.****

*Department of Physics, Tokyo Institute of Technology, Oh-okayama 2-12-1, Meguro-ku, Tokyo, 152-8551, Japan**
*Institute of Physics and Chemical Research, Hirosawa 2-1, Wako-shi, Saitama, 351-0198, Japan***
*Cyclotron and Radioisotope Center, Tohoku University****

A number of nuclear moments were measured during the last decade, by using spin-polarized beams from the fragmentation reaction combined with the β-NMR method. This approach, however, requires several conditions to be fulfilled: One is to find a suitable host material so that the polarization of the implanted nuclei is maintained for a certain length of time. The spin relaxation time is very sensitive to the chemical properties of an implanted atom and the host material. The size of the β-ray asymmetry parameter, which largely determines the performance of the measurement, is another important factor. To avoid the difficulties forecast in such requirements when the measurement is extended to the heavier mass region, we attempt to develop a method which involves a low-energy spin-polarized radioactive isotope (RI) beam, which we call the Atomic-Beam RI Polarization method (ABRIP). The advantage of this method is that neither special host material nor a large β-ray asymmetry is required.

In the following, a method to produce low-energy spin-polarized RI beams is proposed. First, the RI atoms are stopped in a noble gas contained in a cell. The temperature of the gas is kept as low as 90 K. Then, the RI atoms emerge from the cell in a jet of gas into vacuum. A nozzle[1] is mounted on the exit of the cell so that the gas spouts out at forward angles. The spread of the angles of the gas flow can be set within 3 - 4 degrees, as reported in Ref. [1]. A schematic view of the setup is shown in Fig. 1.

A hexapole magnet is installed to converge the beam from the nozzle of the cell. The force on the atoms in a strong magnetic multipole field, $\boldsymbol{B}(r)$, is given as

$$\boldsymbol{F}(r) = -\left[-\mu \cdot \boldsymbol{B}(r)\right] = \mu_{\parallel} \nabla \boldsymbol{B}(r) , \qquad (1)$$

where $\mu_{\parallel} = \mu \boldsymbol{B} / B$ is a component of the atomic magnetic moment parallel to $\boldsymbol{B}$ and $B(r) = |\boldsymbol{B}(r)|$ is the strength of the field. The field distribution $B(r)$ within the magnet bore can be

calculated using formulae derived by Halbach[2]. For a hexapole magnet consisting of M wedge-shaped segments, one finds:

$$B(r)=\frac{\left(\frac{r}{r_i}\right)^2 B_0 \frac{3}{2}\left(1-\left(\frac{r_i}{r_o}\right)^2\right)\cos^3\left(\frac{\pi}{M}\right)\sin\left(\frac{3\pi}{M}\right)}{\left(\frac{3\pi}{M}\right)}, \qquad (2)$$

where r_i and r_0 denote the inner and outer radii of the magnet, respectively, and B_0 the residual field. In our calculation, the hexapole magnet is assumed to consist of 24 segments of permanent magnets. The magnetic field at the pole tip is about 1.5 T. The radius r_i is varied over a region 0.5 - 3.0 cm while r_0 is fixed at 7.5 cm. Comparison of the hexapole $B(r)$ obtained from eq. (2) is compared with the result of numerical calculation using OPERA[3] code in Fig. 2. The $B(r)$ field evaluated from Eq.(2) is in good agreement with the OPERA result. We therefore employed the $B(r)$ value from Eq.(2) to simulate the particle motion in the hexapole field. In Fig. 1, the simulated trajectories for atoms with spins parallel to the field (low-field seekers) are shown, where convergence of the beam is apparent. At the final stage, a quadrupole magnet is installed.

The atoms are spatially selected according to their electron spin following the Stern-Gerlach principle (eq.(1)): Because of the field gradient in radial direction produced by the hexapole magnet, the atoms with $m_s>0$ are converged towards the magnet axis, while those with $m_s<0$ are deflected away from the magnet axis. Thus, the geometry and pole tip field of the quadrupole magnet is designed such that in the ideal case the atoms with $m_s<0$ are transmitted into the entrance of the detector with full transmission efficiency whereas those with $m_s>0$ are completely diverged out.

In the low-field region with a flat field B_0, located between the hexapole magnet and the quadrupole magnet, an RF field is applied in order to induce transitions between different spin states. The entire setup is arranged so that when the frequency ν of the RF field is off the resonance, the detector located behind the quadrupole magnet counts no transmitted particles. When the resonance condition $\nu = \nu_0$ is met, the spin transition occurs and the deflection of the flight paths due to the quadrupole field turns and results in counts at the detector (Fig. 3). Thus the RF resonance is identified unambiguously through an abrupt appearance of the counts at $\nu = \nu_0$ on the way of the ν scanning. The expression for ν_0 contains the nuclear g-factor and quadrupole moment as well as the electron g-factors, and therefore expriment al ν_0 value for several different B_0 setting allow nuclear μ and Q moments to be extracted. Furthermore, the transmitted atoms with the RF resonance executed, involve only a specific (combination of) m_I value(s), thus leading to the realization of a nuclear spin polarization.

The schematic view of the gas-cell nozzle is shown in Fig. 4. In the nozzle, the pressure(P), volume(V), temperature(T) and density(P) of the carrier gas follow relations

$$PV = nRT, \tag{3}$$
$$PV^{\gamma} = \text{const.}, \tag{4}$$
$$\rho Sv = \text{const.}, \tag{5}$$
$$\rho(x)v(x)dv = -dP, \tag{6}$$

where n and v are the quantity of the carrier gas in mole and the gas flow velocity, while R and γ are the gas constant and the Sommerfeld constant, respectively. S(χ) stands for the cross sectional area of the nozzle at position χ. Solving the combined equations (3)--(6), the following expressions for v, T and P are obtained:

$$v(x)^2 = \frac{2}{\gamma - 1}\frac{\gamma RT_0}{Mass}\left[1 - \frac{T(x)}{T_0}\right], \tag{7}$$

$$\frac{T(M)}{T_0} = \frac{1}{1 + \frac{1}{2}(\gamma - 1)M^2}, \tag{8}$$

$$\frac{P(M)}{P_0} = \frac{1}{\left[1 + \frac{1}{2}(\gamma - 1)M^2\right]^{\frac{\gamma}{\gamma - 1}}}, \tag{9}$$

where M is the Mach number. We require that the pressure of the outlet gas does not exceed 10^{-2} Torr, in order for the outlet gas to be a molecular flow. For $M=10$ *and* $\gamma = 3/2$, this means that the base pressure P_0 inside the cell should fulfill $P_0 \leq 1$Torr according to eq. (9). Equation (8) tells that the temperature of the outlet gas is 2.0K, if the initial temperature of the gas is 90K. Then, the velocity of the outlet gas is $v \cong 300$ m/s. The simulation results shown in the Fig. 1 is based on these values, where the S/N ratios around 5 are obtained. Here the S/N is defined as the ratio of the number of counts obtained at the RF resonance to that obtained off the resonance.

In Table 1 we list the simulated performances of the apparatus. Here, the transmission f_{trans} is defined as the ratio of the number of RI atoms reaching the detector to that of the atoms released from the nozzle. The "total efficiency" ε_{total} is a product of several factors: $\varepsilon_{total} = f_{trans} \cdot \varepsilon_{det} \cdot \varepsilon_{RF} \cdot P_{stop}$, where ε_{det}, ε_{RF} and P_{stop} are the detection efficiency, the RF transition efficiency and the probability for the atoms to stop within the gas cell, respectively.

In our simulations, the degree of polarization is evaluated as exceeding 97%. Thus, although the total efficiencies may not be very high, the resonance detection with very high

S/N ratio is expected to be realized, enabling powerful moment measurements for nuclei in regions far from stability.

References

1) Hiller W.J. and Schmidt-Ott., Nucl W.-D., Instr. and Meth. **139** (1976) 331.
2) Halbach K. Nucl. Instr. and Meth. **169** (1980) 1.
3) OPERA-2d and OPERA-3d/TOSCA, Vector Field, Ltd., Oxford, England.

Table 1. Simulation result for the transmission and total efficiency for various mass numbers of RI atoms. For the definitions of the transmission and total efficiency, see text.

A	RF	Transmission(%)	Polarization(%)	Total efficiency
10	ON	25.94	100.00	2.91825E-6
	OFF	0.58	86.21	
20	ON	25.38	100.00	2.85525E-6
	OFF	1.06	52.83	
30	ON	24.01	99.67	2.70113E-6
	OFF	1.22	54.10	
40	ON	22.62	99.65	2.54475E-6
	OFF	1.42	46.48	
50	ON	20.65	99.23	2.32313E-6
	OFF	1.68	34.52	
60	ON	18.69	98.72	2.10263E-6
	OFF	1.86	30.11	
70	ON	17.97	98.55	2.02163E-6
	OFF	1.98	24.24	
80	ON	16.36	97.80	1.8405E-6
	OFF	2.15	16.28	

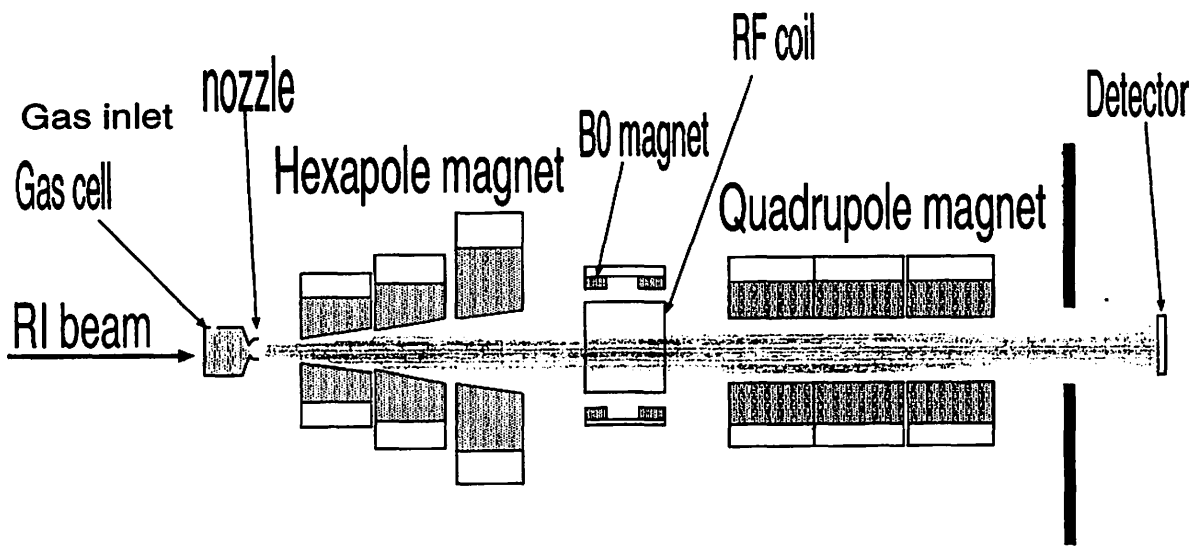

Fig. 1. Schematic view of the ABRIP device. The indicated trajectories for RI atoms are the results of simulation when the RF field is applied.

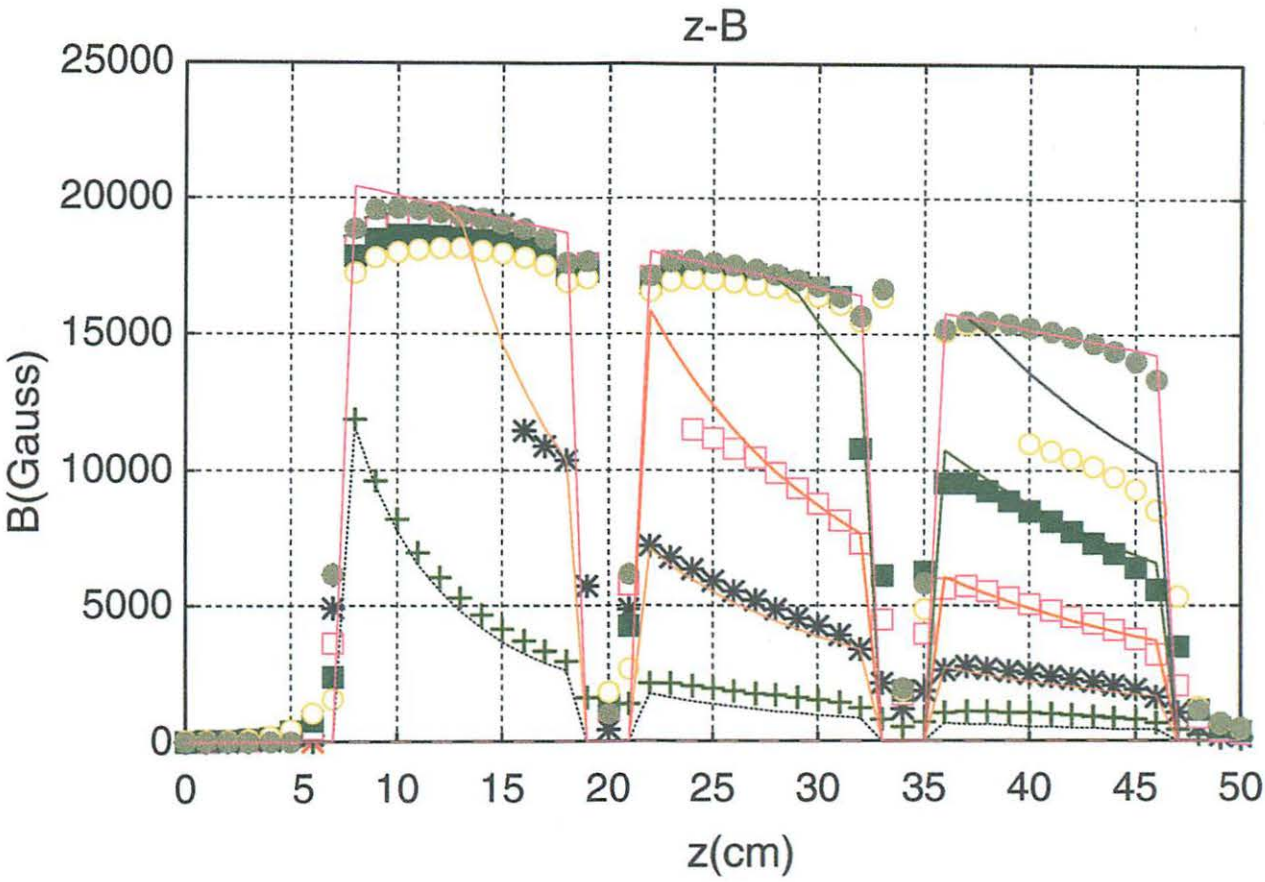

Fig. 2. Comparison of $B(r)$ field obtained from Eq.(2) in the text (dots), with the simulated value from the code OPERA[3] (dotted lines). The three hexapole magnets are assumed to be 12cm long each with 2cm interval spacing.

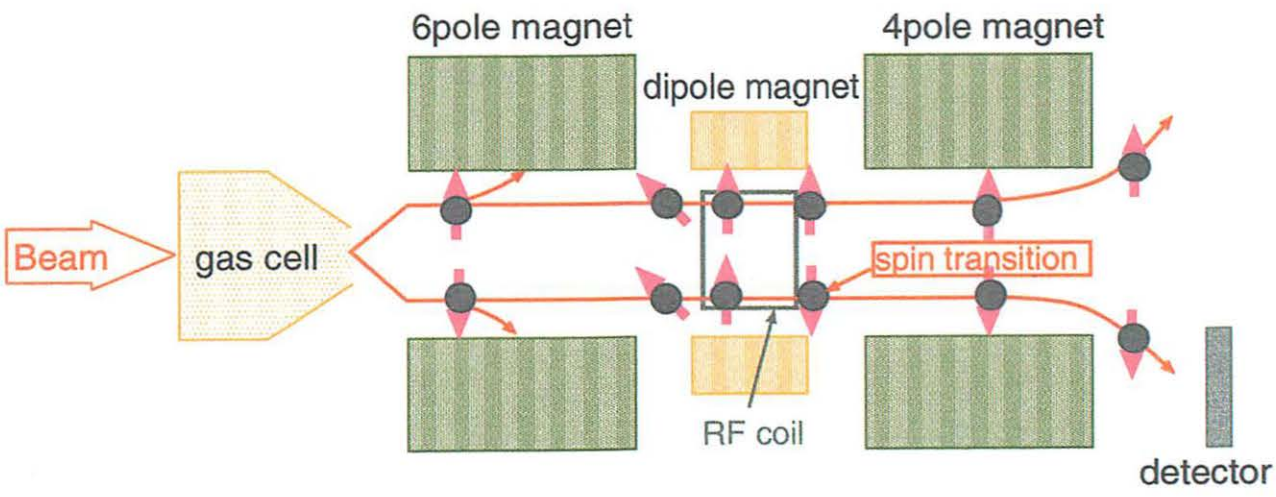

Fig. 3. Schematic representation of ABRIP. The principle is explained in the text.

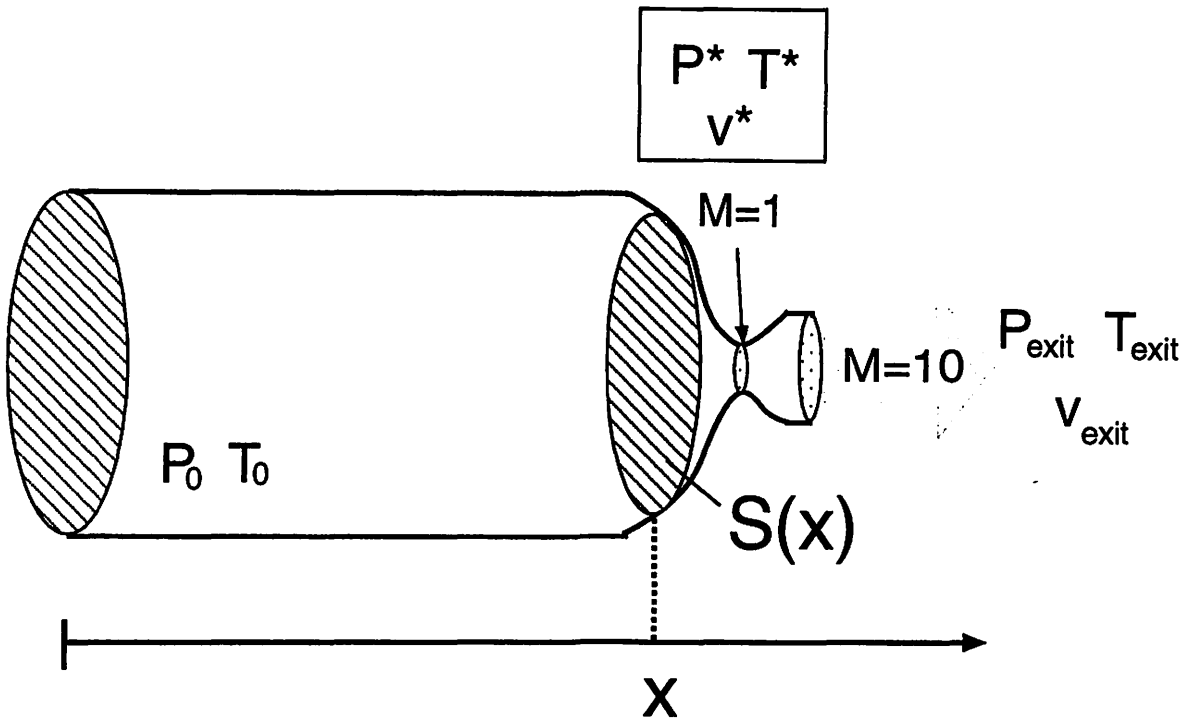

Fig. 4. The view of the gas-cell nozzle. For the form of the nozzle, refer to the ref. (1).

I. 4. Study of Neutron Induced Nuclear Reactions at CYRIC

Hirose K., Inoue M., Kanda H., Kobayashi Y., Maeda K., Orihara H.**, Shinozuka T.**, Suzuki H.**, Terakawa A.**, Terasawa T.*, Utoyama M., and Yamaguchi Y.*

Physics Department, Graduate School of Science, Tohoku University
*Laboratory of Nuclear Science, Tohoku University**
*Cyclotron and Radioisotope Center, Tohoku University***

Data measured by neutron-induced reactions are useful to explore the nuclear isospin structure in comparison with investigations with proton beams. Until now, they have been limited because of difficulties to use clean- and intense- monoenergetic neutron source in the intermediate energy region. The scarcity of neutron-induced reaction data makes the understandings of the nuclear isospin structure to be ambiguous. In order to settle the questions in isospin-related problems, we are going to focus to accumulate the neutron-induced reaction data, especially in the few nucleon system. In this article, we report the brief summary of the neutron beams and the proposed $^2H + n$ experiments[1,2] in the wide kinematical range. In this project, we are going to try to make the nucleon-nucleon interaction clear in nuclei.

One of the most realistic way to produce quasi-monoenergetic neutron beams in an energy range up to 100 MeV is the use of (p, n) reactions on light elements such as ^2H, ^3H, ^6Li, ^7Li and ^9Be. Among these elements, ^7Li is frequently used for the neutron production target material due to the simpler handling than other elements[3-5]. In the $^7Li(p, n)^7Be$ reaction, the neutron beam is consisted of two neutron groups leading to ground and the 0.43 MeV first excited state in the residual ^7Be. They are usually unresolved and limits the energy width of the neutron beam in several hundreds keV. When we assume 1 watt the energy loss in the Lithium target, the obtainable neutron beam intensity is shown in Figure 1. It is a typical situation for the neutron beam experiments, where the achievable neutron beam intensity becomes about 1 MHz on the nuclear reaction target.

The neutron beams used to perform the study of the neutron-induced reactions are produced via the $^7Li(p, n)^7Be$ reaction. A proton beam accelerated by Type-930 Cyclotron[6] is transported and incident upon an enriched ^7Li foil of 6mg/cm^2 at Experimental Hall-5 (EH-5). In Figure 2, the floor plan of EH-5 is presented. The protons incident upon an enriched ^7Li foil of 6mg/cm^2 placed in the scattering chamber, which is located at the end of the beam swinger system. The produced neutrons are collimated and impinge on the target placed at 3 m (first target position) and 10 m (second target position) downstream from the neutron

production target. A typical time profile of the neutron beam at the second target position is shown in Figure 3, where the incident proton energy was 20 MeV and the typical time spread of the beam bunch was 1 nsec corresponding to about 0.3 MeV in the neutron energy resolution. The spatial distribution of the neutron beam is also monitored by using a beam profile camera called GAMERA/NAMERA[7] in front of the first target.

In order to obtain efficient event triggers and reduced background for the $^2H(n,\gamma)$ and $^2H(n,n)$ measurements, a live deuteron target consisting of a deuterized liquid scintillator is examined[7]. The main component of this scintillator is the deuterized benzene (C_6D_6), which was fabricated by ELJEN Technology Ltd (EJ315). A cylindrical aluminum can with internal dimensions of 10.6 cm in diameter and 13.1cm in length is utilized to contain the scintillation material. The density and volume of EJ315 are 0.954 g/cm^3 and 1000 cm^3, respectively. The proton contamination in deuteron is approximately 0.7%. The scintillator is optically coupled to a R1250 (HAMAMATSU Photonics) photomultiplier tube. A pulse shape discrimination technique was employed to separate hadron signals from photon- and electron-signals. In Figure 4, an analyzed pulse shape spectrum is shown. We can observe an enough separation between the electron and hadron events for the live deuteron target.

To summarize the present development of the neutron beam and the experimental equipments for the measurements of the $n + {}^2H$ reactions, we carried out to investigate the performance of the neutron beams and detectors for the $^2H(n,\gamma)$ and $^2H(n,n)$ experiments at CYRIC. Installed apparatuses to produce the monoenergetic-neutron beams have been tested. We found that the quality of the neutron beams satisfies the requirement to carry out the study of the neutron-induced reaction. The detectors for the proposed neutron beam experiments on deuteron target have been equipped and tested. In conclusion, the neutron-related nuclear physics including the presently described projects are still actively in progress at CYRIC.

References

1) Huhn V. *et al*, Phys. Rev. Lett **85** (2000) 1190.
2) Mitev G. *et al*, Phys. Rev. C**34** (1986) 389.
3) Orihara H. *et al*, Nucl. Instrum. & Methods, **188** (1981) 15.
4) Orihara H. *et al*, Nucl. Instrum. & Methods, **A257** (1987) 189.
5) Niizeki T. *et al*, Nucl. Instrum. & Methods **A287** (1990) 455.
6) Shinozuka T. *et al*, *CYRIC Annual Report*, (2000).
7) Kobayashi Y., Master thesis (Tohoku University), 2000.

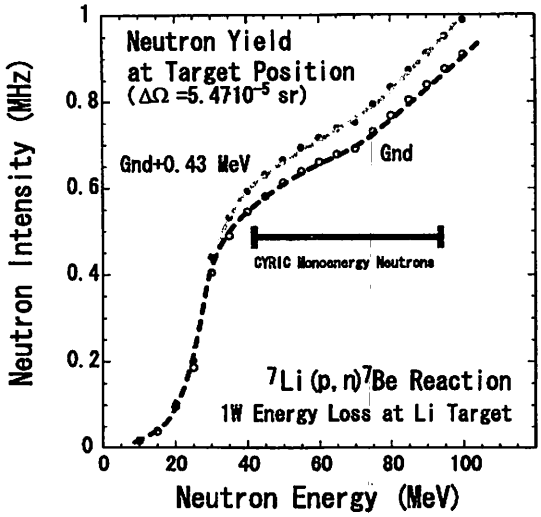

Fig. 1. Neutron yields at the reaction target position by using the ^{7}Li(p, n)^{7}Be reaction. The energy loss in the Lithium target is assumed 1 watt corresponding to $\Delta E = 1$ MeV at $I_p = 1$ μA.

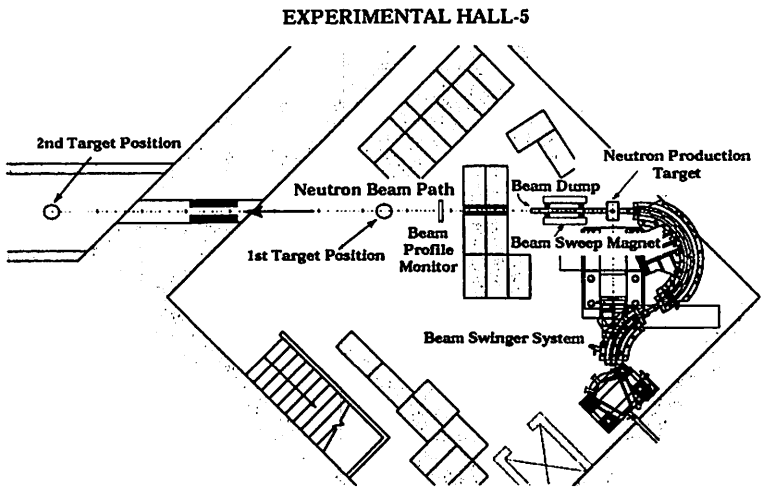

Fig. 2. Floor plan of Experimental Hall-5.

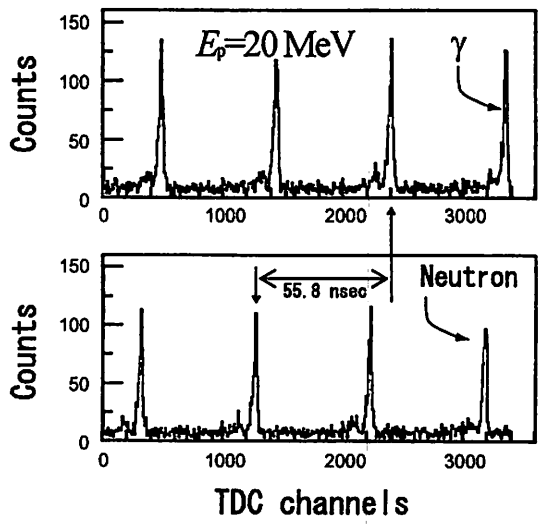

Fig. 3. Time-of-flight spectra, where signals from a neutron detector and RF signals from the cyclotron are used for the start and stop signals.

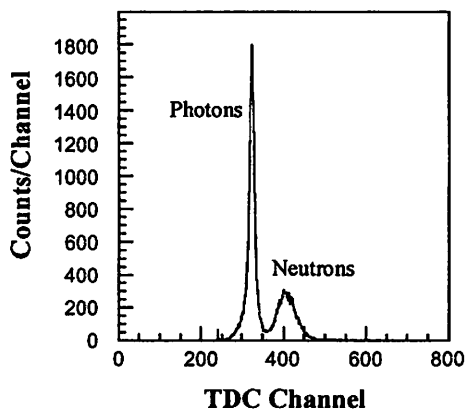

Fig. 4. PSD spectrum for EJ315 scintillation counter.

I. 5. Replacement of the Tohoku Cyclotron (From K=50 MeV to 130 MeV)

Shinozuka T., Fujita M., Terakawa A., Yamazaki A., Tanigaki M., Misu T., Fujioka M., and Orihara H.

Cyclotron and Radioisotope Center, Tohoku University

The AVF cyclotron at CYRIC has been replaced from K=50 MeV AVF cyclotron to K=130 MeV AVF cyclotron. All of the missions for replacement is almost completed. It has started the commissioning for beam tuning and has partly been opened for experiments. Based on the successful results of the 20 years-long multi-purpose use of Cyclotron and Radioisotopes, replacement of the cyclotron with a larger dimension K=130 MeV one, and construction of experimental facilities have been authorized by Japanese government in 1998 and 1999 financial years. After the final operation of old cyclotron with acknowledgement on April 9 1998, the old cyclotron was dismantled and taken away from the cyclotron vaults.

The 110-ton iron yoke, which was divided to 12 pieces, the main coils and the magnetic poles of main constituents of the old cyclotron have been saved for reuse as dipole magnet for spectrometer with treatment of painting to prevent the rusting. The other constituents, mainly Dee electrodes, earth plates with copper materials and vacuum chamber, were cut out for small pieces and stocked in the drums. From summer 1998, the cyclotron vault was refurbished for the fortification of base columns for emplacing the yoke (201 ton) of the new cyclotron and for remodeling of the concrete walls of the cyclotron vault to make a space for installing the new cyclotron.

The new cyclotron has a bending limit of 130 MeV for ^{4}He particle and a focusing limit of 90 MeV for proton. The main characteristics of the cyclotron are shown in Table 1. The cyclotron is of the model 930 of Sumitomo Heavy Industries with a radio-frequency range of 11 – 22 MHz, and is basically the same model as that of Takasaki Laboratory of the Japan Atomic Energy Research Institute.

Furthermore, the cyclotron has been done on some improvements.

1) To avoid beam current instability caused by temperature drift of the yoke, the heat flow from the mail coil to the yoke is blocked by an extra water cooled thin panels between the main coils and the yokes of the upper and the lower.

2) To obtain more intense beam of protons and deuterons, it had a negative ions acceleration mode by turning over the magnetic field direction and by adding the device of

stripper foil for negative ions on 650 mm position from the center of cyclotron. On that account, the cyclotron has two beam exit ports. In the case of negative Hydrogen acceleration, the maximum proton energy has come to 50 MeV according to the 650 mm extraction (electron stripping) radius. This radius is decided from the viewpoints of the electron dissociation limit for negative Hydrogen (70 MeV under maximum magnetic field) and the extraction orbit of protons after stripping of electrons from the negative Hydrogen.

This improvement enables to get an advantage of intense 50 MeV proton beam more than several hundred microampere.

After a successful installation of cyclotron, electrical tests and checks have been done with totally computer controlled system developed by ours; those are positioning checks of the movable devices, magnetic field checks, RF system and vacuum and so on. The power supplies for magnet system and RF system are also newly developed. We have adopted the high frequency switching regulation method for all of the stabilized high current DC power supplies, even for the power supply of main coil over 1000 A. This is realized with recent technological developments of power switching devices of semiconductor and precise current sensing devices. This might be a first cyclotron, which has two exit beam lines and is totally controlled by the switching regulated power supplies. The RF system consists of computer controlled voltage and phase stabilizing devices.

Since the cyclotron has two exit beam lines, the new external beam line is reconstructed. Two beam lines are joined at the switching magnet in the cyclotron vault for delivering the beam for 5 target rooms. In order to obtain an effective use of cyclotron beam, this switching magnet is designed as alternating one, which has a 1 sec time constant for response. This enables a beam time-sharing for concurrent uses of cyclotron beam at several target positions of experiments.

The cyclotron has an axial injection system and has accepted the ions through the injection beam transport lines of underground. It has three ion source stations. The 1st one is located on the underground of cyclotron vault as negative Hydrogen supplier, the 2nd and 3rd are on the underground of another room as positive ions supplier up to Argon's. The negative Hydrogen ion source is based on the sputter ion source of multi-cusp type. The positive ion source is the all-permanent magnets 14 GHz ECR ion source, which is newly designed by ours.

The whole water-cooling system of temperature controlled and de-mineralized has also been reconstructed according to the specification of increased power consumptions of new cyclotron and extended beam transported system.

On March 6 2000, the new CYRIC cyclotron had a first acceleration. Further commissioning and developments are progressing on.

The details about the computer control system, RF system and ion source development are presented in this issue.

Table 1-1. Specification of the new AVF cyclotron.

Electromagnet System	Weight	200 ton
	Extraction Radius	923 mm
	Number of Sector	4
	Max. Average Induction	19.6 kG (over Hill)
	Main Coil Power	230 kW
	Number of Trim Coil	12 pairs
Radio-Frequency System		
	Number of Dee's	2
	Frequency	11-22 MHz
	Max. Dee Voltage	50 kV
	Max. RF Power	70 kW x 2
External Ion Source		
	Negative ion	Cusp-type
	Positive ion	ECR, 14GHz
	Positive ion	ECR, 14GHz, 18GHz(Plan)

Table 1-2. Beam energies of the new AVF cyclotron.

a) Positive ion acceleration

Accelerated Particle	Energy (MeV)	Beam intensity (microA)
P	10-90	50
D	10-65	50
3He	20-170	50
4He	20-130	50
12C	20-397	5p
14N	20-463	5p
16O	20-530	5p
20Ne	20-662	5p
32S	20-698	3p
40Ar	20-744	3p
84Kr	20-695	3p
129Xe	20-748	1p

b) Negative ion acceleration

Accelerated Particle	Energy (MeV)	Beam intensity (micro A)
p	10-50	300
d	10-25	300

I. 6. RF System for the New AVF Cyclotron at CYRIC

Tanigaki M., Chiba S., Fujita M.**, and Shinozuka T.***

Research Reactor Institute, Kyoto University, Noda, Kumatori, Osaka, 590-0494 Japan
*Sumitomo Accelerator Service, Co, Ltd,**
*Cyclotron and Radioisotope Center, Tohoku University***

A new RF system for the newly-constructed K = 130 MeV AVF cyclotron at CYRIC is designed and constructed. This RF system is characterized as the phase control system based on the powerful digital phase shifter and the compatibility with a new controlling system based on PLC(Programmable Logic Controller) and Lab View from National Instruments connected over TCP/IP, which is the controlling architecture of the new cyclotron at CYRIC.

The block diagram of this RF low level system is shown in Fig. 1. Basic specifications of the present system are summarized in Table 1. As shown in the diagram, this system has one signal generator and two independent signal processing circuits, each for the CH1 and CH2 dee terminal, respectively. All the low level units are placed in a box with temperature control to achieve the high stability on both phase and gain. RF signal from the signal generator (SG) is divided to two lines for two respective dee terminals (CH1 and CH2) in the cyclotron acceleration chamber. Automatic phase controller (APC) in each line controls and stabilizes the phase of RF field at the dee terminal. In this cyclotron, there are so called 0 mode and π mode, corresponding to the phase difference between CH1 and CH2 of 0 ±30 degrees and 180 ±30 degrees, respectively. This phase difference is achieved by changing the amount of phase shift in CH2 from 0 to 360 degrees, while CH1 is always

synchronized to SG. The intensity of RF field at each dee terminal is controlled by the gain of the automatic gain control unit (AGC). AGC is consisted of a series of two independent amplifiers with variable gain (0 ~ -10 dB) and a pulse modulator between them. The amplifier at younger stage is used for the voltage setting and the other is for the negative feed back (NFB) loop. The pulse modulator is used during the start-up sequence to avoid the multi-pactorings at low dee voltage. The pulse modulation frequency is usually ~100 Hz. Then the signal is amplified up to 25 W to drive the 50 kW power amplifier on each dee terminal, which is a series of one 4CW800 and one 4CW25000. Since the Q of the dee terminal is very high (Q ~5000, typically), a short plate in the resonance cavity of every dee terminal is used just for the coarse resonance, the fine tuning and the cancellation of the

resonance shift due to the thermal expansion during the operationis are achieved by moving a compensator which is electrically coupled with the dee terminal. In the present system, the compensator controller has the capability to adjust dynamically the position of the compensator to make on resonance condition by following the phase shift between the voltages of the control grid and the plate terminal of 4CW25000. The voltage and phase at dee terminals are monitored via pickup dividers, which supply the monitoring signal to APCs, AGCs and compensator drivers for the phase locked loop (PLL) and NFB in each channel.
One feature in the present system is that each line has its own independent phase controller. While APC for CH1 (APC1) always synchronize to SG, APC for CH2 (APC2) varies the phase of CH2 dee terminal from 0 to 360 degrees by DSP (Digital Signal Processor) to make the relative phase difference between CH1 and CH2. Since the phase of both channels is from the same SG, the stability of the phase difference between these channels is expected to be as good as that of SG. In our preliminary phase stability test, the fluctuation of the phase difference between CH1 and CH2 is as small as 0.1 degrees, which is almost the lower limit of the phase difference detection with our vector volt meter.

The advantage of the present configuration is thatthe electrical length adjustment between CH1 and CH2 is not required. In conventional RF systems, one phase shifter with narrow phase shift range supplies the required phase shift between CH1 and CH2.

Therefore, the electrical length difference of both channels between the phase shifter and the dee terminal directly cause the offset of the phase set range at dee terminal. Since only 2 cm of the total length difference corresponding to the phase offset of 1 degree in the present frequency range, the electrical length must be strictly adjusted. This kind of adjustment is troublesome and expensive because the careful design not only on the cable length but also on print patterns and the wiring are required. In the present system, the phase offset is easily compensated by giving a appropriate phase offset to the powerful digital phase shifter in APC2.

Another feature in this RF system is that the entire system is controlled by PLC and LabView. All sequences are constructed by the software on PLC or LabView, so the maintenances and the future upgrades on the sequences are easily performed. Further more, the compatibility with other remote devices or systems are very good because the remote communications are based on the standard TCP/IP protocol via the ethernet module on PLC. Basically, the program called "vi" written on Labview on the remote computer is responsible for the man-machine interface and overall control. PLC is mainly responsible for or the interface between the RF system and the remote computer and for some low level sequences where the faster responses are required than the network communication speed with the remote PC over TCP/IP(~500 ms typically). Such faster responses are required in the case of discharges at the terminal or the interlocks. In fact, there are a few hardware logic circuits for the control, but these are only limited in the sequence where the very quick response is required, such as the detection of the discharge.

The start-up sequence is shown in Fig. 2. In the initial stage, each dee terminal is driven by 2 kW RF with pulse modulation. "On resonance" condition is searched by sweeping the position of compensators. The dee terminal is regarded as "on resonance" as the dee voltage rise up more than a certain threshold(usually ~4 kV). The pulse modulation and the position sweep of the compensator are stopped. The compensator is dynamically controlled by the driver to establish the "on resonance" condition. The dee voltage gradually sweeps up/down to the desired voltage by changing the gain of AGC under the control of the vi on the remote computer. When the output voltage is in the range where the stabilization of AGC is available (which is usually more than ~90 % of the set voltage), the NFB loop converges the dee voltage on the set value. Once the start-up sequence is completed, both the amplitude and phase of the dee voltage have been kept in a high stability ($\Delta V/V$ ~1×10^{-3}, $\Delta\phi$ ~0.1 degrees) by NFB and PLL during the beam acceleration.

During the operation, discharges at dee terminals sometimes occur. Smooth recovery from the discharge is very important to avoid the damages at dee terminals, power amplifier and its power supply which are caused by the following multiple discharge. The discharge during the operation is categorized into three types,

1) Minor discharge; very small voltage drop within the gain control range of AGC,
2) Moderate discharge; voltage drop over the regulation range of AGC, but more than the threshold of CW/pulse operation,
3) Severe discharge; voltage drop less than the CW/pulse operation threshold.

In the present system, the gain control at AGC by the NFB loop is responsible for the recovery from the minor discharges. It takes several hundreds μs, which is much shorter than the period required for a communication between PLC and RF system (~10 ms) or between PLC and the remote computer (~500 ms).

The moderate discharge process lasts for several ms, so the output from the RF low level is turned down to the level corresponding to the dee voltage of 15 kV to minimize the damage. It takes ~10 ms for the PLC to detect the discharge due to the limit of the scan speed at the I/O modules in PLC, so the hardware logic in AGC is responsible for this turned down process to carry out the quick response (~400 μs). Once the PLC detects the discharge, PLC gives the parameter corresponding to 15 kV to the AGC and notify this discharge to the vi on the remote computer.

In the case of severe discharge, the output from the RF low level is turned down to the level corresponding to the dee voltage of 15 kV, which is the same process in the case of the moderate discharge. Then the RF system simply starts the very beginning of the start up sequence.

Basically, the RF system has been accomplished and working well. With this new

RF system, the first acceleration of α particle at 50 MeV was succeeded on 6th March, 2000. Currently, the parameters for the stable operations on the numerous acceleration conditions have been collected and some minor tunings regarding the man-machine interface and the compatibilities with control programs for other parts of the cyclotron have been performed.

Authors are grateful to Y. Fukumoto and Y. Kumada at Sumitomo Heavy Industries, and A. Fukazawa and J. Ohashi at Thamway for their fruitful discussions and technical supports during the design and construction.

Table 1. Basic Specification of the RF system.

Dee Voltage	5 ~ 60 kV
Dee Voltage Stability	$< 2 \times 10^{-3}$
Frequency	10.5 ~22 MHz
Q at Dee Terminal	4000 ~7500
RF Low Level Output	25 W max
RF ON/OFF Dynamic Ratio	60 dB (typ.)
Phase Shift	0 ~360 deg.
Phase Resolution	0.0625 deg. step
Phase stability	$< \pm$ 0.2 deg.

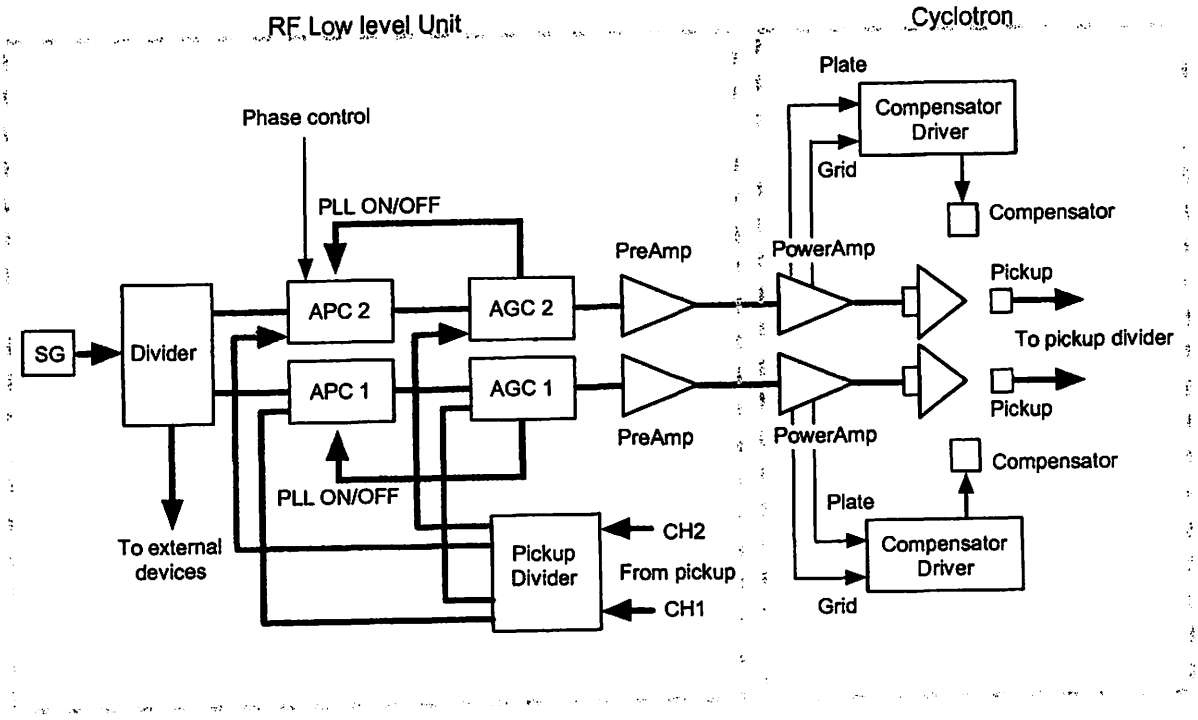

Fig. 1. Block Diagram of the RF system for the new cyclotron at CYRIC.

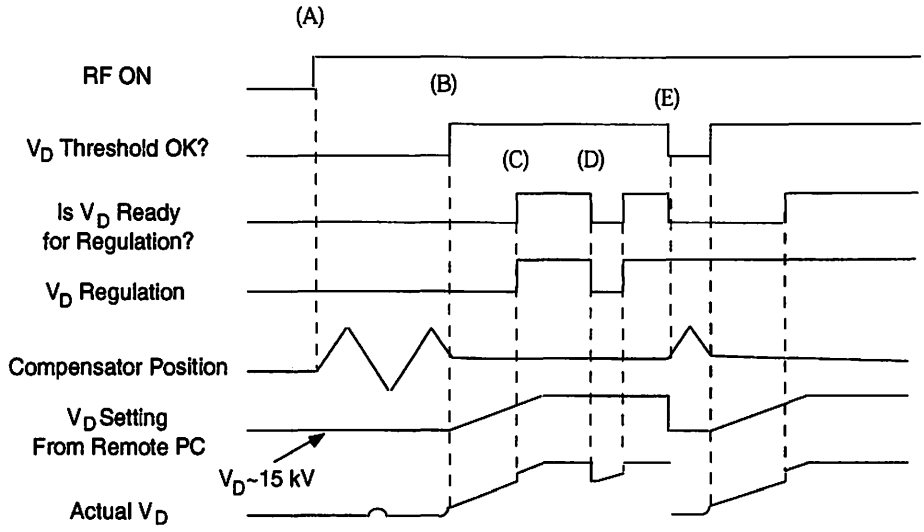

Fig. 2. Start up sequence of the RF system. By "RF ON" (A), the compensator starts the position sweep to find the resonance point. Once the resonance point is found (B), the compensator stop the sweep and Vd setting voltage is gradually risen up by the remote PC. Then real Vd comes up in the regulation range, the Vd regulation is turned on (C). (D) and (E) are the recovery process of the moderate and severe discharge, respectively.

I. 7. A Control System for the New AVF Cyclotron at CYRIC

Fujita M., Chiba S., Ohmiya Y.*, Takahashi N.*, Tanigaki M.**, Terakawa A., and Shinozuka T.*

Cyclotron and Radioisotope Center, Tohoku University
*Sumitomo Accelerator Service, Co. Ltd.,**
*Research Reactor Institute, Kyoto University, Noda, Kumatori, Osaka, 590-0494 Japan***

A control system for the new AVF cyclotron (K=110 MeV) at CYRIC[1] is designed and constructed. The old AVF cyclotron[2], which had K=50 MeV and worked for 25 years, was manually controlled through the whole hard-wiring system. This system was difficult to reuse for the new cyclotron, since they were designed specially for the 680-type cyclotron and its incidental devices. Therefore, we decided to dispose of the old control system, and to construct completely new system. In this report, we describe the characteristics of this new control system in addition to the beam current measurement system, which is also constructed for the new cyclotron.

On the occasion of design for the control system of new cyclotron, we have adopted the following guiding principles;1) totally real-time computer control system,2) robust networking among rooms and instruments for realize less wiring as possible,3) only for human safety by hard wirings.

There are a large number of parameters or statuses to control and monitor of cyclotron whole system, such as vacuum valves, thermal switches, power supplies, motors and so on. The PLCs (Programmable Logic Controller), which are widely used for factory automation, is one of the best candidates for the purpose. The Ladder programs of PLC, which are described by relay-coil diagrams, are very powerful for the sequence control and are more efficient to develop the software. One PLC unit is consist of some CPU modules running the Ladder programs and some useful modules such as digital I/O, analog I/O, Ethernet and so on. With them, one can combine the suitable modules depend on the purpose. This makes easy to modify the system.

APLC unit can be divided into a main block and sub blocks. The main block has CPU modules and it is connected to sub blocks through the optical fiber cable. Then these PLC blocks can work just like one long unit. Since most controlled objects need some hard-wirings to handle them, it is necessary to locate PLC units close to them to reduce wires. On the other hand, it is convenient to set them far from objects in order to avoid from radiation damage in the cyclotron vaults and target rooms. Therefore, we adopt to detach main block

having CPU module from them, since a CPU module seems especially sensitive for radiation damage. However, sub blocks are still located near the targets, the length of wiring could be held to minimum.

Another remarkable feature of this system is that all PLC units can be fully handled through the network. Then TCP/IP protocols, which are the de facto standard protocols in the world, are used to establish communication between PLC and PC. This means no special device drivers need to handle the PLC. While the Ladder Language is very suitable for the sequential control, it needs some interface programs to operate. Therefore human interface programs must be developed. In our cases, all man-machine interface programs have been developed by the software Labview from National Instrument Corporation because of the advantages as follows. The Labview has a programming environment, much like C or BASIC. While other programming environments use text-based languages, Labview uses a graphical programming language, named G, to create programs in block diagram form. In addition, Labview includes libraries for data acquisition, GPIB and serial instrument control, data analysis, data presentation, and data storage. So it is efficient to develop highly intelligent programs.

The whole control system have more than twenty PLC units and more than ten computers, so the heavy traffic jam will be expected. To prevent this network jam, a server-client system is constructed. All the communications between PLC and clients are made via the server machine. All information is stored in this server, and it is send to the client PCs as requested. A server machine can reply requests from many client machines, because the communication between PC and PC is about ten times faster than that between PC and PLC.

There are more than 50 points to measure the beam current such as probes, Faraday-cups and beam-stoppers, where we must measure beam current to operate the cyclotron and beam transport line. Those are distributed extending over seven rooms (Cyclotron vault and 6 target rooms). So far, we need analog ampere meter and long cables connected with them to measure beam current.

A new beam current measurement system, based on WE7000 from YOKOGAWA Electric Company, is constructed. The WE7000 is the computer based measuring device, which has many useful performances as an oscilloscope module and a wave generator module and so on. In addition, a special module for current measurement is available. It has 4 CH input and has a wide input range from 1 nA to 10 mA full scale. At present, more than fifteen modules are available and located near the measuring points. No extra cables across the rooms are required to measure the beam current since all stations with modules are connected through the exclusive optical fibers.

The new control system for the new AVF cyclotron has been almost complete, and working without troubles. The first beam acceleration of α-50 MeV was succeeded on 6th March 2000 and the new AVF cyclotron is now used for regular work.

References

1) Shinozuka T., Fujita M., Terakawa A., Yamazaki A., Tanigaki M., Misu T., Fujioka M., and Orihara H., in this volume.
2) S. Morita et al., IEEE Trans. NS 26 (1979) 1930.

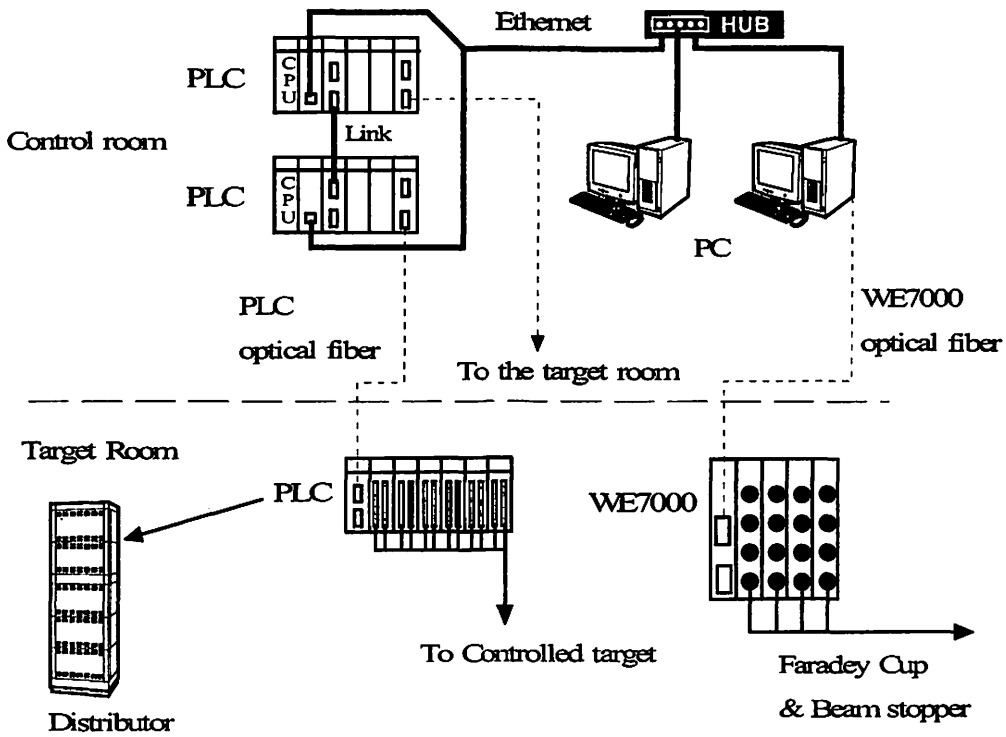

Fig. 1. The diagram of the new control system.

I. 8. Design and Construction of an ECR Ion Source with All Permanent Magnets for the New Cyclotron

Yamazaki A., Tanaka E., Fujita M., and Shinozuka T.

Cyclotron and Radioisotope Center, Tohoku University

A lot of electron cyclotron resonance (ECR) ion sources are installed in various accelerator facility. They are used not only for nuclear and particle physics but also for material and medical sciences.

ECR ion sources can be classified into two different types; with electromagnets or with only permanent magnets. Today, most of small ECR ion sources are with only permanent magnets. Now we selected the type of all-permanent magnets for the first small ECR ion source and designed its geometry.

Advantages of all-permanent magnet type ECR ion source are as follows, (1) simple power supply and cooling system because of no electromagnetic coil (2) low cost of operation (3) compactness of total size. However, this type sources have several disadvantages in comparison with the type of electromagnets, (1) weaker magnetic field (2) difficulty adjusting the distribution of magnetic field in the plasma chamber. The present ECR ion source with all-permanent magnet has been designed to overcome these disadvantages. In this paper we reported the geometry and characteristics of the source, and also reported calculated (by OPERA-3d) and measured magnetic field distributions.

Figure 1 (a) shows a cross-sectional view of the designed ECR ion source. A 550 l/s turbo molecular pump is installed at the extraction stage, and a 100 l/s turbo molecular pump is also installed at the gas injection stage. The base pressure is about 5×10^{-7} Torr at the extraction stage.

The source consists of two mirror magnets for axial confinement, a hexapole magnet for radial confinement, and three additional ring magnets for shaping and correcting a magnetic field around the resonance zone in the plasma chamber. Both the ring magnets are divided into two small rings and the directions of magnetization are leaned forward or against 30 degrees each other. The maximum magnetic field on the axis is stronger than before, while the minimum one is weaker. Three additional ring magnets are placed between the mirror magnets. This grope of magnets consists of a additional center magnet and a pair of additional side magnets with the same size. These ring magnets have magnetization directions of gradually changing from one mirror magnets to the other shown in Fig. 1. The

field strength around the minimum magnetic field on the chamber axis becomes strong and flat because of the extra magnets. Figure 2 (a) and (b) show magnetic distributions along transversal and longitudinal directions to the chamber axis, respectively. On account of a flat field, formation of an ECR zone with considerable thickness, which is called ECR volume, is expected. There are several reports that large volume of the ECR zone increases resonant electrons and as a result increases multiply charged ions[1-3], so the better performance for producing multiply charged ions is expected.

Moreover we can adjust the field distribution by means of moving the extra side magnets along the chamber axis. Figure 2 shows the results of the calculations of the magnetic field in two cases of geometry; one (solid line) is the case that extra side magnets are moved to the extra center magnet, and the other (dashed line) is that they are set away from it. In former case (shallow style in the Fig. 2) the strength of the minimum magnetic field is almost the same as the resonance value (0.518 Tesla). On the other hand, in latter case (deep style in the Fig. 2) it is weaker than that of former case and therefore a ECR zone of conventional shape is formed. This adjusting system will be useful to determine an optimum operating condition for various cases. The specifications of the designed new ECR ion source are shown in Table 1.

Figure 3 shows the measured axial magnetic field distributions (circle) compared with calculated ones (solid line). Measured magnetic field strength was about 8% weaker than calculated value around the plasma chamber. We suppose that one of the causes of this disagreement is the influence of residual magnetism in stainless steel constructing the plasma chamber.

In conclusion, we have designed and constructed an ECR ion source with all-permanent magnets for the new cyclotron. Using the three-dimensional calculation of the magnetic field, we found a new geometry of permanent magnets and field adjusting system that can overcome the disadvantages of all-permanent magnet type ECR ion sources mentioned before. This ion source was installed in February, 2001, and now in test operation. The source will provide multi-charged heavy ions in June, 2001.

References

1) Alton G.D. and Smithe D. N., Rev. Sci. Instrum. **65** (1994) 775.
2) Heinen A., Rüuther M., Ducree J., Leuker J., Mrogenda J., Ortjohann H. W., Reckels E., Vitt Ch., and Andrä J., Rev. Sci. Instrum. **69** (1998) 729.
3) Liu Y., Alton G. D., Mills G. D., Reed C. A., and Haynes D. L., Rev. Sci. Instrum. **69** (1998) 1311.

Table 1. Specifications of the designed ECR ion source.

microwave frequency	14.5 GHz
maximum microwave power	2 kW
plasma chamber length	282 mm
plasma chamber diameter	32 mm
ECR zone length	30(55) mm
ECR zone diameter	6(16) mm
maximum extraction voltage	20 kV
material of permanent magnet	NdFeB
total weight of permanent magnet	51.5 kg
cooling	water
maximum magnetic field (injection side)	1.026(1.055) T
maximum magnetic field (extruction side)	0.925(0.950) T
minimum magnetic field	0.517(0.477) T

( ) is the case that the extra side magnets are set away from the extra center magnet.

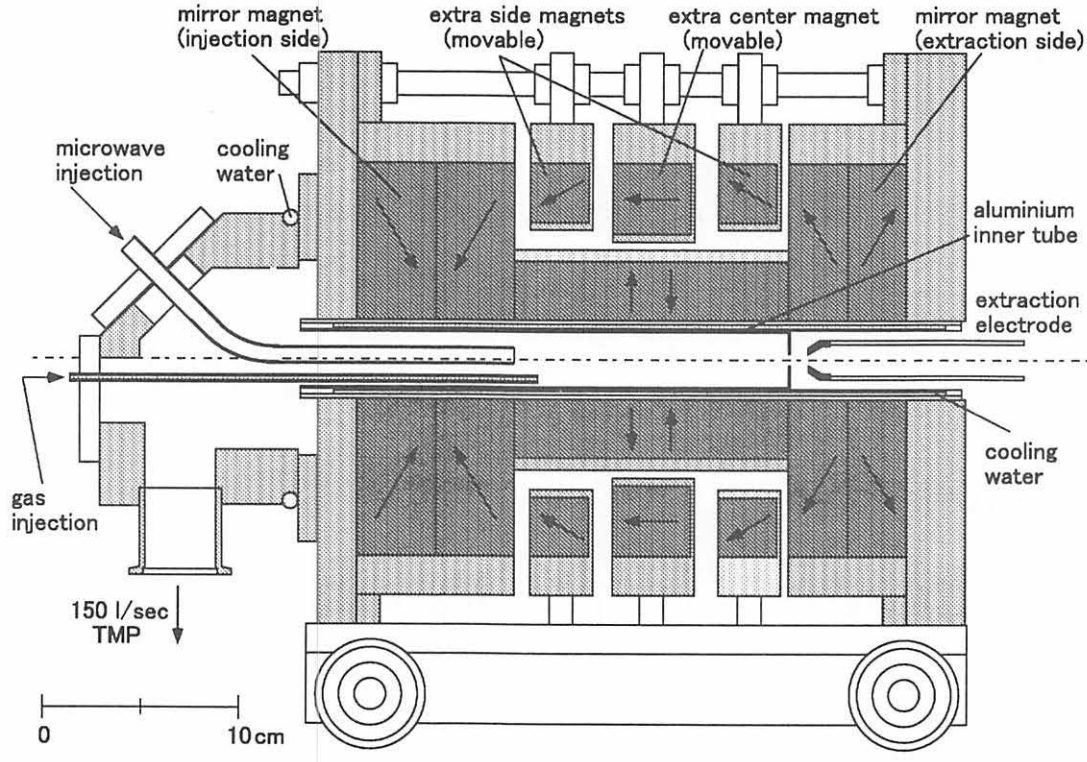

Fig. 1. Cross-sectional view of the new ECR ion source.(a)
Arrows represent magnetization directions of every permanent magnets.

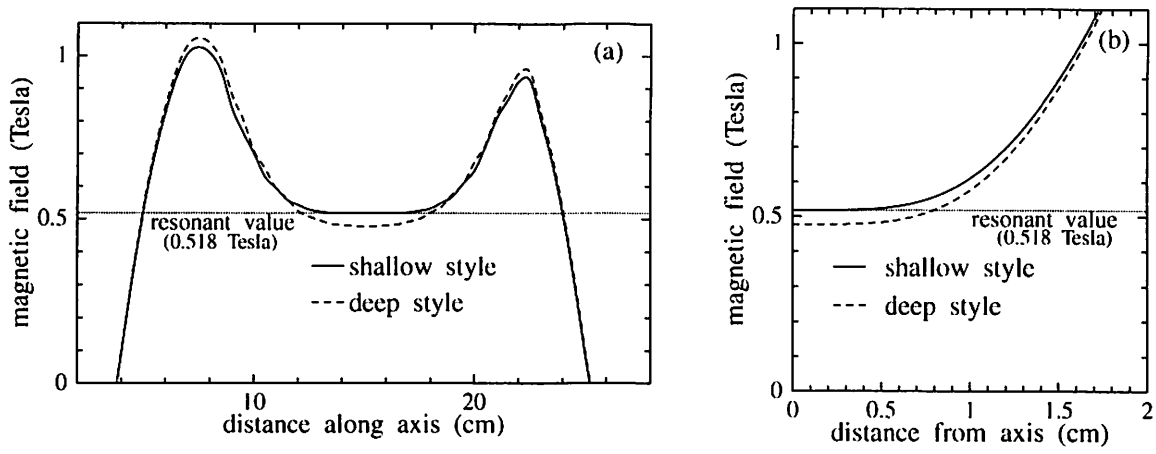

Fig. 2. Examples of the calculated (OPERA-3d) magnetic field distributions on the axis (a) and across the plasma chamber (b).

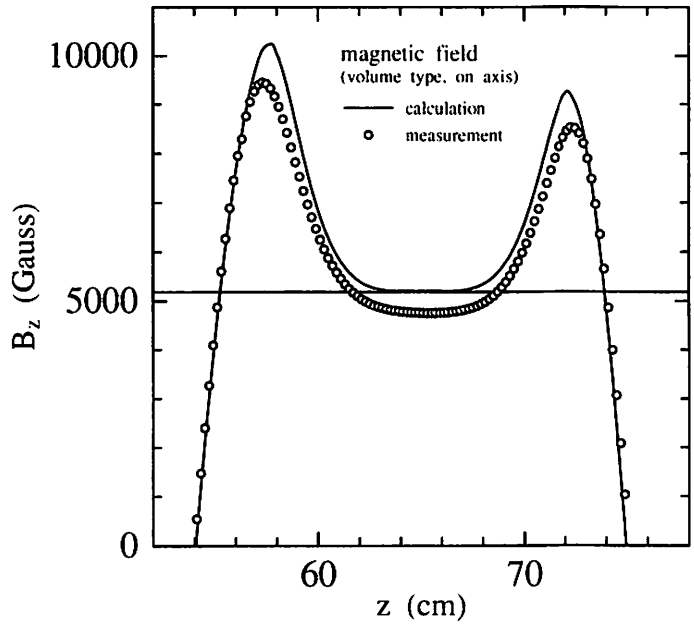

Fig. 3. Measured magnetic field distributions (circle) on the chamber axis. Also calculated value is compared (solid line).

I. 9. New Fast-neutron Time of Flight Facilities at CYRIC

Terakawa A., Suzuki H., Kumagai K., Kikuchi Y., Uekusa T., Uemori T., Fujisawa H., Sugimoto M., Itoh K., Maeda K., Baba M., and Orihara H.*

Cyclotron and Radioisotope Center, Tohoku University
*Department of Physics, Graduate School of Science, Tohoku University**

The fast neutron time of flight facilities at CYRIC has been extensively used, together with the old K=50 MeV cyclotron, for detection and momentum analysis of fast neutrons since 1977[1], being upgraded in 1988[2]. In the two decades of the last century, the TOF facilities worked as the powerful tool for studying isospin and spin-isospin excitation nuclei by the charge-exchange (p,n) reaction[3], particle transfer (d, n)[4], (^{3}He, n)[5] and (α, n)[6] reactions, and neutron scattering[7].

In 1998 and 1999 school years, the cyclotron was replaced to K= 110MeV one[8] along with the beam transport system[9] including beam swinger. Related facilities, for example, neutron detector matrix for TOF experiments have been renewed as well in these year[10].

In this report, a brief description of the new TOF facilities and results of performance test by the (p,n) reaction on ^{6}Li are given. It is remarkable that the measured time resolution of the micro-burst in beams from the new AVF cyclotron has been in the order of several hundred pico-seconds, which gives a quite nice place for fast-neutron time of flight experiments.

BEAM SWINGER AND BEAM DUMP

Figure 1 illustrates the new beam swinger by which the axis of a beam, having magnetic rigidity of 15.5 kG-m in maximum, is rotated from –5 to 110 degrees in order to make it possible to measure the angular distribution of cross sections for reaction products, setting at rest the neutron detector matrixes at distances of ~40-meter long from the target.

Accelerated beams enter through quadrupole-quartet and switching magnets into the –60 degree-bending dipole-magnet forming a image point, then enter into the second +150 degree-bending dipole-magnet which has the horizontal and vertical magnification of one in their absolute values. The beam after target enter into the beam-dump to be measured it's beam current though a beam-dump dipole magnet with a magnetic rigidity of 10 kG-m when measurement is done at forward angles θ_{lab}<5°.

SINUSOIDAL BEAM CHOPPER

In order to obtain sufficient dynamic range in the neutron-momentum measured by TOF with a flight-path in a finite length and to detect neutrons with higher efficiency, it is crucial to have a proper pulse interval of the micro-burst of beams from the AVF cyclotron. Acceleration RF-frequency of the CYRIC cyclotron is ranging in 10.5 though 22MHz, natural beam-burst interval being in 45 through 95 nanoseconds. Thus, one of 1/5 ~ 1/10 beam-chopping is needed to get a pulse interval of several hundred nanoseconds, by which it is capable to measure 90-MeV neutrons with a dynamic range of ~90% in the momentum without overlapping of neutrons in the TOF spectrum. In addition, detection efficiency increases more than one order of magnitudes.

Figure 2 illustrates the electric-power part of the chopper. A 300 watt solid state amplifier drives the push-pull circuit with 2 pieces of power-tetrodes EIMAC 4CW10000, then RF-power is transmitted to a pair of copper electrodes, the dimensions of which are 1m-long, 5cm-wide and 5mm in their thickness with a variable gap ranging 30 through 50 mm. The electrodes are mounted in a 1300mm-long and 600ϕ-dia. vacuum tank located at a position 1300-mm up-stream of a pair of slits with a 4mm gap, to remove unwanted beam pulses from the beam-line. Setting of experimental conditions of the chopping rate and voltage applied to the electrodes is performed through the programmable logic controllers (PLC)[11]. Adjustment are carried out as well by PLC for tuning of the RF-power parts to obtain sufficient RF high-voltage in the order of 40kV, and for the proper phase difference between accelerating RF and that of the chopper to meet with a TOF measurement with a reasonable beam intensity. TTL signal for TOF is used for the stop signal of events.

NEUTRON DETECTOR

The neutron detector is illustrated in Fig. 3. Liquid scintillator Bicron BD50LA is encapsulated in a can, the dimensions of which are 203.2 mm in its diameter and 50 mm thick, thus a detector contains 1.6 litter scintillator. Light events are guided to photo-multiplier EMI 9823KB. A optical fiber is connected for the purpose of monitor for the gain of photo-multiplier. Experimental arrangement of 32 neutron detector matrix are shown in Fig. 4.

Time resolution of the neutron detector has been measured by detecting the energy deposit by cosmic-ray muons passing through two detectors. The typical time resolution of these detectors are ~500 pico seconds. Energy deposit by cosmic-ray muons are utilized for the energy calibration together with those by 4.43-MeV gamma-rays from an Am-Be source, neutrons from which are used for the test of neutron-gamma discrimination power of these detector as well.

Several hundred-hours long run test for light outputs have been carried out by observing Compton edge for 4.43-MeV gamma-rays and lights from LED fed through optical fiber. Results of this measurements are illustrated in Fig. 5 for five detectors labeled as #13, 17, 22, 27 and 28 among 32sets of the present neutron detector.

NEUTRON DETECTION ELECTRONICS

Figure 6 illustrate the electronics diagram of one neutron counter for detecting neutrons and analyzing their flight time, discriminating the light event for them from those for gamma rays. Three dimensional data are stored for one light event. The first one is for the flight-time information(TOF). A timing pulse is generated in a constant fraction discriminator device (CFD) by the signal from photo-multiplier, and is led to a time to digital converter (TDC) to measure the time between neutron arrival and cyclotron RF-signal which corresponds to beam-pulse arrival at the target. For convenience, the logic of "RF-start and neutron-stop" is applied.

The second one is for total light amount generated in the analog to digital converter (ADC) by the analog pulse from the photo-multiplier. This information is used to eliminate the Lapland neutrons which enter into a neutron spectrum due to the limited interval of the cyclotron beam pulses.

The last one is for n-γ discrimination . Deferent mechanism of light yields for neutrons and gamma rays in the liquid scintillator give deferent pulse-shape for these two radiations, thus enabling us to separate the former from latter by delayed integration of their partial light out put. Two dimensional display of two total and partial light out-puts readily provides a spectrum for n-γ discrimination.

DATA ACQUISITION AND ANALYSIS

Figure 7 illustrate the data acquisition system. Digitized event by event data from Analog to Digital Converter (ADC) or Time to Digital Converter (TDC) are received by VME Crate Controller (SBS 617VME bus adapter), controlled by a front-end PC (altair), which is connected to a back-end PC through ethernet for the purposes of on-line and off-line analyses.

A flow chart of the present data analysis software is depicted in Fig. 8. Starting at three-dimensional raw data from 32 pieces of the neutron detector, neutron momentum (TOF) spectrum or excitation energy spectrum is generated with and without two-dimensional n-γ discrimination. Also obtained are summed spectra over the data from each detector, the maximum number being 32. The position of γ -flash peak of each detector is used to adjust the relative time lag in each detector.

PERFORMANCE TEST BY (p,n) REACTION

Figure 9 depicts time spectrum of gamma flush measured for time structure of 70-MeV proton beams from the cyclotron. Gamma rays were detected by 1 inch ϕ and 1 inch thick plastic scintillator, the intrinsic time resolution of which was less than 200 pico seconds. Typical time resolution was indeed in the order of several-handled pico seconds. The time structure of beam burst is adjusted by a pair of slits located at the first-turn region of the cyclotron to limit the phase interval of accelerating RF-voltage. Of course, narrower beam

burst yields less intense beam, thus an intense ion source and the efficient beam injection line is crucial for reliable experiments.

Performance test for the TOF facilities has been carried out by 50- and 70-MeV proton beams. Beams from the new cyclotron are transported successfully to the swinger, then beam axis is rotated from 0 to 20 degree in the laboratory frame without adjusting any beam handling parameters. Almost all beams are collected on the Farady cup in the beam dump after the cleaning dipole-magnet.

Result of performance test has been carried out for the sinusoidal beam chopper, by which unwanted micro-bursts of the beam are completely removed from the beam-line as seen in Fig. 10. With a chopping of 1/8, we are able to obtain a time interval of 0.5 nanoseconds giving, a dynamic range 10~70 MeV for detected neutrons after 44 m-long flight.

In Fig. 11, neutron time-spectrum of the ^{6}Li(p,n)^{6}Be reaction taken with E_p = 70 MeV at θ_{lab} = 0° is illustrated. The flight path is as long as 16 meter, and thickness of the ^{6}Li metal foil is 6mg/cm^2. Overall time resolution is 0.9 nano seconds.

In a summary, construction of the new fast neutron time of flight facilities have been carried out. They contain a system with reliable beam swinger, scattering chamber and beam-dump, and large-angle detector matrix involving 32 pieces of disk-type detector, etc. Performance test has been made successfully by studying (p,n) reactions on ^{6}Li. Excellent time-resolution of a beam-burst makes it quite promising to study nuclear spin-isospin excitation by high-resolution measurements.

Authors are indebted to the cyclotron crew led by Prof. Shinozuka for development of the accelerator, and to messieurs Kan S., Chiba S., Ohmiya Y., and Takahashi N. for their helpful operation of the cyclotron and beam transport system. This work is supported by grant in aid for scientific research of Ministry of Education, Culture, Sports, and Science and Technology No.13640257.

References

1) See for example, Orihara H. et al., Phys. Rev. Lett. **81** (1998) 3607.
2) Orihara H. and Murakami T., Nucl. Instrum. & Methods **188** (1981)15.
3) Orihara H. et al., Nucl. Instrum. & Methods **A257** (1987)189.
4) See for example Terakawa A. et at., Phys. Rev. C **48**(1993)2775.
5) See for example Abe K. et al., Nucl.. Phys. **A459** (1987)358.
6) Hirasaki S., Master Thesis, Tohoku University (1988).
7) Niizeki T. et al., Nucl. Instrum. & Methods **A287**(1990)455.
8) Shinozuka T. et al., CYRIC Annual Report (2000).
9) Terakawa A. et al., CYRIC Annual Report (2000).
10) Orihara H., CYRIC Annual Report (1999).
11) Fujita M. et al., CYRIC Annual Report (2000).

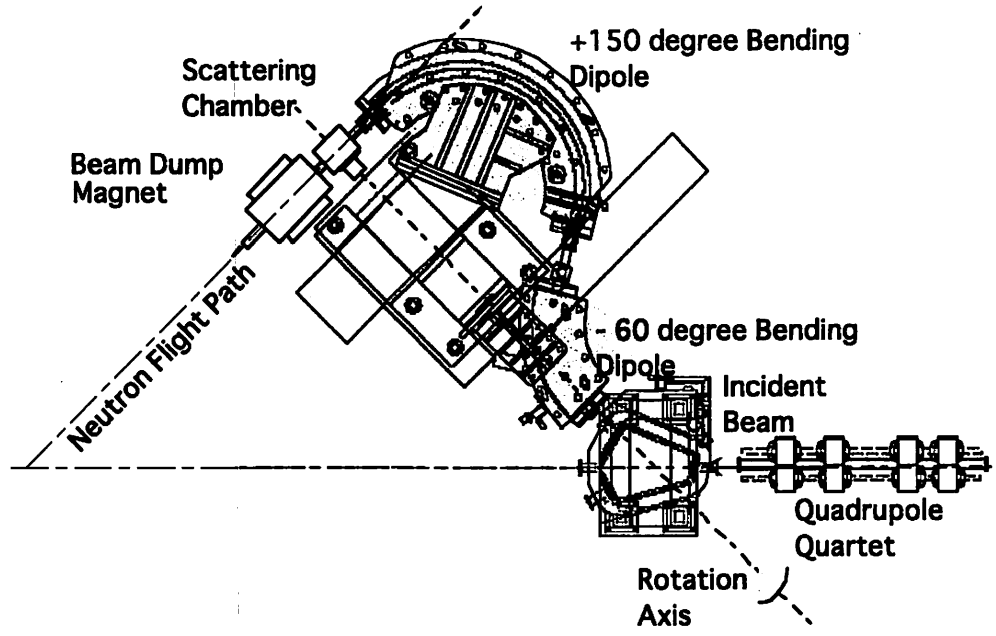

Fig. 1. New beam swinger and beam dumping system.

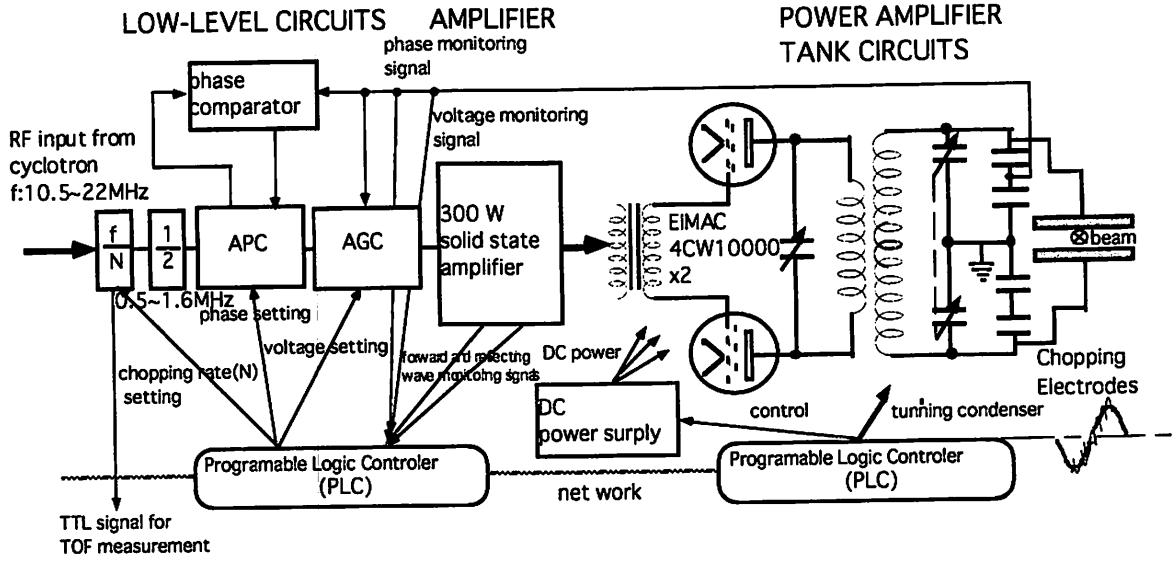

Fig. 2. Schematic drawing of sinusoidal beam-chopping system.

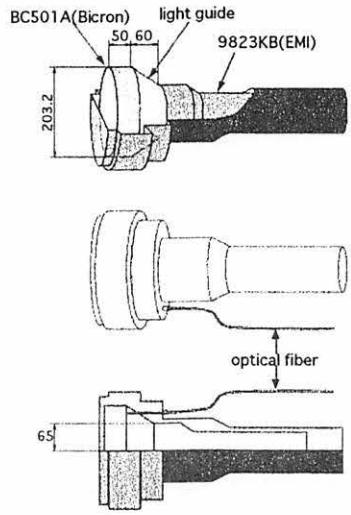

Fig. 3. Liquid scintillator neutron detector.

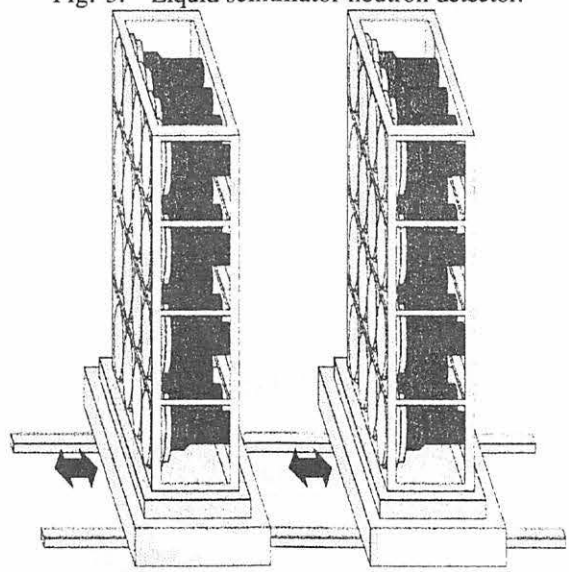

Fig. 4. Experimental arrangement of 32 neutron detector matrix.

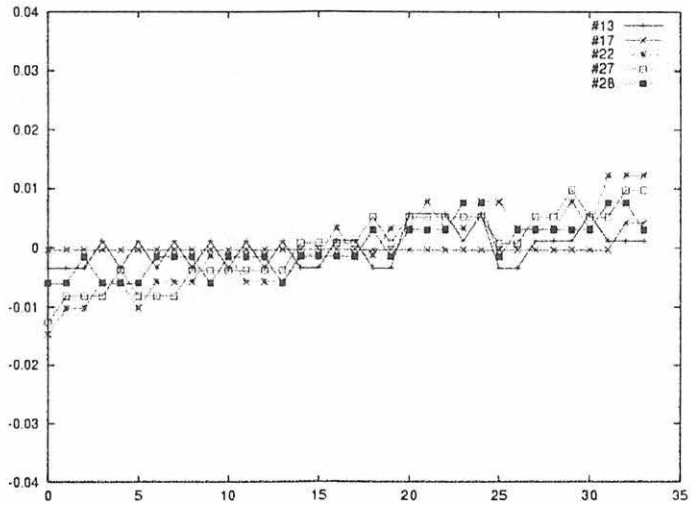

Fig. 5. Long run stability for light output corresponding to the Compton edge of 4.43-MeV gamma rays. Horizontal axis denotes running time in hour, while vertical one does deviation from the average.

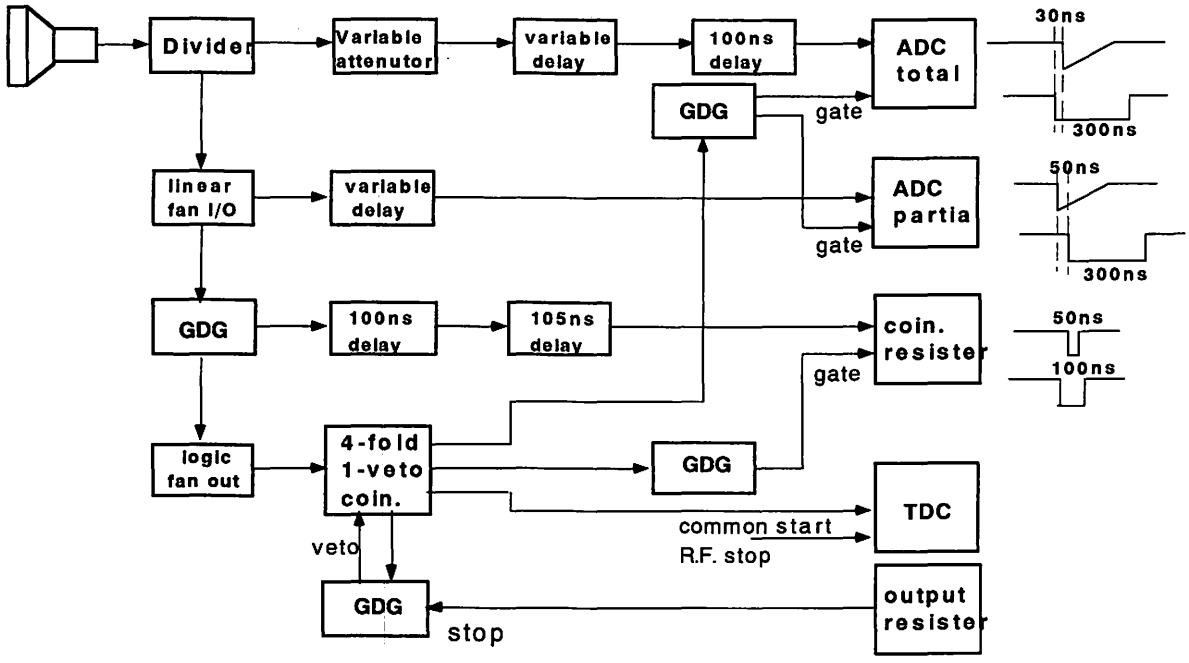

Fig. 6. Electronic setup for TOF measurement.

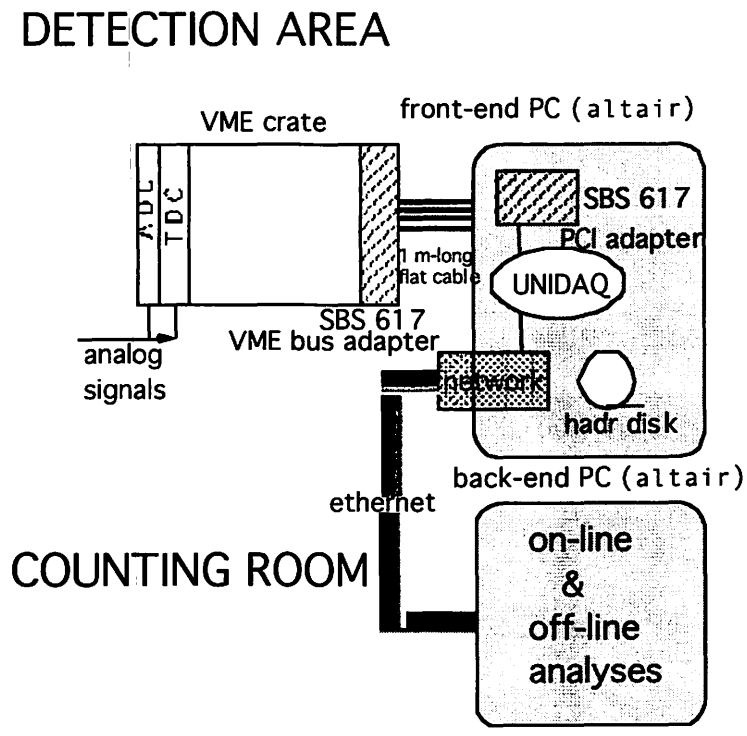

Fig. 7. Schematic Drawing of data acquisition system.

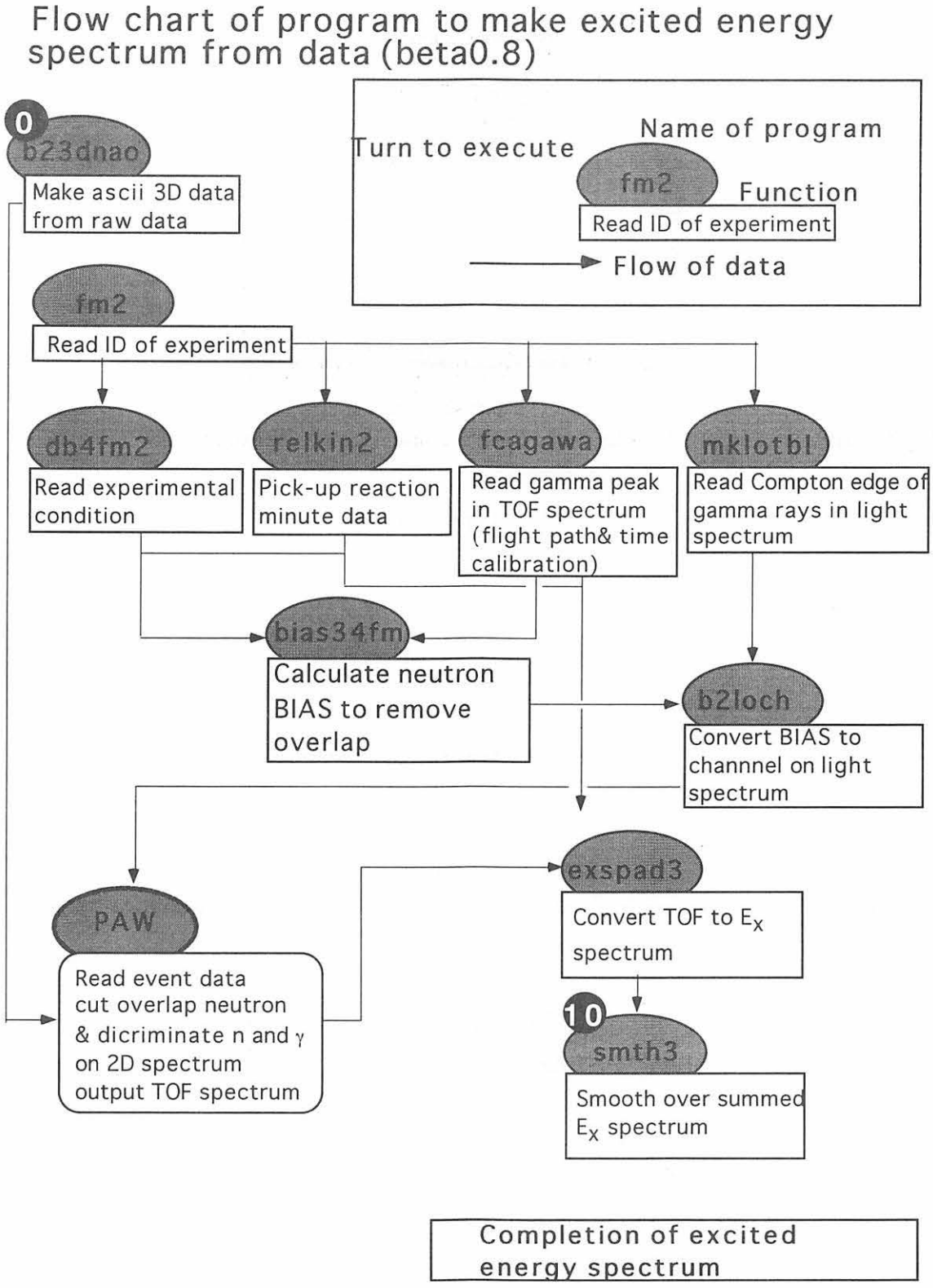

Fig.8. Flow chart of data analysis soft ware.

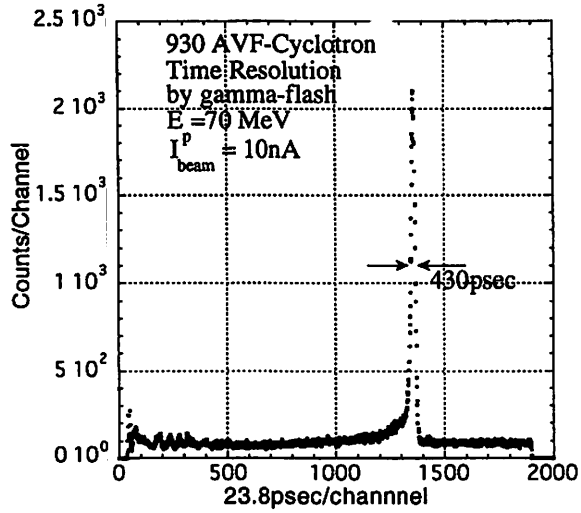

Fig. 9. Time spectrum of γ-flash detected by a plastic counter located at the exit of cyclotron.

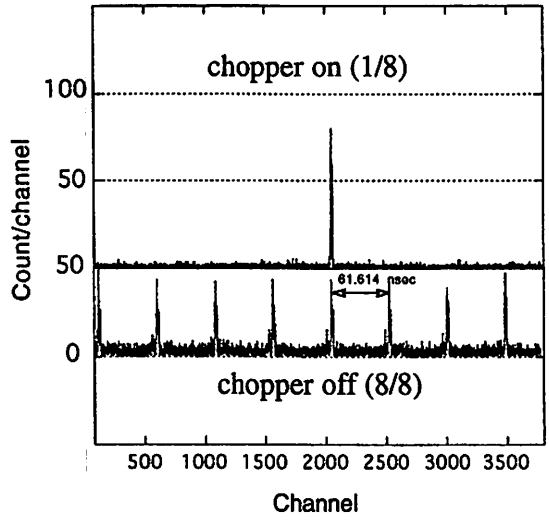

Fig. 10. Result of performance test for the sinusoidal beam chopper, by which unwanted micro-bursts of the beam are removed from the beam-line.

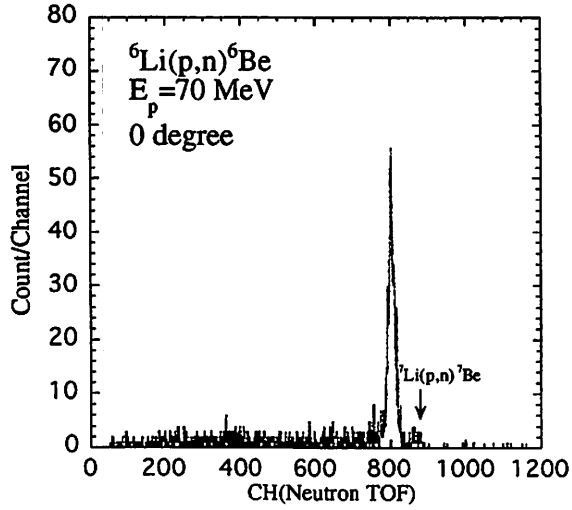

Fig.11. Time spectrum of neutrons taken for the ^{6}Li(p,n)^{6}Be reaction at E_p=70MeV measured at θ_{lab}=0°.

I. 10. Renewal of the ISOL Facilities

Fujita M., Yamazaki A., Sonoda T., Suzuki T., Ohshima T., Mizunuma K., Tanaka E., Tamura H.*, and Shinozuka T.*

Cyclotron and Radioisotope center, Tohoku University
*Department of physics, Graduate School of Science, Tohoku University**

The ISOL facilities located in the 2nd target room at CYRIC have been renewed. The points of improvement are as follows.

The remote control system
The vacuum pumping system
The tape transport system
The new detector system

In this report, a brief description of each item is presented.

The remote control system for the ISOL facilities has been drastically changed. The traditional hard-wiring system has been replaced by some PCs and PLCs (Programmable Logic Controller) like the control system for the new AVF cyclotron[1]. The entire controlled objects, such as power supplies and vacuum pumps, can be controlled by the programs developed by software Labview from National Instrument Corporation. Presently, almost all of the programs have been developed and whole system is working very well.

As for the vacuum pumping system, five oil diffusion pumps have been replaced by the same number of TMPs (turbo molecular pumps). In addition, a high throughput type TMP has also be available. It can be used for the differential pumping under the large amount of flowing of He gas (typically 50 *Torr l/s*). The pumping speed of the three TMPs is 1100 *l/s* and the rest is 800 *l/s* for N_2 gas. They can be operated in any orientation and achieve maintenance free, since all TMPs have active 5-axis magnetic bearing system. Using this vacuum pumping system, a high vacuum condition ($< 1.0 \times 10^{-6}$ Torr) has been achieved.

The tape transport system has been designed and constructed. This tape transport system is located at the end of the ISOL beam line. The mass-separated isotopes from ISOL are implanted in the thin aluminum tape and moved to the detection point where we can measure the radiation under low background environment. In order to measure the radiation emitted from short-lived RI, the tape must run as fast as possible. In this system, it takes less than 200 ms to move to the detection point that is 15 cm away from the irradiation point.

It is sufficiently short compared with the lifetime of the short-lived RI of interest.

The new detector system which consists of six Clover-type HPGe detectors, each is surrounded with twelve BGO anti-Compton suppressors has been installed. Figure 1 shows the dimensions of a detector. The events caused by the Compton scattering can be reduced by means of removing the events that simultaneously hit both Clover and BGO detectors. A Clover has four germanium crystals with 20% relative efficiency and as a whole they works like a large crystal with 120 % relative efficiency. These Clovers can be used for the high-count rate measurement since the transistor-reset type preamplifiers are used to avoid the signal pile-up. In combination with the BIG-IGISOL[2], experiments on search for ^{78}Ni, which is the doubly magic nuclei, are in the planning. In addition, experiments on nuclear g-factor for the short-lived nuclei are also in the planning by the use of the permanent magnets designed for the PAC (Perturbed Angular Correlation) measurement[3].

References

1) Fujita M., Chiba S., Ohmiya Y., Takahashi N., Tanigaki M., Terakawa A. and Shinozuka T., in this volume.
2) Sonoda T., Fujita M., Yamazaki A., Ohshima T., Takeda M., Tanaka E. and Shinozuka T., in this volume.
3) Baba T., Master Thesis Tohoku University, 1999.

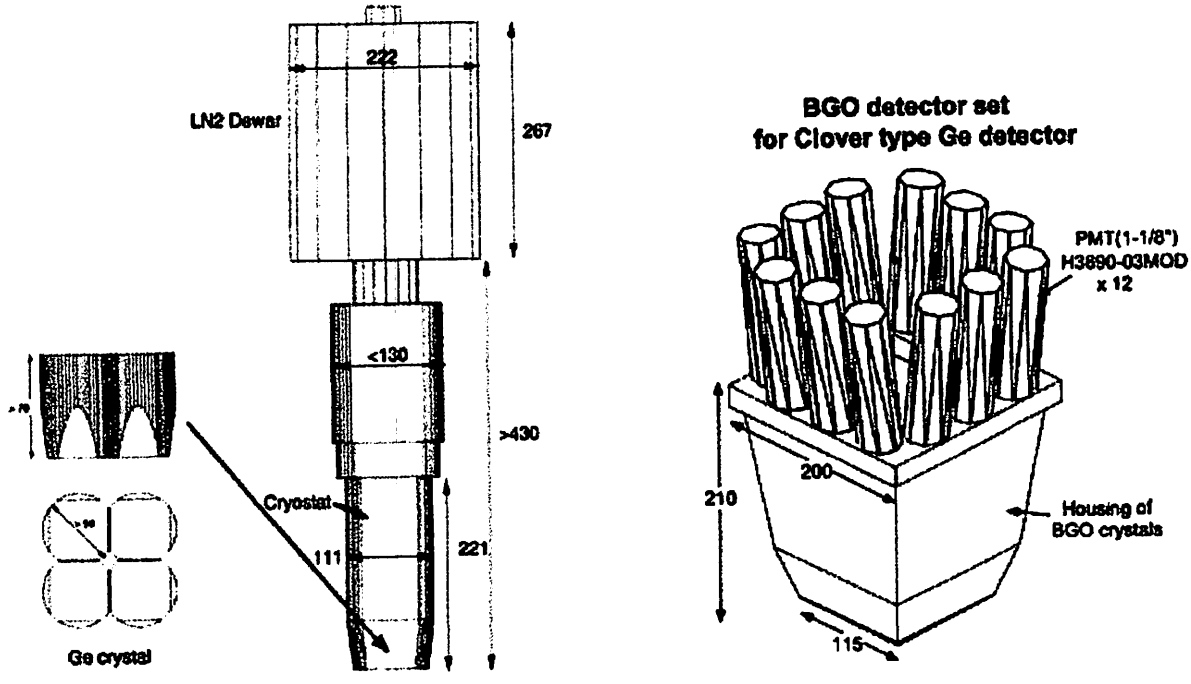

Fig. 1. The drawings of a clover-type HPGe detector (left) and a set of BGO anti-Compton suppressors (right).

I. 11. Development of New – IGISOL at CYRIC

Sonoda T., Fujita M., Yamazaki A.*, Ohshima T., Takeda M., Tanaka E. *, and Shinozuka T. **

Department of Physics, Tohoku University
*Cyclotron and Radioisotope Center, Tohoku University**

The IGISOL(Ion-Guide Isotope Separator On Line)[1,2] technique so far has been used to study short-lived ($T_{1/2}$ <0.1ms) exotic isotopes for more than 15 years. This technique provides radioactive nuclear ions without any restrictions by e.g. chemical property or lifetime limit of the desired ions, while the limitation has been unavoidable problems in the ordinary ion-source-based ISOL.

The stopping capability with gas is, however, not sufficient for high energy reaction products, for fission products in particular. Recently, a new type of IGISOL, RF ion-guide[3] which is possible to solve these problems has been proposed by Wada (RIKEN) and Katayama (KEK). Based on their idea, a test bench for the RF ion-guide system, schematic picture for which is shown in Fig. 2, has been constructed and off-line tests were performed as well.

The system is based on the same principle as that of the ordinary IGISOL, but a significant difference is in its cell size. In the ordinary IGISOL, a typical cell size in volume is 1 cm^3 which corresponds to a stopping capability of 10 keV/u. This limits the effective thickness of the target and the corresponding yields. The reason why a small cell size is used in the IGISOL is that the transport of the ions in the cell is performed only by the gas flow. If a large cell were used in the ordinary IGISOL, it would take many seconds to extract ions which would cause severe loss of ions due not only to the lifetime limit but also to other processes such as neutralization by impurity gas and diffusion to the wall.

In the present system, a large cell size is applied and almost all ions in the cell are totally under the control of a superposition of electric field. Many ring electrodes are placed in the cell, which produces a superposition of a DC field and an RF field. The DC field gives the ions a relatively high velocity in order to extract ions quickly from the cell and the RF field focuses the ion beam on to the small exit hole.

Numerical simulations were performed for the RF ion-guide system. A single ion motion in the electric field was traced by the Runge-Kutta integration method. The effect of gas collision was taken into account by the Monte Carlo method. A typical trajectory of an

ion in the RF ion-guide is shown in Fig. 1.

Bench tests have been done for a characteristic of the discharge ion source located at the opposite side to the exit hole in the He gas chamber as depicted in Fig. 2. Ions transported by the superposed electric fields are stopped by an Al catcher foil to measure the number of ions by the current. Figure 3 shows the dependence of a foil current on DC-voltage as the parameter of RF-voltage in the 10 Torr He-gas condition. Figures show a broad peak in the DC-voltage region of 40 volts, and the peaks move toward high DC-voltage side and rise to high current side along with the increase of RF-voltage. Note that the peak indicates the collected ion current, while flat region mean dark current. With a higher pressure condition, the peak disappear, presumable due to the fact that ions are lost before they reach to the exit hole.

Further tests have been performed with 340kBq ^{252}Cf fission source, which yields a number of hundred thousands spontaneous fission products per second. This source is located at the same position with the discharge ion source described above. The ions of the fission products are transported as well, by the superposed electric fields. A measurement was done with the same condition with the discharge source at the He gas pressure of 10 Torr. Results indicated that the fission products hardly stopped with 15cm long gas cell in such pressure. In order to give more energy losses for the energetic fission product, thin Al foil was used as the degrader, adjusting their thickness. However, optimization by this method failed because of difficulties in thickness control of Al-foil. Since it is significant for the IGISOL to stop interested ions in the He gas chamber. He gas pressure was increased to sufficiently high level of 2.1×10^{2} torr, though such a high pressure condition makes ion transportation less effective as mentioned before.

In the present experiment, a pin is located at the middle of exit hole of the gas cell as shown in Fig. 4. Negative voltage is supplied to this pin for the purpose of collecting positive ions efficiently.

The result shows that a gamma spectrum measured by radioactivities on the pin indicates more than 50% transmission efficiency for Tc ions collection (Fig. 5). It could be confirmed that almost all energetic fission products survive as ions against neutralizing, and ions are transported more than 10-cm long path by only the supplied DC-electric field without diffusing to the wall. More developments for the intense ion beam are progressing.

References

1) Ärje J. et al., Nucl.Instrum.Methods **B26** (1987) 384.
2) Yoshii M. et al., Nucl.Instrum.Methods **B26** (1987) 410.
3) Wada M. et al.,CNS University of Tokyo Annual Report (1998) 58.

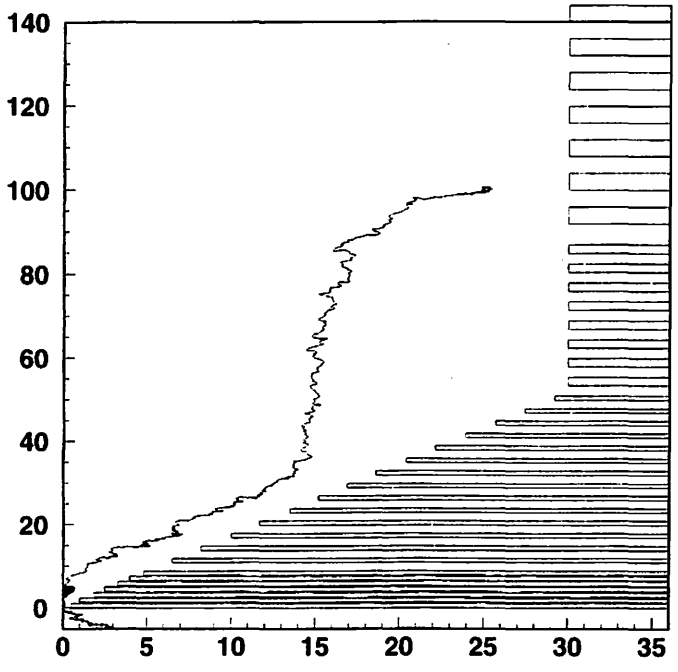

Fig. 1. A typical ion motion in the RF ion-guide gas cell. The condition are: ion mass is 100u, RF amplitude 100V, frequency 1MHz,mean free path in He gas 10μm.

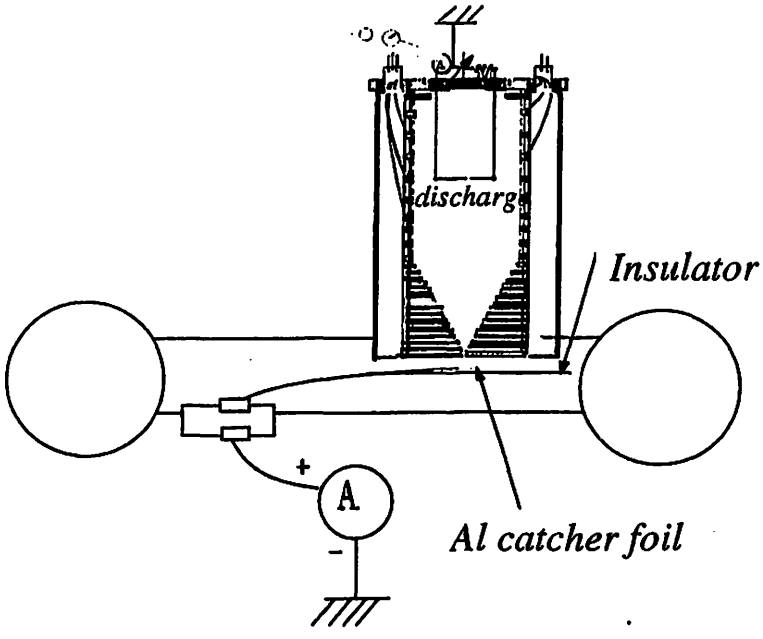

Fig. 2. The rf ion guide test bench. (discharge experiment setup)

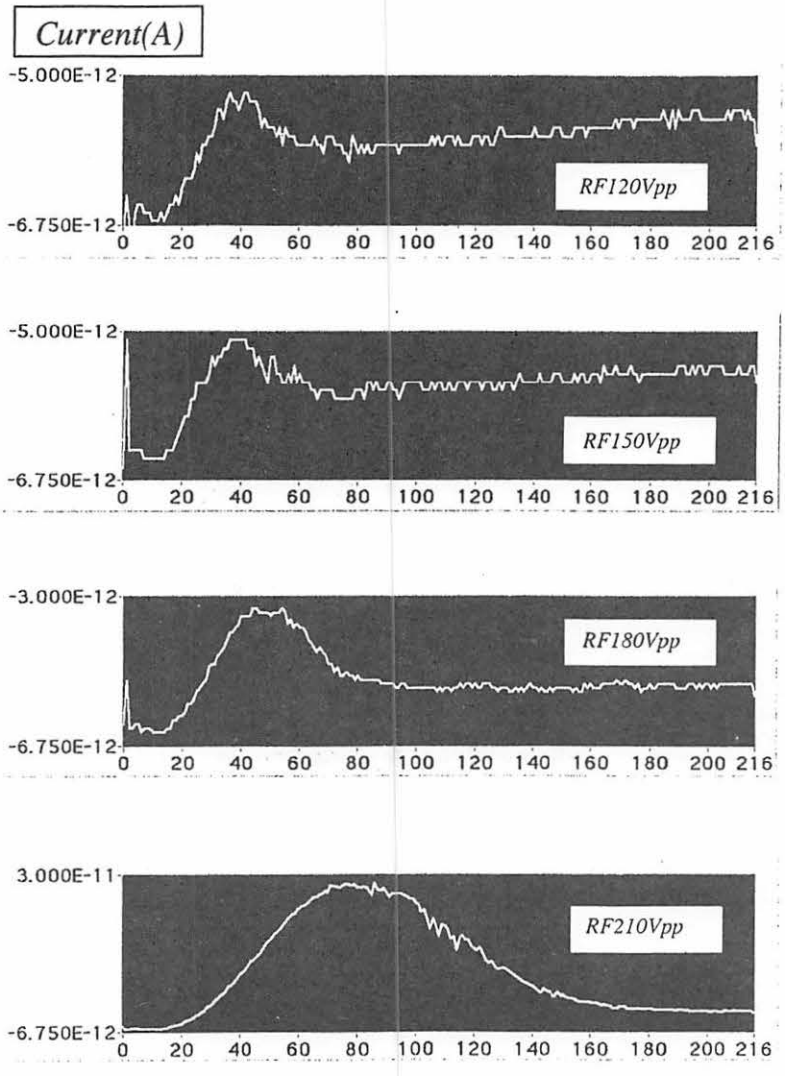

Fig. 3. The dependence of a foil current on RF voltage and DC voltage in 10 Torr He gas condition.

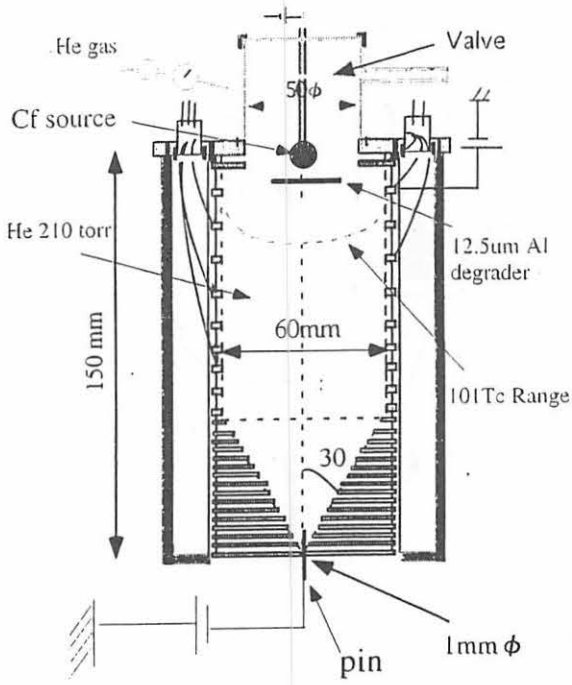

Fig. 4. ^{252}Cf experiment setup.

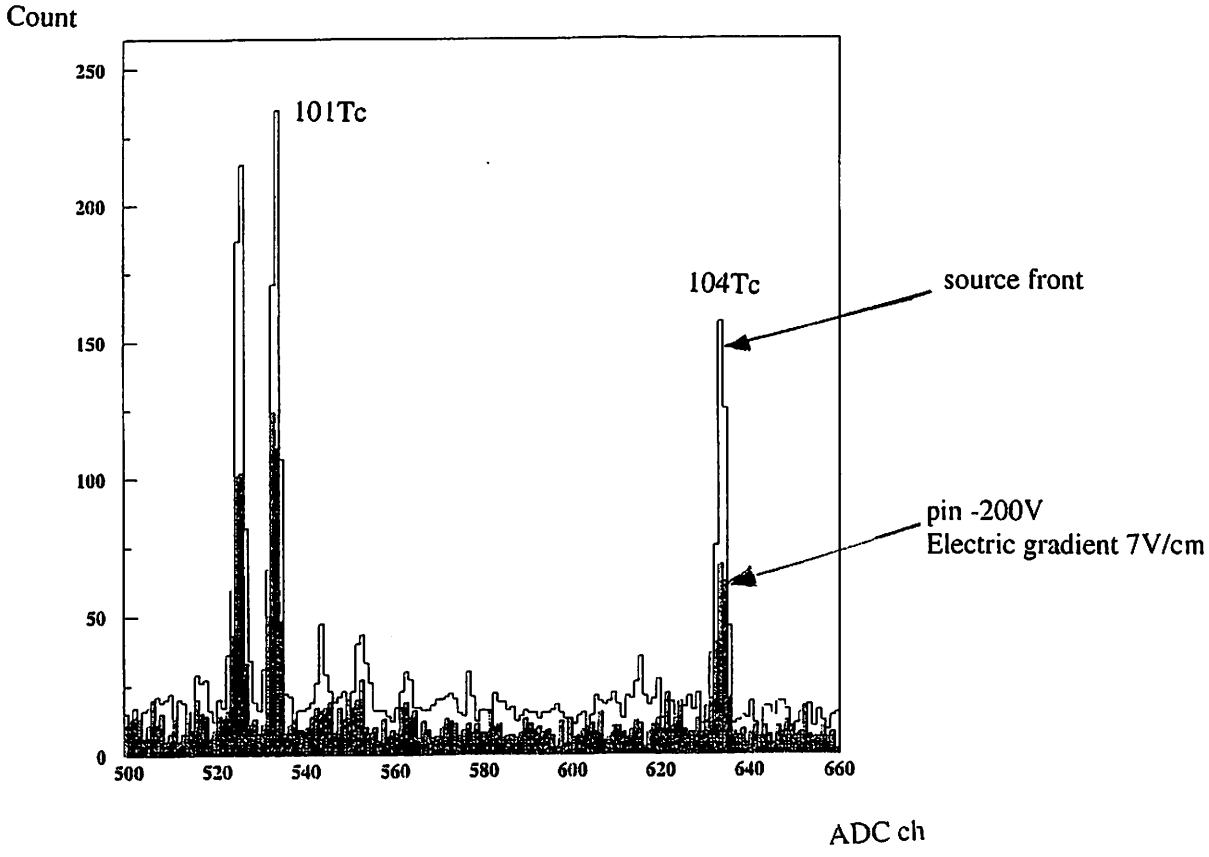

Fig. 5. Energy spectrum of ^{252}Cf spontaneous fission products which guided by DC field.

I. 12. Preparation of Metallic ^{42}Ca Target for Study by the (p,n) Reaction

Suzuki H., Katoh M., Kumagai K., Kikuchi Y., Fujisawa H., Terakawa A., and Orihara H.*

Cyclotron and Radioisotope Center, Tohoku University
*Department of Physics, Division, Graduate School of Science, Tohoku University**

It is of crucial importance to prepare an uniform, thick-enough, and contamination-free target-foil with a sufficient area, for a successful nuclear spectroscopic study by nuclear reactions. In two decades of the last century, a number of nuclear study works by the (p,n) reaction have been carried out at CYRIC[1-5], extending over the periodic table from ^{6}Li to ^{208}Pb, with K = 50 MeV AVF-cyclotron and fast neutron time of flight facilities[6,7]. In 1998 and 1999 school years, the cyclotron was replaced to K= 110MeV one along with the beam transport system including beam swinger. Related facilities, for example, neutron detector matrix for TOF experiments have been renewed as well in these year[8].

Preparation of targets for these works has been, indeed, one of the heavy tasks. Some of them were made of their metallic lump by rolling, though it was not so easy to get such a metallic lump from Fe_2O_3, NiO, SnO etc[1-3]. The others, e.g. Cd and Zn foils[4], were made by electro-deposition method. As for the target made of metals being unstable for oxidation like Magnesium isotopes[5], vacuum deposition by thermal evaporation with deoxidization materials have been applied.

In this report preparation of metallic ^{42}Ca target, the natural abundance of which is 0.674%, for study of the (p,n) reaction is given for further development of studies for isospin and spin-isospin excitation in nuclei with the new cyclotron and TOF system.

Preparation of metallic Ca foil

The presently discussed ^{42}Ca target is classified into the last case mentioned above. Requirements for a target used in the nuclear spectroscopy by the (p,n) reaction at an incident energy ranging 40 ~ 100MeV by the time of flight method are those; (1) Since energy resolution for analyzing neutrons is in the order of several hundred keV, energy loss of protons in the target is less important, thus thicker one of ~10mg/cm^2 in it's thickness is better for reliable experiments. (2) As well, uniformity of thickness over the irradiated area is less important, since the beam spot size is ~5mm in it's diameter, however, sufficient area larger than for example 3 x 3 cm^2 is needed to avoid background neutrons from target-frame. (3)

Moreover, contamination of carbon and oxygen yields serious background in a neutron spectrum. Though the Q-values for the (p,n) reactions on ^{12}C and ^{16}O are large in negative values (~-15MeV) and (p,n) yields by them are small, on the other hand, neutron yields by naturally abundant ^{13}C and ^{18}O are quite large with energetic neutrons due to small negative Q-values of the (p,n) reactions on these targets.

Figure 1(a) illustrates the evaporator unit, which is mounted in a bell-jar evacuated with a 1200l/sec oil-diffusion pump. A standard resistance heated tantalum boat with 3-mm deep dimple is used as an evaporation source, the details of which is depicted in Fig. 1(b). The boat is covered with two sheets of 0.1-mm thick tantalum plate. At the center of this plate there is a 1-mm ϕ hole through which evaporated gaseous Ca reaches to the catcher plate, while there are two same-size holes in the middle plate in order to homogenize evaporation as shown in Fig 1(b). The latter plate is made of quartz, which is expected to be stable for heat-exposure up to 1200°C. The plate is covered by Cu sheet in order to mask Ca deposit onto the quartz plate except for the interested 30 x 30 mm^2 area for the target. This masking makes it easy to remove the target foil from the quartz plate with a thin cutter-knife.

Before mount the enriched $^{42}CaCO_3$ carbonate, test runs with less expensive enriched $^{40}CaCO_3$ carbonate have been carried out many times. As the deoxidization substrate, powder of Zr metal are used[9] since it's vapor pressure is two order of magnitudes as low as that of Ca. The present chemical reactions are;

$$CaCO_3 \rightarrow CaO + CO_2 \uparrow \quad (1)$$
$$2CaO + Zr \rightarrow ZrO_2 + 2Ca \uparrow . \quad (2)$$

Figure 2 depicts vacuum versus time in minute. Initial vacuum is in the order of several 10^{-7} torr, then by heating, pressure in bell-jar increases gradually with evaporation of water combined in the form $CaCO_3 \cdot xH_2O$ up to 1 x 10^{-4} torr. After ~1hr evacuation, with heating up there appears a plateau region of several tens minutes, where decomposition of $CaCO_3$ takes place. Further rapid heating up to 1100°C in several minutes makes deoxidization by Zr and evaporation of Ca completely. Note that vapor pressure of Ca at 1100°C is $10^0 \sim 10^1$ torr.

Results and summary

Metallic Ca foils of several mg/cm^2 in their thickness was stripped off the quartz plate successfully. The ratio of weigh of Zr (300mesh) to that of $CaCO_3$ was optimized to 5 : 1 after a number of trials with naturally abundant $CaCO_3$. An amount of 100mg $^{42}CaCO_2$ powder, enriched to 99.8% ^{42}Ca, was used for final goal . As the summary, three pieces of metallic ^{42}Ca foils, 30 x 30 mm^2 in their area and thickness of 1.5, 2.0 and 1.7 mg/cm^2, have been obtained from 300mg of $^{42}CaCO_2$ powder. These three pieces of foil have been staked into 5.2mg/cm^2-thick one target. Figure 4 illustrates a sample neutron excitation energy

spectrum for the ^{42}Ca(p,n)^{42}Sc reaction at E_p= 50 MeV taken with the presently prepared ^{42}Ca target.

With these targets more promising works by the (p,n) reaction with the K=110 MeV cyclotron and TOF facilities are expected.

References

1) Orihara H. et al., Phys. Rev. Lett.**47** (1981) 301.
2) Maeda K. et al., Nucl. Phys. **A403** (1983)1.
3) Jon G. C. Et al., Phys. Rev. C **62** (2000) 044609.
4) Murakami T. Et al., Nucl. Phys. **A377** (1982) 163.
5) Orihara H. et al., Phys. Rev. Lett.**48** (1982) 469.
6) Orihara H. and Murakami T., Nucl. Instrum. & Methods **188** (1981) 15.
7) Orihara H. et al., Nucl. Instrum. & Methods **A257** (1987) 189.
8) Orihara H., CYRIC Annual Report (1999) p1.
9) Maier H. J. and Kutschera W., Nucl. Instrum. & Methods **167** (1979) 91.

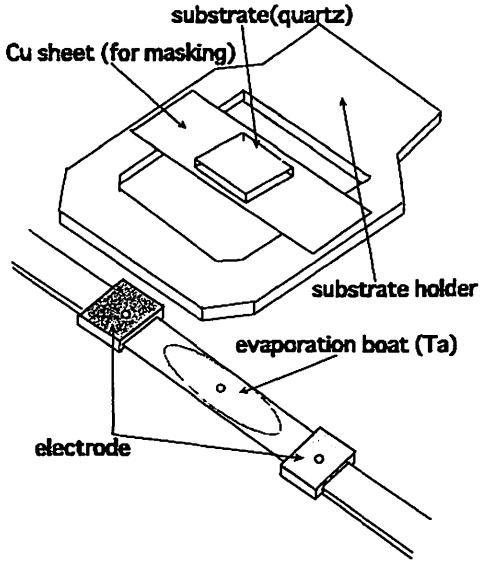

Fig. 1. Schematic representation of the evaporator. The distance between the tantalum boat and quartz plate assembly is optimized to be 25 mm.

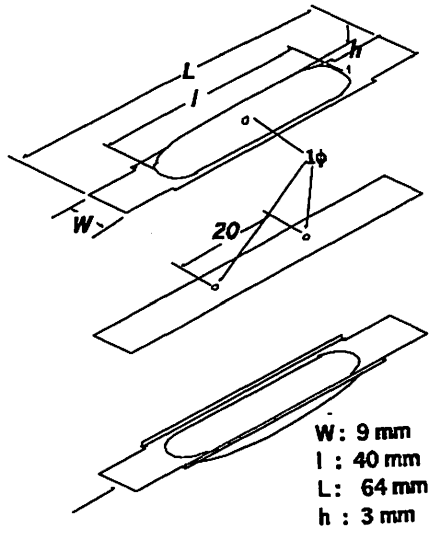

Fig. 2. A sketch of three-layer structure of the tantalum boat.

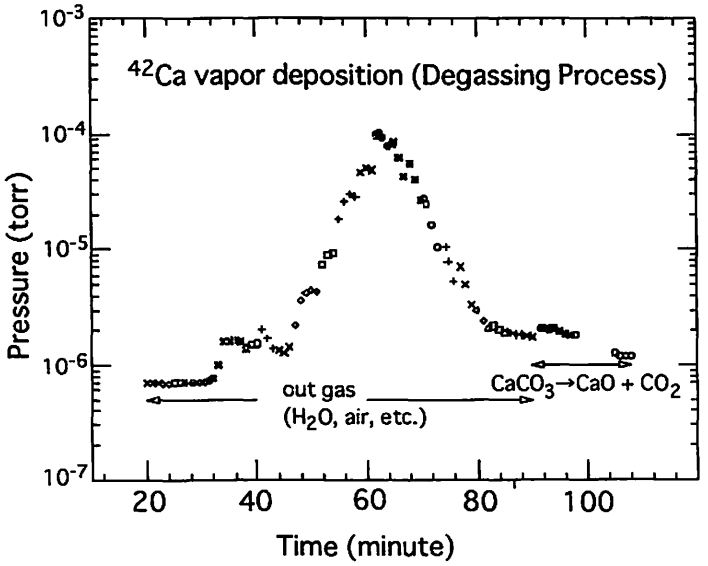

Fig. 3. Pressure in the bell-jar versus time in minutes. Electric power supplied to the electrodes was increased step-wise up to a power by which the temperature of the boat reached to 1200°C.

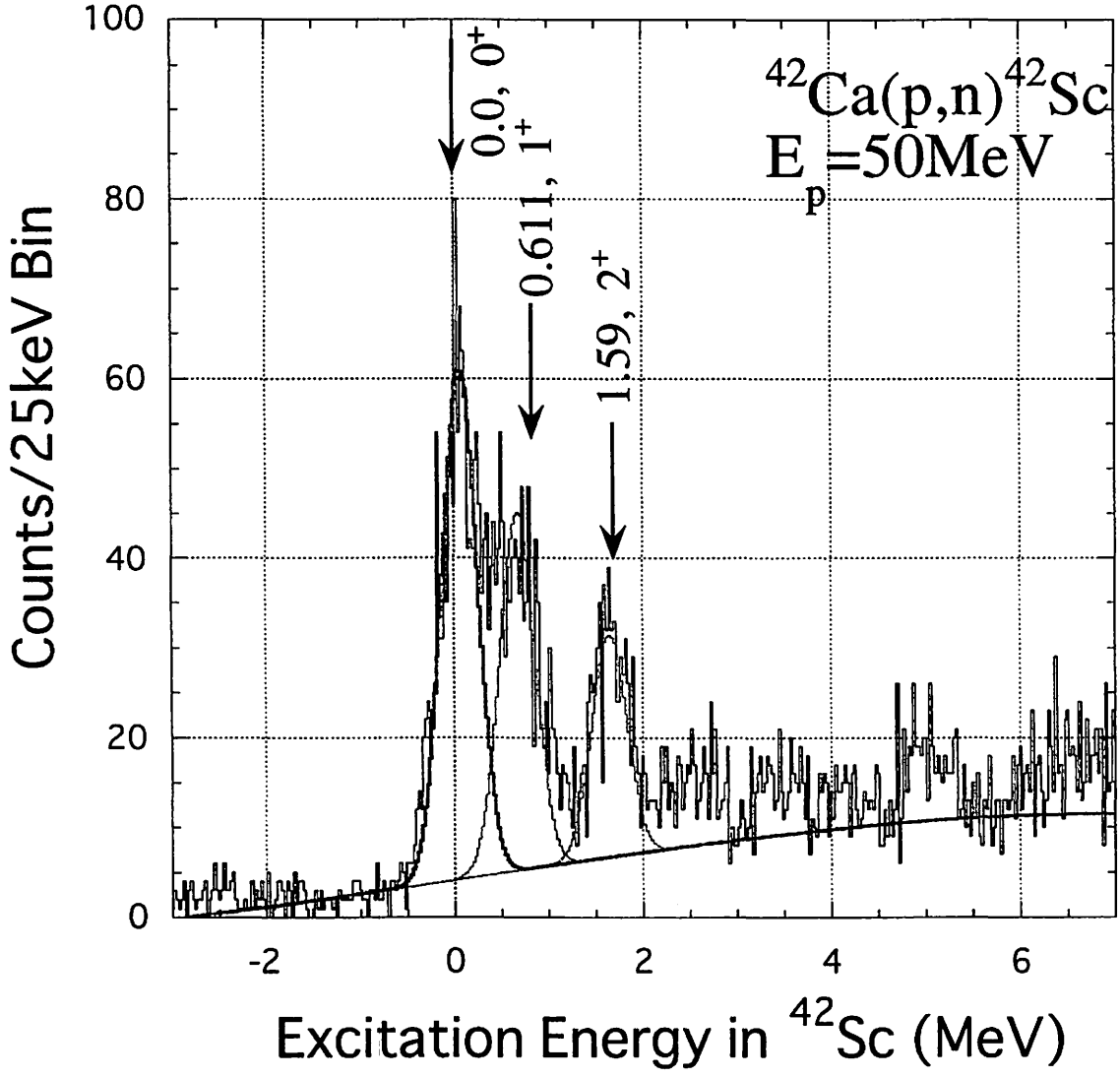

Fig. 4. Neutron excitation energy spectrum taken for the ^{42}Ca(p,n)^{42}Sc reaction at E_p=50MeV.

I. 13. Development of a Neutron Beam Profile Monitor

Hirose K., Kanda H., Kobayashi Y., Maeda K., Takahashi K., Utoyama M., and Yamaguchi Y.

Physics faculty, Graduate School of Science, Tohoku University

We have developed a neutran beam profile monitor to be used in the construction of the new neutron beam line at CYRIC 5th target room. Two plastic scintillator bar detectors were utilized to scan across the beam, one horizontally and the other vertically and to obtain the projected beam intensity distributions. We prepared, as the control unit, a VME on-board PC module, a motorcontroller, a scaler, and a discriminator which were inserted in 7-spanned VME crate. We bring the scanner unit and the VME crate into the beam line and connect the on-board PC to the Ethernet. We can access the PC from anywhere Ethernet connections can be reached in order to control the system and acquire beam profiles.We also aim to apply the beam profile monitor for high energy photon beam profiling with tungsten converter wires attached before the detectors. We call it "GAMERA" from the abbreviation of "GAmma caMERA".

DESIGN

Knowing the profile of the beam is very crucial for the construction of a new beamline. The shape, size, intensity, and core to halo ratio are the important information to decide the quality of the beam and the forthcoming experiments. We have been developing a new neutron beam line at the CYRIC 5th target room. The details of the development of the beam line. Details for planned experiments can be seen in Maeda's article in this annual report. In the beam development, the beam profile monitor is strongly needed.

The beam profile monitor is required to have the following features,

It should detect neutrons with energy ranges from 10MeV to 100MeV.
It should also be applied to high energy photon beam profiling.
The position resolution should be less then 5mm.
It should take beam profiles independent from the other DAQ systems.
It should be easily handled and maintained.

In order to satisfy those requirements, we designed the scanning type beam profile monitor from 3 parts: neutron detectors, scanner with linear motion mechanisms, and a control and DAQ unit.

We chose bulk plastic scintillator(NE102A) for material of the neutron detector. We made a scintillator bar of 5x5x200mm^3 and attached it to the photo-multiplier tube(Hamamatsu R1450) with optical grease. In the case of photon beam profiling, a tungsten wire of 2mmϕ is placed before the cintillator to convert high energy photons into electron-positron pairs. GAMERA is designed to count all the signals from the discriminator, discrimination level should be carefully chosen. In neutron beam profiling, because background is mainly from slow neutrons and the γ rays, discriminator level should be set as high as to enhance the signal from fast neutron. In photon beam profiling, because background is mainly from electrons and positrons, discriminator level should be set as high as excluding signal from passage of single particle. The detection efficiencies were calculated for neutrons and photons using Geant 3.21 based simulation. The simulator for neutron beam calculates reactions of neutrons of 20MeV inside the plastic scintillator and energy losses of the relevant charged particles.When we set the threshold at 2MeV, the detection efficiency is roughly 0.2%. For the simulation of gamma beam, energy deposit by electrons and positrons converted from 100MeV photon in the tungsten converter is calculated. When we set the threshold at 1.3MeV, the detection efficiency is roughly 4%.

The outline drawing of the scanner unit is shown in Fig. 1. Two scanners are placed on the unit; one scans horizontally and the other vertically. The scanning length is both 200mm. We utilized a pulse motor, a ball screw, and a rotary encoder to assureprecise linear motion. We also attached two limiting switches and an electromagnetic break to prevent the scanner to move in destructive motion. All the elements are controlled by a VME pulse motor controller.

In order to make GAMERA portable and easy to handle, we adopted theVME bus system which gradually come to be used in the field of particle physics experiments in succession to CAMAC. VME has following characteristics for our use:

Portable One crate can have a PC module and some IO modules init to build a stand alone control and DAQ system.

Common in the factory automation Because the motion control is the main subject in the factory automation, we can easily find a suitable module for controlling pulse motors.

Common in the particle physics experiments Signals from a photomultiplier attached to a plastic scintillator are easily handled by electronics dedicated to the particle physics. Not only the scaler which was used in our system but ADC and TDC modules on VME standard can also beused to build a simple DAQ system.

We inserted a on-board PC module a motor controller module, a discriminator module, and a scaler module in the 7-spanned VME crate.

The PC module itself is made of Pentium-II 400MHz, 128MB SDRAM, 12GB HDD and other legacy interfaces and Ethernet interface. It works as an ordinary PC in spite of its compactness. We chose vine linux 2.1(kernel version 2.2.10) as an OS for the PC

module for easy network access and economy system construction. Only at the setup period, we connect a keyboard and a display to the module. After the setup of network is finished, we can access the module via Ethernet from anywhere. The PC module utilizes the Tundra Semiconductor Universe PCI/VME bridge inside and we installed the VME driver for linux developed by J. Hannappel. Other useful documents for accessing VME from linux can be found elsewhere and we mostly referred to K. Nakayoshi's report on which described was basic performances of a DAQ SYSTEM using the VME CPU module. Sample programs for VME data access were also supplied by J.Hannappel, and all of our programs for controlling and taking data from VME modules originate from them.

BEAM PROFILING

We placed GAMERA at 50cm downstream from a neutron collimator in the 5th target room. The neutron beam was created from primary proton beam of 20MeV bombarded on a 9Be target of 11.7mg/cm^2. The swinger is set at 20 degrees from horizon.Taking the kinematics and the target thickness into account, neutron beam energy ranges from 17.883MeV to 18.150MeV. We used a 40 cm long iron collimator of 50mm diameter. The center positions of both scanning arms was set at the beam line so that they could cover +-10cm around the beam center. The detectors were programmed to move from -75mm to +75mm with 5mm interval and to stop for 190 seconds after each movement. We set a deuterized neutron detector at 10m downstream from the collimator and used it as the reference counter for the normalization of beam intensity fluctuation.

A NIM discriminator and a CAMAC scaler were also used to count the divided signals of GAMERA detectors. The counts taken from GAMERA were compared to the counts from CAMAC scaler and they showed the good agreement within some systematic errors estimated from the difference of discriminator levels and counting times between them. We are sure our VME system is working correctly.

Our interest is now in reconstructing the 2-dimensional beam profile from vertically and horizontally projected beam intensities. We have tried two methods of reconstruction. One method brutally finds 2-dimensional matrixed beam intensity with least deviation from the horizontal and vertical scanned data. Here I will describe the other method which is based on the simulation result for beam collimation. From our simulation, collimated neutron beam profile is well fitted by Saxon-Woods' form:

$$I(r) = \frac{I_0}{1 + exp(\frac{r-R}{d})}.$$

I(r) is beam intensity at distance r from the center of the beam, R is a beam radius and d is a diffuseness. Because width of peaks in horizontal and vertical scanned data are different, data were fitted with the assumption that the beam is axisymmetric to both

horizontal and vertical axes. The fitting parameters are I0, RH, RV, dH, and dV(the subscript H denotes "Horizontal" and V denotes "Vertical"). Normalized counts and fitting results are shown in Fig. 2. The 2-dimensional intensity distribution derived from the fitting is shown in Fig.3. These reconstruction methods are argued in detail in Y. Kobayashi's master thesis.

SUMMARY

We have developed scanning-type beam profile monitor: GAMERA. It was tested at the CYRIC 5th target room using neutron beam of 18MeV. It proved to be able to measure the beam profile and also able to reconstruct the 2-dimensional intensity distribution with help of simulation results. We are sure that GAMERA can be used for further development of the neutron beam line at CYRIC. This is the first trial of the construction of a full VME based DAQ system. Its portability and reasonableness will be the good example for the construction of future DAQ systems.

References

1) Dynatem DRC1.
2) Comotech VPG-46-2.
3) Comet SD701.
4) Advanet ADVME1805.
5) Hanneppel J. http://lisa2.physik.unibonn.de/~hannape/software/universe.doc/universe.html (1999).
6) The VMELinux Project.
7) J. Huggins and M. Wyrick, VME-HOWTO ,http://www.linux.or.jp/JF/JFDocs/VME-HOWTO.html.
8) K. Nakayoshi and Y. Yasu, KEK Internal 99-12 ,http://onlax2.kek.jp/~nakayosi/vmic.pdf (1999).
9) Y. Kobayashi, Master thesis, Tohoku University.(2000).

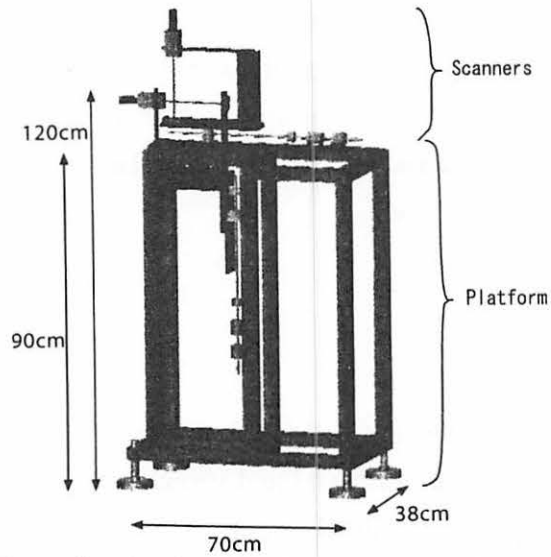

Fig. 1. The outline drawing of the beam profile monitor scanner unit.

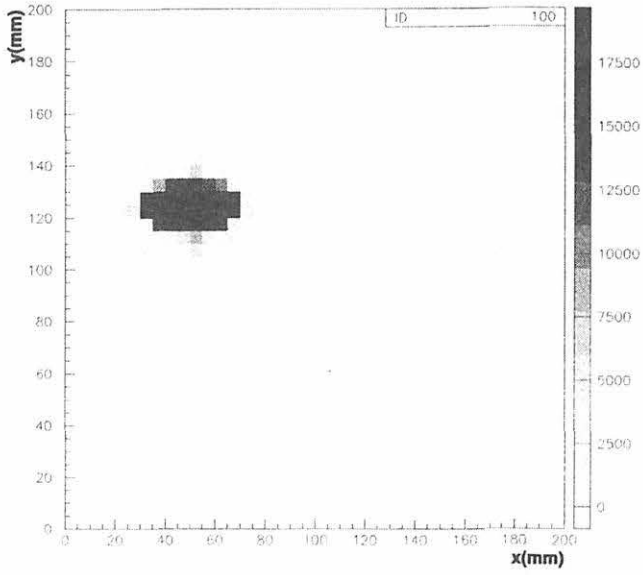

Fig. 2. Normalized GAMERA counts fitted by Saxon-Woods form (a) is the horizontal scanned data and (b) is the vertical one. The curves show the result of the fitting by a Saxon-Woods shaped function.

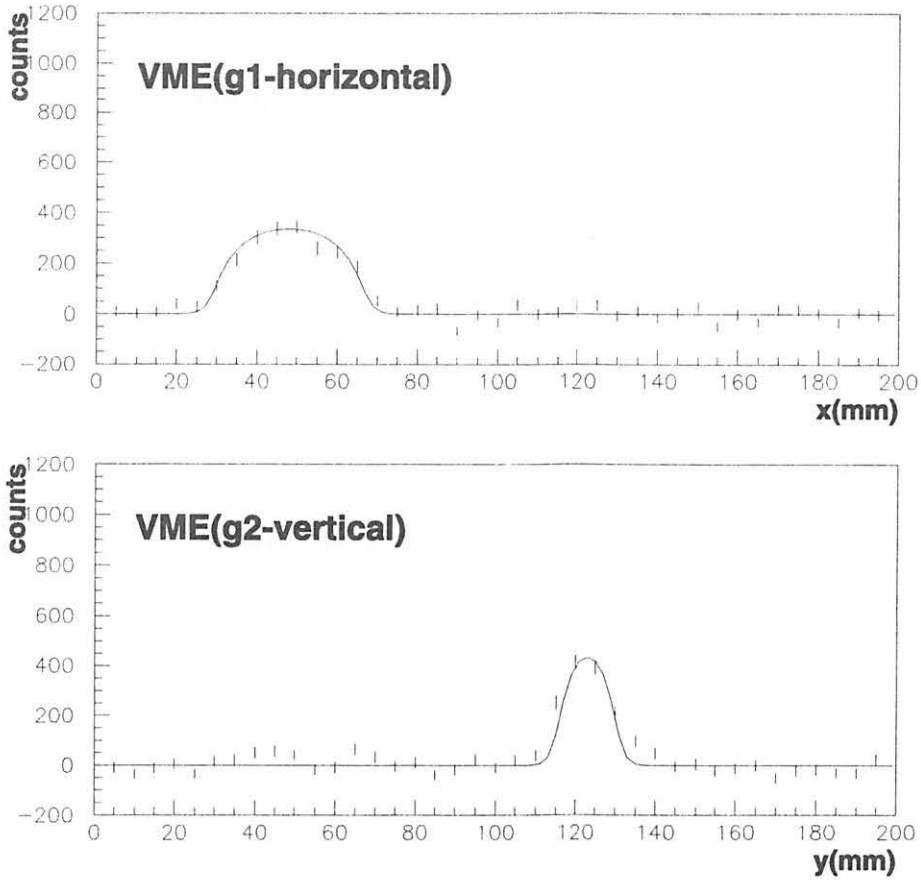

Fig. 3. The fitting result shown as 2-dimensional beam profile.

I. 14. PIXE-Monitoring of Time Variation of Elemental Concentration in Rain Water and River Water

*Yamazaki H., Ishii K., Matsuyama S., Takahashi Y., Satoh T., Endo H., and Orihara H.**

*Department of Quantum Science and Energy Engineering, Graduate School of Engineering, Tohoku University, Cyclotron and Radioisotope Center, Tohoku University**

Introduction

To safeguard the quality of our environment it is necessary to continue the development of improved analytical methods for identification, characterization and measurement of pollutants in our surroundings. Particle-induced X-ray emission (PIXE) has come into extensive use for analyzing airborne particulate matter due to the multielemental nature and high sensitivity[1,2]. The potential for application of PIXE to the determination of trace elements in water is similar to that for aerosols, but PIXE has not often been used for monitoring a water pollution because of some problems in preparing samples[3,4]. Successful application of PIXE to determination of dissolved ions in water will depend upon the development of a reliable sample preparation in a form suitable for the PIXE analysis. It is preferred in practical use to combine preconcentration with sample preparation. In contrast to the analysis by absorptiometry and atomic absorption spectrophotometry, insoluble components in aqueous samples can be easily determined by PIXE after filtration with the membrane itself serving as a suitable backing for a target to be used in PIXE. The PIXE analysis combined with these methods for preparing targets permits convenient determination of both soluble and insoluble constituents in water samples, providing for some useful information about chemical forms of elements in water samples.

The PIXE technique is conveniently applied to the analysis of thin samples and offers the possibility of a high absolute sensitivity (nanogram levels). In our previous studies[5], a combination of chelation by dibenzyldithiocarbamate (DBDTC) ions with subsequent condensation into dibenzylidene-D-sorbitol (DBS) gels has been developed for preconcentra-tion of trace amounts of heavy metals in aqueous samples, in conjunction with rapid preparation of thin uniform targets containing zirconium or palladium as an internal standard. We also have developed a simple preparation method for thin polycarbonate film and used it as a target backing in the PIXE analysis of anions such as sulfate, chromate and arsenate in the wide concentration range (10-2000 ppb)[5]. This methodology for the PIXE analysis of aqueous samples has been successfully applied to the monitoring elemental

concentrations in river water[6].

The process of seeking out and developing a sample preparation technique suitable for water analysis by PIXE requires that we should demonstrate the feasibility of the technique for water samples of a large variety of elemental concentrations. In this study, we intent to confirm the applicability of the procedures for rapid determination of elemental concentrations in both soluble and insoluble fractions of rain water and drinking water.

Experimental

Target Preparation

Water samples were stored in Nalgene linear polyethylene containers and processed into PIXE-targets within 24 hours. After pH measurement, insoluble components in 30 ml of each sample were filtered under suction with a Nuclepore filter of 0.4-μm pores. The filter was mounted on a Mylar target frame and kept in desiccator for several days. The filtration efficiency was over 98 % for colloids of ferric hydroxide and silver chloride in the range of 20-2000 ppb. The targets for these colloids in a known amount (40 and 400 ppb) were prepared in the same manner and used as an external standard for normalization of PIXE spectra for the insoluble components.

In the preparation of PIXE targets for heavy metals in the soluble fraction of river waters, 2.5 ml of 0.1 % (w/v) DBDTC solution and 25 μl of 1000 ppm Pd in 1M HNO_3, respectively, were added to 25 ml of each filtrate as a chelating agent and as an internal standard, and then the pH of solution was kept around 5 for 4 minutes. The solution gelled immediately after addition of 10 μl of 4 %(w/v) of DBS solution, and the DBS gels containing metal-DBDTC complexes were filtered on a Nuclepore filter of 0.4-μm pores. In our previous study[4], quantitative recoveries of 7 metals (Fe, Co, Ni, Cu, Cd, Hg, Pb) were confirmed up to the concentration of 1 ppm, and the coexistence of Mg, Ca and humic acid in 40 ppm did not interfere with the recovery of the heavy metals.

On the other hand, alkali metals, alkaline earth metals and anionic species in the soluble fraction are not picked up in the preconcentration step described above. The targets for these elements were prepared by depositing 30 μl of filtrate on an user-made polycarbonate film; 10 μl of 1000 ppm Ga in 1M HNO_3 was added to 4 ml of filtrate beforehand. After drying at 60°C, the procedure was repeated four more times to give a total of 150 μl dried on the foil. As we have revealed in our previous study[5], a polycarbonate film of thin and uniform thickness is prepared by dropping a polycarbonate solution in chloroform-benzene mixture slowly on a water surface within a 20-mm aperture of Mylar target frame floating on 50 wt% sucrose aqueous solution. The film offers a good combination of mechanical strength, chemical stability and low X-ray continuum background.

PIXE Analysis

The samples were analyzed by in-air PIXE system at Tohoku University and by a vacuum PIXE system at Nishina Memorial Cyclotron Center (NMCC) of Japan Radioisotope Association (apparent current of 3-MeV protons: 10 nA; 5-min irradiation). The in-air PIXE system at Tohoku University has a vertical beam line and a beam exit assembly composed of a Si(Li) detector and a Si-PIN photodiode detector. The solid angle of Si-PIN photodiode detector is much larger than that of Si(Li) detector, but the maximum energy of X-ray detection of Si-PIN photodiode detector is limited to 15 keV[7,8]. In the PIXE system of NMCC, X-rays from targets were measured with two Si(Li) detectors; one having 300-μm Mylar absorber and high geometric efficiency allows the detection of X-rays > 4 keV, and the other one with a low geometric efficiency is well suited for the detection of elements of the atomic number $Z \leq 20$[9]. For PIXE spectra analysis, we used a least-squares fitting computer program, which has been developed in our laboratory based on a theoretical approach for the background continuum in PIXE spectra[10]. The detector's intrinsic efficiency and the transmission through absorbers were determined experimentally in the X-ray range of 1-60 keV. The values for the total production cross-sections of X-rays of interest and the correction factors for the relative intensities of multiplets for each characteristic X-ray were obtained from the text book by S.A.E. Johansson and J. L. Campbell[11].

For all kinds of solutions tested, the reproducibility of PIXE analysis for soluble and insoluble components was checked by using four targets independently prepared under the same condition. In all types of targets, a close agreement in concentrations between four prepared targets (within ± 7% deviation) was obtained for many detected elements except highly hydrolyzable elements such as Al, Si, Ti, Fe and Zr. A much larger fluctuation (30-65 %) was detected for the analyzed concentrations of these hydrolyzable elements, although such a large deviation was not always observed. This indicates the variation in the amount of very fine particles of colloidal metal hydroxides passing through Nuclepore filters of 0.4-μm pores. Although it is difficult to strictly meet the separation requirement, the residues on filters are classified into an insoluble fraction of samples for convenience. On the other hand, a higher value which was detected either in deposit targets or in preconcentration ones was regarded as a concentration of highly hydrolyzable element in a soluble fraction. The soluble fractions of V, Cr and Mn were determined in the same way, since these elements in the high oxidation states exist as the anionic species in aqueous solutions of wide pH range.

Results and Discussion

Rain water

The chemical composition in rain water is an important indication to a global environmental problem because of the wet scavenging of aerosols by rain drops. Kasahara et al. have demonstrated that the PIXE analysis with multielemental nature and high sensitivity serves to detect the change in chemical compositions of rain water as a function of rainfalls[12].

It is expected that the combined use of PIXE with a preconcentration technique provides more detailed information for trace elements of importance as an indication to pollution problems.

Rain water was sampled 24 times in 3 different rain episodes between December 7 and May 19, 1998-1999, on the rooftop of our department building, located on 100-m height hill in the outskirts of Sendai city; rain water was collected at each one-hour rainfall from about the beginning of rain by using a plastic pail (35-cm long x 55-cm wide x 7-cm high). After the temperature of collected rain water was kept at 20 ± 2°C for two hours in an electric oven, its pH was measured and the target preparation for the soluble and insoluble fractions was carried out in the manner described in Experimental.

The changes of rainfall intensity, pH and sulfur-concentration are shown in Fig. 1. For the rain episodes on December 7, 1998 and on May 19, 1999, the pH values seem to decrease when the rainfall-intensity decreases and the S-concentration increases. In contrast, the pH value increases gradually with decreasing the S-concentration over whole rainfall of high intensity on March 15, 1999. Almost all S-species are detected in soluble fractions, as will be shown in Figs.3 and 4. Provided that rain drops become smaller at rainfall of low intensity, the results in Fig.2 indicate the fast wet-scavenging mechanism of SO_x-components of aerosols with fine raindrops having a large ratio of the interface to the volume.

Figure 2 shows the PIXE spectra obtained from three types of targets, which were prepared from rain water collected in one hour at the beginning of rain on March 15, 1999; the insoluble components on a Nuclepore filter (in the left-hand side), the soluble components deposited on a polycarbonate film (in the middle), and the soluble heavy metals preconcentrated into DBS gels on a Nuclepore filter (in the right-hand side). The Ga and Pd peaks are from the internal standards used. The K and L X-ray lines are observed for 17 elements in the spectra. This indicates that the PIXE technique has the advantages of a truly multielemental character and a high speed analysis using a small amount of samples. The X-ray lines of many heavy metals are clearly detected in the spectrum of the target prepared with the DBDTC-DBS preconcentration. From this result, we can understand why the preconcentration step is indispensable to the PIXE analysis for heavy metals in very low concentrations (< 10 ng/ml). In contrast to this, the spectra obtained from the deposit of filtered rain water allows us to determine the concentrations of major soluble elements such as alkali metals, alkaline earth metals and anionic species of S and Cl which cannot be picked up in the preconcentration step. An important result is that the PIXE analysis for the three types of targets reveals elemental distribution in the widespread concentration range between the soluble and insoluble fractions of rain-water samples.

Figures 3 and 4 show the two different patterns of the changes in elemental fallout per one-hour rainfall over 7-10 hours from the beginning of rain. For the rain episode on May 19, 1999 (Fig. 4), the fallout amounts of 17 elements in both soluble and insoluble fractions decrease gradually with the sampling time (the increase of the total amount of

rainfall), with only one exception of the first sample collected at the beginning of rain. This suggests the scavenging of elements in aerosol particles by raindrops. The similar pattern as in Fig. 4 was observed in the case of rainfall on December 7, 1998. As can be seen from Fig. 5, on the other hand, the elemental fallout is rather constant over the whole sampling period of rain on March 15, 1999, although the rainfall in this case was much heavier relative to the other cases, as shown in Fig. 1. In this rain episode, the wet scavenging mechanism was most strongly expected but this mechanism was not manifested in the experimental result; it is considered that rain drops passed through atmospheric layer in which the amount and the composition of aerosols were kept rather constant probably due to a high wind. In any event, most of alkali metals, alkaline earth metals and anionic species of S, Cl and Br were present as soluble components in rain water. The insoluble fraction included Al, Si, and Fe as the principal elements which were originated mainly in the soil dust. The PIXE analysis with high sensitivity reveals that heavy metals such as Cr, Mn, Ni, Cu, Zn and Pb in either the minor component or the trace component distribute appreciably between both soluble and insoluble fractions of rain.

The total fallout amounts of typical elements in three different rain episodes are tabulated in Table 1. The values are the sum of elemental amounts in both soluble and insoluble fractions, and they are averaged to the fallout amount in a 1-mm rainfall. The fallout amounts of Si, Ca and Fe, which are originated mainly in the soil dust, deviate largely among different rain episodes. On the other hand, a rather constant fallout is detected in the three rain episodes for S, Cu, Zn and Pb, which are discharged mainly by an industrial activity. As a cause of the high sulfur-fallout it is considered that gaseous sulfur (SO_x) is adsorbed by rain drops during the transportation. Deposition of SO_x gas on the surface of solid dusts also may play an important role.

Drinking water

The quality assurance of drinking water is indispensable for our health. Here the methodology developed in this study was applied to monitoring quality of drinking water. Sixty ml of drinking water were collected from a faucet in our laboratory at 4-hour intervals over 72 hours by using Advantec fraction collector, Model SF-2120. Immediately after collection, the samples were filtered with Nuclepore filter of 0.4-μm pores, but no residue on the filter was detected in an appreciable amount. Hence, the samples were processed into two kinds of PIXE targets, that is, the preconcentration target for heavy metals as minor or trace component and the deposit target for major component.

Figure 5 shows the time-variation of elemental concentrations for major components (Na, Mg, Si, S, K and Ca) in the upper side, minor components (Cl, Ni, Fe and Zn) in the middle, and trace constituents (Ti, Cr, Mn, Cu, As, Br and Pb) in the bottom, respectively. The concentrations of the major components are in around ppm-level, while many kinds of transition metals distribute in widespread concentrations of 0.2 to 250 ppb (three orders of

magnitude). These concentrations are within the limit of quality of water to drink; [Na] ≤ 200 ppm, [Mg] and [Ca] ≤ 300 ppm, [Cu] and [Zn] ≤ 1 ppm, [Fe] ≤ 300 ppb, [pb] and [Mn] ≤ 50 ppb, [Ni] and [As] ≤ 10 ppb[16]. The analytical errors estimated from the spectral fitting program, respectively, were less than ±14 % for major components and more than ± 40 % for trace components in sub-ppb concentration. The PIXE analysis with high sensitivity and wide dynamic range reveals the changes in elemental concentrations of both major and minor components; the changes in concentrations of minor elements such as Ni, Fe, Zn and Cu correlate closely with that in Si-concentration as a major component. This result suggests the transportation mechanism of transition metals adsorbed on very fine particles of silica colloids in high concentration. The relatively high concentrations of Na, Si, Ca and S are attributable to blending city tap water with well water at our departmental facility of a water supply.

Conclusion

In this study, a procedure has been developed and tested for the PIXE analysis of soluble and insoluble constituents in river waters. The target preparation and the PIXE measurement are not time-consuming; the preconcentration step requires less than 10 minutes, and the samples are analyzed by PIXE in which targets are irradiated by a 3 MeV proton beam for 5 minutes. Many kinds of elements can be detected simultaneously in the widespread range of concentrations from several tenths of ppb to a few tens of ppm. The elemental concentrations largely vary with time, and the change in the soluble fraction is not correlated to that of the insoluble fraction. Moreover, some heavy metals of importance as an indication to water-pollution problem are predominant in the insoluble fraction of river waters. Hence, the methodology for preparing targets of both soluble and insoluble components promotes the PIXE analysis to a truly effective means for monitoring a pollution problem of rivers.

References

1) Akselsson, K.R., Nucl. Instr. and Meth., **B3** 1984) 425.
2) Kasahara, M., et al., Nucl. Instr. and Meth., **B109** (1996) 471.
3) Tanaka, S., et al., Environ. Sci. Technol., **15** (1981) 354.
4) Johansson, E. M. and Johansson, S. A. E., Nucl. Instr. and Meth., **B3** (1984) 154.
5) Yamazaki, H., et al., Int. J. PIXE, **6(3&4)** (1996) 483; ibid, **7(1&2)** (1997) 31, 101.
6) Yamazaki, H., et al., American Institute of Physics Conference Proceedings. **475** (1999) 443.
7) · Iwasaki, S., et al., Int. J. PIXE, **5(2&3)** (1995) 163.
8) Matsuyama, S., et al., Int. J. PIXE, **9(1&2)** (1999) 51.
9) Futatsukawa, S., et al., Int. J. PIXE, **7(3&4)** (1997) 171.
10) Murozono, K., et al., , Int. J. PIXE, **6(1&2)** (1996) 135; Nucl. Instrum. Meth., **B150** (1999) 76.
11) Johansson, S.A.E. and Campbell, J.L., "PIXE. A Novel Technique for Elemental Analysis," John Wiley &Sons, New York, 1988, pp.313-329.
12) Kasahara, M. et al., Nucl. Instrum. Meth., **B118** (1996) 400.

Table. 1. Total (soluble + insoluble) fallout amounts of typical elements as either major or minor component in three rain episodes

Element	Fallout Amount (ng/cm^2/1-mm rainfall)		
	Dec. 7, 1998	Mar. 15, 1999	May 19, 1999
S	61	65	56
Si	46	9.7	26
Ca	21	10	14
Fe	3.9	1.6	2.5
Cu	0.32	0.28	0.35
Zn	1.1	1.1	1.0
Pb	0.27	0.28	0.23

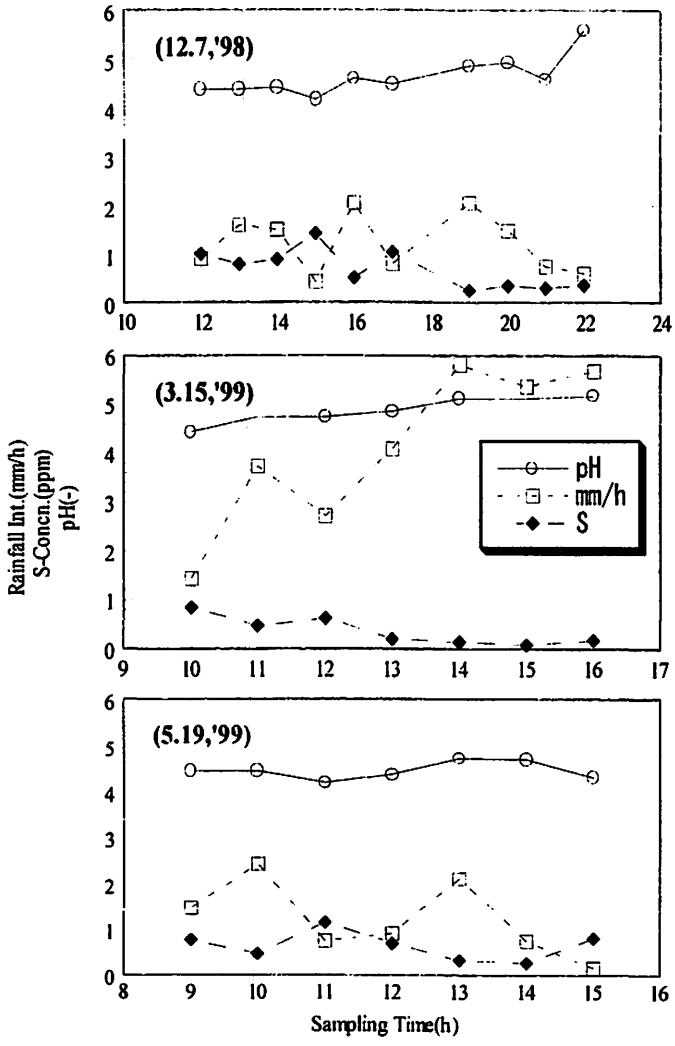

Fig. 1. The changes of rainfall intensity, pH and sulfur-concentration in one-hour rainfall (three rain episodes).

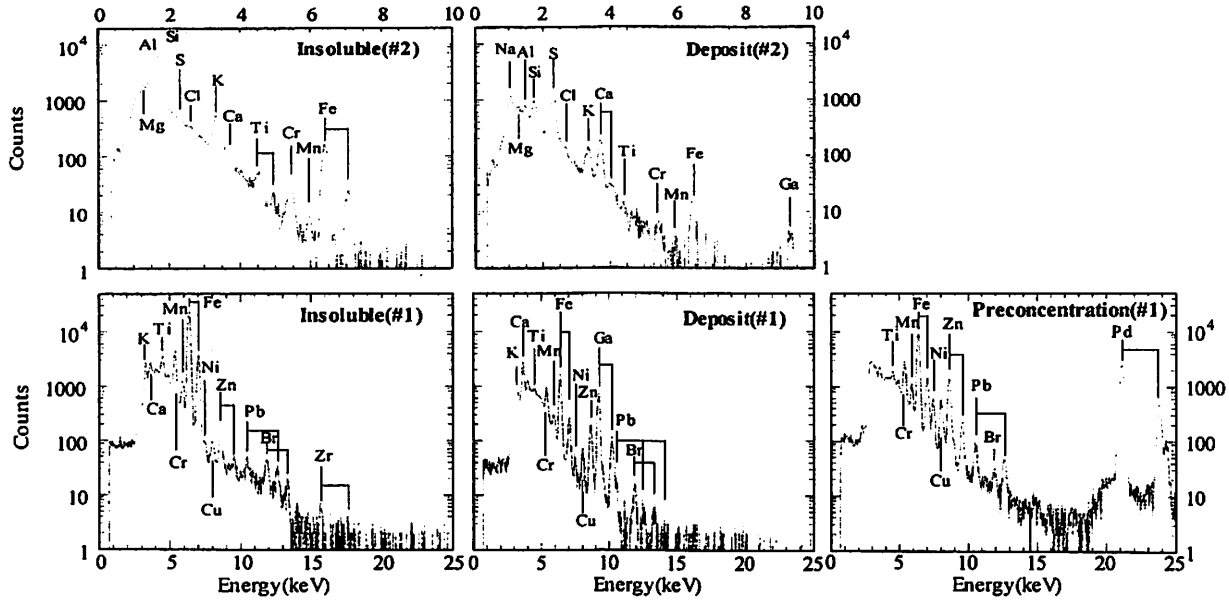

Fig. 2. PIXE spectra for rainwater samples collected on March 15, 1999. The upper spectra were obtained with No.2-detector directed to X-rays of low energy. The lower spectra were obtained with No.1-detector. The experimental condition was the same as described in Experimental.

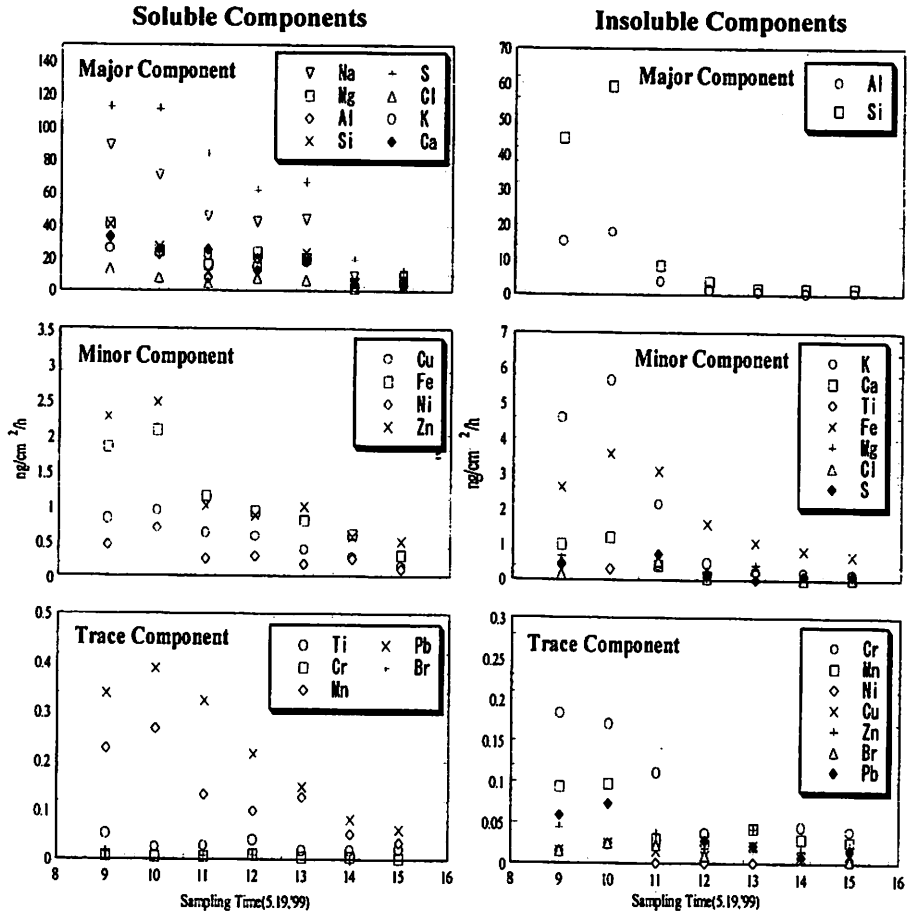

Fig. 3. Change in elemental fallout per one-hour rainfall on May 19, 1999 (Scavening Mechanism).

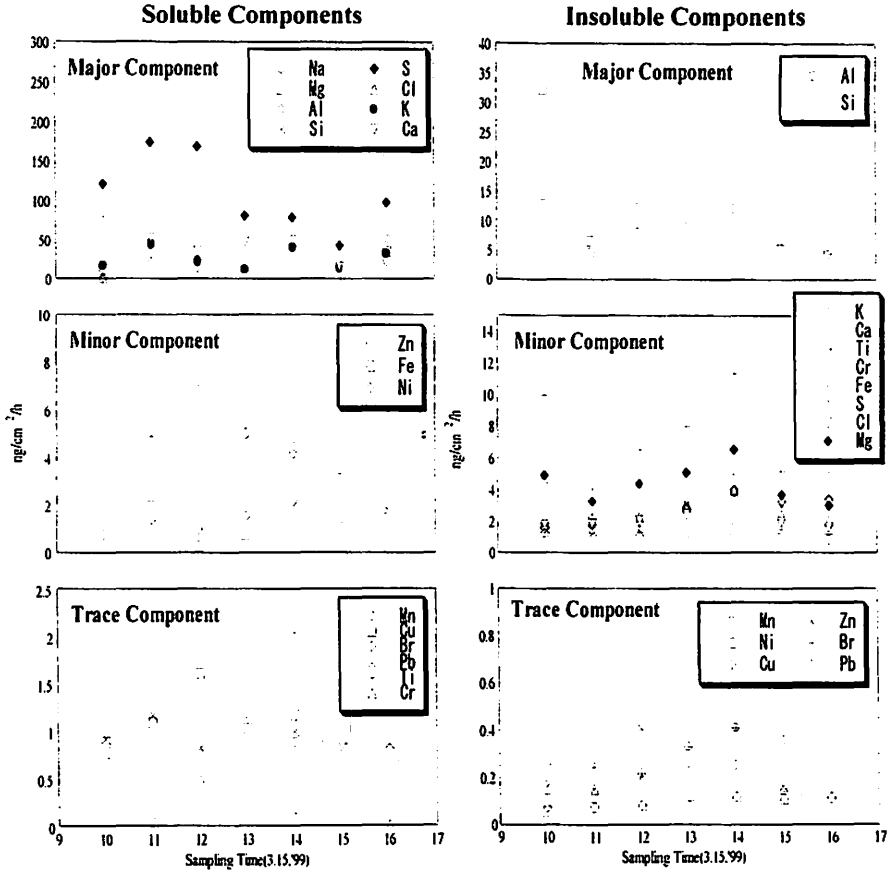

Fig. 4. Change in elemental fallout per one-hour rainfall on March 15, 1999 (No-Scavenging Mechanism).

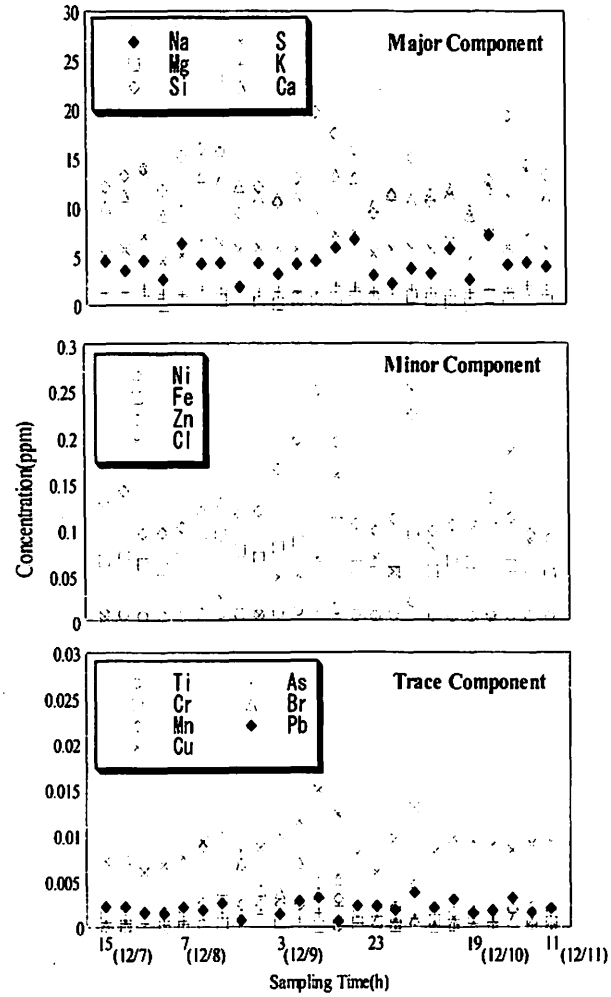

Fig. 5. Tine-variation of elemental concentrations in drinking water. Samples were collected at 4-hour interval over 72 hours.

II CHEMISTRY

II. 1. Preparation of ^{11}C-radiopharmaceuticals from [^{11}C]methyl Triflate by Loop Method

*Iwata R. *, **, Miyake Y. ***, Kato M. ****. Yanai K. ****, Ido T **, and Ishiwata K. ******

Quantum Science and Energy Engineering, Tohoku University, CYRIC Tohoku University**,. National Cardiovascular Center***, School of Medicine, Tohoku University**** and Tokyo Metropolitan Institute of Gerontology*****.*

Since [^{11}C]methyl triflate ([^{11}C]MeOTf) was introduced as a more reactive [^{11}C]methylation agent than [^{11}C]methyl iodide ([^{11}C]MeI)[1], several radiosyntheses of ^{11}C-labelled compounds have been improved by substituting [^{11}C]MeOTf for [^{11}C]MeI[2-4]. Especially it is reported that radiochemical yields and reproducibility in the synthesis of frequently used [^{11}C]raclopride can be greatly increased using [^{11}C]MeOTf[5].

Noting that [^{11}C]MeOTf is a more reactive and less volatile agent, we expected that it could be easily trapped by a small volume of precursor solution and rapidly reacted without heating. This led us to develop a simple loop method suitable for automated preparation of ^{11}C-radiopharmaceuticals from [^{11}C]MeOTf. It is a very simple, convenient method using a loop of narrow plastic tubing as a reaction vessel to retain a precursor solution[6].

[^{11}C]Carbon dioxide was produced with a Cypris HM12 cyclotron (Sumitomo Heavy Industries, Inc.) and converted to [^{11}C]MeI by the catalytic gas-phase iodination reaction *via* [^{11}C]CH_4 (GE MeI MicroLab). [^{11}C]Methyl iodide, swept with a He flow at 35 mL/min, was passed through the AgOTf-Graphpac GC column[1] heated at 200°C, affording [^{11}C]MeOTf.

Demethylraclopride triflate or nordoxepin triflate (approx. 1 mg) was dissolved in methylethylketone (MEK; 0.1 mL) and NaOH (1.2 M, 2 mL) was added. The whole precursor solution was injected into a looped PTFE tube (i.d. 0.75 mm x 50 mm long), which was then flushed with He for a short while. The loop was then connected to an automated system (Fig. 1). The automated procedure consists of the following 5 steps (Fig. 2).

1. The [^{11}C]MeOTf was passed through the loop.
2. The loop was rinsed with 1 mL of HPLC solvent and this volume was collected into a glass reservoir.
3. The reaction mixture was transferred into an HPLC injection loop using a suction syringe.
4. The mixture was injected onto an HPLC column.

5. The desired product eluting from the column was collected.

[^{11}C]Raclopride was purified on a YMC ODS A-324 column with a solvent system of 10 mM H_3PO_4-MeCN (65/35) at a flow rate of 5 mL/min and [^{11}C]doxepin on a Tosoh TSG-Gel ODS-80 with a solvent system of 33 mM HCO_2NH_4-MeCN (62.5/37.5) at a flow rate of 8.5 mL/min.

As expected trapping efficiencies of flowing [^{11}C]MeOTf by the loop were high enough with less than 0.1 mL of precursor solution. They were 65±10% for [^{11}C]raclopride and 92±7% for [^{11}C]doxepin.

After trapping of [^{11}C]MeOTf, the reaction was quenched by passing the HPLC solvent through the loop and more than 80% of the ^{11}C-radioactivity collected from the loop was usually found as [^{11}C]raclopride. Thus the reaction of [^{11}C]MeOTf with demethylraclopride seems to be very prompt even at room temperature. The overall radiochemical yield of [^{11}C]raclopride from [^{11}C]MeOTf was usually more than 50% (EOB).

On the other hand, radiochemical yields of [^{11}C]doxepin were observed to vary from 20% to over 80%, depending on the mass ratio nordoxepin to methyl triflate. The rest of ^{11}C-radioactivity was assigned to [^{11}C]methyldoxepin. Considering that the formation of this [^{11}C]dimethylated product was almost negligible with [^{11}C]MeI, this can be explained by the difference in reactivity between [^{11}C]MeOTf and [^{11}C]MeI. As it is known that the order of the S_N2 reaction rate of methylation with amines is normally tertiary amine > secondary amine > primary amine, more reactive MeOTf produces the dimethylated product, methyldoxepin from the methylated product, doxepin (Fig. 3). Thus, higher radiochemical yield of [^{11}C]doxepin can be achieved only by using high specific activity [^{11}C]MeOTf or, as a less desirable alternative, by increasing the amount of precursor. [^{11}C]Doxepin was prepared in over 50% radiochemical yields (EOB) from high specific activity [^{11}C]MeOTf.

References

1) Jewett D.M., *Appl. Radiat. Isot.* **43** (1992).
2) Någren K., Müller L., Halldin C., Swahn C.-G., Lehikoinen P.,. *Nucl. Med. Biol.* **22** (1995) 235.
3) Någren K., Halldin C.,. *J. Label. Comp. Radiopharm.* **41** (1998)831.
4) Lundkvist C., Sandell J., Någren K., Pike V. W., Halldin C., *J. Label. Comp. Radiopharm.* **41** (1998) 545.
5) Langer O., Någren K., Dolle F., Lundkvist C., Sandell J., Swahn C.-G., Crouzel C., Maziere B., Halldin C., *J. Label. Comp. Radiopharm.* **42** (1999) 1183.
6) McCarron, J. A., Turton D. R., Pike V. W., Poole K. G., *J. Label. Comp. Radiopharm.* **38** (1996) 941.

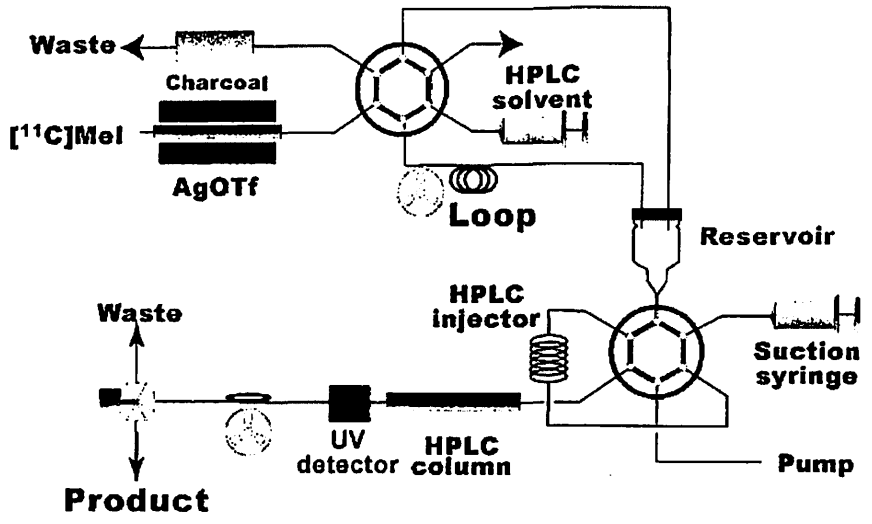

Fig. 1 A flowchart of the automated loop system.

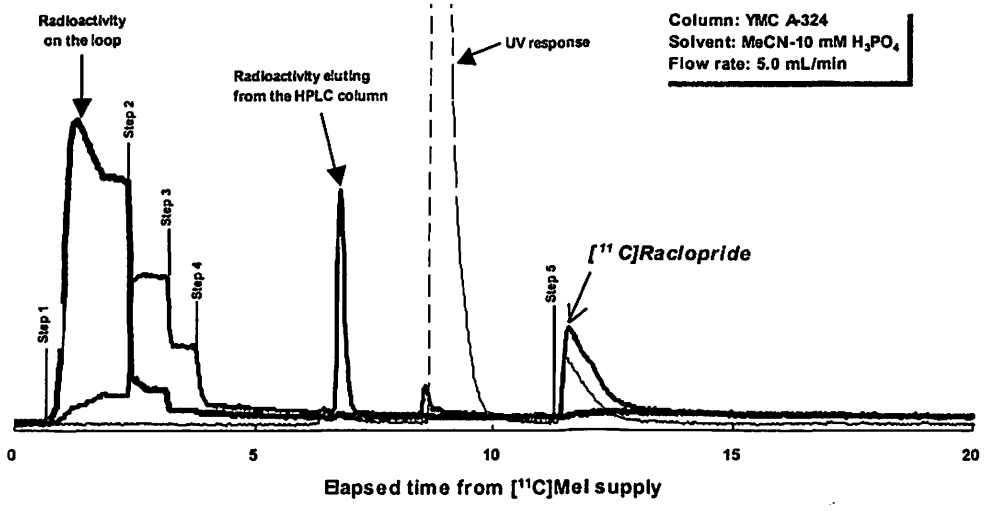

Fig. 2 A typical profile of radioactive and UV traces during [^{11}C]raclopride preparaation.

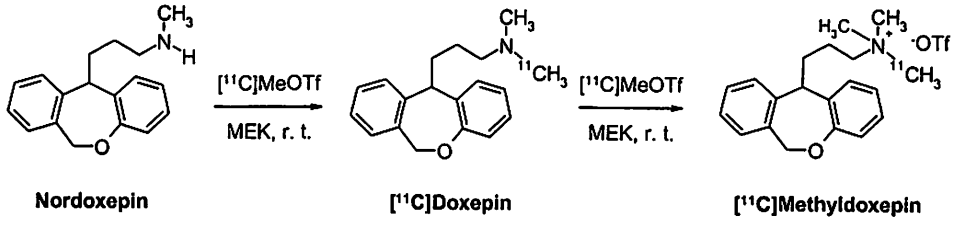

Fig. 3 The reaction of [^{11}C]MeOTf with nordoxepin.

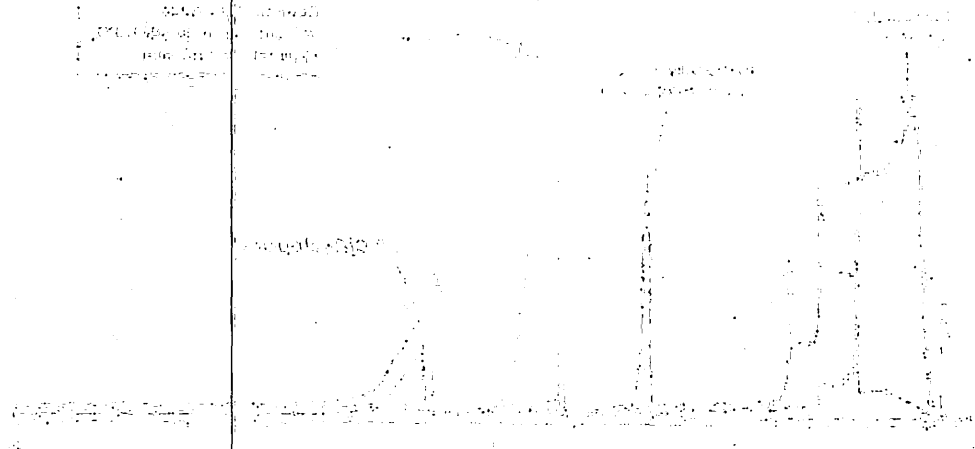

III. MEDICINE AND BIOLOGY (Basic)

III. 1. Membrane Ganglioside Composition: Important Factor in Beta-Amyloid Accumulation on cell Surface

Valdes-Gonzalez, T., Inagawa J. and Ido T.*

Cyclotron and Radioisotope Center, Tohoku University
*Biacore, Tokyo**

Interactions between β -amyloid (Aβ) peptides and neuronal membranes play an important role in Alzheimer's disease (AD). Using Surface Plasmon Resonance we assayed a kinetic model to study the interactions of Aβ25-35, Aβ40 and Aβ42 with surfaces containing single glycolipids (Asialo-GM1, GM1, GD1a or GT1b) or ganglioside mixtures. For the interactions of Aβ with single gangliosides a special group of sensorgrams with linear association phases appeared due to the accumulation of Aβ on the membranes. This kind of sensorgrams did not occur when Aβ interacted with surfaces containing mixed gangliosides. Our results indicate that some uniformity in membrane gangliosides is required for Aβ to accumulate on cell surfaces.

Introduction

Alzheimer's disease (AD), the major form of progressive senile dementia in the elderly, is pathologically characterized by the deposition of abnormal fibrous protein in senile plaques and in neurofibrillary tangles in the brain. The main component of the senile plaques, β-Amyloid (Aβ) protein[1], (a family of 39-43-residue peptides) is a fragment derived from a much larger amyloid precursor protein (APP)[2,3].

Several studies indicate that Aβ effect may be mediated, in part, by direct interactions between Aβ and membrane lipids and, especially the interactions with glycolipids have been investigated[4,5]. In AD brains, the ganglioside patterns significantly change compared to the normal elderly brain[6,7] and the proportion of major gangliosides are different in the early-onset and late-onset forms of the disease in the hippocampus, cerebral cortex, basal ganglia and amygdala[8].

Materials and Methods

Liposome and HPA chip preparation: Liposomes containing single gangliosides or mixed gangliosides (GM1: GD1a: GT1b (1:1:1)) were prepared and injected on the HPA sensor chip[9].

Injection conditions- The peptides were dissolved in the HEPES buffer (pH 7.4, 7.0, 6.5 or 6.0), to obtain concentrations from 400 to 3.65 ug/mL and 15 uL were injected on the the HPA surfaces contaning gangliosides, at 5 uL/min flow rate, using the multi-channel pathway to shorten the experiment, and this way to avoid the effects of Aβ aggregation. The liposomes containing only DMPC were used as controls to determine the non-specific binds.
Kinetics of Aβ-ganglioside interaction- Kinetic parameters were calculated using the BIA evaluation 3.1 software. The dissociation rate constant (k_{off}) was derived using the equation:

$$R_t = R_{t0} e^{-koff(t-t0)} \quad (1)$$

where R_t is the response at time t and R_{t0} is the amplitude of the initial response. The association rate constant (k_{on}) can then be derived using the equation:

$$R_t = [k_{on}\, CR_{max}(1-e^{-(konC+koff)t})] / (k_{on}C+k_{off}) \quad (2)$$

where R_t represents the response at time t, R_{max} is the maximum response; C, the concentration of peptide in solution and k_{off}, the dissociation rate constant.
Affinities were calculated from rate constants:

$$KD = k_{off}/k_{on} = 1/KA \quad (3)$$

KD is the dissociation constant and *KA*, the affinity constant.

Ca^{2+} effect- The flow-cell surfaces were washed with 10mM HEPES, pH 7.4 containing 2.8 mM $CaCl_2$, then Aβ40 and Aβ42 (100 ug/mL in the same buffer, but without Ca^{2+}) were injected individually. All the measurements and surface regenerations were carried out in the initial HEPES buffer, which contained Ca^{2+}.

Results

Aβ-ganglioside Binding Kinetics-. The profiles of Aβ40, Aβ42 and Aβ25-35 binding the surfaces at pH 7.4 are shown in Fig. 1 and Fig. 2, respectively.

For Aβ40 (Fig. 1A, B, C) the interactions depended on the number of molecules of sialic acid in the ganglioside sugar moiety because the kinetics of the Aβ40 binding to surfaces containing monosialo gangliosides and polysialo gangliosides were different. For surfaces containing GD1a or GT1b, the sensorgrams showed normal shapes at low Aβ40 concentrations, but at 5.8 uM, the association phase of the sensorgrams became linear and the dissociation was slow. At 11.5 uM the sensorgrams recovered the normal shape and RU values dramatically increased with a rapid association rate, but the dissociation was still slow. From this concentration on, the Rmax decreased with the increasing Aβ40 concentration. In the sensorgrams describing the interaction of Aβ40 with surfaces containing GM1 (Fig. 1A), the linear shape did not appear. For Aβ42 (Fig. 1D, E, F), at 5.5 uM the association phase

of the sensorgrams became linear in the interactions with all the surfaces containing single gangliosides. Similarly to Aβ40, at higher Aβ42 concentrations the specificity decreased with the increasing concentration.

The interactions with the DMPC or asialo-GM1 surfaces showed low specificity and affinity and in no cases was the linear shape observed (Fig.3).

All the experiments under acidic conditions gave lower RUs than those at neutral pH. Besides, the sensorgrams became linear at lower Aβ concentrations, even for the interaction of Aβ40 with surfaces containing GM1, where the linear shape was not observed at all at the neutral pH nor pH 7.4 (Fig. 4).

The interactions of Aβ25-35 with the ganglioside-containing surfaces under neutral conditions were characterized by low specificity at any concentration, similar to the interactions with DMPC. Nevertheless, with the decreasing pH, the RU values increased (Fig. 2).

In the experiments at pH 7.4 where Aβ40 and Aβ42 bound to surfaces containing the ganglioside mixtures the linear shapes did not appear (Fig. 6), but some differences were found in these interactions. For Aβ40, the Rmax of the sensorgrams decreased with the increasing concentrations from 23.1 uM, similar to the interaction with surfaces containing GM1; for Aβ42 this effect was observed from a concentration of 11.1 uM, similar to the interactions that promoted linear shapes in the sensorgrams. All the interactions with surfaces containing the ganglioside mixtures were higher for Aβ42 than for Aβ40.

Aβ- ganglioside affinities- The association and dissociation rates, as well as the affinity constants for the bindings of Aβ to surfaces containing single gangliosides were characterized at pH 7.4, 7.0, 6.5 and 6.0, as shows the Table I.

Table II shows that the differences observed in the interactions of peptides with the ganglioside mixtures result in higher affinity for Aβ40 than for Aβ42.

Effect of Ca^{2+} on Aβ binding to liposomes- We found that for the interaction of both Aβ40 and Aβ42 with all the surfaces containing gangliosides, the sensorgrams had a normal shape and the Rmax values of the association phases significantly increased (Fig. 6).

These observations suggest that the Ca^{2+} contained in the extracellular space promote the interaction of Aβ40 and Aβ42 with surfaces containing gangliosides.

Discussion

The most significant finding in our experiments are the two different groups of Aβ-ganglioside interactions: those that promoted a linear shape of the sensorgrams and those that do not. Our results suggest that the linear shape is related with the accumulation of Aβ on the membranes as follows: at low concentrations Aβ interacts directly with the gangliosides (the sensorgrams have normal curves at low concentrations with high affinity). With the increasing Aβ concentration, some molecules remain bound to gangliosides even during the dissociation phase after finishing the injection. The number of these Aβ molecules fixed to

the gangliosides increases proportionally with the concentration, to form an Aβ layer fixed on the surface containing gangliosides. Consequently, from a determined concentration the newly injected Aβ does not bind to the gangliosides, but to the Aβ fixed on the surface. This way a laminar-arranged Aβ accumulate is progressively formed on the membrane surface and fixed there. The affinity for these accumulate formations is defined by the binding of Aβ in solution to Aβ fixed in the surface, where for each Aβ molecule bound, new binding sites are activated on the surface in a linear ratio, which explains the linear shape of the sensorgrams. Thus, for Aβ to accumulate some uniformity of the ganglioside sugar moiety is required.

Actually, in the normal brain the gangliosides are presented in the membrane as a mixture of different gangliosides, thus under normal conditions the probability of Aβ accumulation on the brain membrane would be low. There are neurological disorders that promotes dramatic changes in the membrane ganglioside composition[10,11], which may induce modifications in the Aβ interaction with the cell membrane. Especially if the same kind of gangliosides is concentrated in a determined area, creating uniform clusters in the membrane surface, the Aβ accumulation would be more probable to occur.

References

1) Glenner, G.C., Wong, C.W. Biochem. Biophys. Res. Comm. **120** (1984) 885-890.
2) Kang, J., Lemaire, H.-G., Unterbeck, A. et al. Nature **325** (1987) 733-736.
3) Goldgaber, D., Lerman, M. I., McBride, O. W. et al. Science **235** (1987) 877-880.
4) MacLaurin, J.; and Chakrabatty, A. J. J. Biol. Chem. **271** (1996) 26482-26489.
5) MacLaurin, J.; Franklin, T.; Fraser, P., Chakrabatty, A. J. Biol. Chem **273** (1998) 4506-4515.
6) Crino, P.B., Ullman, M, D., Vogt, B. A., et al. Arch. Neurol. **46** (1989) 398-401.
7) Kracun, I., Kalanj, S., Talan-Hranilovic, J., Cosovic. Neurochem. Int. **20** (1992) 433-438.
8) Svennerholm, L., Gottfries, C. J. Neurochem. **62** (1994) 1039-1047
9) Valdes-Gonzalez, T., Inagawa, J; Ido, T. (2001) Peptides **22** (2001) 1099-1106.
10) Valdes-Gonzalez, T., Morita, Y., Suzuki, K., and Ido, T. Neuroscience Res. **39** (2001) 197-203.
11) Rahmann, H. Behav. Brain Res. **66** (1995) 105-116.

Table 1. Kinetic parameters for the interactions of Aβ 40and Aβ42 with single ganglioside at different pH.

pH	Ganglioside	k_{on} ($M^{-1}s^{-1}$)	k_{off} (s^{-1})	KD (M)	k_{on} ($M^{-1}s^{-1}$)	k_{off} (s^{-1})	KD (M)
7.4	GM1	$3.05x10^{2}$	$1.62x10^{-3}$	$1.32x10^{-6}$	$1.05x10^{3}$	$1.39 x10^{-3}$	$1.4 x10^{-6}$
		1.4**	1.2	1.4	0.1**	2.1	2.2
	GD1a	$6.38x10^{2}$	$1.22x10^{-4}$	$1.65x10^{-7}$	$8.41 x10^{2}$	$5.05 x10^{-3}$	$1.1 x10^{-7}$
		0.8	1.6	1.1	2.5	1.0	0.01
	GT1b	$7.30x10^{2}$	$5.09x10^{-4}$	$2.89x10^{-7}$	$7.76 x10^{2}$	$9.87 x10^{-6}$	$4.2 x10^{-7}$
		0.7	1.0	3.0	6.0	0.1	1.5
7.0	GM1	$5.11x10^{3}$	$4.61x10^{-3}$	$1.29x10^{-7}$	$4.84 x10^{3}$	$8.50 x10^{-3}$	$1.9 x10^{-6}$
		3.1	2.4	0.5	2.0	0.4	0.9
	GD1a	$6.91x10^{2}$	$1.82 x10^{-4}$	$2.69 x10^{-7}$	$3.13 x10^{4}$	$8.38 x10^{-3}$	$3.3 x10^{-7}$
		1.0		2.5	2.3	5.1	1.6
	GT1b	$2.99x10^{3}$	$2.72 x10^{-3}$	$1.63 x10^{-7}$	$4.61 x10^{3}$	$2.86 x10^{-3}$	$8.5 x10^{-7}$
		2.3	1.6	0.9	3.0	0.9	5.3
6.5	GM1	$1.79x10^{3}$	$9.87 x10^{-6}$	$5.72 x10^{-9}$	$2.34 x10^{3}$	$1.00 x10^{-5}$	$4.3 x10^{-9}$
		4.6	2.1	1.4			
	GD1a	$1.48x10^{2}$	$2.09 x10^{-5}$	$1.38 x10^{-7}$	$8.55 x10^{3}$	$3.65 x10^{-3}$	$4.3 x10^{-7}$
		0.1	1.6	0.9	1.2	0.7	0.9
	GT1b	$2.98x10^{2}$	$1.63 x10^{-6}$	$6.20 x10^{-9}$	$2.25 x10^{3}$	$1.02 x10^{-5}$	$4.8 x10^{-9}$
		1.1	0.4	0.3	0.6	0.01	1.4
6.0	GM1	$2.32x10^{4}$	$1.09 x10^{-4}$	$4.69 x10^{-9}$	$1.88 x10^{4}$	$5.80 x10^{-6}$	$1.5 x10^{-10}$
		1.7	1.3	1.2	2.7	0.1	2.1
	GD1a	$1.98x10^{3}$	$8.03 x10^{-4}$	$4.57 x10^{-8}$	$4.72 x10^{4}$	$3.13 x10^{-3}$	$1.7 x10^{-8}$
		0.5	2.0	3.5	6.7	2.3	1.5
	GT1b	$2.96x10^{4}$	$2.55x10^{-8}$	$8.62 x10^{-13}$	$6.45 x10^{4}$	$4.82 x10^{-5}$	$2.9 x10^{-10}$
		0.7	1.5	0.9	3.9	0.2	3.1

** are the % of standard error.

Table 2. Kinetic parameters of the interactions of Aβ40 and Aβ42 with gangliosides containing ganglioside mixture.

	k_{on} ($M^{-1}s^{-1}$)	k_{off} (s^{-1})	KD_R (M)
Aβ40	$7.7x10^{3}$ (±0.7)**	$5.0x10^{-4}$ (±0.8)	$6.5x10^{-8}$ (±0.4)
Aβ42	$5.0x10^{3}$ (± 0.4)	$2.3x10^{-3}$ (±0.5)	$5.7x10^{-7}$ (±0.5)

The association rate (k_{on}), the dissociation rate (k_{off}) and the real dissociation constant (KD_R) are the mean values for the interactions of Aβ at low concentrations (lower than 5.5uM for Aβ40 and 5.8uM for Aβ42). ** are the % of standard error.

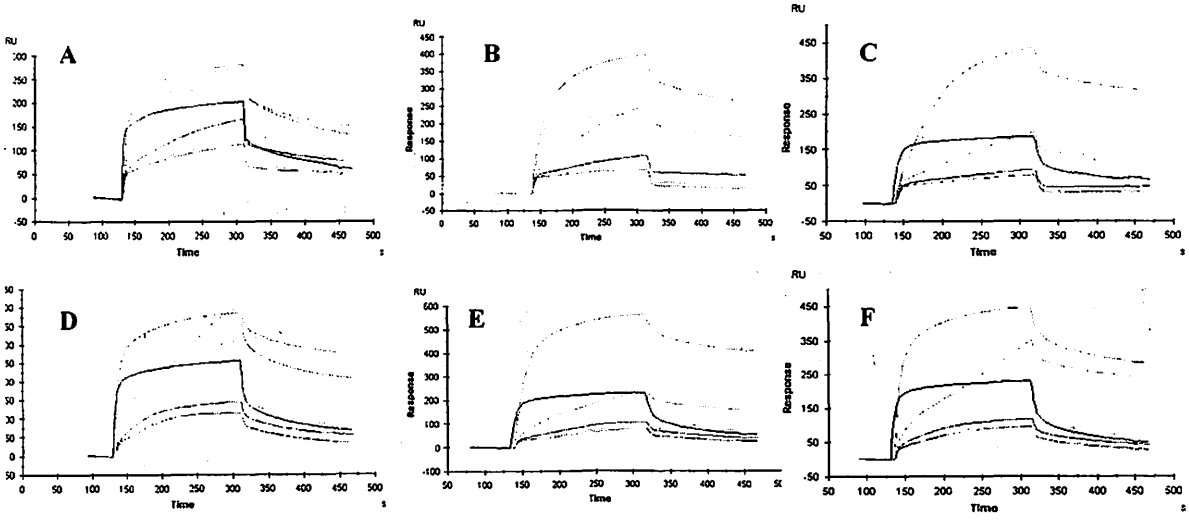

Fig. 1. Overlays plots of the interactions at different concentrations of Aβ40 with (A) GM1, (B) GDla and (C) GT1b and Aβ42 with (D) GM1, (E) GDla and (F) GT1b fused to HPA sensor chip at pH7.4.

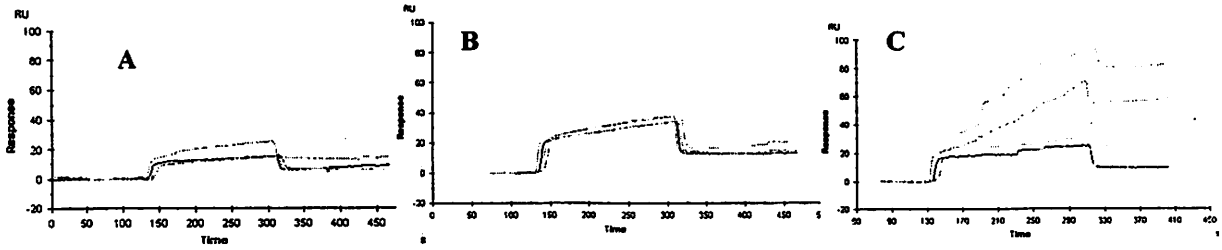

Fig. 2. Sensorgrams of Aβ25-35 (12.5uM) binding to liposomes fused to HPA sensor chip, at pH (A) 7.0, (B) 6.5 and (C) 7.0.

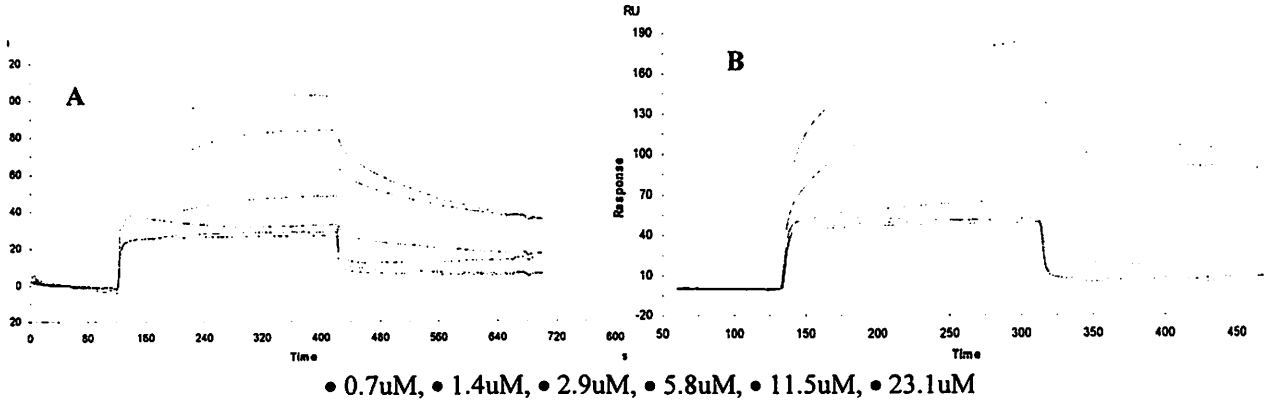

Fig. 3. Sensorgrams for interactions of (A) Aβ40 with asialo-GMl containing surfaces and (B) Aβ42 with DMPC surfaces at pH7.4.

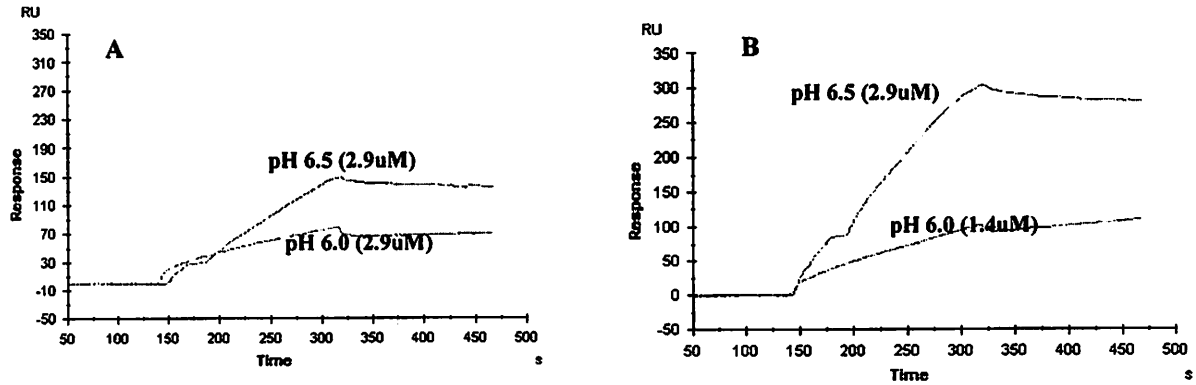

Fig. 4. Overlays plots representing the critical concentrations at which the linear shape appears at pH6.5 and 6.0 for the interaction of Aβ40 (A) GMl and (β) GTlb.

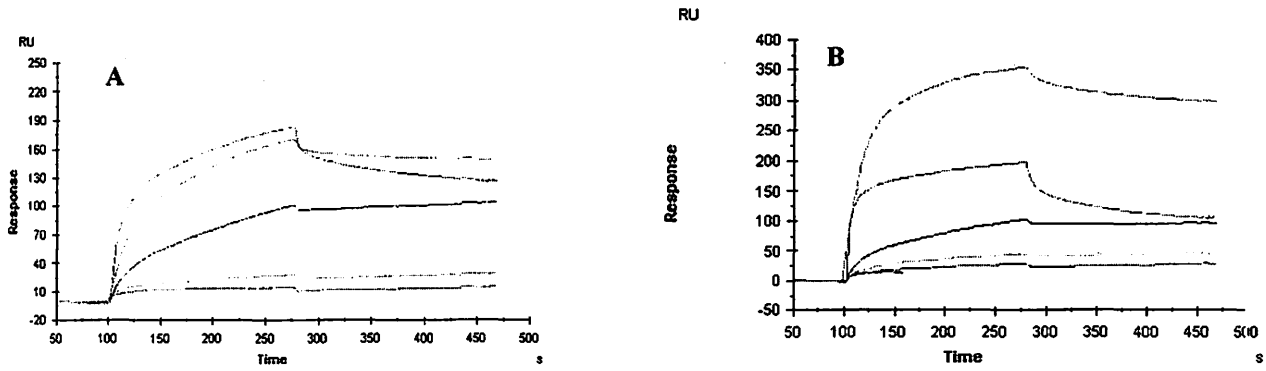

• 0.7uM, • 1.4uM, • 2.9uM, • 5.8uM, • 11.5uM,

Fig. 5. Overlays plots representing the interactions of different concentrations of (A) Aβ40 and (B) Aβ42 at pH 7.4 with liposomes containing GM1:GD1a: GT1b=1:1:1.

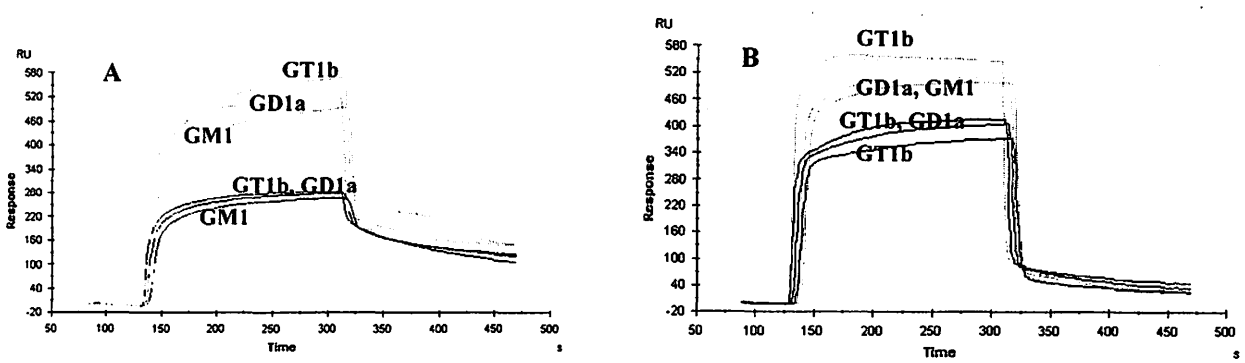

Fig. 6. Effect of 2.8 mM Ca^{2+} on the interactions of 100 μg/mL of (A) Aβ40 and (B) Aβ42 with ganglioside containing surfaces.

III. 2. Effect of Metal Ions on Beta- Amyloid Aggregation: Surface Plasmon Resonance and Atomic Force Microscopy

Valdes-Gonzalez T., Kitamura I., Matsumoto J.*, Saji H.*, and Ido T.*

Cyclotron and Radioisotope Center, Tohoku University
*Faculty of Pharmaceutical Sciences, Kyoto University**

Introduction

The establishment of the role that metal ions have in AD has been contradictory; some reports show the metal ions as AD promoting factors and other attribute them protective effects[1-4].

The main component of the senile plaques in Alzheimer disease (AD) is the β-Amyloid (Aβ) protein[5], (a family of 39-43-residue peptides) is a fragment derived from a much larger amyloid precursor protein (APP)[6].

Using Surface Plasmon Resonance and Atomic Force Microscopy we characterized the effect of Aβ incubation on the interactions with gangliosides and the effect of different metal ions on Aβ aggregation.

The Surface plasmon resonance (SPR) is a sensitive method that relies on the changes of angle of polarized light that occur at a metal-liquid interface. The continuous measuring of angle changes when an analite is injected, forms a sensorgram from which it is posible to calculate the different kinetic parameters of the analite-ligand interaction[7,8]. The use of SPR allows the on-time evaluation of the interactions between Aβ peptides and Gangliosides.

The Atomic Force Microscopy (AFM) provides three-dimensional images of a surface. The sample is analyzed by sensing the surface with a silicon tip attached to a sensitive cantilever. The interactions tip-cantilever are due to repulsion force, that promotes a deflection of the cantilever which is detected by the Position-sensitive Detector. This way, the resulting map of the sample surface is converted into visual images[9,10].

Materials and Methods

Aβ aging: The peptides β-Amyloid 1-40 (Aβ40, F.W 4329.8) and β-Amyloid 1-42 (Aβ42, F.W. 4514.1) were dissolved in HEPES 7.4 to 12.5uM on ice and incubated for 3 h at 37 °C. Next, the peptides dissolved at 0.7uM in HEPES were incubated with different metal ions (Ca^{2+}, Cu^{2+}, Zn^{2+} or Al^{3+}) at ratios Aβ/metal ion 1:1 or 10:1. The peptides incubated without any metal ion were used as controls.

Surface Plasmon Resonance: The liposomes containing different gangliosides were prepared[11]. Then, 30 uL of liposome solution were fused at 1 uL/min to the surface of the sensor flow cells to form flat hybrid bilayers and 5 uL of 10 mM NaOH were injected to remove the incompletely fused liposomes. The preparation of each flow cell was made individually, to obtain DMPC, asialo-GM1, GM1, GT1b and GD1a monolayers in the different flow cells. 10 mM HEPES pH 7.4, which contained 150 mM NaCl was used as a running buffer. All the analyses were performed at 25 °C. The samples of the incubated peptides were injected on the ganglioside containing surfaces.

Atomic Force Microscopy: 5uL of the samples were dispensed individually onto a mica surface, dried on a clean box and washed carefully with distilled water. Then the samples were dried overnight. The samples were measured with the Nanoscope IIa and analyzed with the analyzer Nanoscope Software 4.1.

Results

Surface Plasmon Resonance: Under our experimental conditions the formation of Aβ aggregates was accelerated by incubation at 37 °C of freshly dissolved Aβ at very low concentrations. A short time after incubation the interactions of Aβ with liposomes were measured and it was found that the interactions of Aβ40 and Aβ42 with all the surfaces (Fig. 1) increased. Even the Rmax for the interactions with surfaces without gangliosides became very high (about 10 times higher than for the interaction of peptides without incubation). All the interactions showed fast association rates, but the dissociation rates were similarly rapid and the affinities very low, suggesting that the formed aggregates only adsorb onto the liposome surfaces, being rapidly washed out after the injections finished.

For the samples containing metal ions we found differences between Aβ40 and Aβ42 at the both ratios studied (Fig. 2, 3). In the case of Aβ40, at ratio 10:1 all the ions promoted the sensorgram RU increase, as follows: $Al^{3+}=Ca^{2+}<Cu^{2+}<Zn^{2+}$ and at ratio 1:1, significant increases were found only after incubation with Ca^{2+} or A^{l3+} when compared with the Aβ40 control. For Aβ42, at ratio 10:1 the presence of ions promoted Aβ aggregation as follows: $Zn^{2+}=Al^{3+}<Ca^{2+}<<Cu^{2+}$.

Atomic Force Microscopy: When the samples were observed using Atomic Force Microscopy, we found for both Aβ40 and Aβ42 two different kinds of structures: fibers and aggregates. In the controls the fibers appeared, but the aggregates were few and small (Fig. 4). In general, the aggregate formation decreased as follows: $Cu^{2+}>Al^{3+}>Control>Zn^{2+}$ and the fibril formation, on the contrary increased as follows: $Cu^{2+}>Al^{3+}<Control>Zn^{2+}$ (Fig. 5,6, 7).

Discussion

It has been demonstrated that during the aging process, Aβ assembles into fibril[12]. Under our experimental conditions the formation of Aβ aggregates was accelerated by the incubation at 37 °C of freshly dissolved Aβ at very low concentrations.

After Aβ seeding, the sensorgrams for Aβ-ganglioside interactions showed a characteristic shape: rapid association and dissociation, and low affinity. The sensorgrams indicate that the formed aggregates only adsorb to the liposome surfaces, which means that once large Aβ aggregates are formed, the gangliosides do not interact with them. The effect of metal ions on aggregation depends on Aβ/ ion ratio: the Aβ42 aggregation is higher at ratio 1:1, and for Aβ40 this effect occurs at ratio10: 1. The highest increase was observed for Cu^{2+} with Aβ42 at 1:1. These observations suggest that the metal ions promote higher Aβ42 aggregation when the ratios of Aβ42:ion are similar, while for Aβ40 this effect occurs at higher concentrations of the peptide. Our observations indicate that the effect of metal ions is higher on Aβ42 than for Aβ40. The results with Al^{3+} agree with reports about the aggregation effect that this ion promotes on Aβ[3].

In the samples observed by AFM, both Aβ40 and Aβ42 showed two different kinds of structures: fibers and aggregates. The effect of metal ion in general seems to be related with aggregate formation and not with fiber formation, because in the controls the aggregates were few and small. The correlation between SPR and AFM experiments suggests that Aβ aggregate formation promoted by some metal ions could inhibit the Aβ fibril formation.

References

1) Esler, W.P., Stimson, E.R., Jennings, et al. J. Neurochem. **66** (1996) 2723-2732.
2) Horning, M. S., Blakemore, L. J., and Trombley, P. Q. Brain Res. **852** (2000) 56-61.
3) Exley, C., Schley, L., Murray, S., et al. FEBS Lett. **364** (1995) 2182-2184.
4) Borchardt, T., Camakaris, J., Cappai, R., et al. J. Biochem. **344** (1999) 461-467.
5) Glenner, G.C., and Wong, C.W. Biochem. Biophys. Res. Comm. **120** (1984) 885-890.
6) Kang, J., Lemaire, H.-G., Unterbeck, et al. Nature **325** (1987) 733-736.
7) MacKenzie, R.; Hirama, T.; Lee, K. et al. J. Biol. Chem. **272** (1997) 5533-5538.
8) Harrinson, B., MacKenzie, R.; Hirama, T. et al. J. Immunol. Meth. **212** (1998) 29-30.
9) Harper, J.D., Wong, S.S., Lieber, C.M. et al. Chem. Biol. **4** (1997) 119-125.
10) Harper, J.D., Wong, S.S., Lansbury, P. Chem. Biol. **4** (1997) 951-959.
11) Valdes-Gonzalez, T., Inagawa, J; Ido, T. (2001) Peptides **22** (2001)1099-1106.
12) Simmons, L.K., May, P.C. et al Mol. Pharmacol. **45** (1993) 373-379.

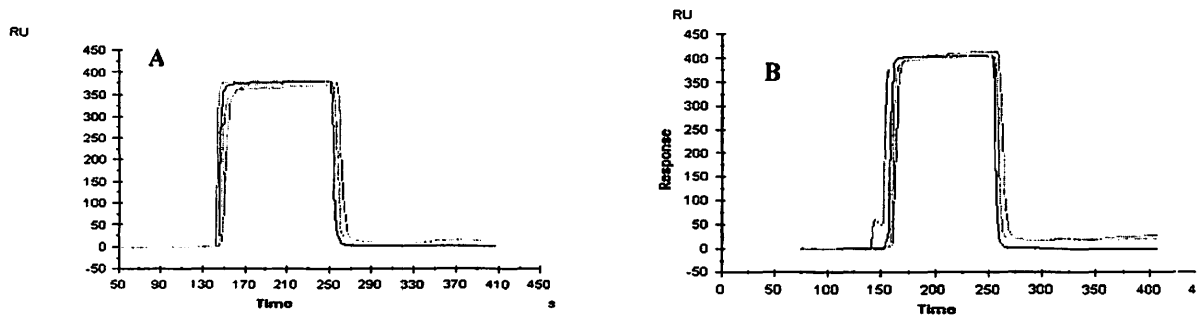

Fig. 1. Effect of incubation on the Aβ-ganglioside interactions (A) Aβ40 and (B) Aβ42.

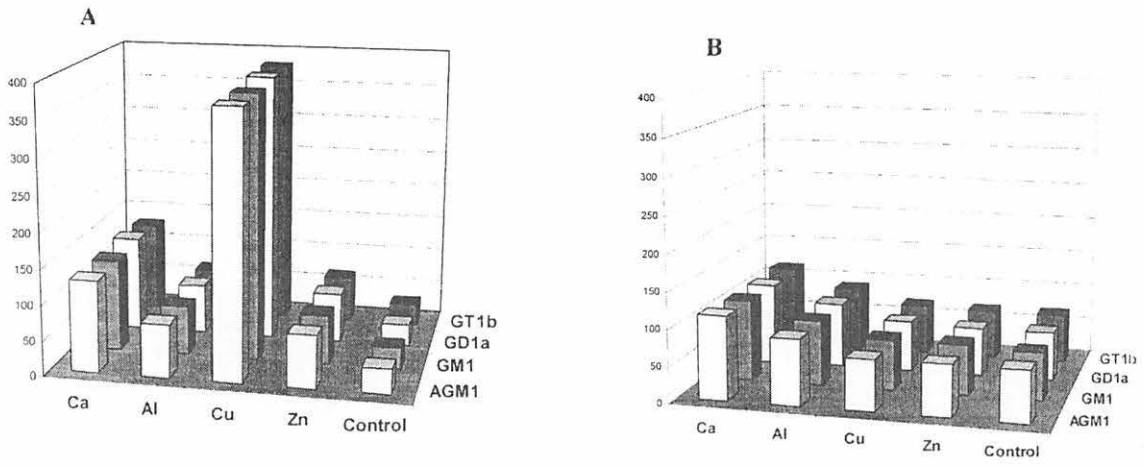

Fig. 2. Effect of metal ion on the interaction of (A)Aβ40 and (B)Aβ42 with gangliosides.

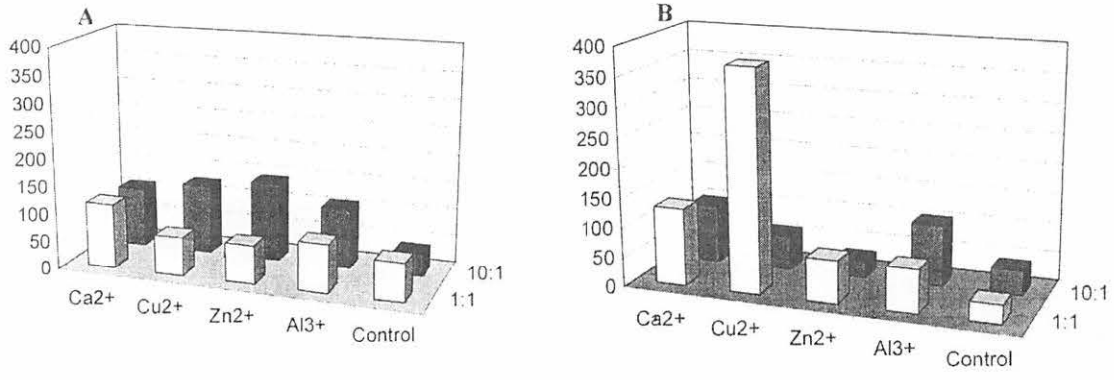

Fig. 3. Effect of metal ion on (A) Aβ40 and (B) Aβ42 aggregation.

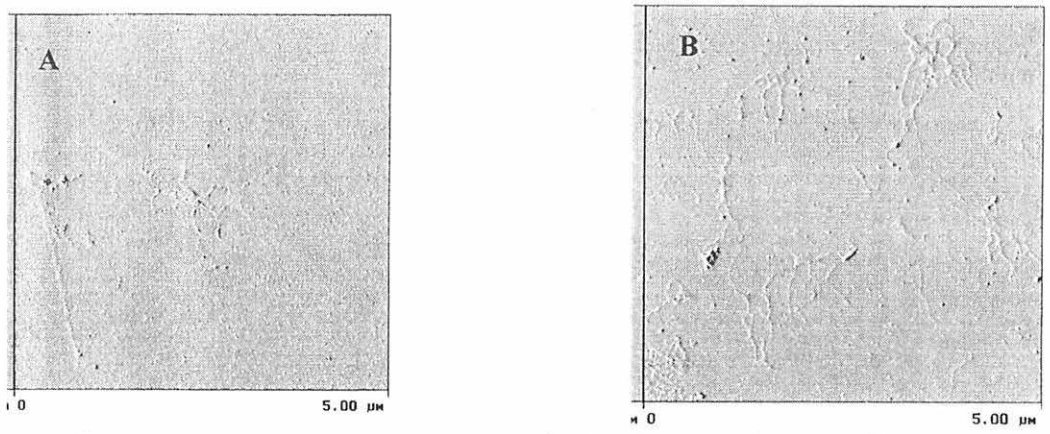

Fig. 4. Effect of incubation on (A) Aβ40 and (B) Aβ42 aggregation (controls).

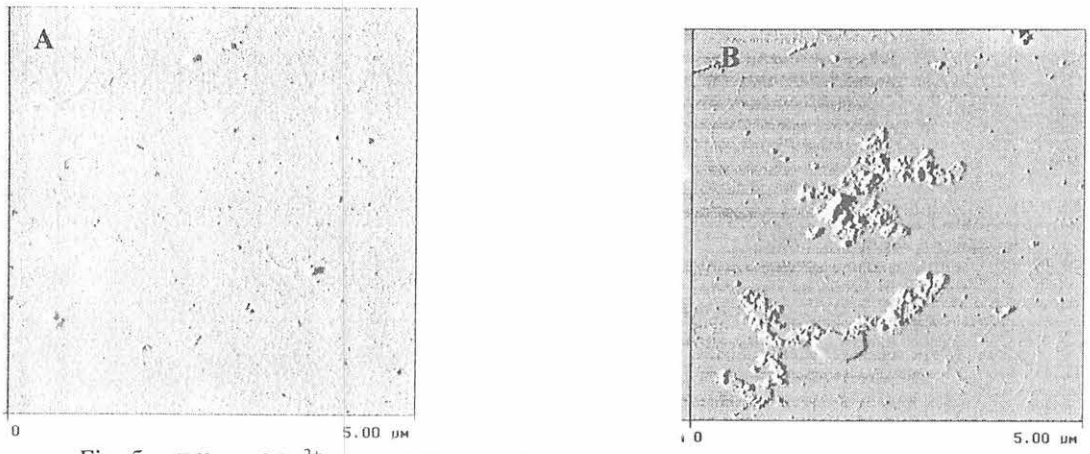

Fig. 5. Effect of Cu^{2+} on (A) Aβ40 and (B) Aβ42 aggregation.

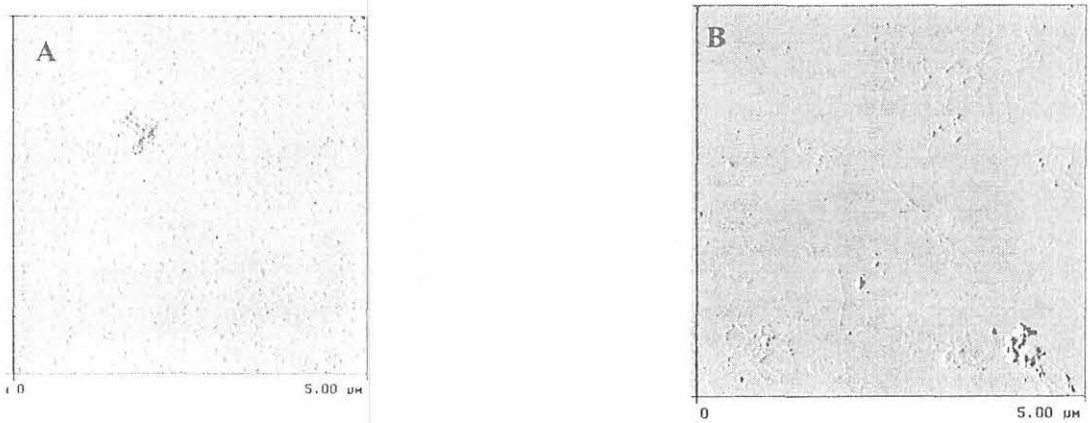

Fig. 6. Effect of Al^{3+} on (A) Aβ40 and (B) Aβ42 aggregation.

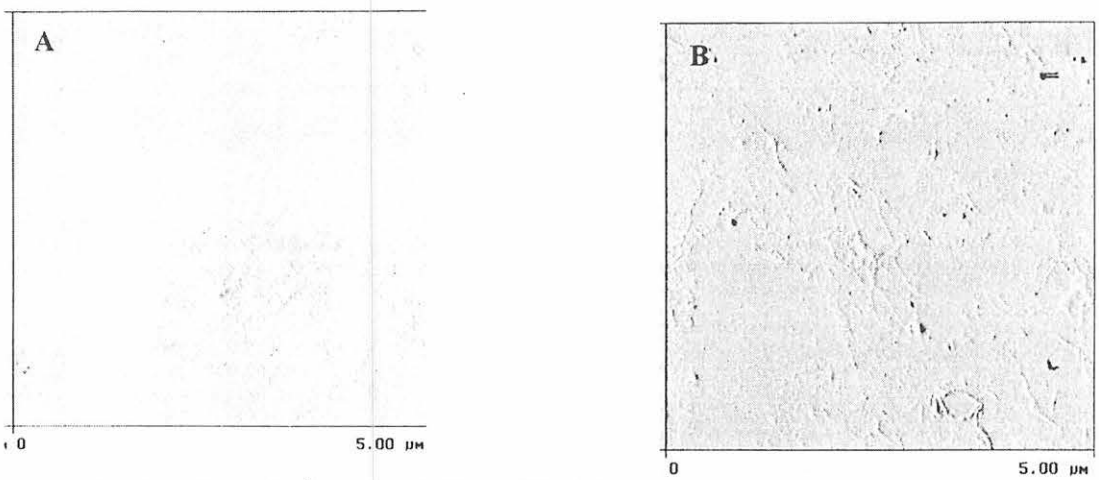

Fig. 7. Effect of Zn^{2+} on (A) Aβ40 and (B) Aβ42 aggregation.

III. 3. Protective Effect of Riluzole on MPTP-Induced Depletion of Dopamineand Its Metabolite Content in Mice

Akasaka M., Kumagai T., Ido T., Araki T., Matsubara M.*, Imai Y.*, and Itoyama Y.***

Cyclotron and Radioisotope Center, Tohoku University
*Department of Clinical Pharmacology and Therapeutics, Tohoku University Graduate School of Pharmaceutical Science and Medicine**
*Department of Neurology, Tohoku University School of Medicine**

INTRODUCTION

1-Methyl-4-phenyl-1,2,3,6-tetrahydropyridine (MPTP) is well known to produce clinical, biochemical and neuropathological changes analogous to those observed in idiopathic Parkinson's disease[1,2]. This neurotoxin also leads to a decrease of dopamine content in the striatum and loss in the number of nigrostriatal dopaminergic neurons in several species including monkeys, dogs, cats and mice. The neurotoxic effects of MPTP are thought to be initiated by MPP^+ which is a major metabolite formed by the monoamine oxidase (MAO) B-mediated oxidation of MPTP. MPP^+ is taken up by high-affinity dopamine and noradrenaline uptake systems and is subsequently accumulated within mitochondria of nigrostriatal dopaminergic cells[3]. There it disrupts oxidative phosphorylation by inhibiting complex I of the electron transport chain[4]. This can lead to a number of deleterious effects on cellular function, resulting in neuronal cell death. Therefore, the MPTP-treated mouse is widely used as a rodent model of Parkinson's disease.

Riluzole (2-amino-6-trifluoromethoxy benzothiazole) has been reported as an antagonist of excitatory amino acid neurotransmission[5]. This compound stabilizes voltage-dependent Na^+ channels in their inactivated state and inhibits the release of glutamate. A previous study demonstrated that riluzole did not prevent MPTP-induced dopamine depletion in the mouse striatum[6]. In contrast, Boireau et al.[7] reported that riluzole antagonized the MPTP-induced decrease in dopamine levels in mice. Thus, there is no consensus in the literature whether riluzole has neuroprotective activity in the brain of MPTP-treated mice. To make it clear whether riluzole is useful, we investigated a possible effect of riluzole.

MATERIALS and METHODS

Male C57BL/6J mice (22-28 g) were used in this study. The mice received intraperitoneal four injections of MPTP (10 mg/kg) at 1h intervals, the total dose per mice

being 40 mg/kg, as described previously[8]. The mice were sacrificed by cervical dislocation at 3 days after the last injection of MPTP for biochemical study as described below.

After decapitation, brains were quickly removed and the two striata were rapidly dissected out freehand on an ice-cold glass Petri dish. Samples were immediately weighed, then frozen and stored at -80°C until assay. The dissection procedure was performed in less than 2 min. Striata were sonicated in ice-cold 0.2M perchloric acid containing 100 ng/ml isoproterenol as internal standard. Homogenates were centrifuged at 3,000 rpm for 15 min at 4°C. The supernatant was filtered (pore size 0.45 μm, Millipore filter) and a 30-ul aliquot of the supernatant was used for determination of the dopamine, 3,4-dihydroxyphenyl acetic acid (DOPAC) and isoproterenol by high-performance liquid chromatography (HPLC) with an electrochemical detector (ECD) (Eicom, Japan). The mobile phase consisted of 0.1M sodium citrate-0.1M sodium acetate solution (pH 3.5) including 1.064 M octane sulfonic acid and 0.013 mM Na_2EDTA and 15% (v/v) methanol. The recoveries of dopamine, DOPAC and isoproterenol through the present procedures were > 93%. Levels of dopamine and its metabolite were calculated from the comparison of sample peak area with internal standard peak region and are expressed as μg/g tissue weight.

For the effect of riluzole, the animals were divided into 6 groups; (1) Vehicle (0.5 % carboxymethyl-cellulose, CMC)-treated group; (2) Riluzole (10 mg/kg)-treated group; (3) MPTP- and 0.5% CMC-treated group; (4) MPTP- and riluzole (3 mg/kg)-treated group; (5) MPTP-and riluzole(10 mg/kg)-treated group. The mice were injected intraperitoneally (ip) with riluzole or 0.5% CMC 30 min before and 90 min after the first administration of MPTP (Groups 3,4 and 5). For groups 1 and 2, 0.5% CMC-treated or riluzole (10 mg/kg)-treated animals were injected i.p. in the same manner with saline treatment instead of MPTP. Each group contained 5 animals. For additional study, the animals were divided into 2 groups; (6) MPTP- and 0.5% CMC –treated group; (7) MPTP- and riluzole (20mg/kg) -treated group. The mice were injected i.p. with riluzole or 0.5% CMC 30 min before and 90 min after the first administration of MPTP (Groups 6 and 7). Riluzole was generously provided by Rhone-Poulene-Rorer. Each group contained 5-7 animals.

The mice were killed by cervical dislocation at 3 days after the last MPTP treatment. As described above, striatal extracts were prepared for HPLC monoamine measurements.

All values were expressed as means±S.E. and statistical significance was evaluated using an analysis of variance (ANOVA) followed by Williams multiple range test.

RESULTS

Riluzole dose-dependently prevented a significant reduction in striatal dopamine and DOPAC levels of mice 3 days after MPTP treatments (Table 1). Furthermore, riluzole at a higher dose of 20 mg/kg prevented a significant reduction in striatal dopamine, DOPAC, and HVA levels of MPTP-treated mice (Table 2). In addition, rectal temperature showed no significant changes in riluzole (10 mg/kg)-treated mice, as compared to vehicle-treated

animals, although the temperature showed approximately 0.5°C decrease in mice 1 hr after riluzole injection.

DISCUSSION

In the present study, MPTP caused a significant reduction in dopamine and DOPAC levels from 3 days after MPTP treatments. In the present study, therefore, we evaluated the effects of riluzole on the striatal dopamine and DOPAC levels at 3 days after MPTP treatments.

The present study showed that riluzole antagonized the MPTP-induced decrease in dopamine and DOPAC levels in the striatum of mice in a dose-dependent manner. The present results demonstrate that riluzole can protect against MPTP-induced decrease in dopamine levels.

Riluzole is an inhibitor of glutamatergic transmission in the central nervous system. This drug is currently given to patients with amyotrophic lateral sclerosis (ALS) in an attempt to improve their prognosis, possibly via blockade of the glutamate neurotoxic effects[9]. Interestingly, a previous study suggested that riluzole can partially antagonize the increase in the release of dopamine induced by superfusion with MPP^+, the active metabolite of MPTP[10]. Furthermore, they reported that riluzole can protect against MPTP-induced striatal dopamine depletion in mice either by blocking the entry of Na^+ or by reducing the release of glutamate[7]. In contrast, Jones-Humble et al.[6] demonstrated that riluzole had no significant effect on dopamine depletion in the striatum of mice. Therefore, the neuroprotective effect of riluzole against MPTP-induced striatal dopamine depletion in mice is still unclear. However, a recent interesting study reported that riluzole delayed the appearance of parkinsonian motor abnormalities in a chronic monkey model of MPTP toxicity, designed to resemble more closely Parkinson's disease[11]. Furthermore, this drug was shown to alleviate the circling behavior in 6-hydroxydopamine-treated rats and to decrease the suppression of dopamine metabolism, at both striatal and nigral levels[12]. Both neuroprotective and palliative effects of riluzole have also been obtained in an acute model of MPTP intoxication in monkeys[13]. These observations are, at least in part, consistent with our present findings.

In the present study, of interest is that riluzole showed a significant effect on MPTP-induced striatal dopamine and DOPAC depletion in a dose-dependent manner. Interestingly, a previous study in mice indicated that voltage-dependent Na^+ channel blockers can prevent MPTP-induced dopamine depletion in the striatum[6]. The blockade of Na^+ entry is known to prevent the cascade of events that follows the neuronal depolarization after ATP (adenosine triphosphate) depletion. Furthermore, the neurotoxic effects of MPP^+ increase the release of neurotransmitters, by a mechanism which was proposed to be Na^+ dependent. Thus, inactivation of voltage-dependent Na^+ channels by riluzole might be involved in any protective effects on MPTP-induced striatal dopamine and DOPAC depletion. However, we cannot

rule out the possibility that riluzole exerts its protective effect through a modulation of glutamate release.

In conclusion, our results show that riluzole can protect against MPTP-induced striatal dopamine and DOPAC depletion in mice. The protective effect may be caused by inactivation of voltage-dependent Na^+ channels of riluzole. These findings demonstrate that riluzole with ability to block voltage-dependent Na^+ channels may be useful in the treatment of neurodegenerative diseases.

REFERENCES

1) Heikkila, R.E., Manzino, L., Cabbat, F.S. and Duvoisin, R.C., *Nature* **311** (1984) 467-469.
2) Turski, L., Bressler, K., Rettig, K.J., Lschmann, P.A. and Wachtel, H., *Nature* **349** (1991) 414-418.
3) Nicklas, W.J., Vyas, I. and Heikkila, R.E., *Life Sci.* **36** (1985) 2503-2508.
4) Gluck, M.R., Krueger, M.J., Ramsey, R.R., Sabin, S.O., Singer, T.P. and Nicklas, W.J., *J. Biol. Chem.* **269** (1994) 3167-3174.
5) Benavides, J., Camelin, J.C., Mitrani, N., Flamand, F., Uzan, A., Legrand, J.J., Gueremy, C. and Le Fur, G., *Neuropharmacology* **24** (1985) 1085-1092.
6) Jones-Humble, S.A., Morgan, P.F., and Cooper, B.R., *Life Sci.* **54** (1994) 245-252.
7) Boireau, A., Dubédat, P., Bordier, F., Peny, C., Miquet, J.M., Durand, G., Meunier, M. and Doble, A., *Neuroreport* **5** (1994) 2657-2660.
8) Tanji, H., Araki, T., Nagasawa, H. and Itoyama, Y., *Brain Res.* **824** (1999) 224-231.
9) Bensimon, G., Lacomblez, L., and Meininger, V., *New Engl. J. Med.* **330** (1994) 585-601.
10) Boireau, A., Miquet, J.M., Dubédat, P., Meunier, M. and Doble, A., *Neuroreport* **5** (1994) 2157-2160.
11) Bezard, E., Stutzmann, J.-M., Imbert, C., Boraud, T., Boireau, A. and Gross, C.E., *Eur. J. Pharmacol.* **356** (1998) 101-104.
12) Barnéoud, P., Mazadier, M., Miquet, J.M., Parmentier, S., Dubédat, P., Doble, A. and Borireau, A., *Neuroscience* **74** (1996) 971-983.
13) Benazzouz, A., Boraud, T., Dubédat, P., Boireau, A., Stutzmann, J. M. and Gross, C., *Eur. J. Pharmacol.* **284** (1995) 299-307.

Table 1. Effects of riluzole on the striatal dopamine and its metabolites content in MPTP-treated mice.

Treatments	Dopamine (μg/g tissue)	DOPAC (μg/g tissue)	HVA (μg/g tissue)
Vehicle (0.5% CMC)	13.44±0.75**	4.23±0.51**	2.83±0.24
riluzole (10 mg/kg)	12.09±0.73**	4.92±0.28**	2.73±0.07
MPTP+0.5% CMC	3.81±0.13	2.01±0.31	2.46±0.36
MPTP+riluzole (3 mg/kg)	4.71±1.26	3.49±0.38**	2.73±0.23
MPTP+riluzole (10 mg/kg)	6.27±0.64*	4.27±0.17**	2.48±0.16

Values are expressed as mean±SE. *$p<0.05$, **$p<0.01$ compared with MPTP+0.5% CMC group (Williams multiple range test). n=5 mice. Drug treatment schedules were expressed in experimental design section.

Table 2. Effects of riluzole (20 mg/kg) on the striatal dopamine and its metabolites content in MPTP-treated mice.

Treatments	Dopamine (μg/g tissue)	DOPAC (μg/g tissue)	HVA (μg/g tissue)
Vehicle (0.5% CMC)	13.44±0.75**	4.23±0.51**	2.83±0.24**
MPTP+0.5% CMC	2.70±0.37	0.93±0.06	1.38±0.16
MPTP+riluzole (20 mg/kg)	5.36±0.44**	1.39±0.08**	1.86±0.14**

Values are expressed as mean±SE. **p<0.01 compared with MPTP+0.5% CMC group (Williams multiple range test). Drug treatment schedules were expressed in experimental design section. n = 5-7.

III. 4. The examination of Image Reconstruction Parameter of the Three-dimensional PET Data Using OSEM

Watanuki S., Ozaki K., Miyake M., Itoh M. and Orihara H.

Cyclotron and Radioisotope Center, Tohoku University

Introduction

The maximum likelihood-expectation maximization (ML-EM), an iterative reconstruction algorithm, is known to produce higher quality images with lower noise level without streak-like artifacts when compared with the images reconstructed by conventional filtered back projection (FBP) method[1-3]. However, iterative methods including ML-EM require long convergence time[2], and this requirement prevents the iterative methods from the use of clinical practices. But recently, ordered subset EM (OS-EM) algorithm has been developed that accelerates convergence time[4], and suitable for clinical use routinely. In positron emission tomography (PET) studies, 3D data acquisition is often preferred because of higher counting sensitivity and consequently lower radiation dose than the conventional 2D mode. However, the reconstruction of 3D mode data using conventional 3D re-projection algorithm (3DRP)[5] needs a large amount of calculation, therefore the high performance computer is required to perform it. The Fourier rebinning algorithm (FORE) method[6] was proposed to decrease the amount of calculation as an alternative for the 3DRP.

A combination of FORE and OSEM had enabled the iterative reconstitution of the 3D data practical in the clinical studies. However, images reconstructed by FORE+OSEM are not completely equal with the 3DRP images in the resolution[7] and contrasts. Moreover, reconstructed images are affected by selection of parameters for the OSEM. Therefore, it is necessary to search the optimum reconstruction parameters in the OS-EM to be comparable or with higher quality images with by 3DRP.

The purpose of the present work was to investigate the effects of parameter selection on the quality of images and possibly to find appropriate reconstruction parameter sets in the FORE + OS-EM reconstruction.

Materials and Methods

The data in 3D mode were collected with SET-2400W (Shimadzu Corp. Kyoto, Japan) PET scanner[5]. Images were reconstructed with the FORE + OS-EM on the XP-1000 workstation (Compaq computer Corp. Woburn, USA), while 3DRP reconstruction was

performed with the aid of SX-4/128H4 super computer (NEC Corp. Tokyo, Japan) of Tohoku University Computer Center. The reconstruction filter Cut-off and order, which are the common parameters in both 3DRP and OS-EM reconstruction, were set at 8mm and 2 respectively. OS-EM has other two parameters those are termed as the number of iterations and subsets. The image resolution improves apparently as these values increase. In general, OS-EM produces a similar image, when the product of the iteration and subset numbers is constant6). In this study the iteration was fixed at 4, and the subset were varied within the range from 4 to 16 in the experimental studies.

A Derenzo phantom filled with ^{18}F solution was scanned to evaluate the image resolution. The peak value at rod in the image was obtained at 3.5 and 5 mm diameter in both 3DRP and OS-EM. The differences of count recovery were calculated by the following expression.

$$\text{Difference} = \frac{\text{OS - EM Value - 3DRP Value}}{\text{3DRP Value}} \times 100 \qquad (1)$$

A sphere phantom was scanned to evaluate the quantitative accuracy, which is a 20 cm inner diameter cylinder, 12cm long, containing six spheres with inner diameter of 38, 27, 20, 16, 13, 10mm. Outer cylinder filled with ^{18}F solution as background activity. The activity in spheres was varied from 0, 0.5, 2.5 to 5 as the ratio between the sphere and the background.

A 20 mm diameter circular region of interest(ROI) was draw on the background and spheres with diameter 38, 20 and 13mm. The discrepancies in the ROI mean pixel value between OS-EM and 3DRP was also evaluated by the equation (1).

A pool phantom, a 20 cm inner diameter cylinder and12cm long, filled with ^{18}F solution, was scanned to explore the image noise level. The total collected counts varied in the range of 1 M to 20 M(mega) counts, the coefficient of variations (CV) is compared between the OS-EM and the 3DRP images at each image plane.

Clinical FDG images were reconstructed by 3DRP and FORE + OS-EM for comparison.

Results and Discussion

The results of Derenzo phantom experiments are shown in the figure 1. The count recoveries were less for FORE + OS-EM than 3DRP and its difference extremely depended on the number of iterations and subsets. It was less than 10% when the subset was set at 16. Therefore, the product of the iteration and subset are recommended to be 64 or more to produce higher image resolution to bear comparison with the 3DRP.

Figure 2 shows the results of another count recovery experiments using sphere phantoms of different diameter. The count differences tended to increase the decreases of subset numbers, but it was less than 10% in all ROI positions, when the subset was set at 16.

This result supports that the product of iteration and subset needs to be 64 or more to produce the quantitative images comparable to the 3DRP.

Figure 3(a) and (b) show the CV differences between 3DRP and OS-EM. The CV value of FORE + OS-EM with the 16 subsets was lower than the 3DRP at the total counts less than 2M counts. This result supports the report by Rosenqvist et al.2) that OS-EM prevails more effective upon 3DRP at the low statistical data. When the total counts exceed up to 4M counts, the CV value of FORE + OS-EM image indicates the almost same value as 3DRP except planes at the near edge of axial field-of-view (FOV) (Figure 3(a)). This increased CV value at the edge of FOV was caused by FORE5) and not by OS-EM. The lower statistics in FORE + OS-EM is problematic for the whole body scans by reducing effective axial field of view. On the other hand, when the subset was set at 4, the CV values became lower than 3DRP at all the planes of all experiments (Figure 3(b)). It was supposed that the overlapping plane should be increased compared with the 3DRP or the number of subset or iteration should be decreased though trade off the resolution at the whole body studies with FORE + OSEM.

Figure 4 shows the ^{18}F-FDG brain images reconstructed by FORE + OSEM and 3DRP. When the subsets were set at the 4 and 8, the image value was higher than the 3DRP in the low activity area, while it was lower at high activity area. But this trend did not be observed when subset was set at 16. These results well agree with the data by the phantom experiments (figure 1 and 2). ^{18}F-FDG whole body images in the figure 5 showed the image qualities by OS-EM algorithm. The streak artifacts from the high activity area were not seen in the OS-EM images. But the apparent noise of inside the body was higher than 3DRP at the edges of the axial field of view in the OS-EM, however, it was less remarkable at the subset 4 and agrees with the phantom experiments.

Table 1 emphasizes the calculation time of 3DRP and FORE + OS-EM for the head and body mode data respectively. The calculation time was 3.1 and 3.4 minutes per one frame in the head and body mode respectably in the FORE + OS-EM method, and those were 1.5 times longer by the 3DRP using a supercomputer. This calculation time of FORE + OSEM is well tolerable to routine use.

Conclusion

The parameter product of iteration and subset was recommended to be 64 or higher in order to have the image resolution similar to the 3DRP. In this case, the difference in the pixel values with FORE+ OS-EM was around 10% or less for small objects. However, this condition requires longer overlapping planes compared to 3DRP. Smaller number of product such as 16 may be useful for whole body studies like tumor localization.

References

1) Sheep LA, Vardi Y, IEEE Trans. Med. Imag. **1** (1982) 113-122.
2) Rosenqvist G, Dahlbom M, et al., IEEE Trans. Nucl. Sci.**36** (1989) 1113-1116.
3) Holte S, Schmidlin P, et al., IEEE Trans. Nucl. Sci. **37** (1990) 629-635.
4) Hudson HM, Larkin RS, IEEE Trans. Med **13** (1994) 601-609.
5) Rogers JG, Harrop R, et al., IEEE Trans Med. Imag. **6** (1987) 239-243.
6) Defrise M, Kinahan PK, et al., IEEE Trans Med. Imag. **16** (1997) 145-158.
7) Krzywinski M, Sossi V, et al., IEEE Trans. Nucl. Sci. **46** (1999) 1114- 1120.

Table 1. Calculation time of FORE + OS-EM and 3DRP in the head and body mode data are shown. Reconstruction with FORE + OS-EM and 3DRP were performed on the XP-1000 workstation and SX-4/128H4 super computer respectively.

	Head mode			Body mode		
	FORE + OSEM		3DRP	FORE + OSEM		3DRP
Iteration	4	4	-	4	4	-
Subset	4	16	-	4	16	-
Reconstruction time (min)	3.0	3.1	2.0	3.3	3.4	2.3

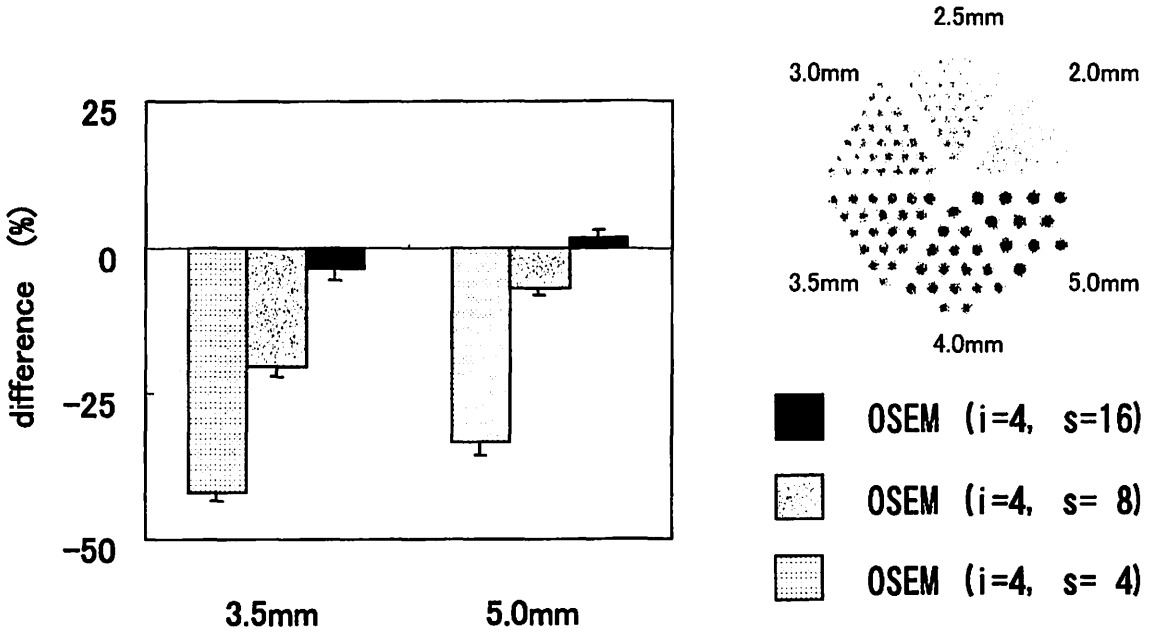

Fig. 1. Derenzo phantom image is shown at the upper right. Bar graph shows the difference between FORE + OS-EM and 3DRP in peak value at the rod of 3.5 and 5.0mm diameter. OS-EM reconstruction was performed with three different the number of subsets: 4, 8 and 16 accordingly, while the number of iteration was fixed at 4. Left and right bar groups are different at the 3.5 and 5.0mm diameter rods respectively.

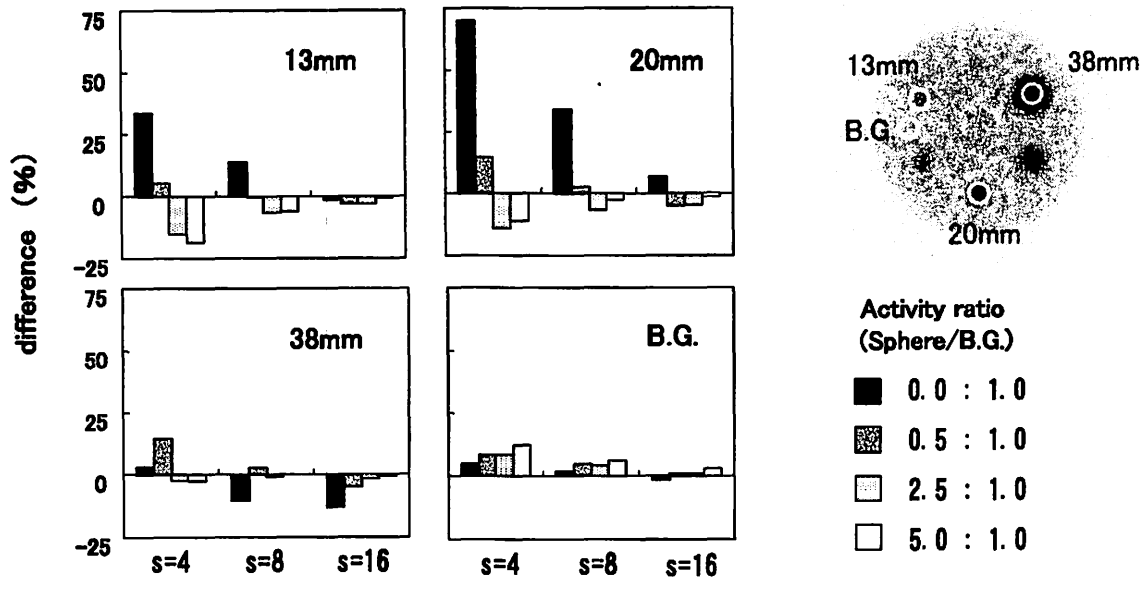

Fig. 2. Sphere phantom image is shown at the upper right. Bar graph shows the difference between FORE + OS-EM and 3DRP in the value at four different positions indicated in the phantom images. The difference was obtained at the four different activity ratios of sphere and B.G.

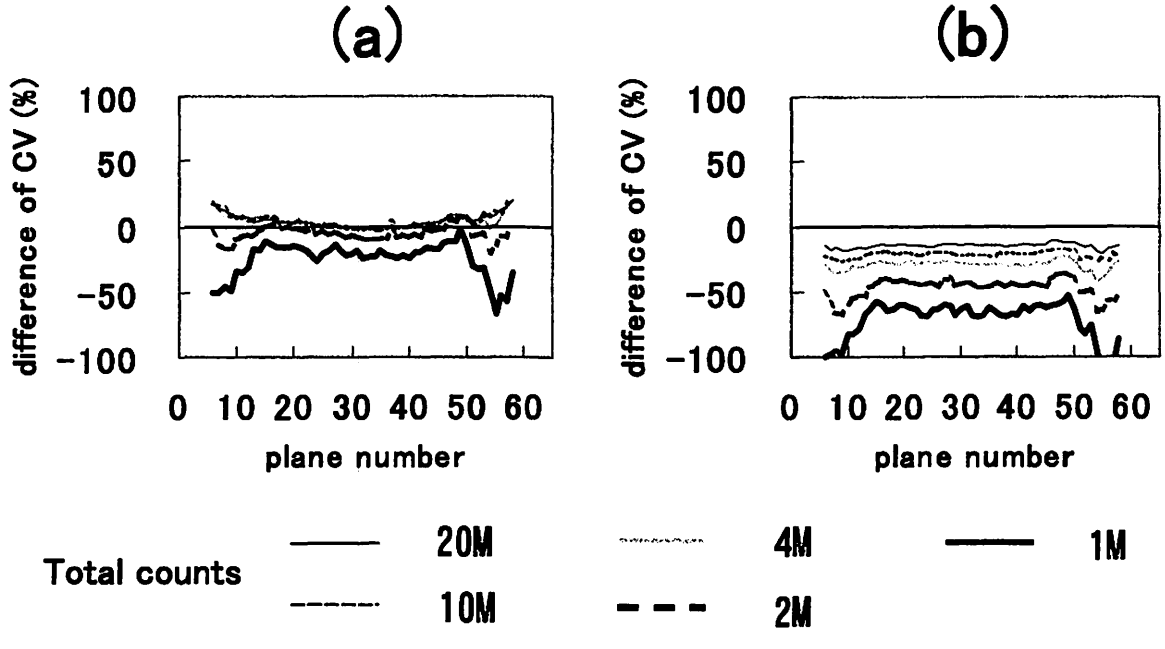

Fig. 3. Graphs shows the differences of CV between FORE + OS-EM and 3DRP in the pool phantom images with two different number of subsets (number of iteration was fixed at 4) illustrating figure (a) and figure (b) as 16 and 4 subsets respectively. Pool phantom was scanned at the different total counts as 1, 2, 4,10 and 20M counts consequently.

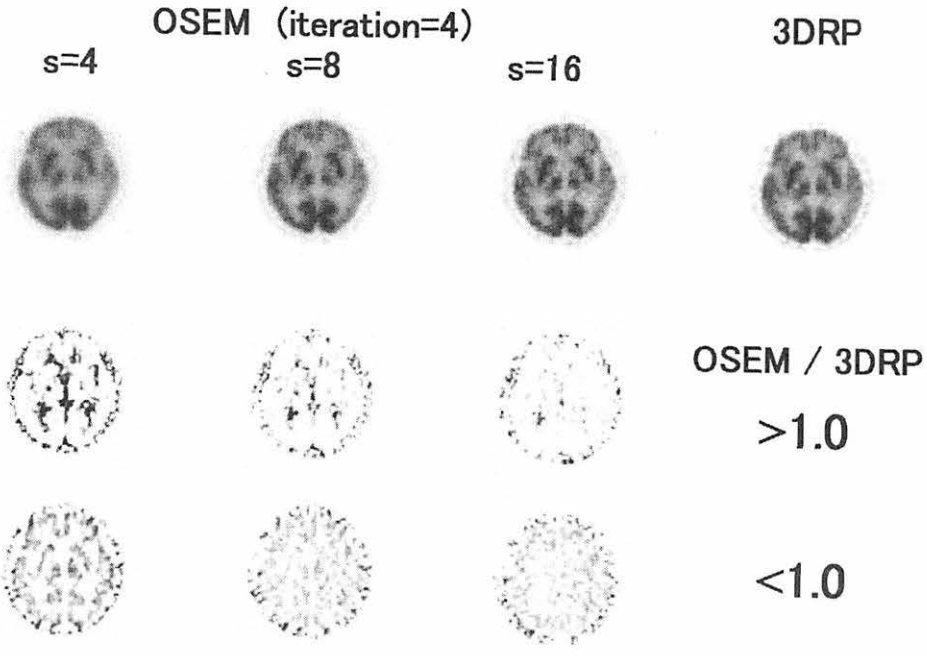

Fig. 4. FDG brain images are shown in the top row, three images from the left, are reconstructed by using OS-EM with three different number of subsets such as 4, 8 and 16 respectively from left, and the fourth image is reconstructed by using 3DRP. Images in the middle bottom rows are the ratio of OS-EM and 3DRP. Upper images show the ratio that measures >1.0 and lower images show the ratio that measures <1.0 respectively.

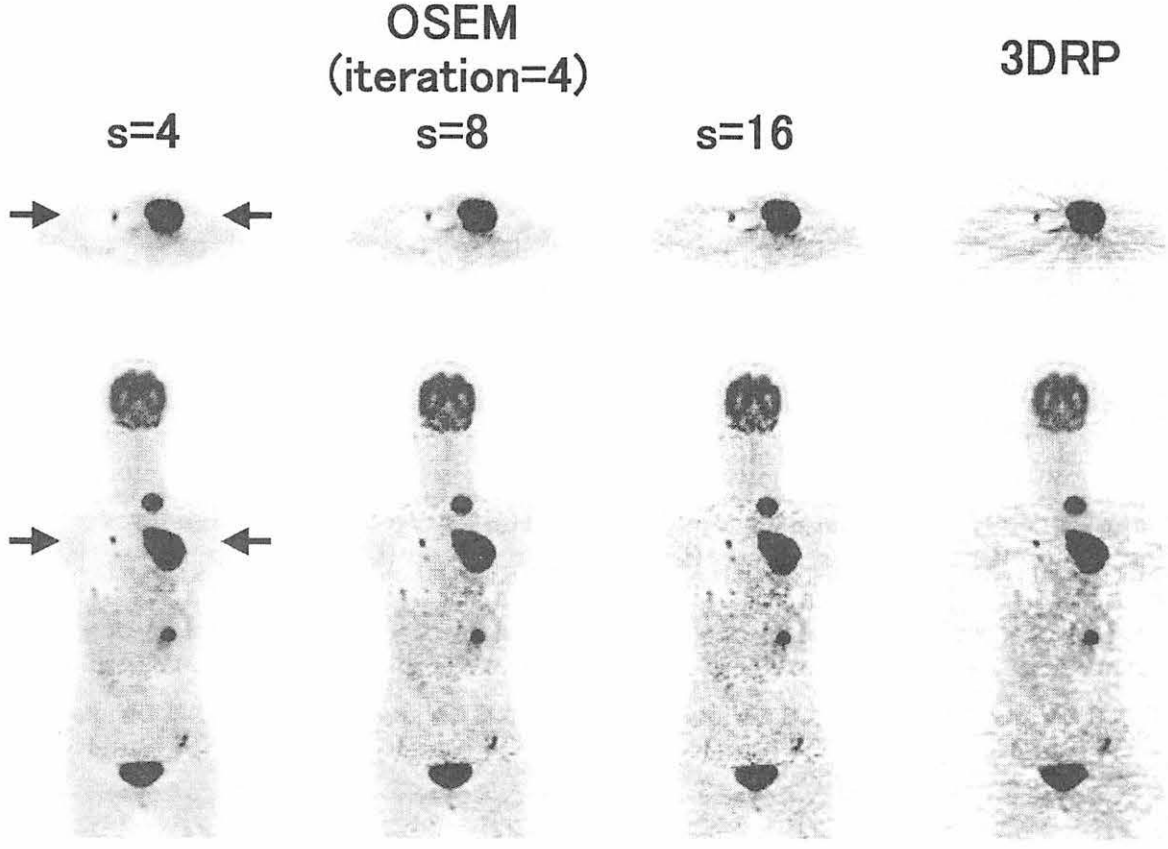

Fig. 5. FDG whole body images are shown as the three images from left reconstructed by using OS-EM with the three different number of subsets set at 4, 8 and 16 respectively from left, and the fourth image is reconstructed by using 3DRP. Arrows indicate the place of transaxial and coronal sections.

III. 5. Effect of Capsaicin and Atropine on Uptake of F-18 Fluorodeoxyglucose in Rat Salivary Glands

Fujiwara K., Yamaguchi K., Rikimaru H.*, Taniguchi M., Iikubo M., Sakamoto M., Sasano T., and Ito M*.*

Division of Oral Diagnosis & Radiology, Tohoku University Graduate School of Dentistry
*Division of Nuclear Medicine, Cyclotron and Radioisotope Center, Tohoku University**

Introduction

Positron emission tomography (PET) with F-18 fluorodeoxyglucose (FDG) has been used for diagnosis of malignant tumors because of its nature of glucose metabolism. However, FDG uptakes increase the activities not only in the malignant tumors but also in the some normal tissues and/or organs. As reported previously[1,2], PET scan with FDG revealed that increased activity in normal salivary glands and the degree of the accumulation was various in each in individual or condition. Especially, FDG uptake in salivary glands can occasionally been seen in even resting condition. However, the cause of the variations of FDG uptakes in salivary glands is yet unknown. Anrep *et al.*[3] reported that salivary glands could serve efficiently glucose as an energy source for salivation. Consequently, a question has been raised as to whether FDG uptake in normal salivary glands is related to salivation. To answer this question, we examined the effects of 2 chemical matters (*i.e.*, capsaicin (CAP) as activator of salivation and atropine (ATR) as an inhibitor of that) on the FDG activity in salivary glands.

Materials and methods

Thirty-three male adult Wister rats, 300-330g in weight, were used for study. The rats were randomly divided into three groups. The first group (REST group) was used under resting conditions, the second group (CAP group) was applied 300 μM CAP on the oral cavity for 30s, and the third group (ATR group) was administrated 0.1mg/kg atropine intramuscularly in the calf muscle 30 minutes before FDG injection. Prior to this study, the Laboratory Animal Care and Use Committee of Tohoku University approved our protocol.

Salivation studies

Under anesthesia with diethyl ether, one preweighed cotton swab (0.5×0.5×0.5 cm: 0.0005g) was placed in the oral cavity of every rat, and then the all swabs were removed after 30s and the weight was measured. The procedure was immediately repeated and the values

of the salivary collections for 30s were taken as a measure of salivary secretion rate (SSR). The rates were assessed 30s before stimulation, at the stimulation period and every 30s thereafter over 180s. The measured values were expressed as means±one standard deviations. Statistical analysis was performed using repeated measures analysis of variance (ANOVA) for comparison of individual means. Significance was accepted as $p<0.05$.

Distribution studies

One hundred μCi (3.7MBq) FDG was administered intravenously under anesthesia with diethyl ether. After injection of FDG, anesthesia was discontinued and animals were allowed free until decapitation. The rats were sacrificed at 30 min after FDG injections. Some fresh tissues (*i.e.*, brain, heart, liver, parotid gland, submandibular gland, sublingual gland, lacrimal gland, muscle tissue and fat tissue) were excised and were weighed, and the tracer activities in the tissues were measured using a gamma counter (Wallac 1480 Gamma counter, Turku, Finland). After correcting for the physical decay of ^{18}F (110-minutes half-life) and for the gamma counter efficiency, tissue radioactivity was expressed as the differential uptake ratio [DUR: = (tissue counts / tissue weight) / (injection dose counts / body weight)[4)]]. DURs were expressed as means±SD. Statistical analysis was performed using one-way analysis of variance followed, where appropriate, by Scheffe's F test for comparison of individual means. Significance was accepted as $p<0.05$.

Results

Salivation studies

Time-course of SSRs is shown in Figure 1. As can be seen in the REST group, SSR kept constant low rates at any time points. In the CAP group, SSR increased promptly and reached peak level immediately after CAP application. However, SSR rapidly peaked off and decreased to the resting level within only 1 min. In the ATR group, SSR showed no distinguish change, similar to time-course of resting levels at any time points.

Distribution studies

DURs in all of the tissues are shown in Figure 2. In the REST group, DURs in salivary glands showed the following hierarchy: parotid gland < submandibular gland < sublingual gland. Especially, FDG uptake in sublingual gland was as high as that in the brain. DURs in the CAP and ATR groups in salivary glands were found to be the similar hierarchy on the REST group. FDG uptake of the submandibular gland and sublingual gland in the CAP group were significantly higher than that in the REST group ($p<0.05$). Besides, the FDG uptakes of liver and heart in the CAP group were also significantly higher than that in the rest group ($p<0.05$), while there was no significant difference in brain, muscle and fat tissues. FDG uptake in the ATR group was indistinguishable from that in the REST group except submandibular gland and heart.

Discussion

REST conditions

In this study, the salivary glands, especially the sublingual gland, demonstrated high FDG uptake. The result in the REST group was similar to Jabour's report[1] in that the sublingual gland had increased FDG uptake on PET imaging although the reason it is unclear why FDG uptake increased activities in that organ. As reported previously[5], some organs which have distributions of the mucous glands, *e.g.*, stomach, small intestine and colon, including sublingual gland, often show high FDG uptake on FDG-PET images. Taking account these reports, it is possible to postulate that FDG accumulated in the mucinous cell.

CAP applications

Capsaicin, the pungent chemical matter from red chili pepper, is well-known to induce salivation in humans when applied to the oral cavity. We applied CAP as activator of salivation in this study. In the CAP group, SSRs and DURs in salivary glands showed increase, especially in FDG uptakes in the submandibular and sublingual gland, compared with those in the REST group. Engstrom *et al.*[6] reported that in the secretion rate from submandibular-sublingual was faster than that from parotid gland. The normal FDG uptake in the salivary glands may be related to salivation.

In humans, local applications of CAP produce a sensation referred to as "burning-pain" due to the activation of primary afferent *C*- and probably *A*δ-neurons[7]. A burning-pain generally elicits the systemic effects, such as sympathetic activations and cardiac changes[8]. Consequently, we investigated some organs except the salivary glands. The FDG uptakes of liver and heart in the CAP group were significantly increased compared with that in the REST group. FDG uptake in the liver, where phagocytosis occurs, might increase in response to defense against toxicity (a burning pain)[9]. FDG uptake in the heart might increase in response to catecholamines release.

ATR administrations

Atropine, the muscarinic cholinoceptor receptor blocker[10], is known to produce a prolonged inhibitory effect on salivation when administered intramuscularly in humans. However, in our ATR group, salivation was indistinguishable from that in the REST group, while FDG uptake in the submandibular gland was significantly increased compared with the REST group. At the present time, we cannot explain the accurate mechanism. It is generally known that salivations are under the regulation of both sympathetic and parasympathetic nerve systems. Moreover, it is reported that the only activation of sympathetic nerve elicits salivation[11]. The functions of heart are also under autonomic nerve systems and FDG uptake was increased. It may be difficult to decrease FDG uptake in the organs that were dominated by autonomic nerve systems, even if suppress only one.

In conclusion, FDG uptake increased the activities in salivary glands, and the uptake in the normal salivary glands might be related to salivation. However, as above-mentioned, there may be some other factors that increase FDG uptake in the normal salivary glands except for salivations. Further investigations are required to determine the mechanisms that influence the pattern of FDG uptake in the normal salivary glands.

References

1) Jabour B. A., Choi Y. et al., *Radiology* **186** (1993) 27-35.
2) Rege S. D., Chaiken L. et al., *Radiology* **189** (1993) 807-812.
3) Anrep G. V. and Cannan R. K., *J Physiol* **56** (1922) 248-258.
4) Kubota K., Kubota R. et al., *J Nucl Med* **37** (1996) 1713-1717.
5) Kato T., Tsukamoto E et al., *Jpn. J. Nucl. Med.* **36** (1999) 971-977.
6) Engstrom M. D., Fredholm B. B. et al., *J. Physiol.* **373** (1986) 87-96.
7) Dickenson A. H., and Dray A., *Br. J. Pharmacol.* **104** (1991) 1045-1049.
8) Sugawara Y., Gutowski T. D. et al., *Eur. J. Nucl. Med.* **26** (1999) 333-341.
9) Coghill. R. C., Sang. C. N. et al., *J. Cereb. Blood Flow Metab.* **18** (1998) 141-147.
10) Jadvar H., Schambye R. B. et al., *Clin. Nucl. Med.* **24** (1999) 965-967
11) Izumi. H. and Karita. K., *Amer. J. Physiol.* **266** (1994) 1517-1522.

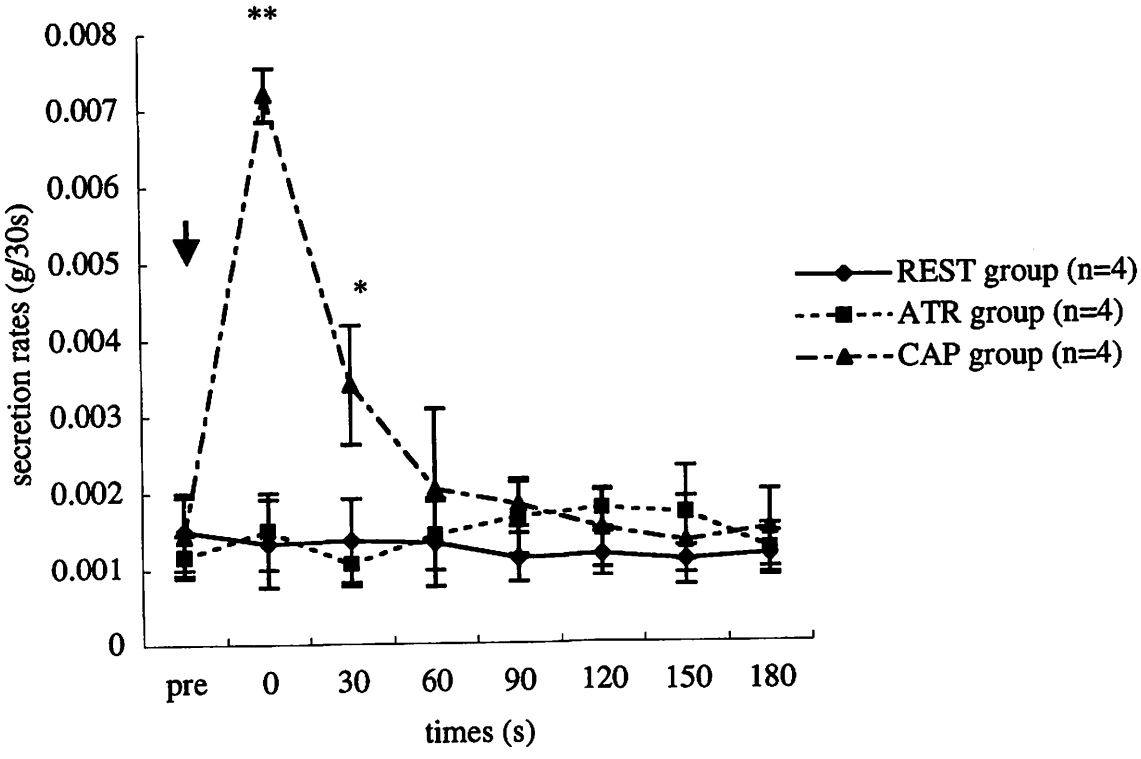

Fig. 1. Time-course curves for salivary secretion rate in the REST (◆), CAP (▲) and ATR(■) groups. Values are means±SD. * P<0.05 ** P<0.01, ↓; CAP was applied on the oral cavity in the CAP group.

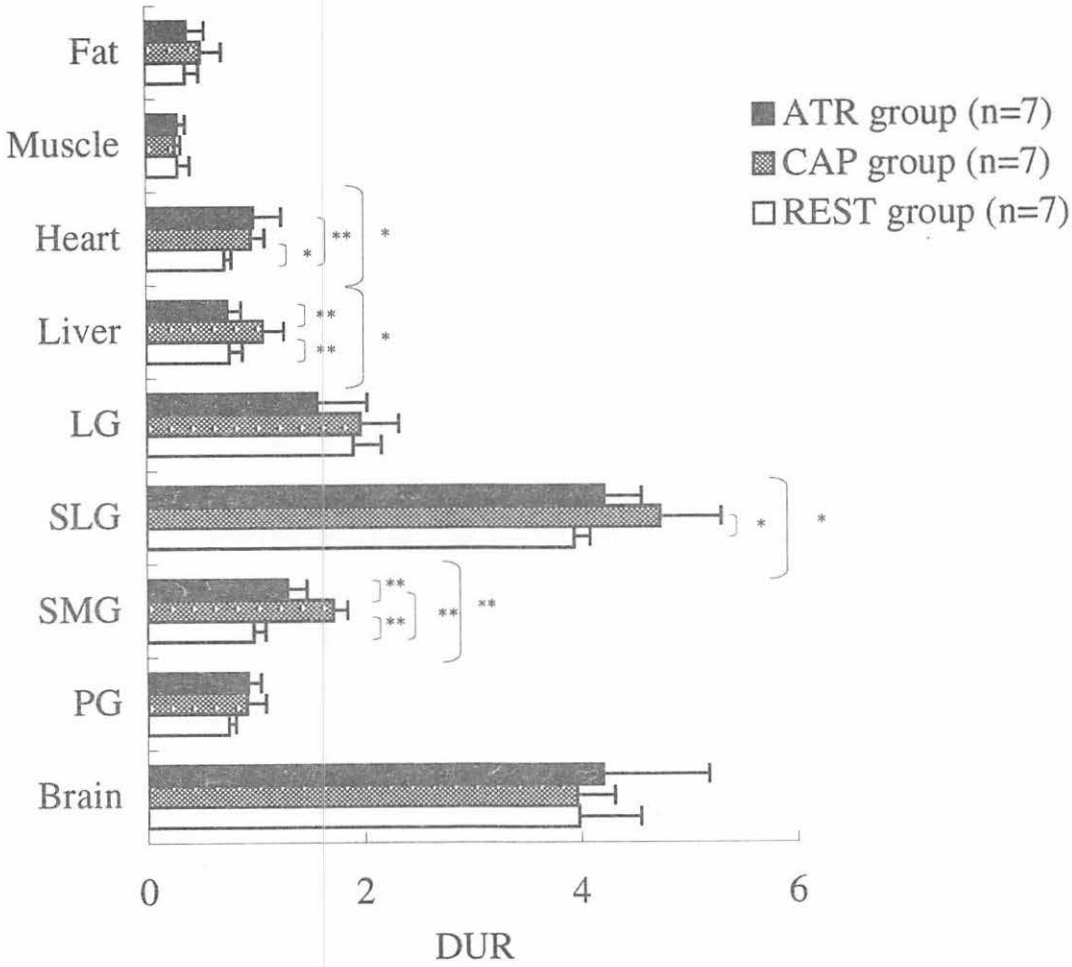

Fig. 2. Tissue distribution of FDG in the REST (white bars), CAP (gray bars) and ATR (black bars) groups. Values are means±SD. * P<0.05 ** P<0.01, PG; parotid gland, SMG; submandibular gland, SLG; sublingual gland, LG; lacrimal gland.

IV. MEDICINE AND BIOLOGY (Clinical)

IV. 1. Current states of Clinical Use of Positron Emission Tomography: Examples of Western Countries

Tashiro M.,**,****, Kubota K.***, Itoh M.***
Yanai K., and Sasaki H.*****

*Division of Clinical Pharmacology, Tohoku University Graduate School of Medicine**
*Division of Nuclear Medicine, Cyclotron and Radioisotope Center, Tohoku University***
*Division of Radiology and Nuclear Medicine, Institute of Development, Aging and Cancer****
*Department of Geriatric and Respiratory Medicine, Tohoku University Graduate School of Medicine*****

Introduction

Positron Emission Tomography (PET) was invented initially as a tool for basic research and did not attract much attention as a clinical diagnostic tool in the United States in the beginning. Similarly in Japan, PET was initially introduced as a research tool in the field of neuroscience. Recently, the term "clinical PET" has become a common key word for hot discussions in the field of nuclear medicine. It seems that the term "clinical" has double meanings. In a broader sense, it simply means all types of studies using human subjects while the term "basic" implies animal studies. In a narrower sense, "clinical" means medical investigations to make clinical decisions for diagnosis and treatment. The international standard is shifting to take the latter definition for "clinical PET" studies. Doctors in many Western countries such as the United States, the United Kingdom, Germany and so on use this term for the investigations already validated and reimbursed by health insurance organizations.

Nowadays, the most important field in clinical PET diagnosis would be oncology. It is interesting to note that the main part of pioneering works in this field was done at Tohoku University. The Cyclotron and Radioisotope Center (CYRIC) at Tohoku University was founded in 1978 as the first PET institute under the Ministry of Education in Japan. Various novel findings in the field of PET oncology have been reported from here. A PET research group at Tohoku University[1-3] proposed potential use of PET for detection of malignant neoplasm. This was one of the precursors of clinical PET in the world. Use of glucose analogues other than deoxyglucose (FDG)[4-8], such as deoxymannose[8] and deoxygalactose[9] were proposed, too. Other tracers have been also introduced for diagnosis of brain tumors[10], epilepsy[11-13] and heart disease[14], too. Nowadays, requirements for clinical PET are expanding in many parts of the world. The main purpose of this report is to overview the current situation of PET use in leading countries such as United Kingdome, Belgium, and

United States and Germany.

United Kingdom

In the United Kingdom, St. Thomas & Guy's hospital already started clinical PET investigations as a selected center for clinical PET in 1991. At that time, it was the sole clinical PET center in UK, and other PET institutes were being run mainly for scientific research. At the same time, the British government started financial support for the clinical PET investigations performed at St. Thomas & Guy's hospital through National Health Service (NHS). Nowadays, the number of clinical PET institutes is gradually increasing in this country. The total number of the PET institutes doing human studies is said to be 12 (2001 present)[15,16]. Some of PET centers are not equipped with their own cyclotrons and are getting FDG delivered from nearby cyclotrons. This style of running a PET institute is often called a "satellite PET". Many clinical indications for PET studies have been carefully evaluated and determined by a PET group at St. Thomas & Guy's hospital[17]. They have published and constantly updating an excellent list of clinical indications, which is available from their Internet site[17].

Belgium

Belgium is also one of the most important countries in the point that they started clinical PET investigations in early days. It is said that they started discussions over clinical PET investigations as early as in the late 1980s. FDG-PET, having been started for diagnosis of epilepsy, ischemic heart disease and recurrent brain tumors, were reimbursed in the late 1980s. Since July 1999, more indications have been added to the list of clinical PET indications reimbursed. It was partly because of drastic changes that took place in the US health administration policy concerning clinical PET. In this country, various malignant diseases, heart diseases and epilepsy are reimbursed in a similar fashion to the UK. The total number of PET scanners in this country is estimated to be 10 or so, but the number of PET per population is calculated to be the highest in the world, rivaling to Germany[15,16].

United States

The Medicare coverage of clinical PET investigations is being constantly widened. In 1995, PET investigations with ^{82}Rb for cardiac perfusion test were passed for Medicare support. After that, there had been almost no changes for a few years until the diagnosis of lung cancer was approved in 1998. In 1999, FDG-PET investigations for recurrent colon cancer, malignant lymphoma (staging), and malignant melanoma were approved. It is said that this decision influenced the political decision of Belgian government, which started reimbursement for oncology indications. Commercial-based FDG supply networks such as PET-Net has been significantly expanded until now. Establishment of the PET-Net has enabled medium to small sized hospitals to start PET service for clinical diagnosis, getting

FDG supply from nearby cyclotrons[15,18].

Germany

As for the organizational efforts to bring clinical PET into reality, situation in Germany is worth mentioning here. They have put forward "the satellite concept". In this country, the number of PET institutes without cyclotrons (PET satellites) is larger than the number of Cyclotron Centers that own both cyclotron and PET scanners. PET facilities can save much amount of money for installation and maintenance of cyclotrons if they are able to purchase radioactive pharmaceuticals from other facilities.

As to clinical PET indications, health insurance system should be one of the most important issues. There are private and public health insurance systems in Germany. And when one makes a contract with a private health insurance company, he does not have to keep the contract with public insurance organization. Private health insurance companies would pay basically for all clinical PET indications recommended by German Society of Nuclear Medicine. But, public health insurance organizations do not always reimburse for PET investigations even when the purpose of the study done is listed in the German Society's indication list.

Additionally in Germany, interdisciplinary groups of nuclear oncologists, neurologists and cardiologists have already held "clinical consensus conferences" several times and have completed lists of clinical indications for PET. Summary of the list of indications for oncology PET, approved by German Society of Nuclear Medicine, is as follows: differentiated thyroid cancer, brain tumors, gastrointestinal tumor, head and neck tumor, malignant melanoma, lung cancer (NSLC), and pancreatic carcinoma as class1 indications. Additionally, class2 indication is given to bladder carcinoma, malignant lymphoma, breast cancer, germinal cell carcinoma, ovarian tumor, neuroendocrine tumor, renal cell carcinoma, prostatic carcinoma, and seminoma. An indication list for brain PET is prepared for cerebrovascular disease, brain tumor, basal ganglion disorder, dementia, depression, schizophrenia, and epilepsy. Class 1a indication is given for brain tumor, basal ganglion disease, dementia, and epilepsy only. Class 2 indication is given to cerebrovascular disease, depression, and schizophrenia. For cardiology PET, evaluation of myocardium viability, evaluation of cardiomyopathy etc. are included.

Current Situation in Japan

In Japan, full reimbursement by health insurance is approved only for ^{15}O gas inhalation studies mainly for patients with cerebrovascular disease. Full reimbursement for FDG PET has not been approved yet. FDG PET applications can be applied as a special procedure of advanced medicine at selected institutions, where a part of medical costs can be charged to patients. A Clinical PET Working Group of Japan, evaluating previous FDG studies to clarify clinical efficacy of PET, has submitted the list of clinical indications for FDG

PET. It is expected that the Ministry of Health and Labor, in near future, make a decision toward approval of FDG PET as a fully reimbursed diagnostic procedures.

FDG supply from nearby cyclotrons to PET satellites has not been started yet, either. Since there are a large number of cyclotrons in Japan, satellite concept seems to be very useful to maximize cyclotron's potential because one cyclotron have a capacity of supplying FDG to 10 or more PET scanners. The current situation that every PET unit has its own cyclotron is not cost-effective. Among countries already doing PET studies, countries without satellite PET centers may be only Japan in the world. It is heard that a radiopharmaceutical company has already established a laboratory that fulfill strict safety-regulations and is ready for the delivery of FDG to nearby satellites at this moment. We hope that the PET environments change at last in Japan, too.

Acknowledgments

The authors thank Prof. E. Moser, Dr E. Nitzsche, Dr. M. Reinhardt, and all the staffs at the Division of Nuclear Medicine, Albert-Ludwigs University in Freiburg, Germany, for their support and cooperation. This survey was conducted by the financial support by German Japanese Radiological Affiliation, Sumitomo-Seimei Social Welfare Foundation, and Nuklearmedizin Stiftung (Nuclear Medicine Foundation in Germany).

References

1) Kubota K.et al., Lancet **19** (1983) 1192.
2) Kubota K. et al., J. Nucl. Med. **26** (1985) 37.
3) Kameyama M. et al., Acta Neurochir. **104** (1990) 8.
4) Takahashi H. et al.,. Sci. Rep. Res. Inst. Tohoku Univ. Med. **33** (1986) 38.
5) Kubota K. et al.,. J. Comput. Assist. Tomogr. **13** (1989) 1097.
6) Kubota K. et al., J. Nucl. Med. **31** (1990) 1927.
7) Kubota K. et al., J. Comput. Assist. Tomogr. **12** (1988) 794.
8) Fukuda H. et al., Eur. J. Nucl. Med. **7** (1982) 294.
9) Fukuda H. et al., Eur. J. Nucl. Med.**11** (1986) 444.
10) Tsurumi Y. et al., J. Neurosurg. **72** (1990) 110.,
11) Iinuma K. et al., Lancet **341** (1993) 238.
12) Iinuma K. et al., Pediatr. Neurol. **3** (1987) 12.
13) Yanai K. et al., Eur. J. Nucl. Med. **13** (1987).
14) Kagaya Y. et al., Am. J. Cardiol. **69** (1992) 242.
15) Tashiro M. et al., Lancet. **357** (2001) 886.
16) Tashiro M. et al., Kaku Igaku 38:255-267. In Japanese.
17) The Clinical PET Centre, Guy's and St Thomas' Hospital Homepage. http://www-pet.umds.ac.uk/pet-home.html.
18) Keppler J. S., Supplement to Diagnostic Imaging EUROPE. 2000 June:2-3.
19) Tashiro M. et al., Kaku Igaku. **36** (1999) 761. In Japanese.

IV. 2. Brain Function Evaluated by ^{18}F-FDG PET in Spinocerebellar Ataxia Type7

Tsuda T., Tanji H., Onodera Y., Koyama T., Ono S.*, Fukuda H.*, Itoh M.**, and Itoyama Y.*

Department of Neurology Tohoku University School of medicine
Department of Nuclear Medicine and Radiology, Division of Brain Sciences
*Institute of Development, Aging and Cancer, Tohoku, University**
*Cyclotron and Radioisotope Center, Tohoku University***

Introduction

Hereditary spinocerebellar ataxia (SCA) is a clinically and genetically heterogeneous group of neurological disorders characterized by dysfunction of the cerebellum and its afferent and efferent connections. Aberrant expansions of coding sequence in trinucleotide repeat assays of genes on 6p22-23, 12q24.1, 14q32.1, 19p13 and 3p12-13 have been identified in type1, type2, type3 / Machado-Joseph disease (MJD), type6 and type7 respectively[1-5].

SCA7 is the first clinical entity in which the neurodegenerative process affects the macula and/or retina in addition to other brain structures. In a previous classification of inherited ataxia, this SCA is categorized as an autosomal dominant cerebellar ataxia (ADCA) typeII and as an olivopontocerebellar atrophy (OPCA) typeIII in which the clinical manifestation is cerebellar ataxia with progressive pigmentary macular dystrophy and/or retinal degeneration[6-9]. Recently, the mutated gene of this SCA has been identified. Subsequent pathological studies have revealed that SCA7 is epitomized by the selective degeneration of Purkinje cells and the dentate nucleus in the cerebellum with the inferior olivary complex and the pontin nuclei. Immunohistochemical studies have shown that neuronal intranuclear inclusions are most frequent in atrophic brain regions. These inclusions were also observed in the cerebral cortex considered to be unaffected, suggesting that the observed distribution of neuronal intranuclear inclusions is unlikely to be found in the other ataxias[10].

Although the clinical, pathological and molecular features of SCA7 have been reported in several ethnic groups, these aspects of the Japanese patients have not been reported except our ophthalmologic report[11-16]. Furthermore, the mechanisms underlying the neurological manifestations associated with this type of SCA are still unclear[17]. Therefore, we described the clinical aspects of the two Japanese probands, then the brain function of the two probands was investigated by evaluating the cerebral metabolic rate for

glucose (CMRGlc).

Subjects and methods

Patients:

Probands of 117 Japanese families with autosomal dominant spinocerebellar ataxia (SCA) were recruited from clinics at Tohoku University. Among these probands, two patients (the proband 1 and 2) were diagnosed both clinically and genetically as SCA type7. The purpose and necessity for the genetic and the other studies were carefully explained, and informed consents were obtained from the patients and/or their families.

Genetic studies:

Gnomic DNA was isolated from fresh peripheral leukocytes of each subject. PCR products representing trinucleotide repeat coding regions were amplified from gnomic DNA with the primer pair 4U1024: 5'-TGTTACATTGTAGGAGCGGAA-3'/ 4U716: 5'-CACGACTGTCCCAGCATCT-3'. For PCR amplification and definition of the mutated gene bearing the aberrantly expanded CAG repeats, the same method was used as previously reported[16,18].

MRI study:

Magnetom 1.5 teslar MRI (Magnetom Vision SIEMENS) scanning was performed to estimate morphological impairments of the brain for T1 and T2 weighted images of the axial, coronal and sagittal sections.

PET scanning:

PET study was performed with a model SET-2400W scanner (Shimazu, Japan) at the Cyclotron and Radioisotope Center, Tohoku University. The two age matched control groups consisted of healthy normal volunteers ranging in age from 18-27 years (n=11, mean±SD, 20.9±2.9) and 49-74 years (n=6, mean±SD, 63.5±9.0). They had no history of recent medical illness, neurological diseases, developmental disorders or substance abuse. MRIs of the brain were also normal.

CMRGlc was measured in the proband 1 and 2, then in 17 control members. Between 6 and 7mCi of [^{18}F] 2-fluoro-2-deoxy-D-glucose (^{18}F-FDG) was injected to each member as an intravenous bolus. Positron emission scans were performed at 45min after the injection. For the other conditions of this study and data analysis, the same method was used as previously reported[19].

Results

The proband 1 and 2 clinical manifestations:

The proband 1 (age 26, male) with 47/10 heterozygous CAG repeats had an onset of gate disturbance at 20 years of age. The development of the symptoms was very mild, then slurred speech and slightly decreased visual acuity occurred subsequently at age 24. Neurological findings at age 26 included slurred speech, mildly decreased visual acuity, viscous eye movement, upward gaze palsy, mild ataxia and generalized hyperreflexia. Neuropsychologically, he had mild naming difficulty and a moderately delayed verbal memory disturbance. Laboratory analysis of the blood and cerebrospinal fluid indicated that the data were within normal limits.

The proband 2 (age 48, female) with 48/10 heterozygous CAG repeats noticed decreased visual acuity at 28 years of age. Since 40 years, she has subsequently been affected by slurred speech and ataxic gate. These symptoms developed relatively more aggressively than in the proband 1. Neurological findings at 46 years of age included subcortical dementia, slurred speech, remarkably decreased visual acuity, prominently viscous eye movement, upward gaze palsy, severe truncal and limb ataxia and generalized hyperreflexia. Laboratory analysis of the blood and cerebrospinal fluid indicated that the data were within normal ranges.

MRI studies and PET scanning:

Axial, coronal and sagittal images obtained by ^{18}F-FDG PET from the proband 1 and 2 are shown in Fig.1 (A,B,C) with MRI at the levels of the corresponding brain slice. In the proband 1, a prominent attenuation in ^{18}F-FDG uptake of the inferior bi-temporal cortex and the cerebello-brainstem was observed. In contrast, MRI studies showed no atrophic changes in the temporal lobi but mild atrophy of the cerebello-brainstem was observed (Fig.1B, C). In the brain of the proband 2, scattered reduction of ^{18}F-FDG uptake was observed in the fronto-parieto-temporal cortex and the cerebello-brainstem as well. In contrast to this, MRI studies showed only mild atrophy of the bi-temporal lobi in cerebrum, while remarkable atrophic changes were observed in the cerebello-brainstem regions (Fig.1 A,B,C).

As shown in Table 1, CMRGlc values were tabulated in order to compare levels in each of proband's brain structures with those of age matched controls. In the proband 1, the values in the inferior bi-temporal cortex and the bi-temporal pole were lower in comparison with the normal controls. CMRGlc values in the brainstem and the cerebellum were also lower than that of the controls. In the proband 2, scattered decrease in CMRGlc values was observed in the fronto-parieto-temporal cortex. CMRGlc reduction was also observed in the cerebello-brainstem region.

Discussion

The clinical manifestations of SCA7 are characterized by cerebellar ataxia with pigmentary macular and/or retinal degeneration. The clinical aspects of this SCA, including central and peripheral neural impairment, have been reported in several ethnic groups[5,13-15]. However, due to the fact that there is a low prevalence of this SCA in Japan, Japanese cases have not been reported except our ophthalmologic report[16,20]. To date, the reported symptoms are mental deterioration, visual impairment, slow eye movement, ophthalmoplegia, hearing impairment, facial myokymia, involuntary movement (such as chorea and dystonia), parkinsonian symptoms and sensory loss[5,13-15]. It is likely that in other types of SCA, this constellation of clinical features are presented in varying degrees in members of the same family and/or at different times during the course of illness[21].

Recently, several pathogenetic findings related with these clinical aspects have been reported to provide insight into the pathogenesis of SCA7. Using SCA7 cDNA clones, the subcellular localization of ataxin-7 was examined in transfected COS-1 cells. The study demonstrated that ataxin-7 is the protein encoded from the SCA7 gene, and that this protein is distributed intranuclearly with a portion localizing in the nucleolus. Thus, it is speculated that the expanded ataxin-7 carries out its pathogenetic effect in the nucleus by altering a matrix-associated nuclear structure and/or by disrupting nucleolar function[17]. In recent studies, two new immunohistological observations have been reported[10,22]. First, ataxin-7 accumulates as a single nuclear inclusion in neuronal cells of the brain. Second, these intranuclear structures were shown to be most frequent in the neurons of the inferior olive, the lateral geniculate body and the substantia nigra, which are also regions of frequent degenerative changes. However, these inclusions were also observed in the cerebral cortex, a region that is normally considered to be an unaffected in this and the other types of SCA[10].

Taken together with these observations, our data suggests that investigating the role of mutant ataxin7 in neural impairments would be of great interest. In several brain regions including non-atrophic areas, an attenuation of glucose metabolism was observed. This observation raises the possibility that mutant ataxin7 might be associated with the deleterious effects on neurons that result in attenuation of the neural activity and hypometabolism of glucose in several brain regions.

Although we were not able to ascertain the specific pathological mechanism underlying SCA7, the present study suggests that attenuation of neural activity may occur in several non-atrophic brain regions and that these impairments may be associated with the diverse neurological manifestations characteristic of this neurodegenerative disorder.

Acknowledgments

We thank Mr. Shemaiah Okamoto for reading the manuscript. This work was supported by Research on Specific Diseases, the Ministry of Health and Welfare, Japan.

References

1) Orr H.T. et al., Nature Genet. **4** (1993) 221-226.
2) Sanpei K. et. al., Nature Genet. **14** (1996) 277-284.
3) Kawaguchi Y. et al., Nature Genet. **8** (1994) 221-228.
4) Zhuchenko O.et al., Nature Genet. **15** (1997) 62-69.
5) David G. et al., Nature Genet. **17** (1997) 65-70.
6) Harding A.E., Advances in Neurology **61** (1993) 1-14.
7) Harding AE. Brain **105** (1982) 1-28.
8) Neetens A. et al., Neuro-ophthalmology **10** (1990) 261-275.
9) Koningsmark B. W. and Weiner L. P. Medicine; **49** (1970) 227-241.
10) Holmberg M. et al., Hum Mol. Genet. **7** (1998) 913-918.
11) David G. et al., Hum Mol. Genet. **7** (1998) 165-170.
12) Gouw L.G. et al., Hum. Mol. Genet **7** (1998) 525-532.
13) Giunti G. et al., Am. J. Hum. Genet. **64** (1999) 1594-1603.
14) Johansson J. et al., Hum. Mol. Genet.**7** (1998)171-176.
15) Benton C.S. et al., Neurology **51** (1998) 1081-1086.
16) Abe T. et al., Arch. Ophthalmol. **118** (2000) 1415-1421.
17) Kaytor M.D. et al., Hum. Mol. Genet. **8** (1999) 1657-1664.
18) Aoki M. et al., Hum. Mol. Genet. **3** (1994) 1197-1198.
19) Nagasawa H. et al., J. Neurol. Sci. **139** (1996) 210-217.
20) Onodera Y. et al., J.Neurol. Sci. **178** (2000) 153-158.
21) St George-Hyslop P. et al., Am. J. Hum. Genet. **55** (1994) 120-125.
22) Mauger C. et al., Mol. Brain. Res.**74** (1999) 35-43.

Table 1. In each structure of the brain, values of CMRGlc are shown in age matched controls and the two probands (mean±SD mg/100g/min). In the proband 1, the values in the inferior bi-temporal cortex and the bi-temporal pole are lower than the normal values. Remarkable reductions of the values are also shown in the cerebello-brainstem region. In the proband 2, CMRGlc values decrease in both the fronto-parieto-temporal cortex and the cerebello-brainstem.

	Control (n=11): Age 20.9±2.9	Proband 1: Age 26		Control (n=6): Age 63.5±9.0	Proband 2 : Age 46	
Frontal cortex		rt.	lt.		rt.	lt.
Superior frontal cortex	8.82±3.38	7.92	7.50	8.67±0.66	6.07	6.51
Medial frontal cortex	10.63±3.46	7.63	7.32	8.63±0.97	6.30	6.11
Medial mesial frontal cortex	10.52±3.21	7.86	8.10	8.53±1.10	6.37	6.93
Inferior frontal cortex	10.43±2.92	7.42	7.30	8.72±1.31	6.28	6.26
Lateral frontal cortex	10.35±2.92	7.60	7.31	8.16±1.30	6.87	6.16
Lateral posterior frontal cortex	10.28±2.28	8.35	8.02	8.23±0.92	6.24	6.05
Parietal cortex						
Primary motor and sensory cortex	10.29±2.37	8.15	8.12	9.17±0.77	6.36	6.73
Posterior parietal cortex	11.56±2.94	8.41	8.20	8.64±0.51	7.34	7.55
Lateral parietal cortex	10.93±2.71	7.46	7.71	8.66±1.21	7.37	7.06
Temporal cortex						
Superior temporal cortex	9.05±2.91	7.06	7.30	8.70±0.88	6.83	6.25
Medial temporal cortex	10.73±2.65	7.19	6.86	8.64±0.51	6.09	6.55
Inferior temporal cortex	10.18±2.53	4.72	5.14	7.70±0.80	5.48	5.84
Temporal pole	10.45±2.53	4.49	4.33	7.25±0.99	5.51	5.65
Occipital cortex						
Primary visual area	8.92±2.50	8.84	9.12	9.45±0.88	6.69	6.80
Associative visual area	10.40±2.36	8.74	8.58	9.45±1.11	9.10	8.68
Thalamus	8.98±2.86	9.59	10.13	8.79±0.95	8.04	7.63
Caudate nucleus	8.40±3.14	9.59	9.42	9.13±0.88	8.02	7.82
Putamen	11.50±3.11	11.01	10.42	8.67±0.88	8.66	8.23
Brainstem	7.46±2.10	5.20		7.06±0.46	5.24	
Cerebellum	10.26±2.24	4.39	4.10	7.70±1.23	3.85	3.84

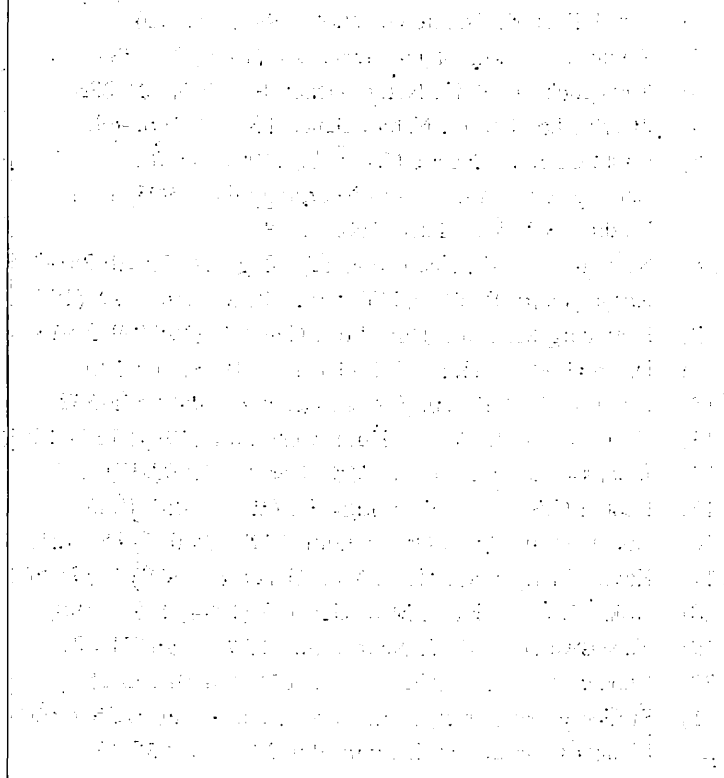

A

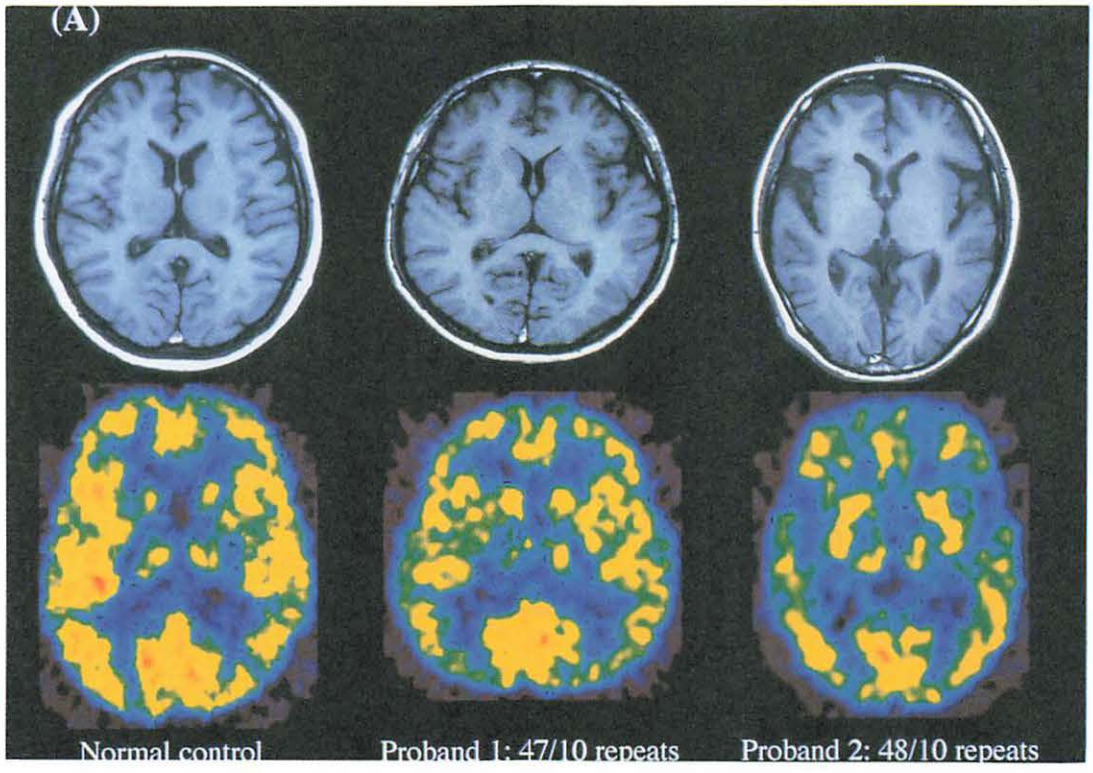
(A)
Normal control
Proband 1: 47/10 repeats
Proband 2: 48/10 repeats

B

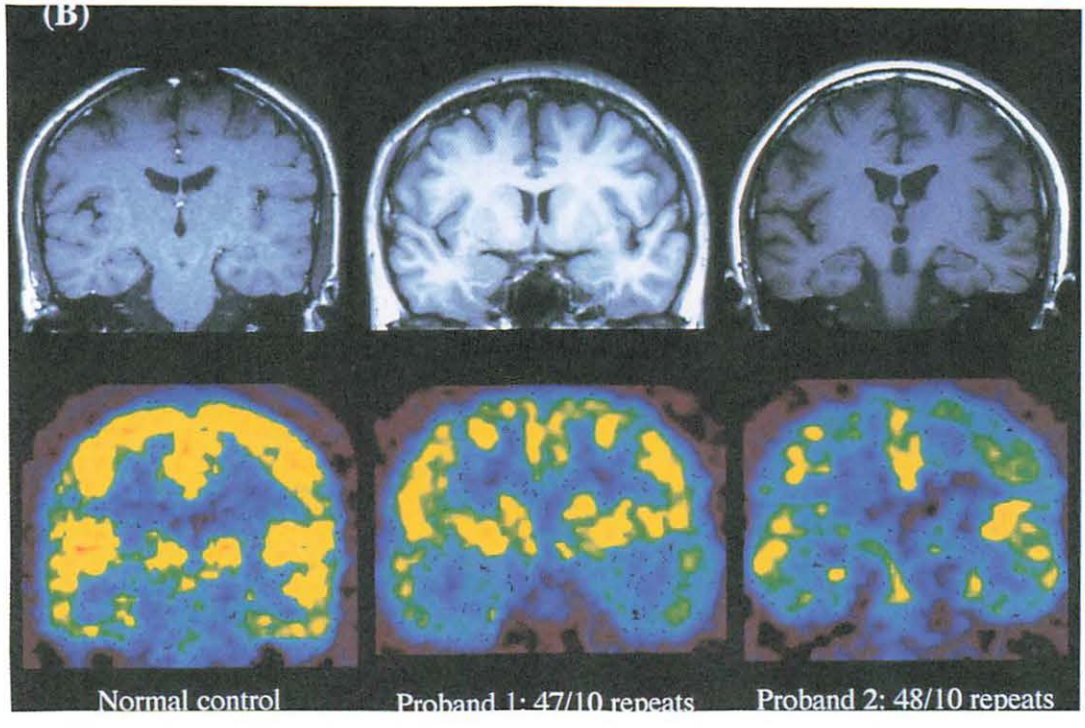
(B)
Normal control
Proband 1: 47/10 repeats
Proband 2: 48/10 repeats

C

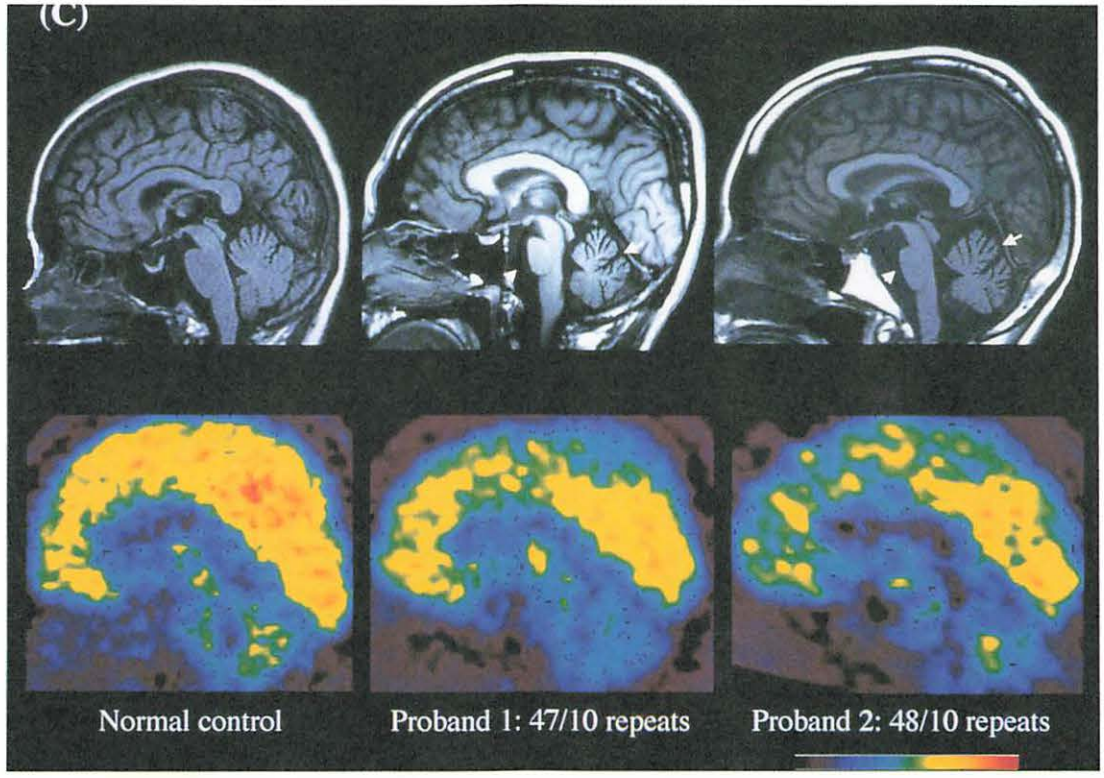

Fig. 1. Representative images obtained by ^{18}F-FDG positron emission tomography (PET) and MRI T1W.I. at the levels of corresponding brain slices in a normal control (age52, male), the proband 1 and the proband 2. The color scale in the present study ranges from 0 to 12mg/100g/min. (A): Axial images (B): Coronal images (C): Sagittal images.

IV. 3. Effect of Stereotactic Pallidal Surgery on Dopamine D2 Receptor in Advanced Parkinson's Disease

Nakajima T, Nimura T., Ando T.*, Shirane R, Ozaki K.**, Chida Y.**, Yamaguchi K.**, Itoh M.**, Yoshimoto T*

Department of Neurosurgery, Tohoku University School of Medicine
*Department of Neurosurgery, Miyagi National Hospital**
*Cyclotron and Radioisotope Center, Tohoku University***

Introduction

Parkinson's disease (PD) is characterized by degeneration of the dopaminergic neurons originated from the substantia nigra pars compacta[1]. Administration of levodopa has been established as a standard therapy. However long-term treatment with levodopa leads to a decline in its therapeutic efficacy with fluctuating response to treatment[2].

Stereotactic pallidal surgery has been established as an alternative therapy for advanced PD patients[3]. Although several studies have demonstrated that posteroventral pallidotomy (PVP) or deep brain stimulation (DBS) of the internal segment of the globus pallidus (GPi) could relieve drug-induced symptoms in advanced PD[4,5], the physiological mechanism of these procedures has not been understood yet.

Several studies showed up-regulated D2 function as measured as the binding potential (BP) in the putamen in early PD and its reduction in advanced stage[6,7]. Recent study disclosed a decrease of BP in extrastriatal regions such as anterior cingulate cortex, dorsolateral prefrontal cortex and the thalamus in advanced PD patients[8]. These findings imply the crucial role of dopaminergic system as a definitive factor of symptoms in PD.

We have quantified BP of striatal and extrastriatal dopamine D2 receptor before and after pallidal surgery using positron emission tomography (PET) and ^{11}C-nemonapride, which is selective antagonist to dopamine D2 receptor, to investigate physiological changes of dopaminergic system induced by the stereotactic pallidal surgery.

Subjects and methods

Subject

Six patients with advanced PD (3 men and 2 women, mean age 56.2±10.2 years) were included in this study. All the patients have undergone either PVP or DBS of the GPi because of both PD symptoms of rigidity-dominance and severe fluctuating response to levodopa treatment with drug induced dyskinesia. The patients were rated according to the

Unified Parkinson's Disease Rating Scale (UPDRS) before and after the surgery. The clinical characteristics of the patients are presented in Table 1.

PET imaging

We performed PET studies before and after the surgical treatment. PET scan was carried out using Shimadzu HEADTOME-V scanner in 3-D data acquisition mode. The subjects lay comfortably in the scanner couch with their eyes closed in a dim room in quiet environment. All scans were performed at 'off' state, levodopa administration was suspended at least 9 hours before the PET scanning.

^{11}C-nemonapride was synthesized according to the method previously described[9]. Radiochemical purity was more than 99 %, and the specific activity ranged from 250 mCi/μmol to 1200 mCi/μ mol at the end of the synthesis.

The tracer was injected intravenously in 3 - 5 ml of saline over a period of 60 seconds. The maximal mass dose of nemonapride was below either 0.25 nmol/kg body weight or 12.5 nmol/whole body weight, which is estimated to occupy less than 5 % of D2 receptors in human. Emission scan was performed for 90 minutes starting 30 seconds after the administration of the ligand: 6 x 60 s scans, 8 x 180 s scans, 6 x 300 s scans, 3 x 600 s scans.

Image analysis

Regions of interest (ROI) analysis was carried out on average ^{11}C-nemonapride images of 70 to 90 minutes after injection. Irregular ROIs were set on the bilateral striatum, frontal cortex, dorsolateral prefrontal cortex in each hemisphere with reference to the patients' MR images. We also set ROIs on occipital cortex as reference region since little specific binding was observed in the occipital cortex[9]. We adopt an equilibrium model where the BP is expressed as follows.

$$BP = Cs / Cr - 1$$

Where Cs and Cr express radioactivity in the specific region and reference region respectively.

Statistical analysis

The differences of changes in the clinical score and BP between before and after pallidal surgery were statistically analyzed using paired t-test.

Results

The UPDRS score were obviously improved after the pallidal surgery. The UPDRS total was 73.5±35.4 (average±SD) before operation and 55.8±30.8 after operation ($p<0.05$). UPDRS III, an index of motor function, also improved significantly, 38.5±20.9 to

29.1±19.4 ($p<0.05$). Though all the patients developed drug-induced dyskinesia before the operation, the symptom was significantly improved in all patients after surgery (data not shown).

Significant decrease of BP was found in the striatum ($p<0.01$), dorsolateral prefrontal cortex ($p<0.05$), frontal cortex ($p<0.05$) in the operated-side, while these regions did not reveal significant changes in contralateral hemisphere (Table 2).

Discussion

Deterioration of dopaminergic system and subsequent pathological dysfunction in the basal ganglia-thalamocortical circuit is believed to be the cause of the symptoms of PD. Previous studies showed that BP of dopamine D2 receptor in the striatum is up-regulated to compensate exhausted endogenous dopamine in early PD patients[7]. However, it significantly reduced to 82 % of normal levels in the advanced stage[6]. Furthermore in vivo study using PET revealed existence of D2 receptor in the extrastriatal brain regions[10] and much attention has been paid on its roles in schizophrenia and Parkinson's disease. Kaasinen et al disclosed that BP of D2 receptor in medial thalamus, anterior cingulate cortex and dorsolateral prefrontal cortex were deteriorated, as the severity of PD progressed[8]. This finding indicated that not only striatal but also extrastriatal dopaminergic system contributed to the pathogenesis of PD.

Our study disclosed that pallidal surgery led to a significant BP decrease in the striatum, dorsolateral prefrontal cortex and frontal cortex of the operated hemisphere. According to the theory of 'cortico-basal ganglia-thalamocortical circuit', the GPi has inhibitory output to the ventrolateral thalamus using γ-aminobutyric acid as a neurotransmitter and the thalamic nucleus has excitatory project to motor, premotor, supplementary motor and prefrontal cortex[11,12]. Thus PVP or DBS of GPi might have reduced inhibitory output to the thalamus, subsequently leading to increased excitatory projection to the cortex. Some authors have investigated the effects of pallidal manipulations on the primary motor cortex. Activation studies using $H_2{}^{15}O$ PET demonstrated that PVP and DBS had potential to improve motor performance and enhance the cerebral blood flow associated to the motor task[13]. This phenomenon may lead the concept that artificial manipulation of GPi can modify the cortical functions through the basal ganglia-thalamocortical network. Furthermore previous reports demonstrated that the striatum received an excitatory, glutamatergic input from all of cerebral cortex except for primary visual and auditory area[14]. The cortical afferents to striatum terminate primarily on the shafts of the dendritic spines of medium spiny neurons[15]. In addition to that, dopaminergic input from substantia nigra pars compacta also terminate the spines of medium spiny neuron in striatum and subsequently modulates the cortical inputs to the neurons[16]. The mechanism underlying the decreasing change of BP in the operated-side striatum could not be clearly elucidated. However, it is possible that the pallidal surgery

leads the activation of the cortex that subsequently enhances the cortical input to striatal neurons though the basal ganglia-thalamo-cortical circuit and this functional alternation modulates the physiological status of medium spiny striatal neuron and its dopaminergic system. Some authors reported that drug-induced dyskinesia is due to unbalanced interaction between exogenous dopamine and dopaminergic system in striatum. Therefore physiological changes of BP in striatum demonstrated in our study might be strongly relevant to the clinical improvement of drug-induced dyskinesia.

We also found BP decreases in the frontal cortex and dorsolateral prefrontal cortex of the operated hemisphere. The reciprocal neural network between mediodorsal nuclei of the thalamus and prefrontal cortices, such as the frontal eye field, the superior frontal convexity and the dorsolateral prefrontal cortex has been reported[17]. This circuit has been acknowledged to be pathophysiologically important role in schizophrenia. Furthermore Robbins demonstrated that the network participated in psychiatric and cognitive function in PD and proposed 'frontostriatal dementia' as a more apt description[18]. Correlation between the function of D2 like receptor in dorsolateral prefrontal, anterior cingulate, medial thalamus and cognitive function in PD was also reported[19]. In our series such adverse complications have not been observed. However, surgery-related alternations in D2 receptors possibly related to the 'frontostriatal circuit' may not completely exclude disturbances in patient's cognitive function occasionally developed after pallidotomy.

This study demonstrated that the dopaminergic neural circuit including extrastriatal areas such as prefrontal cortex has an important role in modulating the pathophysiological status in PD patients. Pallidal surgery has potential to modulate this network relating to the 'cortico-basal ganglia-thalamocortical circuit' and consequently improves the motor related disorders and drug-induced dyskinesia. PET study using ^{11}C-nemonapride has successfully disclosed the physiological changes of dopaminergic system underlying the clinical effects of the stereotactic surgical treatment in advanced PD.

References

1) Bethlem J.and Den Hartog Jager W.A., Neurology **43** (1993) S23-27.
3) Goetz C.G.et al., Neurology **43** (1993) 1-7.
4) Lang A. E. et al., N. Engl. J. Med. **337** (1997) 1036-1042.
5) Ghika J. et al., J. Neurosurg **89** (1998) 713-718.
6) Brooks D. J. et al., Ann. Neurol. **31** (1992) 184-192.
7) Rinne J. O. et al., Mov. Disord. **8** (1993) 134-138.
8) Kaasinen V. et al., Neurology **54** (2000) 1482-1487.
9) Hatano K. et al., J. Nucl. Med. **30** (1989) 515-522.
10) Farde L. et al., Psychopharmacology **133** (1997) 396-404.
11) Alexander G.E. and Crutcher M.D., Trends. Neurosci. **13** (1990) 266-271.
12) Parent A., Hazrati and L.N., Brain Res. Rev. **20** (1995) 91-127.
13) Fukuda M. et al., Ann. Neurol. **49** (2001) 155-164.

14) Cherubini E. et al., J. Physiol. **400** (1988) 677-690.
15) Bouyer J.J. et al., Brain Res. **302** (1984) 267-275.
16) Smith A.D. and Bolam J.P., Annual Rev. Neurosci. **9** (1986) 357-381.
18) Robbins T.W., Willner P, Scheel-Kruger J., eds. The mesolimbic system. Baffins Lane, Chichester, England: John Wiley & Sons, 1991: 529-538.
19) Tamaru F., Eur. Neurol. **38** (1997) 33-36.

Table 1. Clinical feature of patients

Patient	Age/sex	Age at onset	H&Y	UPDRS total	UPDRS motor	DID	Surgical site
1	50 M	15	3	58	25	1	left
2	65 F	55	2.5	59	36	1	right
3	55 F	33	3	78	47	2	right
4	48 M	40	2	21	6	1	left
5	72 F	55	5	113	53	3	bilateral
6	47 M	38	4	112	64	2	left

M = male; F = female; H&Y = Hoehn and Yahr scale
UPDRS = Unified Parkinson's Disease Rating Scale; DID = drug induced dyskinesia

Table 2. Binding potentials (Bmax/Kd) at before and after the operation

Brain region	Operation side Before	Operation side After		Contralateral side Before	Contralateral side After	
Striatum	1.86±0.44	1.72±0.43	*	1.68±0.42	1.60±0.38	ns
Frontal cortex	0.28±0.16	0.20±0.11	†	0.21±0.11	0.26±0.11	ns
Dorsolateral prefrontal corte	0.16±0.08	0.10±0.08	†	0.11±0.12	0.11±0.19	ns

values are mean ± SD.
* $p < 0.01$
† $p < 0.05$

IV. 4. Assessment of Nigrostriatal Dopaminergic Function in Patients with Dementia with Lewy Bodies

Okamura N., Hu X. S., Arai H., Maruyama M., Higuchi M., Tashiro M., Matsui T., Itoh M. and Sasaki H.*

Department of Geriatric and Respiratory Medicine, Tohoku University School of Medicine
*Division of Nuclear Medicine, Cyclotron and Radioisotope Center, Tohoku University**

Introduction

Dementia with Lewy bodies (DLB) is characterized by progressive cognitive decline, extrapyramidal symptoms, episodic confusion, hallucinations and fluctuating cognitive impairment. Pathologically DLB is characterized by the presence of numerous Lewy bodies in the cortical and subcortical brain regions with variable Alzheimer-type pathology[1]. Recently it is suggested that DLB represents the second frequent cause of degenerative dementia in the elderly. The consortium on dementia with Lewy bodies (CDLB) proposed clinical diagnostic criteria of DLB[2]. However, some follow-up studies indicated a relatively poor sensitivity of the CDLB criteria to detect living DLB patients in contrast to an appropriate specificity[3]. This highlights a need to develop another clinical or laboratory diagnostic tool to provide a greater precision in the antemortem diagnosis of DLB. Since positron emission tomography (PET) using ^{18}F-fluorodopa (FDOPA) provides a direct method of assessing pre-synaptic nigrostriatal dopaminergic function in living patients[4], we analyzed FDOPA uptake with PET in the regions of caudate nucleus and putamen.

Subjects and methods

Ten patients with probable Alzheimer's disease (AD) (70.5±8.4 years, range: 58-86), seven patients with probable DLB (66.9±10.0 years, range: 51-79) and eight age-matched normal subjects were examined. All of the patients and the normal subjects were evaluated by medical and neurological examinations as well as by MRI to exclude other causes of dementia. The diagnosis of "probable AD" was established by the NINCDS-ADRDA criteria. We followed CDLB criteria for the diagnosis of probable and definite DLB. Normal subjects were all volunteers without any confirmed neuropsychiatric or major medical illnesses. The severity of dementia as assessed by Mini-Mental State Examination was not significantly different between DLB (15.7±6.7 points) and AD (16.3±5.0 points).

All subjects underwent PET scans using PT931 PET scanner (CTI, USA) with 7mm axial and transaxial resolution. Following an intravenous bolus injection of 2.5-8.3 mCi of

FDOPA, a series of 5 min emission scans was carried out for 60 minutes and emission data were simultaneously collected from seven contiguous axial sections. The tissue FDOPA concentration was measured by defining regions of interest (ROIs) on three image planes that included the caudate nucleus and putamen. ROIs in the caudate nucleus and putamen were defined on a summed image of data collected during the PET scan. An influx rate constant (Ki) of FDOPA into the selected regions was then calculated by the method described by Patlak et al[5] with radioactivity of the cerebellar hemisphere as an input function as described previously[4].

Results

In the DLB group, Ki values were significantly reduced in the caudate nucleus (0.0064 ± 0.0017, $p<0.001$) and in the putamen (0.0051 ± 0.0019, $p<0.005$) compared to the AD group (caudate nucleus: 0.0119 ± 0.0021; putamen: 0.0092 ± 0.0014). However, there was no significant difference in the Ki values between the AD and the aged normal group in either caudate nucleus or putamen (Figure 1). Using a cut-off value of 0.0062 (mean-2S.D. of the age-matched normal group) in the putamen, DLB could be distinguished from AD with a sensitivity of 86% and a specificity of 100% (For further details, see Ref. 6).

Discussion

According to the CDLB criteria, DLB patients are characterised by a variable combination of cognitive decline, parkinsonism and other symptoms. A considerable clinical heterogeneity or a complex array of the order of the onset of symptoms in DLB was documented in the literature. In this study, there was only a small overlap in the FDOPA-Ki values between the DLB group and the AD group, suggesting that nigrostriatal dopaminergic function using PET and FDOPA may be an informative diagnostic adjunct in distinguishing DLB from AD. Our observations are in good agreement with a series of pathological findings that there is a consistent loss of substantia nigra neurons and depletion of striatal dopamine content in DLB[7,8]. Assessment of nigrostriatal dopaminergic function with PET and FDOPA alone or in combination with other PET images of glucose metabolism[9,10] will help to improve sensitivity to detect living DLB patients so that these patients will benefit by an appropriate treatment during life.

References

1) Kosaka K. J. Neurol. **237** (1990) 197-204.
2) McKeith I.G., Galasko D., Kosaka K., et al. Neurology. **47** (1996) 1113-1124.
3) Holmes C., Cairns N., Lantos P., et al. Br. J. Psychiatry. **174** (1999) 45-51.
4) Itoh M., Meguro K., Fujiwara T., et al. Ann. Nucl. Med. **8** (1994) 245-251.
5) Patlak C.S., Blasberg R.G. J Cereb Blood Flow Metab. **5** (1985) 584-590.
6) Hu X.S., Okamura N., Arai H., et al. Neurology. **55** (2000) 1575-1576.
7) Galvin J.E., Lee V.M.-Y., Schmidt M.L., et al. Adv Neurol. **80** (1999) 313-324.
8) Piggott M.A., Marshall E.F., Thomas N., et al. Brain. **122** (1999) 1449-1468.
9) Higuchi M., Tashiro M., Arai H., et al. Exp. Neurol. **162** (2000) 247-256.
10) Okamura N., Arai H., Higuchi M., et al. Prog. Neuro-Psychopharmacol. Biol. Psychiat. **25** (2001) 447-456.

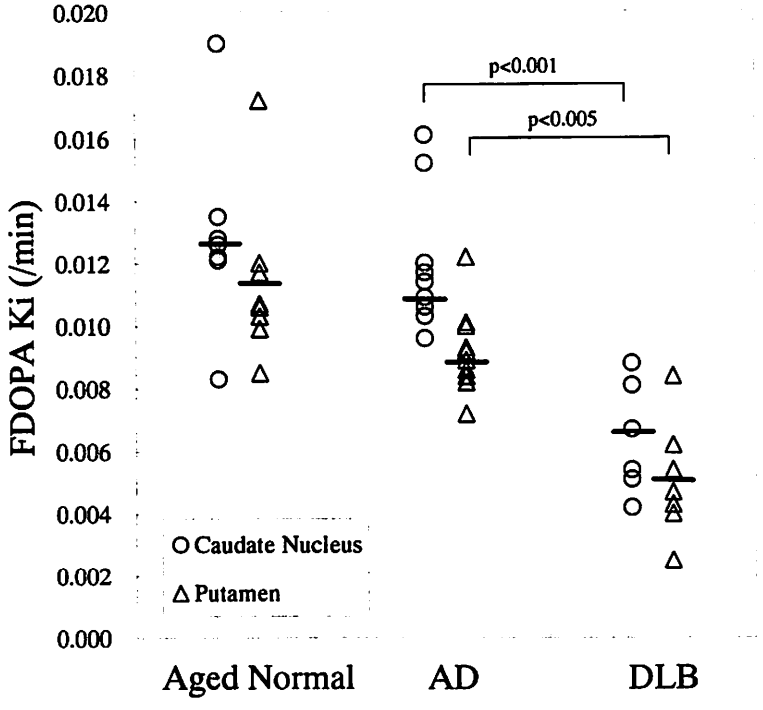

Fig. 1 Individual influx rate constant (Ki) value of ^{18}F-fluorodopa (FDOPA-Ki) in the caudate nucleus (O) and the putamen (Δ) in age-matched normal control (Aged Normal), Alzheimer's disease (AD), and dementia with Lewy bodies (DLB) are shown. Each bar represents mean Ki value. In the caudate nucleus, Ki values were 0.0129±0.0029 in aged normal, 0.0119±0.0021 in AD, and 0.0064±0.0017 in DLB. In the putamen, Ki values were 0.0114±0.0026 in aged normal, 0.0092±0.0014 in AD, and 0.0051±0.0019 in DLB. Statistical analysis was performed by one-way ANOVA.

IV. 5. Regional Glucose Hypometabolism in Brain of Patients with Dementia with Lewy Bodies and Alzheimer's disease

Okamura N., Arai H., Higuchi M., Tashiro M., Maruyama M., Matsui T., Hu X. S., Itoh M. and Sasaki H.*

Department of Geriatric and Respiratory Medicine, Tohoku University School of Medicine
*Division of Nuclear Medicine, Cyclotron and Radioisotope Center, Tohoku University**

Introduction

Dementia with Lewy bodies (DLB) is a neurodegenerative disorder that is characterized by a progressive cognitive decline and the presence of numerous Lewy bodies (LB) in the cortical and subcortical brain regions. In 1996, the consortium on dementia with Lewy bodies (CDLB) proposed clinical and pathological criteria of DLB[1]. However, some groups indicated a relatively poor sensitivity of the CDLB criteria to accurately detect DLB[2,3]. It is clinically important to discriminate DLB patient from AD patients because the patients with DLB often exhibit life-threating neuroleptic adverse effects[4]. Therefore, the objective diagnostic aid for the antemortem diagnosis of DLB is desperately needed. In this article, we report functional neuroimaging features of one autopsy-confirmed case of DLB. Furthermore, we describe the characteristic features of cerebral glucose metabolism in a larger sample of DLB.

Case Report

Patient had been well until 55 years old when depression developed with prominent headache, anxiety and loss of interest. At age 58, she became progressively disorientated and had memory deficits. She also developed difficulty with performing fine movements such as using chopsticks and buttoning her clothing. On neurological examination performed at age 59, she was emotionless and hypophonic, lost her facial expression, was slowed down and shuffled on walking with reduced arm swing. Cog-wheel rigidity was present at both wrists and elbows. Bilateral hand tremor was noted as well. She drew a clock poorly, and she scored 12 out of 30 on Mini-Mental State Examination (MMSE). Deep tendon reflexes were normally active. Brain CT and MRI revealed diffuse cortical atrophy, while 7-8 Hz slow background activity was noted on EEG. At age 60, PET scans were performed using [^{18}F]-2-fluoro-deoxy-D-glucose (FDG) and [^{18}F]-6-fluorodopa (FDOPA). On FDG-PET images showing widespread cortical hypometabolism, the occipital metabolic deficit was

particularly noticeable. The glucose metabolic ratio in the visual association cortex (normalized by the radioactivity in cerebellar vermis) was 0.78, which was lower than an average value (1.02) in AD patients[5]. FDOPA-PET image revealed low dopamine uptake rate of FDOPA, representing a reduction in the number of nigrostriatal dopaminergic neurons at the presynaptic sites. The rate of influx (Ki) in the striatum, calculated by the graphical analysis, was 0.0062 min^{-1}, that was lower than the average values in AD (0.0110) and aged normal subjects (0.0116)[6]. Levo-dopa with carbidopa produced a transient improvement in the motor features of parkinsonism, while cognitive impairment continued to deteriorate with a persistent visual hallucination and delusion that was unrelated to the levo-dopa therapy. At age 63, she became wheelchair bound and had a difficulty in verbal communication. At age 64, she was unable to feed herself because of progressive dysphasia, and died of aspiration pneumonia and congestive heart failure 9 years after the onset of the disease. Postmortem brain examination revealed numerous LBs and LB-neurites that were immunoreactive to anti-α-synuclein and anti-ubiquitin antibodies as well as abundant senile plaques and neurofibrillary changes. Hence, final pathological diagnosis was made as "DLB plus AD". In addition to such well-documented hallmarks, there was an extensive spongiform change and gliosis throughout the white matter. The most extensive white matter change was observed in the occipital region. An extensive gliosis also was present in the white matter with relative sparing of the gray matter.

Subjects and methods

Eleven patients with probable AD, seven patients with probable DLB and ten age-matched normal subjects were examined. All of the patients and the normal subjects were evaluated by medical and neurological examinations as well as by MRI to exclude other causes of dementia. The diagnosis of "probable AD" was established by the NINCDS-ADRDA criteria. We followed CDLB criteria for the diagnosis of probable and definite DLB. Normal subjects were all volunteers without any confirmed neuropsychiatric or major medical illnesses. The severity of dementia as assessed by Mini-Mental State Examination (MMSE) was 18.8±3.3 points (range 12-24 points) in the AD group and 16.1±7.1 points (range 6-24 points) in the DLB group.

Measurement of cerebral gluc ose metabolism with PET and FDG was performed using a PET scanner (SET2400W, Shimadzu Inc., Japan). Subjects were scanned in a quiet and dimly-lit room with their eyes open after at least 4 hours of food restriction. Following a $^{68}Ge/Ga$ transmission scan of 7 min duration, an emission scan was performed which lasted 60 min after intravenous injection of FDG. Arterial blood was sampled from the radial artery during the scan, and an input function was obtained by measuring plasma radioactivity. The cerebral metabolic rate of glucose (CMRglu) was calculated using the autoradiographic method by Hutchins et al. [7].

Volume of interest (VOI) with an area of 1 cm^2 was drawn on individual MR images that were matched to the PET images by a linear spatial transformation. Multiple VOIs were placed to cover the whole target anatomical structure, and were transferred to the PET images. CMRglu was then calculated for cortical and subcortical structures. The whole brain CMRglu was defined as an average over both gray and white matter structures. Among many brain structures included in the VOI analysis, the absolute glucose metabolism in the cerebellar vermis was most preserved in AD and DLB. Therefore, normalized CMRglu values or metabolic ratios were calculated using the cerebellar vermis as a reference region. The metabolic ratio was estimated in VOIs including the lateral frontal cortex (Brodmann's area [BA] 8, 9, 10, 44, 45, 46 and 47), lateral temporal cortex (BA 21, 22, 37 and 38), medial temporal cortex (BA27, 28, 34 and 35), lateral parietal cortex (BA39 and 40), posterior parietal cortex (BA 5 and 7), anterior (BA 24 and 32) and posterior (BA 23 and 31) cingulate cortices, and primary (BA 17) and association (BA 18 and 19) visual cortices. Averaged values of right and left hemispheric VOIs were used for statistical analysis. Statistical analysis was performed by analysis of variance (ANOVA).

Results

Absolute CMRglu values in the whole brain of each group were as follows; the AD group: 3.66±1.26 mg/100g/min, the DLB group: 3.59±0.54 mg/100g/min, and the aged normal group: 7.52±1.20 mg/100g/min. Statistically, the whole brain CMRglu was significantly lower ($p<0.0001$) in the AD and DLB groups compared to that in the normal group. The results demonstrate a significant difference in the metabolic ratio between the AD and normal group in the posterior parietal cortex ($p<0.0001$), the posterior cingulate cortex ($p<0.0001$), the lateral parietal cortex ($p<0.001$) and the medial and lateral temporal cortices ($p<0.01$). The metabolic ratio was relatively preserved in the frontal and occipital cortices. When comparing metabolic ratios between the DLB and normal groups, the metabolic decline in the DLB group was evident virtually throughout the entire cortical region extending from the frontal to occipital cortex. Notably, the reduction in the metabolic ratio in the DLB group compared to the AD group was most pronounced in the visual association cortex (Figure 1) (For further details, see Ref 5).

Discussion

Our results indicated that occipital hypometabolism is the feature of DLB that discriminate it from AD. Previous functional imaging studies in DLB showed a characteristic pattern of regional glucose hypometabolism and hypoperfusion in the primary visual cortex and occipital association cortex in addition to the patterns of abnormal metabolism found in AD[8,9]. Our results are comparable to the finding of these previous reports. In our study population using a metabolic ratio of 0.92 in the visual association

cortex as a cut-off, DLB could be distinguished from AD with a sensitivity of 86% and a specificity of 91%[5]. Therefore, these findings suggest that PET measures of glucose metabolism may help in enhancing the clinical diagnosis of DLB particularly in the early stages of the disease. In our examination, the patient described in the case report showed the lowest value of metabolic ratio in the visual association cortex among DLB patients. In addition, there was a severe spongiform change and gliosis mainly in the occipital cortex at postmortem examination in this patient. These findings suggest a possibility that the white matter spongiform pathology is likely to be a pathological substrate for a characteristic pattern of glucose hypometabolism in DLB, although there is only limited information in the pathological basis of the spongiform change.

References

1) McKeith I.G., Galasko D., Kosaka K., et al. Neurology. **47** (1996) 1113-1124.
2) Holmes C., Cairns N., Lantos P., et al. Br. J. Psychiatry. **174** (1999) 45-51.
3) McKeith I.G., O'brien J.T., Ballard C. Lancet. **354** (1999) 1227-1228.
4) Ballard C., Grace J., McKeith I.G. et al. Lancet. **351** (1998) 1032-1033.
5) Higuchi M., Tashiro M., Arai H., et al. Exp. Neurol. **162** (2000) 247-256.
6) Itoh M., Meguro K., Fujiwara T., et al. Ann. Nucl. Med. **8** (1994) 245-251.
7) Hutchins G.D., Holden J.E., Koeppe R.A., et al. J. Cereb. Blood. Flow Metab. **4** (1984) 35-40.
8) Albin R.L., Minoshima S., D'Amato C.J., et al. Neurology **47** (1996) 462-466.
9) Ishii K., Imamura T., Sasaki M., et al. Neurology **51** (1998) 125-130.

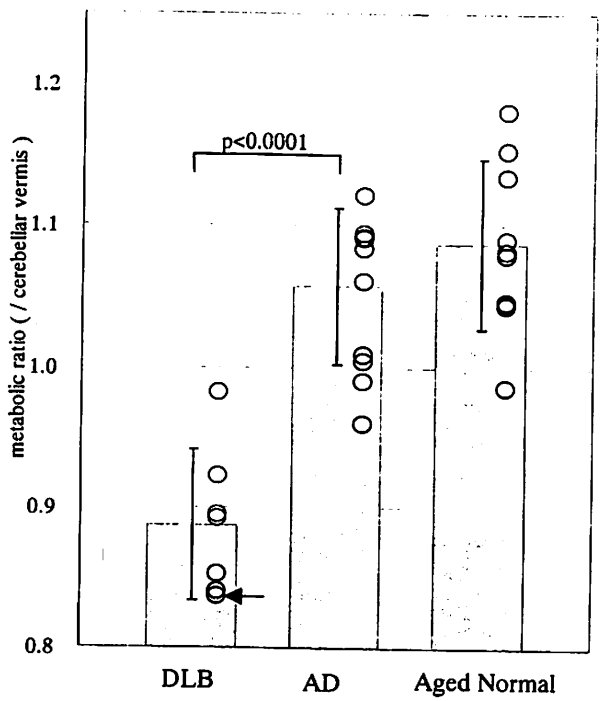

Fig. 1 Glucose metabolic ratio in the visual association cortex in dementia with Lewy bodies (DLB), Alzheimer's disease (AD) and age-matched normal control (Aged Normal). An arrow indicates the metabolic ratio of the autopsy confirmed case with DLB.

IV. 6. The Efflux Transport of Dehydroepiandrosterone Sulfate at the Blood-Brain Barrier

Asaba H., Hosoya K.*,***, Takanaga H.*,**,***, Ohtsuki S.*,**,***, Tamura E.*, Takizawa T.* and Terasaki T.*,**,****

Department of Molecular Biopharmacy and Genetics, Graduate School of Pharmaceutical Sciences, New Industry Creation Hatchery Center**, Tohoku University*
*CREST of Japan Science and Technology Corporation (JST) ****

We have investigated transport characteristics of dehydroepiandrosterone sulfate (DHEAS), a neuroactive steroid, at the blood-brain barrier (BBB) in functional in vivo study. The apparent BBB efflux rate constant of [^{3}H]DHEAS evaluated by Brain Efflux Index method was 2.68×10^{-2} min^{-1}. The DHEAS efflux transport was a saturable process with a Michaelis constant (K_m) of 32.6 μM providing the direct evidence that most of DHEAS is transported from brain to the circulating blood across the BBB. This efflux transport of [^{3}H]DHEAS was inhibited by the common organic anion transporting polypeptide (oatp) substrates such as taurocholate, cholate, sulfobromophtalein, estrone-3-sulfate demonstrating that DHEAS is predominantly transported from the brain to blood across the BBB.

Introduction

Dehydroepiandrosterone sulfate (DHEAS), which is termed 'neurosteroid', possesses multiple effects in the central nervous system, including interacting with GABA type A receptor and sigma receptor, an increase of memory and learning, and protection of neurons against excitatory amino acid-induced neurotoxicity[1]. In multi-infarct dementia (MID) patient, DHEAS concentration in CSF was 400 ± 180 pg/ml, which was significantly lower than that in non-demented patients (800 ± 400 pg/ml)[2]. This evidence raises that DHEAS concentration may afford the vulnerability of the brain.

The BBB is well recognized to regulate not only the entry of nutrients, and drugs into the brain from the circulating blood[3,4], but also the efflux of compounds such as *p*-aminohippuric acid, 3'-azido-3'-deoxythymidine, 2',3'-dideoxyinosine, L-glutamic acid, and L-aspartic acid[5-7].

The purpose of the present study was to investigate the DHEAS transport across the BBB in both the blood-to-brain and brain-to-blood directions in vivo.

Materials and methods

Brain Efflux Index (BEI) Study

The BEI study was performed according to the method of Kakee et al[8]. Rats were anesthetized and mounted on a stereotaxic frame. Then, 0.50 μl of [^{3}H]DHEAS (0.08 μCi) and [^{14}C]inulin (4 nCi) dissolved in the ECF buffer (122 mM NaCl, 25 mM $NaHCO_3$, 10 mM glucose, 3 mM KCl, 1.4 mM $CaCl_2$, 1.2 mM $MgSO_4$, 0.4 mM K_2HPO_4, 10 mM HEPES, pH 7.4) was administered over 1 min via 5.0 μl-microsyringe fitted with a needle at a depth of 4.5 mm from the surface of the scalp, i.e., Parietal Cortex Area 2 (Par2) region. At predetermined time period, an aliquot of cerebrospinal fluid (CSF) was collected from the cisterna magna as reported previously[8]. The whole brain was subsequently isolated and the brain specimen was divided into the left cerebrum, the right cerebrum and the cerebellum. After weighing, dissolving tissue in 2N NaOH, and mixing with scintillation cacktail, the associated radioactivity was measured with a liquid scintillation counter (LS-6500, Beckman, Fullerton, CA).

Determination of BEI from the Brain

The BEI was defined as equation (1) and the percentage of substrate remaining in the ipsilateral cerebrum was determined using equation (2).

$$\text{BEI (\%)} = \frac{\text{test substrate undergoing efflux at the BBB}}{\text{test substrate injected into the brain}} \times 100 \qquad (1)$$

$$\text{100-BEI (\%)} = \frac{\text{(amount of test substrate in the brain/ amount of reference in the brain)}}{\text{(concentration of test substrate injected / concentration of reference injected)}} \times 100 \qquad (2)$$

As the percentage of DHEAS remaining in the brain is given by (100-BEI), apparent BBB efflux rate constant (K_{eff}) was estimated by fitting the semilogarithmic plot of (100-BEI) *versus* time data to the nonlinear least-squares regression analysis program, MULTI[9].

Results

In Vivo Brain-to-Blood Transport of DHEAS

The in vivo brain-to-blood efflux of DHEAS was evaluated by means of the BEI method[8] over 20 min after intracerebral administration by comparing the BEI value with that of [^{14}C]inulin as a non-efflux compound. The [^{3}H]DHEAS in rat brain decreased in a time-dependent manner, with a K_{eff} of $2.68 \times 10^{-2} \pm 0.02 \times 10^{-2}$ min^{-1} (mean ± S.D.) (Fig. 1), whereas [^{14}C]inulin did not significantly decrease over 20 min (data not shown).

Concentration-dependence of DHEAS Efflux from the Brain

The excess unlabeled DHEAS in the injectate solution reduced the DHEAS efflux transport from rat brain in a concentration-dependent manner (Fig. 2). Eadie-Scatchard plot exhibited the single saturable process of [^{3}H]DHEAS efflux (Fig. 2 inset). Nonlinear least-squares regression analysis provided a K_m of 32.6 ± 4.8 μM at cerebral concentration, which was calculated from the concentration of DHEAS in the injected solution and dilution factor as reported by Kakee et al.[8], and a V_{max} of 4.14 ± 0.39 nmol/(min·g brain) (mean ± S.D.).

Effect of Several Organic Anions on DHEAS Efflux from the Brain

To characterize the [^{3}H]DHEAS efflux transport process at the BBB in vivo, the effects of several organic anions on [^{3}H]DHEAS efflux transport from rat brain was investigated (Table 1). Bile acids, at 20 mM (0.66 mM in the brain), such as taurocholate (TCA), and cholate (CA) inhibited [^{3}H]DHEAS efflux transport by 70.5 ± 2.1%, and 47.9 ± 14.6% ($p<0.001$), respectively. A thyroid hormone, 3,5,3'-triiodo-L-thyronine at 5 mM (0.17 mM in the brain) inhibited [^{3}H]DHEAS efflux transport by 37.9 ± 4.3% ($p<0.01$). Sulfate conjugated hormones such as E_1S at 10 mM (0.33 mM in the brain) and E_2S at 20 mM inhibited [^{3}H]DHEAS efflux transport by 81.5 ± 3.1, and 81.5 ± 6.8% ($p<0.001$), respectively. Organic anions such as sulfobromophtalein (BSP) at 20 mM and probenecid at 100 mM (3.3 mM in the brain) also reduced [^{3}H]DHEAS efflux by 62.8 ± 2.4%, and 87.5 ± 3.8% ($p<0.001$), respectively. By contrast, other compounds such as PAH and GABA at 100 mM did not affect the DHEAS efflux transport.

Discussion

In the present study, in vivo evidence provided that DHEAS, a neuroactive hormone, is transported via a carrier-mediated efflux transport process from brain to the circulating blood across the BBB. DHEAS is produced in the brain and plays physiological roles of neurosteroid in the brain[1]. Our results exhibit that the BBB undergoes efflux of DHEAS, suggesting that the BBB acts as an efflux pump for DHEAS as is neurotransmitters such as L-Glu and L-Asp[7] and may regulate DHEAS concentration in the brain interstitial fluid. The efflux transport process of DHEAS from rat brain to the circulating blood across the BBB was saturable and concentration-dependent (Fig. 2). This result supports the hypothesis that DHEAS is transported via a carrier-mediated efflux transport process across the BBB.

Both oatp1 and oatp2, which transport DHEAS, are well known to play important roles of drug disposition in rat liver[10,11]. The K_m values of these transporters are also relatively similar to that determined by BEI method (Fig. 2)[10,11]. The [^{3}H]DHEAS efflux transport from rat brain was significantly inhibited by TCA, CA, BSP, E_1S, E_2S, and probenecid (Table 1). This inhibition pattern was in good agreement with that of oatp1- and oatp2- mediated steroid hormone transport in the liver and kidney[11,12]. Both oatp2 and oatp3 have been shown to mediate transport of the thyroid hormone such as T_3, and T_4, and

the oatp3 is mainly expressed in the kidney[13,14]. Taken together, DHEAS would be undergone efflux across the BBB via oatp2 which is located in the brain capillary[15].

In conclusion, DHEAS, a neurosteroid hormone, was eliminated from the rat brain. This is the first in vivo direct evidence of restricted brain distribution of DHEAS from circulating blood at the BBB, and is also important in helping us better understand how the BBB functions with regard to steroid hormone. Functional in vivo studies suggest that the BBB is involved in efflux transport of DHEAS at least via oatp2.

References

1) Wolf O. T. and Kirschbaum C., *Brain Res. Rev.* **30** (1999) 264-288.
2) Azuma T., Nagai Y., Saito T., Funauchi M., Matsubara T. and Sakoda S., *J. Neurol. Sci.* **162** (1999) 69-73.
3) Cornford E. M., *Mol. Physiol.* **7** (1985) 219-260.
4) Pardridge W. M., Triguero D., Yang J. and Cancilla P.A., *J. Pharmcol. Exp. Ther.* **253** (1990) 884-891.
5) Kakee A., Terasaki T., and Sugiyama Y., *J. Pharmcol. Exp. Ther.* **283** (1997) 1018-1025.
6) Takasawa K., Terasaki T., Suzuki H. and Sugiyama Y., *J. Pharmcol. Exp. Ther.* **281** (1997) 369-375.
7) Hosoya K., Sugawara M., Asaba H. and Terasaki T., *J. Neurochem.* **73** (1999) 1206-1211.
8) Kakee A., Terasaki T. and Sugiyama Y., *J. Pharmacol. Exp. Ther.* **277** (1996) 1550-1559.
9) Yamaoka K., Tanigawara Y., Nakagawa T. and Uno T., *J. Pharmaco-Dyn.* **4** (1981) 879-909.
10) Eckhardt U., Schroeder A., Stiger B., Höchli M., Landmann L., Tynes R., Meie P. J. and Hagenbuch B., *Am. J. Physiol.* **39** (1999) G1037-G1042.
11) Reichel C., Gao B., van Montfoort J., Cattori V., Rahner C., Hagenbuch B., Stieger B., Kamisako T. and Meier P. J., *Gastroenterology* **117** (1999) 688-695.
12) Kanai N., Lu R., Bao Y., Wolkoff A. W., Vore M. and Scuster V. L., *Am. J. Physiol.* **270** (1996) F326-F331.
13) Abe T., Kakyo M., Sakagami H., Tokui T., Nishio T., Tanemoto M., Nomura H., Hebert S. C., Matsuno S., Kondo H. and Yawo H., *J. Biol. Chem.* **273** (1998) 22395-22401.
14) Kakyo M., Sakagami H., Nishio T., Nakai D., Nakagomi R., Tokui T., Naitoh T., Matsuno S., Abe T. and Yawo H., *FEBS Lett.* **445** (1999) 343-346.
15) Gao B., Stieger B., Noé B., Fritschy J-M. and Meier P. J., *J. Histochem. Cytochem.* **470** (1999) 1255-1263.

TABLE 1. Co-administration effect of several organic anions on [^{3}H]DHEAS efflux from rat brain

Inhibitors	Concentration in Injectate (mM)	Concentration in ipsilateral cerebrum[a] (mM)	No. studied	BEI[b] (%)
Control			12	59.3 ± 1.8 (100)
p-Aminohippuric acid (PAH)	100	3.3	4	50.6 ± 2.7 (85.4)
γ-Aminobutylic acid (GABA)	100	3.3	4	58.1 ± 1.9 (97.9)
Sulfobromophthalein (BSP)	20	0.66	4	22.1 ± 1.4 (37.2)**
Taurocholate (TCA)	20	0.66	4	17.5 ± 1.2 (29.5)**
Cholate (CA)	20	0.66	4	30.9 ± 8.7 (52.2)**
Estrone-3-sulfate (E_1S)	10	0.33	4	11.0 ± 4.0 (18.5)**
Estradiol-3-sulfate (E_2S)	20	0.66	4	10.4 ± 3.0 (18.4)**
3,5,3'-Triiodothyronine (T_3)	5	0.17	4	36.9 ± 2.5 (62.2)*
Probenecid	100	3.3	4	7.44 ± 2.2 (12.5)**

[^{3}H]DHEAS was used at a concentration of 10 μM, i.e., 330 nM as a cerebral concentration.

[a]The cerebral concentration was estimated from the injectate concentration divided by the dilution factor, *i.e.*, 30.3, which was reported previously (Kakee *et al.*, 1996).

[b]Data, determined 20 min after intracerebral microinjection, are mean ± SEM values (percent of control).

* $p<0.01$, ** $p<0.001$, significantly different from control.

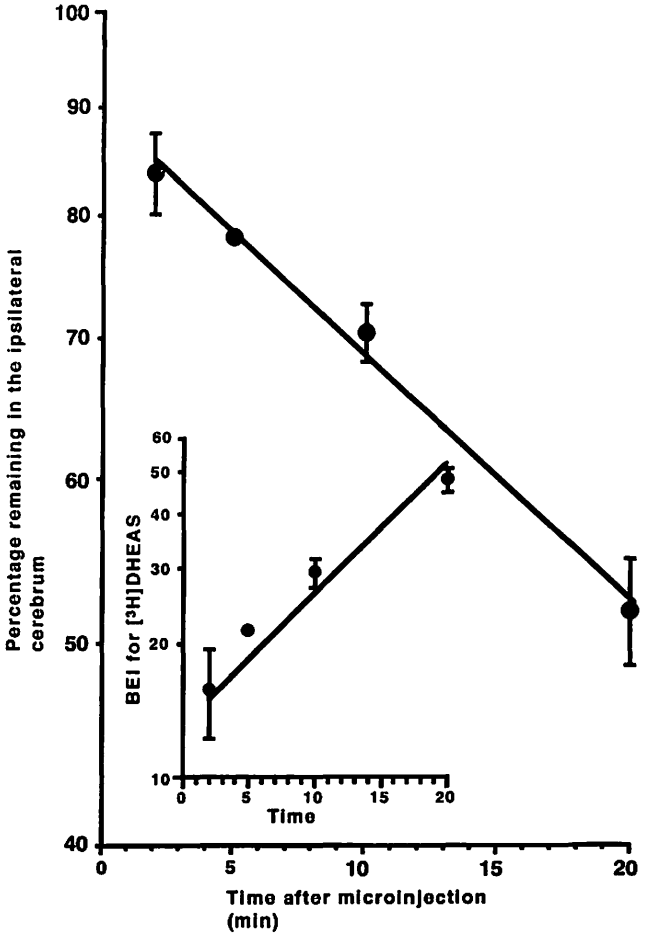

Fig. 1. Time-course of [^{3}H]DHEAS in the ipsilateral cerebrum following intracerebral microinjection to the Par2 region in the presence of [^{14}C]inulin as an internal reference. The solid line was obtained by the nonlinear least-squares regression analysis program. Each point represents the mean ± S.E.M. (n=3).

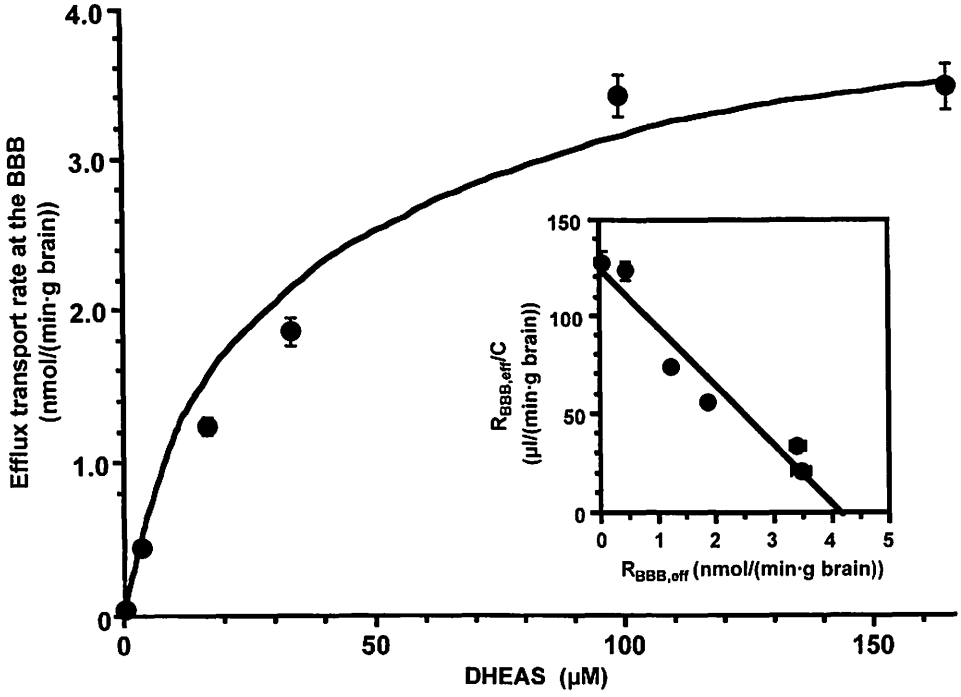

Fig. 2. Concentration-dependence of DHEAS efflux from the brain across the BBB. The solid line was estimated using the nonlinear least-squares regression analysis program. The cerebral concentration was estimated from the injectate concentration divided by the dilution factor. Inset: Eadie-Scatchard plot for [^{3}H]DHEAS efflux transport at the BBB. Each point represents the mean ± S.E.M. (n=3-7).

IV. 7. Functional Module of the Brain in Response to Colonic Distention in Human

Hamaguchi T., Kano M., Kanazawa M., Rikimaru H.**, Tomiie T., Yanai K.*, Itoh M.**, and Fukudo S.**

Department of Behavioral Medicine, Tohoku University Graduate School of Medicine
*Department of Pharmacology, Tohoku University Graduate School of Medicine**
*Division of Nuclear Medicine, Cyclotron and Radioisotope Center, Tohoku University***

Introduction

It is well-known that psychological stress induces symptoms in the lower digestive tract of humans such as abdominal pain, diarrhea or constipation[1]. These phenomena are explained by stress-induced colonic motility[2] and visceral perception abhorred by the stress[3]. Irritable bowel syndrome (IBS) is a functional gastrointestinal disorder characterized with chronic abdominal pain and abdominal bowel habituation. Recently, research of IBS is paid much attention because of high prevalence and the great influence on the medical economy. However, the cause and the pathophysiology are uncertain. Functional relation between central nervous system and gastrointestinal tract begins to be clarified[2] and brain-gut interactions are considered to be major pathophysiology of IBS[2]. Silverman et al.[4] reported that rectal distention induced activation of anterior cingulate cortex in healthy persons but not in IBS patients. In contrast, Mertz et al.[5] reported that in IBS patients, but not in healthy persons, painful stimuli to the rectum led to greater activation of the anterior cingulate cortex than did non-painful stimuli. Therefore, functional module of the brain in response to colorectal distention is not determined yet. Moreover, the stimulated part is the rectum, but the pain-producing part in IBS patients is the colon. In addition, there are a lot of uncertain points in the brain area that relates to emotion provoked by visceral perception.

This study aims to verify the following hypotheses: 1) the visceral perception and emotion are caused by stimulation of the colon, and 2) there is the brain regions which relate to the visceral perception and emotion provoked by the visceral sensation.

Method

Fifteen volunteers participated in this study. Their were all male, right-handed, and aged 22 ± 1 (mean $\pm$ SE). All subjects were free from gastrointestinal symptoms or signs. All subjects gave consent as approved by the Ethics Committee in Tohoku University School of Medicine.

The colonic distention stimuli were provided with computerized barostat pump (maximal volume is 700ml, 10cm diameter when fully inflated). The sham stimulation with 0mmHg was given at first. The colon was then stimulated with the bag pressure of 0mmHg, 20mmHg, and 40mmHg for 80 seconds. The intensity of stimulus was at random. The subjects closed their eyes with waking. After the stimulation, subjects were asked the following 7 items of visceral sensation or emotion: abdominal discomfort, abdominal distention, abdominal pain, urgency, perceived stress, sleepiness, and anxiety. They judged the sensation from "not sensed" to "maximally sensed" with ordinate scale of the 0-10 point.

Injected $H_2{}^{15}O$ comes in the systemic circulation and radiation concentration detected in the brain is proportional to the volume of cerebral blood stream[6]. Increase in regional cerebral blood flow (rCBF) is an index of the neural activity evoked with the stimulation[7,8]. The PET scanning then started and continued for 70 seconds. We measured rCBF during 4 scans (70 seconds each) using a PET scanner[9] in 3 dimension sampling mode (HEADTOME V SET-2400W, Shimadzu, Japan).

The image reconstruction was carried out using Three Dimensional Filtered Back Projection Algorithm[10-12]. The PET image analyzed for brain image analysis software (Statistical Parametric Mapping; SPM99, The Wellcome Department of Cognitive Neurology, London) according to the method of Friston et al[13-18]. The multiple regression analysis was done on each voxel of each ordinate scale and whole brain in each stimulation in order to clarify the region where the rCBF fluctuates by correlating with visceral perception and emotion. We set 0.1% level of significance or less (uncorrected, $Z \geqq 3.30$) as the region of significant correlation. The region which showed the activity correlation was identified on the basis of the Talairach coordinate[19]. Visceral perception and emotion were analyzed with one-way analysis of variance (ANOVA). Cluster analysis using average coupled method in the group by square Euclidean distance was carried out in order to evaluate the similarity between items.

Results

The abdominal pain was induced by colonic distention intensity-dependently ($F[3,14] = 16.02$, $p<0.001$). Abdominal discomfort ($F[3,14] = 17.95$, $p<0.001$), abdominal distention ($F[3,14] = 13.22$, $p<0.001$), and urgency ($F[3,14] = 9.65$, $p<0.001$) were also induced by the colonic distention intensity-dependently. Conversely, the sleepiness showed the maximum value in the resting and it significantly lowered with the stimulation ($F[3,14] = 3.85$, $p<0.05$). Perceived stress ($F[3,14] = 14.92$, $p<0.001$) and anxiety ($F[3,14] = 3.48$, $p<0.05$) were increased for stimulation with intensity-dependently.

Visceral perception and emotion for colonic distention were classified into 4 clusters based on the cluster analysis. Urgency and sleepiness formed independent clusters. Stress

and anxiety formed an identical cluster. Abdominal discomfort, abdominal distention, and abdominal pain formed an identical cluster on the basis of stimulatory conditions. The multiple regression analysis showed positive relation between ordinate scale and rCBF ($p<0.001$, Table 1). Abdominal discomfort, abdominal distention and abdominal pain showed significantly positive relation to rCBF in the right medial frontal gyrus (Brodmann's areas: BA46, 44 and 8), right superior temporal gyrus (BA42), right orbitofrontal gyrus (BA11), left inferior occipital lobe (BA19), left insula, left anterior cingulate gyrus (BA32), right thalamus and right cerebellum (Fig. 1-A). Perceived stress and anxiety showed significantly positive relation to rCBF in the left transverse temporal gyrus (BA41), left superior temporal gyrus (BA22), left precentral gyrus (BA6) and right insula (Fig. 1-B). Urgency revealed significantly positive relation to rCBF in the left inferior frontal gyrus (BA11), right insula and right pons (Fig. 1-C). Sleepiness showed significantly positive relation to rCBF in the left precentral gyrus (BA6) and left insula (Fig. 1-D).

Discussion

The most important part of this study is that visceral perception and emotion showed the correlation with prefrontal cortex. The prefrontal cortex is recently considered to be a projected area of visceral perception[4,5,20]. The signal from the visceral organ is projected to the prefrontal cortex from the lateral thalamic nucleus group[21]. The prefrontal area checks the given stimulation with experience and memory accumulated and may be the position which finally determines the meaning of stimulation; comfort or discomfort[22]. Luc et al[23]. reported the decreased neural activity of bilateral prefrontal cortex in the depressive state. Martinot et al[24]. reported hypometabolism of the prefrontal cortex in patients with depressive state and greater affection of the left prefrontal cortex. These differences vanished when the treatments were effective. Our data of positive relation between stress-anxiety and rCBF of the left superior temporal cortex are consistent with the earlier report. In patients with panic disorder, the dysfunction of left temporal pole is reported[25]. It is likely that the association cortex, especially prefrontal cortex, is important for the formation of emotion induced by visceral perception.

Several reports[4,5,20] indicated that the anterior cingulate cortex is activated with the stimulation of the colorectam. The results of this study is consistent with the earlier reports[4,5,20]. Moreover, increased rCBF in the anterior cingulate cortex is proportional to the visceral perception, suggesting this limbic cortex plays a major role in gastrointestinal symptoms in humans. Goldberg et al.[26] has advocated the idea the intermediation role of the supplementary motor cortex. The supplementary motor area may choose order and strategy of dealing with motion for a realization of the externality. The supplementary motor cortex is between the limbic cortex and the primary motor cortex. The relation between stress-anxiety and rCBF of the right prefrontal cortex in this study may indicate the preparation of motion against stress and avoidant behavior at the sensation of unease.

Blood et al.[27] reported increased blood flow of the cingulate cortex and the right orbitofrontal cortex at the time of pleasant feeling by the music stimulation. In contrast, the blood flow of left cingulate cortex and right parahippocampal cortex increases at the time of the unpleasant feeling[27]. Hamann et a[28]. reported that memory retained longer in the happy, unpleasant, or interesting than in the neutral feeling. Memory and intensity of the emotion was related to the activity of bilateral hippocampus and bilateral amygdala[27,28]. In this study, multivariate correlation analysis clarified that rCBF in the cingulate cortex, insula and thalamus correlated of abdominal discomfort, abdominal distention and abdominal pain. It is considered that this is based on the property of the emotion induced.

References

1) Drossman D. A.et al., Gastroenterology **83**, 529 (1982).
2) Fukudo S.et al., J. Clin. Gastroenteol **16**,133(1993).
3) Accarino A. M., Azpiroz F. and Malagelada J. R., Gastroenterology **113**, 415(1997).
4) Silverman D. H.et al., Gastroenterology **112**, 64 (1997).
5) Mertz H., et al., Gastroenterology **118**, 842 (2000).
6) Collins R. C., *Exploring brain functional anatomy with positron tomograpy*, New York: John Wiley & Sons 6-22, 1991.
7) Fox P. T., Mintun M.and Raichle M. E., Nature **323**, 806 (1986).
8) Fox P. T., Mintun M. and Raichle M. E., J. Cereb. Blood Flow Metab **8**, 642 (1988).
9) Fujiwara T. et al., Ann. Nucl. Med. **11**, 307 (1997).
10) Colsher J. G. Phys. Med. Biol. **25**, 103 (1980).
11) Kinhan P. E.and Rogers J. G., IEEE Trans. Nucl. Sci. **36**, 964 (1989).
12) Cherry S. R., Dahlbom M.and Hoffman E., J. Phys. Med. Biol. **37**, 779 (1992).
13) Friston K. J.et al., J. Cereb. Blood Flow Metab. **10** 458 (1990).
14) Friston K. J. et al., J. Cereb. Blood Flow Metab. **11**, 690 (1991).
15) Friston K. J.et al., J. Cereb. Blood Flow Metab. **13**, 5 (1993).
16) Friston K. J.et al., Hum. Brain Mapp. **1**, 10 (1994).
17) Friston K. J. et al., Hum. Brain Mapp. **2**, 165 (1995).
18) Friston K. J. et al., Hum. Brain Mapp. **1**, 189 (1995b).
19) Talairach J., Tournoux P., *Co-Planar stereotaxic atlas of the human brain* 37-110, Thieme Medical Publishers, New York, 1998.
20) Fukudo S.et al., *Proceeding of Brain-Gut 2000 Symposium*, in press.
21) Resenkilde C. E., Behav. Neural Biol. **25**, 301 (1979).
22) Dolan R. J.and Fletcher P. C., Nature **358**, 582 (1997).
23) Luc M., Bernard M.and Jean-Luc M., Psychiat. Res. **82**, 83 (1998).
24) Martinot J. L.et al., Am. J. Psychiat. **147**, 1313 (1990).
25) Meyer H. J. et al., Psychiat. Res. **98**, 133 (2000).
26) Goldberg G., Behav. Brain Sci. **8**, 567 (1985).
27) Blood J. A. et al., Nature Neurosci. **2**, 382 (1999).
28) Hamann S. B. et al., Nature Neurosci. **2**, 289 (1999).

Table1 Covariation of rCBF with rating of perception and emotion

emotion		region	Brodmann Area	Coodinates X	Y	Z	Z-score P<0.001
Positive correlations							
Cluster 1	Abdominal Discomfort, Distention and Pain	R medial frontal gyrus	46	34	44	14	4.02
				42	46	2	3.73
				44	48	14	3.44
			44	58	18	16	3.45
			8	36	22	42	3.90
		R superior temporal gyrus	42	66	-26	16	3.86
		R orbitofrontal cortex	11	34	30	-8	3.76
		L inferior occipital lobe	19	-22	-44	26	3.93
		L insula		-32	8	18	3.51
		L anterior cingulate gyrus	32	-2	40	18	3.44
		R thalamus		12	-22	12	3.34
		R cerebellum		6	-80	-40	3.60
				36	-70	-50	3.45
Cluster 2	Perceived Stress and Anxiety	L transverse temporal gyrus	41	-38	-28	26	4.22
		L superior temporal gyrus	22	-46	-24	6	3.80
		L precentral gyrus	6	-6	-24	66	3.41
		R insula		42	-14	22	3.85
				40	-20	14	3.60
Cluster 3	Urgency	L orbitofrontal gyrus	11	-34	28	-28	3.61
				-34	32	-18	3.34
		R insula		26	-30	26	3.66
		R pons		28	-26	-44	3.83
Cluster 4	Sleepiness	L precentral gyrus	6	-48	6	48	3.55
		L insula		-32	6	22	4.33
				-44	-4	4	3.43

Coodinates refer to location in stereotaxic space19)

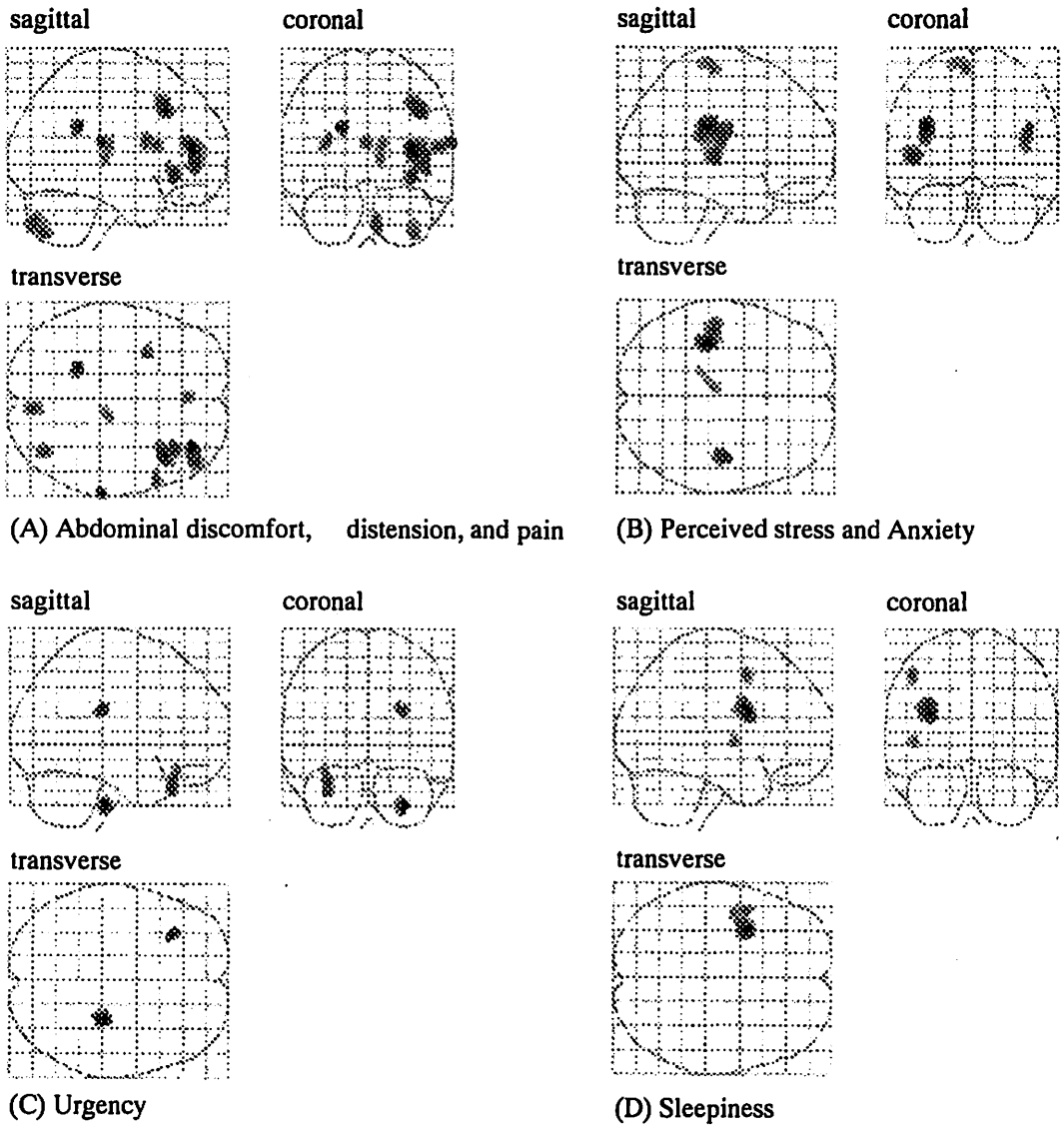

Statistical parametric maps (SPMs) for increasing rCBF with rating of perception and emotion

Fig. 1. The multiple regression analysis showed positive relation between ordinate scale and rCBF. Coordinates refer to location in stereotaxic space[19]. Voxels are thresholded at $p<0.001$ ($Z=3.30$, uncorrected). (A) Abdominal discomfort, abdominal distention and abdominal pain showed significantly positive relation to rCBF in the right medial frontal gyrus (Brodmann's areas: BA46, 44 and 8), right superior temporal gyrus (BA42), right orbitofrontal gyrus (BA11), left inferior occipital lobe (BA19), left insula, left anterior cingulate gyrus (BA32), right thalamus and right cerebellum (B) Perceived stress and anxiety showed significantly positive relation to rCBF in the left transverse temporal gyrus (BA41), left superior temporal gyrus (BA22), left precentral gyrus (BA6) and right insula. (C) Urgency revealed significantly positive relation to rCBF in the left inferior frontal gyrus (BA11), right insula and right pons. (D) Sleepiness showed significantly positive relation to rCBF in the left precentral gyrus (BA6) and left insula.

IV. 8. Recall of Embedded Words from a Story: A PET Study

Ohtake H., Fujii T., Okuda J., Tsukiura T., Kawashima R., Ito M.**, Fukuda H.*** and Yamadori A.*

Section of Neuropsychology, Division of Disability Sciences,
New Industry Creation Hatchery Center,*
*Division of Nuclear Medicine, Cyclotron and Radioisotope Center**,*
Department of Nuclear Medicine and Radiology, Institute of Development, Aging and Cancer,
*Tohoku University****

Introduction

To establish an episode as a correct memory, components of the episode must be integrated into a unity based upon appropriate contextual information such as time and place. These contextual memory functions are thought to be related with the prefrontal areas on the basis of both lesion studies[1,2] and neuroimaging studies.

In the case of retrieving more complex consecutive events, thematic linkage among each component may play a role in correct retrieval. Although contextual memory has been the subject of several neuroimaging studies, little is known about neural basis of this thematic context. To clarify this problem, we used PET and compared neural activities during retrieval of words from specified stories with those during retrieval of words without any thematic context.

Methods

Subjects

Eight healthy right-handed male volunteers participated in the study. Mean age was 22.1years (range 19-25). All subjects were informed of the nature of the experiments and gave written informed consent.

Procedure

Before PET scan, the subjects memorized 15 short stories, each describing one scene and containing information about time, person, animal, place, and object. For example, "One rainy morning, a girl heard a mewing at her feet in the park. There was a kitten. She took it home and belled it." The stories were presented auditorily until the subjects could repeat all of them correctly.

During PET scan, the subjects took part in three different tasks: the story recall, item

recall, and word generation tasks. Order of tasks was counterbalanced across the subjects. Each stimulus was presented through a pair of earphones. In the story recall task, the first phrase of a story (information about time) was presented. The subjects were asked to recall the story starting with that phrase and to say three items included in it (animal, place, and object). In the item recall task, names of category (same as in the story recall task) were presented and the subjects were required to retrieve as many items relevant to the category name from the stories they previously learned as possible. In the word generation task, names of category differing from those used in the item recall task (for example, sports) were presented and the subjects were asked to retrieve as many words belonging to the category name as possible.

PET data acquisition

The regional cerebral blood flow (rCBF) was measured using a SET2400W PET scanner (Shimadzu). A bolus injection of 180MBq of 15O labeled water was done through a forearm canula. Each PET data acquisition time was 90 sec and all tasks were started 30 seconds after the time of bolus injection.

PET data analysis

All rCBF images were transformed into the standard anatomical format using Human Brain Atlas system[3] and each subject's MRI T1 weighted images. The data were analyzed with statistical parametric mapping (SPM99; Wellcome Department of Cognitive Neurology, London, UK) executed in MATLAB (Mathworks, Sherborn, Mass., USA). The images were transformed into standard stereotactic space[4]. All standardized rCBF images were smoothed using a Gaussian filter set at 12 mm full-width at half-maximum. The rCBF-equivalent measurements were adjusted to a global CBF mean of 50 ml/dl/min. Contrasts of the condition effects of each voxel were assessed using the t statistics, giving a statistical image (SPMt transformed into an SPM z) for each contrast. The chosen threshold of significance for main effects of conditions was set at $P < 0.001$ (uncorrected for multiple comparison, K>50 voxels).

Results

Behavioral results

The mean number of correctly retrieved items was 21.6 (S.D. = 4.93, Max = 27) for the story recall task, 26.6 (S.D. = 2.51, Max = 45) for the item recall task, and 26.6 (S.D. = 4.7) for the word generation task.

Areas activated associated with item recall

To evaluate brain activity associated with episodic retrieval of previously learned

items, we compared all the recall tasks with the word generation task. In addition, this contrast was masked with two contrasts (i.e., the word recall task - the word generation task, and the story recall task - the word generation task) to exclude voxels other than common activated areas between these two contrasts (threshold for masking $P<0.05$). Results showed strong activations in bilateral precunei and posterior cingulate gyri, the left lateral parietal lobe and weak activations in the left frontal pole, right dorsolateral prefrontal cortex and right lateral parietal lobe (Figure 1, Table 1).

Areas activated associated with story recall

To clarify neural substrates related to the recall and utilization of previously learned stories to retrieve words, we compared the story recall task with the item recall task. This comparison revealed significant increases in rCBF in the right frontal pole, the left ventrolateral prefrontal area and supramarginal gyrus, bilateral supplementary motor areas and superior and middle temporal gyri (Figure 2, Table 2).

Discussion

Activated areas associated with item recall

The right dorsolateral frontal area and the left frontal pole, bilateral medial parietal lobes extending to posterior cingulate gyri and lateral parietal lobes were activated during recalling previously learned items. This result is in accordance with results of many activation studies on episodic retrieval. The right dorsolateral frontal lobe is commonly activated in episodic recall tasks and it is thought to be related to monitoring and manipulating retrieved items[5]. The medial parietal lobes seem to be related with visual imagery evoked during recall processes[6]. The left prefrontal area is known to be related to episodic encoding processes[7]. But, this area has also been activated in relatively complex episodic retrieval tasks which require reflective processes[8]. The left prefrontal activation in our study might be related to this reflective demands because of the complexity of our materials to be remembered.

Brain regions involved in thematic context

Our result shows that retrieval of thematic context (i.e., stories) mobilized the neural network including the right frontal pole (BA10) and left ventrolateral frontal areas (BA45, 47), left supramarginal gyrus, bilateral SMA and lateral temporal lobes. Shergill et al. reported that auditory verbal imagination of a narrative causes activation in bilateral superior temporal gyri, SMA, inferior frontal gyri including frontal operculum and inferior parietal lobule[9]. This general overlap with our results suggests that auditory imagery was recruited as a strategy to recall previously learned stories. These areas are also known to be associated with storage and rehearsal process of verbal working memory[10].

Another and the most strong activation was detected in the right frontal pole (BA 10). This activation may be interpreted as representing various processes such as generation of thematic frameworks from key phrases, evocation of auditory imagery, regulation of searching, and evaluating words retrieved depending upon specified thematic context. BA10 of the right prefrontal lobe has also been reported to be activated in association with retrieval mode[11] and retrieval success[12]. So, this activation may be related with these processes depending on thematic context.

References

1) Janowsky J. S., Shimamura A. P. and Squire L. R., Neuropsychologia **27** (1989) 1043-1056.
2) Milner B., Corsi P. and Leonard G., Neuropsychologia **29** (1991) 601-618.
3) Roland P., Graufelds C. J. and Wahlin J., Hum. Brain Map. **1** (1994) 173-184.
4) Talairach J. and Tournoux P., Co-Planar stereotaxic atlas of the human brain. Stuttgart: Theime; 1988.
5) Fletcher P. C., Shallice T., Frith C. D. et al., Brain **121** (1998) 1249-1256.
6) Fletcher P. C., Shallice T., Frith C. D. et al., Brain **119** (1996) 1587-1596.
7) Tulving E., Kapur S., Craik F. I. et al., Proc. Natl. Acad. Sci. U. S. A. **91** (1994) 2016-2020.
8) Nolde S. F., Johnson M. K. and Raye C. L. Trends Cognit. Sci. **2** (1998) 399-405.
9) Shergill S. S., Bullmore, E. T., Brammer M. J. et al., Psychol. Med. **31** (2001) 241-253.
10) Smith E. E. and Jonides J. Science **283** (1999) 1657-1661.
11) Duzel E., Cabeza R., Picton T. W. et al., Proc. Natl. Acad. Sci. U. S. A. **96** (1999) 1794-1799.
12) Rugg M. D., Fletcher P. C., Frith, C. D. et al., Brain **119** (1996) 2073-2083.

Table 1. Regions activated in relation with item recall.

Region of activation	Left/right	BA	Coordinates	Zscore
Superior frontal gyrus	R	8	-36, 50, 13	4.33
Middle frontal gyrus	L	10	33, 15, 46	4.19
Precuneus	B	7, 31, 23	11, -61, 32	7.72
Supramarginal gyrus	L	40	-41, -56, 39	8.12

L = left; R = right; B = bilateral.

Table 2. Regions activated in relation with story recall.

Region of activation	Left/right	BA	Coordinates	Zscore
Superior frontal gyrus	R	10	15, 60, 19	4.43
Inferior frontal gyrus	L	45	−50, 35, 4	3.94
	L	47	−45, 20, −4	3.54
Medial frontal gyrus	R	6	6, −12, 64	3.73
	L	6	−25, 0, 64	3.51
Superior and middle temporal gyrus	R	22, 21	53, −3, −16	4.37
	L	21	−58, −34, 0	4.06
	L	22	−60, −11, 7	3.94
Supramarginal gyrus	L	40	−58, −51, 25	3.56

L = left; R = right; B = bilateral.

Figure 1

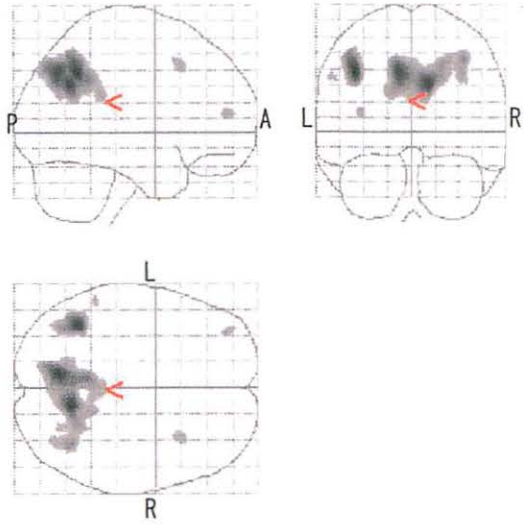

Figure 1. Regions related with item recall (height threshold P<0.001, k>50 voxels, uncorrected).

Figure 2

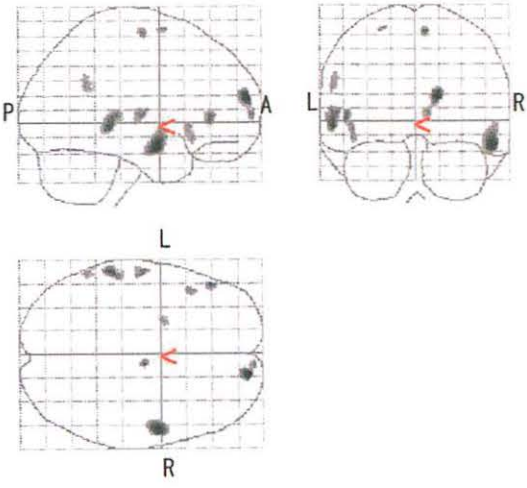

Figure 2. Regions related with story recall (height threshold P<0.001, k>50 voxels, uncorrected).

IV. 9. Localization of ^{18}F-FDG in a Mouth Cavity Using Oral Intake PET Study

Ozaki K., Rikimaru H., Yamaguchi K., and Itoh M.

Cyclotron and Radioisotope Center, Tohoku University

Introduction

[^{18}F]-2-deoxy-2-fluoro-D-glucose (FDG), which has positron emitter, is an analogue of glucose. The FDG is accumulated to high metabolic organs or tissues. We can observe accumulated FDG as a tracer for evaluation of organ or tissue glucose metabolism by Positron Emission Tomography (PET). The FDG-PET method is widely applied to investigate physiological functions of the organs or tumor detection in vivo in human.

Ingestion of foods is one of the most basically behavior of the creatures. Especially a sugar is the most important material for creatures as energy sources. However, sugar reception mechanism by gustatory receptors in the mouth is not still clearly. Because binding force between receptors and ligands is very weak and many kind of receptor exist, we can hardly separate and purify the receptor proteins. So it is difficult to investigate the taste receptors. Recently some kind of candidate receptor proteins is reported[1-3]. But there are few reports about receptor function and the properties of taste stimuli localization to specific areas of oral cavity.

We attempt to apply the FDG oral intake method to identification of the glucose receptor localization.

Materials and Methods

Seven normal male volunteers (mean age 29.4 ± 3.3 y.o.) were examined using ^{18}F-FDG and SET-2400W (Shimadzu, Japan) in three-dimensional data acquisition mode.

The Volunteers took in the FDG 0.37 ± 0.02 MBq (10 ± 0.5 μCi) in 10 ml water or sucrose water by 30 seconds gargling. After gargling, solution was immediately taken out from the mouth. A sucrose concentration is 100 mM or 500 mM for observation of competitive inhibitions against the FDG. After that they immediately took 30 ml water gargling for twice to wash out non-specific binding the FDG.

Pet scanning time is 15 minutes for emission scanning immediately after taking the FDG. Normally we have one emission scanning, but some case has 3 times. Transmission scanning is performed last 15 minutes using a ^{68}Ge/^{68}Ga external rotating line

source (370 MBq). PET image data were reconstructed by 3D back projection algorithm using a supercomputer SX-4 (NEC, Japan)[4].

Results and Discussion

Figure 1 shows one of the typical examples of the PET scan data. We applied about 0.37 MBq for each volunteer. But almost 70 % of administration dose is washed out from the mouth. It is means that 30 % (almost 0.11 MBq) of FDG was remained of their mouth. It is reasonable result that we estimated from the figures. Left hand side of figure 1 is a copy of PET console display. Right hand side is the 3D image made from the left hand side image plus transmission image. Red one is the tongue or the mouth cavity. Actually it is not so easy to determine the anatomical location of the FDG, but it looks like a tongue. This result shows that some FDG were trapped in the mouth cavity.

Figure 2 shows the summary of the data. The sucrose 0 mM means only water and the FDG. The FDG dose of mouth cavity is decrease on 50 mM and 100m M sucrose data as against no sucrose one. If it is true, it means that there is possibility that the FDG is competitive inhibition material for sucrose binding receptor. But we cannot apply for statistical analysis because number of test is not enough. Anyway now we can observe the FDG binding localization in the mouth cavity. Hopefully it is reflected sugar binding receptor. We need to have another data to confirm.

Figure 3 shows that a time course of remaining the FDG in the mouth cavity. We have 2 data of this protocol. Both of them have no deference depending of the time for about 30 minutes. It means that the FDG is hardly removed from receptor or something another binding site in the mouth cavity.

We attempted to make a visualization of taste receptor localization in the mouth cavity. We can show that one of the possibility for this purpose using the FDG-PET. If it is confirmed, we can apply this method not only to investigate receptor characterizations but also to diagnose the illness of the taste reception.

References

1) Huang L. et al., Nat. Neurosci. **12** (1999) 1055-62.
2) Ishimoto H., Matsumoto A.and Tanimura T., Science **289** (2000) 116-9.
3) Ozaki M.et al., Eur. J. Biochem. **230** (1) (1995) 298-308
4) Fujiwara T. et al., Ann. Nucl. Med. **11** (1997) 307-13.

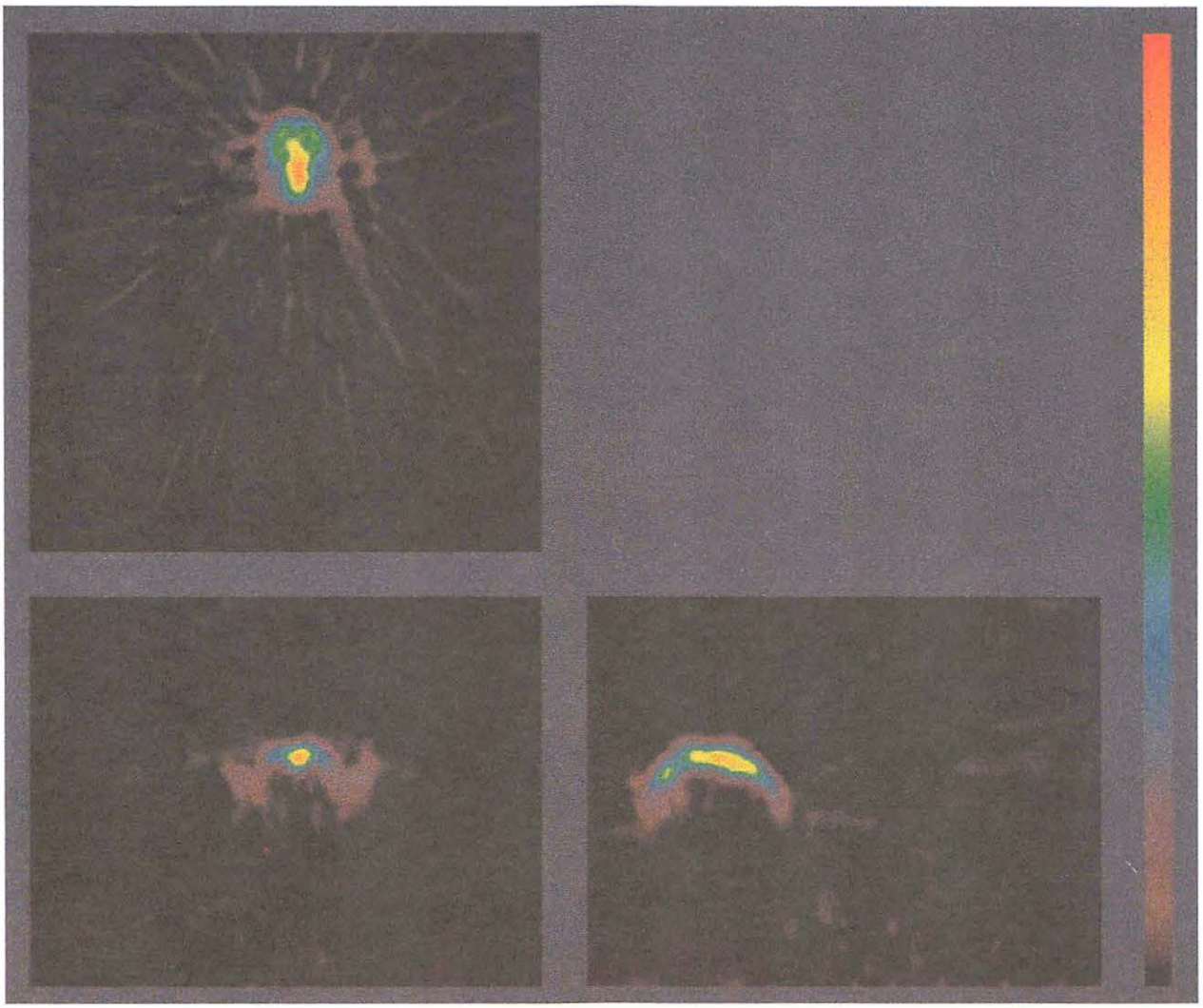

Fig. 1(a). The tongue and the mouth cavity image of oral intake ^{18}F-FDG.

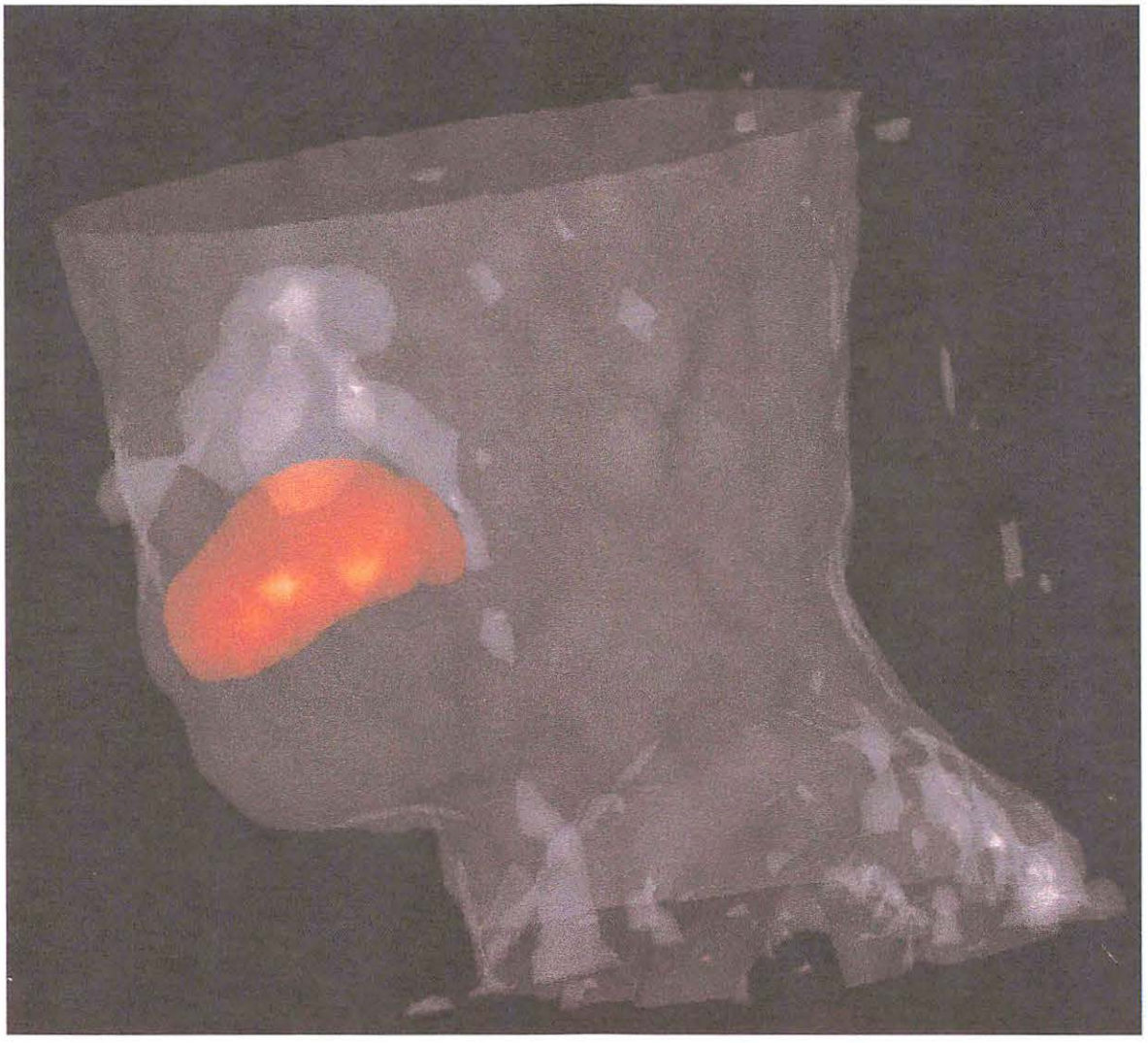

Fig. 1(b). The tongue and the mouth cavity image of oral intake ^{18}F-FDG.

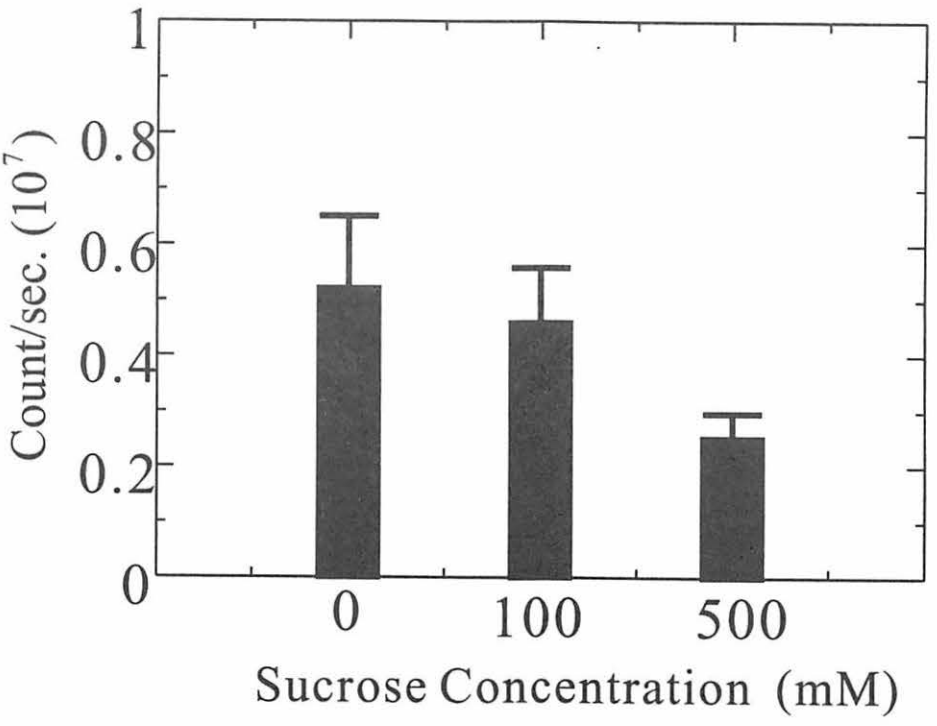

Fig. 2. The result of the analysis. Axis of ordinates shows the data of PET counts (multiply seventh power of ten) per seconds. Axis of abscissas shows the concentration of sucrose. N=15 (0 mM sucrose), N=5 (50 mM sucrose), N=3 (100 mM sucrose). Error bar shows standard deviation.

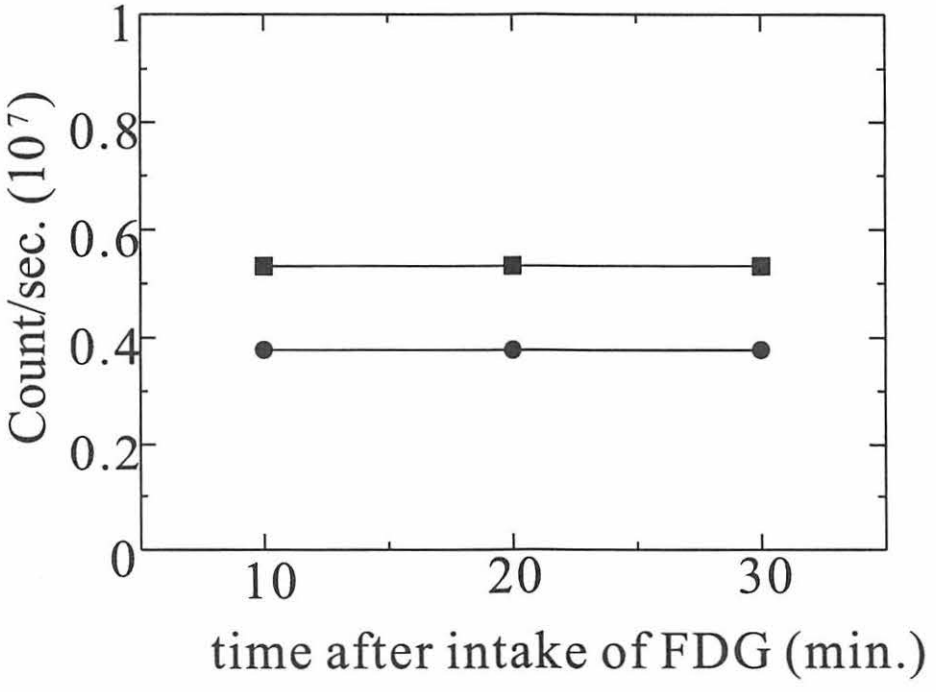

Fig. 3. Time course of remaining FDG in the mouth cavity.

IV. 10. Fluorodeoxyglucose Template for Statistical Parametric Mapping

Rikimaru H., Itoh M., Yamaguchi K., Tashiro M., Watanuki S., Miyake M., Watanabe M.*

Division of Nuclear Medicine Cyclotron and Radioisotope Center, Tohoku University
*Department of Aging and Geriatric Dentistry, Tohoku University Graduate School of Dentistry**

Introduction

Statistical parametric mapping[1-3] (SPM99; the Wellcome Department of Cognitive Neurology, London, UK) is a commonly-used software package for analysis of functional brain images taken by imaging techniques such as positron emission tomography (PET) and functional magnetic resonance imaging (fMRI). SPM combines the general linear model and the Gaussian fields to make statistical inferences about regional effects[4,5] First, to analyse such functional images, we must transform them into a standard space[6,7] The stereotactic space is based on 152 brains from Montreal Neurological Institute. The spatial normalization involves linear and nonlinear three-dimensional transformations to match each scan to a reference image that is already conformed to the standard space. SPM contains reference images such as MRI, PET and SPECT for use as templates for spatially normalizing images to the same stereotactic space. The PET template was created by Oxygen-15 labeled water images (CBF images) from 12 subjects spatially normalized to International Consortium for Brain Mapping (ICBM).

Recently, brain-mapping studies using FDG-PET and SPM have been reported[8]. Until now, there has been no other way to normalize FDG-PET images than to use CBF image as template, since FDG template is not included in SPM. Some errors might occur in normalizing FDG-PET images by using CBF template, because there are some differences between FDG and CBF images in contrast of images and in distribution of tracer.

Purpose in our study is to create an averaged FDG-PET image for use as a template for spatial normalization.

Materials and Methods

Five healthy male subjects aged 23-35 (mean ± SD: 27.0 ±4.7y) volunteered the study. Written informed consent was obtained from each subject after a full explanation of the experiment. All subjects refrained from eating and drinking for at least four hours before the PET study. They were requested to remain silent as control throughout the study starting

from 5 min prior to the injection until the end of the study. All subjects kept sitting posture in a dimly room for 30 min just after intravenous injection of approximately 46MBq (mean ± SD: 45.9 ± 3.7MBq) of FDG. PET scans were obtained on a 3D-PET scanner (SET-2400W, Shimadzu Co., Japan) with a spatial resolution of 4.5mm (axial) and 3.9mm (trans-axial) at full-width half-maximum at the center of the field of view9). Sixty-three slices were produced over a 20.0cm axial field of view. After voiding, they were positioned on a PET couch and head and neck images were acquired starting 35 min post-injection by obtaining two consecutive 5-min images from the subject's head to below the lower jaw. Tissue attenuation of annihilation gamma rays was corrected by post-injection transmission scans using a rotating ^{68}Ge/ ^{68}Ga-line source. T1-weighted MR images (Signa 1.5T, General Electric Co., USA) of the brain were also obtained in each subject.

Acquired PET and MRI data were converted to Analyze format (Mayo clinic, USA), then image processing and analysis were carried on SPM99. PET images of each subject were first registered to the T1-weighted MR images using SPM, and spatially transformed using the same transformation. These PET and MR images from five subjects were averaged and smoothed using 8mm FWHM Gaussian filter. This is the way to create homemade FDG template.

To assess the FDG template image analyses were performed. We put the seventeen marks to representative neural structures: the cerebellum, pons, midbrain, insula, anterior commissure, posterior commissure, central sulcus, parietal region, gyri parahippocampi, gyri rectus and gyri lingualis in coregistered PET and MRI images of each subject. The marked MR images of subjects were spatially transformed. The marked PET images of each subject were also spatially transformed in three different way such as homemade template, CBF template contained in SPM and using the same parameter of MR images. We checked and compared the coordinate of the MR and PET images that spatially normalyzed in three different ways.

Results

FDG template is shown in Fig. 1. There were no obvious morphological differences between our homemade template and the templates contained SPM. However, there were some minor differences in contrast and distribution of tracer. MR and PET images normalized using different templates are shown in Fig. 2. Morphological differences were found in the PET image normalized using CBF template between other normalized images. The PET image normalized using CBF template seemed to expand along Z-axis and showed asymmetry especially in the coronal section (Fig. 3). The locations of the marks were also different from other images (Fig. 2).

Differences in the location of each mark between normalized MR image and other images are summarized in Table 1. There was no difference in coordinates of each mark between normalized MR images and PET images using the same parameter of MR images.

Some differences were found in coordinates of each mark between normalized MR images and PET images using homemade FDG template, while many differences were found in coordinates of each mark between normalized MR images and PET images using CBF template.

Discussion

We created an averaged and smoothed FDG-PET image from five subjects as a template for spatial normalization of images to the same stereotactic space. Remarkable morphological differences were not found among those templates. However there were certain differences in contrast and distribution of radioisotope. These findings suggest that different radio-tracers give different contrast and distributuin. Then, images of FDG and CBF are not always same.

Morphological differences were also found in the FDG-PET images normalized using CBF template between other normalized images. The PET image normalized using CBF template tended to expand along Z-axis and showed asymmetry especially in the coronal section (Fig. 3). The locations of the marks were also different from other images (Fig. 2). In general, FDG is accumulated in cells, while Oxygen-15 labeled water distributes in blood vessels. These physiological differences might be affected by the radioactivitiy from sinus venosus.

Although SPM is widely accepted to analyze functional images such as PET and fMRI in the brain, templates for other tracers have not yet been validated. Our data indicate that each template corresponds to tracer is required to brain PET images correctly. Another PET and MR images from normal subjects are necessary to complete the FDG template.

In conclusion, we propose to create each template corresponds to tracers to avoid errors in analyses or normalize in using SPM.

References

1) Friston K. J., Frith C. D., Liddle P. F. et al. *Cereb. Blood Flow Metab.* 10 (1990) 458-466.
2) Friston K. J., Frith C. D. Liddle PF, et al. *J. Cereb. Blood Flow Metab.* 13 (1993) 5-14.
3) Friston K. J., Ashburner J, Frith C. D., et al. *Hum. Brain Mapp.* 3 (1995a) 165-189.
4) Friston K. J., Frith C. D., Liddle P. F , et al. *J. Cereb. Blood Flow Metab.* 11 (1991) 690-699.
5) Friston K. J., Worsley K. J., Frackowiak R. S., et al. *Hum. Brain Mapp.* 1(1994) 210-220.
6) Talairach J., Tournoux P. Co-Planar stereotaxic atlas of the human brain. Stuttgart, Thieme, 1988.
7) Friston K. J., Holmes A., Worsley KJ, et al. *Hum. Brain Mapp* 1 (1995b) 189-210.
8) Tashiro M., Freimut D. J , Michael JR, et al., *Psycho-Oncology* 9 (2000) 157-163.
9) Fujiwara T., Watanuki S., Yamamoto S., Miyake M., Seo S., Itoh M., *et al.*, *Ann Nucl Med* 11 (1997) 307-313.

Table 1. Differences in the location of each mark between normalized MR image and other images (mm). R = right, L = left, M = middle, Ant = anterior, Post = posterior

		MRI parameter			FDG template			Water template		
		X	Y	Z	X	Y	Z	X	Y	Z
R-gyri parahippocampi	average	0.0	0.0	0.0	0.0	-0.4	0.0	-0.6	-2.2	-3.8
	SD	0.0	0.0	0.0	0.0	0.9	2.1	1.9	4.9	2.8
L-gyri parahippocampi	average	0.0	0.0	0.0	0.4	-0.4	-0.4	2.8	-2.4	-3.8
	SD	0.0	0.0	0.0	0.9	0.9	0.9	1.8	2.8	1.9
R-cerebellum	average	0.0	0.0	0.0	0.0	0.0	0.0	-0.6	0.0	-5.6
	SD	0.0	0.0	0.0	0.0	0.0	0.0	1.3	2.3	4.2
L-cerebellum	average	0.0	0.0	0.0	0.0	-0.4	0.0	2.0	-0.4	-5.2
	SD	0.0	0.0	0.0	0.0	0.9	0.7	2.0	3.4	3.5
M-cerebellum	average	0.0	0.0	0.0	0.4	0.0	0.0	1.8	-2.4	-6.0
	SD	0.0	0.0	0.0	0.5	0.0	0.0	2.5	2.5	4.6
gyri lingualis	average	0.0	0.0	0.0	0.8	0.0	0.2	2.8	-2.6	-4.8
	SD	0.0	0.0	0.0	1.3	0.0	0.4	2.8	4.6	3.4
R-insula	average	0.0	0.0	0.0	0.0	0.0	0.2	0.2	-1.6	-2.2
	SD	0.0	0.0	0.0	0.0	0.0	0.4	1.8	2.8	1.8
L-insula	average	0.0	0.0	0.0	0.0	0.2	0.4	2.8	0.6	-3.0
	SD	0.0	0.0	0.0	0.0	0.4	0.9	1.9	2.6	5.9
R-central sulcus	average	0.0	0.0	0.0	0.0	0.0	0.0	-1.4	-1.2	-2.0
	SD	0.0	0.0	0.0	0.0	0.0	0.0	1.5	2.3	2.7
L-central sulcus	average	0.0	0.0	0.0	0.0	0.0	0.4	4.0	-0.2	-2.8
	SD	0.0	0.0	0.0	0.0	0.0	0.9	2.8	1.8	3.3
Ant commissure	average	0.0	0.0	0.0	0.0	-0.6	0.0	0.6	-2.2	-3.2
	SD	0.0	0.0	0.0	0.0	1.3	0.0	1.5	3.1	1.9
Post commissure	average	0.0	0.0	0.0	0.0	0.0	0.0	1.6	-0.8	-1.0
	SD	0.0	0.0	0.0	0.0	0.0	0.0	2.1	4.1	1.7
pons	average	0.0	0.0	0.0	0.0	0.0	0.0	0.8	1.2	-5.4
	SD	0.0	0.0	0.0	0.0	0.0	0.0	1.3	2.4	4.7
midbrain	average	0.0	0.0	0.0	0.0	0.0	0.0	0.2	10.0	-4.8
	SD	0.0	0.0	0.0	0.0	0.0	0.0	0.4	23.5	4.0
gyri rectus	average	0.0	0.0	0.0	0.4	0.0	0.0	1.6	-0.6	-2.4
	SD	0.0	0.0	0.0	0.9	0.0	0.0	2.3	1.7	2.7
parietal	average	0.0	0.0	0.0	0.8	0.2	0.0	1.2	-0.6	2.2
	SD	0.0	0.0	0.0	1.8	0.4	0.0	3.4	1.9	4.3

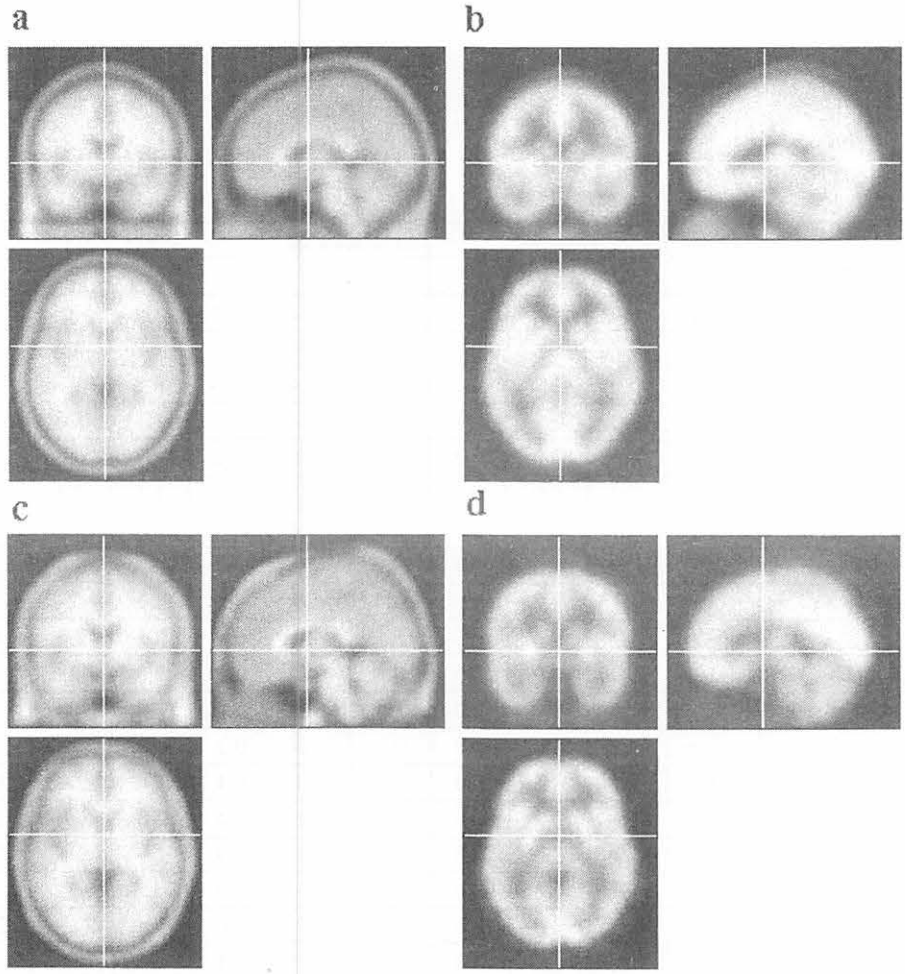

Fig. 1 MR and PET templates.

a T1 weighted image contained in SPM package as a template.

b CBF image contained in SPM package as a template.

c Averaged and smoothed MR image from five subjects using 8mm FWHM Gaussian filter.

d Averaged and smoothed PET image from five subjects using 8mm FWHM Gaussian filter.

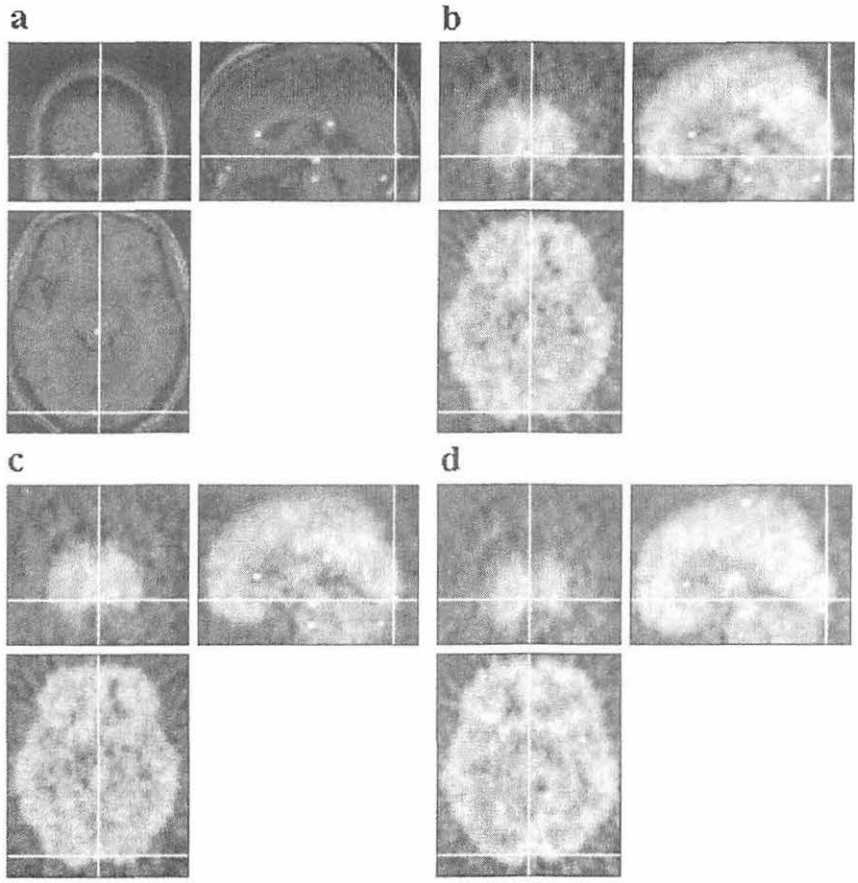

Fig. 2 Normalized images in one subject using different templates.
a MR image normalized using T1 weighted template contained SPM.
b FDG-PET image normalized same parameter of MR image.
c FDG-PET image normalized our homemade FDG template
d FDG-PET image normalized using CBF template contained SPM.

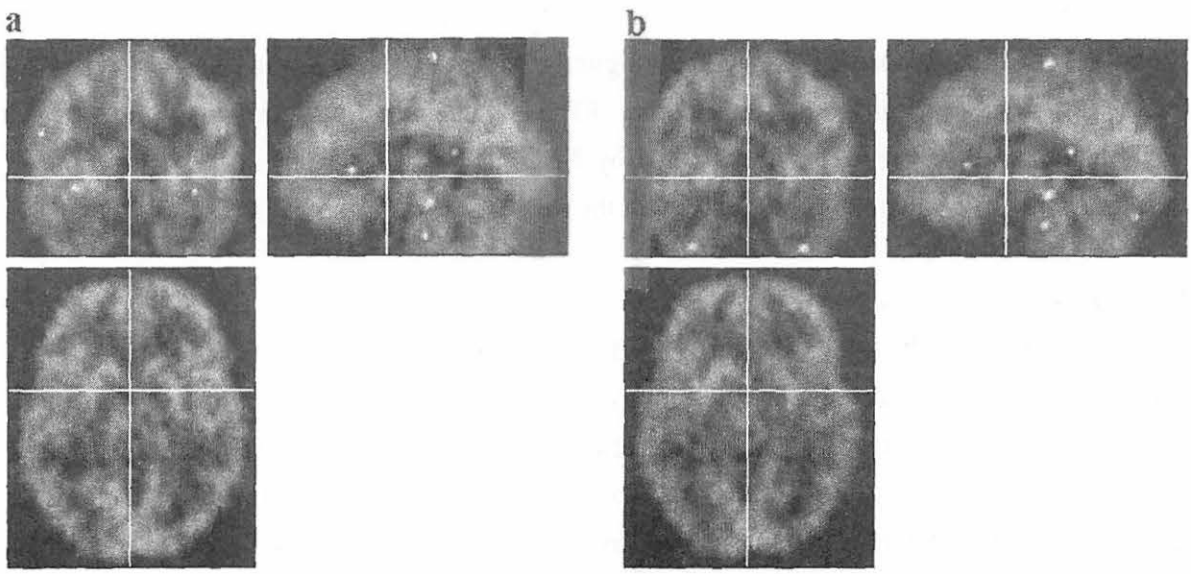

Fig. 3 Normalized images in one subject using different templates.
a FDG-PET image normalized our homemade FDG template
b FDG-PET image normalized using CBF template contained SPM.

IV. 11. Measurement of Salivary Radioactivity after Injection of Fluorodeoxyglucose

*Rikimaru H., Ozaki K., Itoh M., Tashiro M., Watanuki S., Miyake M., Yamaguchi K., Watanabe M.**

Division of Nuclear Medicine Cyclotron and Radioisotope Center, Tohoku University
*Department of Aging and Geriatric Dentistry, Tohoku University Graduate School of Dentistry**

Introduction

Positron emission tomography (PET) with a radiolabeled glucose analog, fluorodeoxyglucose (FDG) is an important tumor imaging modality, particularly for staging of cancers and in the differentiation of post-therapy changes from residual or recurrent tumors. It is therefore important to accurately define patterns of physiological uptake of FDG to avoid false-positive results that may lead to inappropriate patient management. Although FDG has been widely used as a PET tracer, the literature still suffers from a paucity of data relating to the normal tissue distribution of FDG. Knowledge of this normal distribution is vital to differentiation of pathological from physiological tracer uptake. It is necessary to differentiate the normal FDG distribution from the abnormal uptake as abnormal artifactual accumulation reported by Barrington et al.[1] and Segall2) is often seen in the head and neck region.

We have previously reported the normal distribution of FDG after gum chewing. We found the intense glucose uptake in the tongue, masticatory muscles and salivary glands3) However, it is not fully known whether FDG is excreted into saliva or not. High accumulation in the tongue may be affected by FDG included in the saliva. The purpose of this study was to evaluate the radioactivity in the saliva after injection of FDG.

Materials and Methods

Thirteen healthy male subjects aged 21-32 (mean ± SD: 26.4 ±3.6y) with normal masticatory function and complete dentitions volunteered for the study. Written informed consent was obtained from each subject after a full explanation of the experiment. All subjects refrained from eating and drinking for at least four hours before the test. They were randomly divided into two groups. The first group (6 subjects) was requested to remain silent as control throughout the study starting from 5 min prior to the injection until the end of the study. The second group (7 subjects) was asked to keep on chewing one sheet of chewing gum (3g, apple mint, Ezaki Glico Co, Japan). All subjects performed each task for

30 min just after intravenous injection of approximately 40MBq of FDG. All tasks were performed with sitting posture in a dimly-lit room. The mixed saliva of each subject was sampled by spitting to disposable cup every 5 min (total seven times sampling) after injection of FDG. The Radioactivity of sampled saliva was measured for 60 sec using Well counter (Shimadzu Inc., Japan).

The salivary radioactivity was normalized for both the amount injected and the weight of sample according to the following.

$$\text{Radioactivity (cps/g/mCi)} = \frac{\text{Decay corrected saliva concentration}}{\text{Weight / Injected dose}}$$

The statistical significance of differences between chewing and resting was examined with a Mann-Whitney U test. A p value of less than 0.05 was considered significant.

Results

The salivary radioactivity in control and chewing group is summarized in Figure 1. The salivary radioactivity in the control group was immediately increased 5 min after the injection of FDG, and showed a plateu pattern 10 to 30 min after the injection. However, the degree of the salivary radioactivity varied among subject. The salivary radioactivity in chewing group was also immediately increased 5 min after the injection, and decreased 15 to 30 min after the injection. The salivary radioactivity level in control and chewing group amounted to 1/60-1/20 of arterial radioactivity. The salivary radioactivity in control group was generally higher than that in chewing group, and there was a statistically significant difference ($p<0.05$) at 15, 20, 25 and 30 min after injection, when combined data were compared.

Discussion

FDG metabolism regarding the salivary glands has not been fully investigated, although the enhanced uptake of FDG into brain, cardiac muscle and skeletal muscle is well recognized. The results of our study confirm that the saliva include the radioactivity after the injection of FDG. FDG may be excreted through the salivary glands. Saliva is made from blood plasma in the salivary glands, which generally include glucose 1/100 to 1/50 of blood sugar4,5). As the salivary radioactivity level in the control and chewing group amounted to 1/60-1/20 of arterial radioactivity in our experiment, FDG may be also excreted in the same way of blood sugar. In this study, we used previous data regarding arterial radioactivity that measured other experiment as we omitted blood sampling.

The amount of salivary radioactivity was 7-10 cps/g/mCi and 4-6 cps/g/mCi in the control and chewing group respectively, while tissue radioactivity of the tongue muscle was 100-150cps/g/mCi and 300-600cps/g/mCi on PET image in the control and chewing group

respectively. Tissue count on PET images would not be affected the radioactivity excreted into saliva.

In our study, the salivary radioactivity in chewing were lower than that in control group, and there was a statistically significant difference ($p<0.05$). It is widely known that glucose concentration in saliva excreted by stimulation such as taste and chewing, decreases as glucose consumption increase in salivary glands.

In conclusion, we found that, the saliva include the radioactivity after the injection of FDG, however, tissue count on PET images would not be affected the radioactivity excreted to saliva. The level of salivary radioactivity would vary depending on the condition of saliva excretion.

References

1) Barrington S. F. Maisey M. N., Nucl. Med. **37** (1996) 1127-1129.
2) Segall G. M., J. Nucl. Med. **37** (1996) 1918.
3) Rikimaru H., kuchi M., Tashiro M., Itoh M., Ido T., Watmanabe M., CYRIC Annual Report IV1996: 153-157.
4) Darwazeh A. M., Mac Farlane T. W., McCuish A., LameyPJ., Clin. Chem. **38** (1992) 1956-1600.
5) Ginsberg BH An overview of minimally in vasive technologies. Clin. Chem. **38** (1992) 1596-1600.

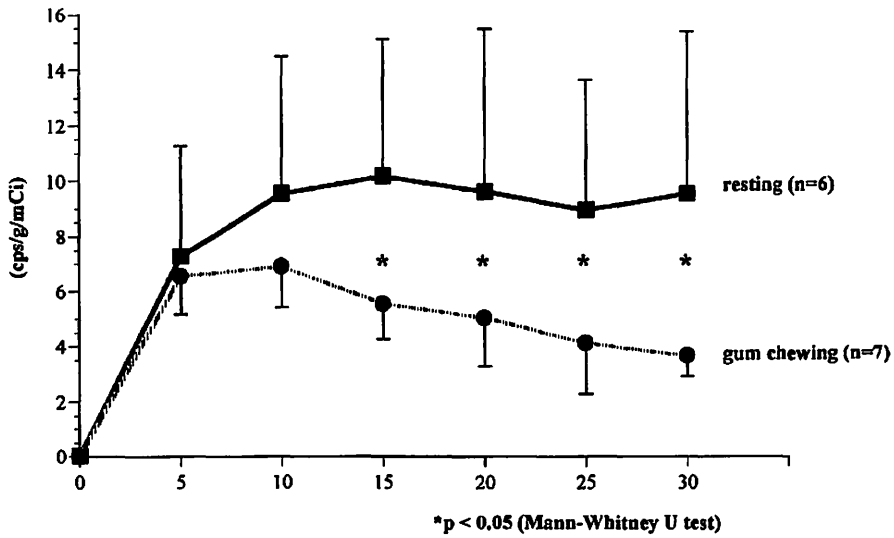

Fig. 1 The radioactivity of saliva in resting and chewing group. The statistical signifincance of diffrences between chewing and resting was examined with a Mann-Whitney U test. *Statistically significant at $p<0.05$.

IV. 12. PET Imaging Based on the Fourier Rebinning Algorithm

Oishi Y., Ishii K., Yamazaki H., Matsuyama S., Watanuki S., Itoh M.*, and Orihara H.**

Department of Quantum Science and Energy Engineering, Tohoku University
*Cyclotron and Radioisotope Center, Tohoku University**

Introduction

The quest for increased sensitivity in positron emission tomography (PET) has led to the interest of acquisition of all possible coincidence lines in a gantry. It has become feasible with the advent of commercial scanners equipped with retractable septa. This technique significantly improves the sensitivity over conventional slice-orientated methods (2-D PET), but the time for image reconstruction is much longer. This drawback must be solved in actual clinical application based on dynamic imaging or whole body imaging. The necessary time for 3-D image reconstruction can be significantly reduced with the use of the super computer. However, it cannot be always available from the side of cost. Therefore, we need some methods to speed up the 3-D reconstruction without using the super computer. Recently, a rebinning algorithm has been proposed as a promising approach for overcoming time-consuming images reconstruction in 3-D PET.

This report is especially focused on the Fourier rebinning (FORE) algorithm which was implemented in Shimadzu SET-2400W scanner at Cyclotron and Radioisotopes Center of Tohoku University (CYRIC). It is well known that images become very noisy in the edge region of axial direction because of lack of the rebinned data. We aimed at developing an algorithm which utilizes maximally images reconstructed with the FORE algorithm. A new developed algorithm should suppress noises in the edge slices and maintain the quantification of small spots.

Fourier rebinnig algorithm

For a PET scanner with N rings, the data acquired in 3-D mode consist of N^2 sinograms, in which N direct sinograms ($\theta = 0$)θ and $N(N-1)$ oblique sinograms are included. The four variables s, ϕ, z and δ are defined as follows (See Fig.1)[1]: s is the distance between the axis of the scanner and the projection line onto a transaxial plane, ϕ is an angle of the projection direction with respect to the Y-axis on the transaxial plane, z is the axial coordinate of the middle point between two detectors. The δ coordinate is defined as the tangent of the angle θ between a line of response and the transaxial plane.

We take the Fourier transform of oblique and directed sinograms with respect to the parameters of s, ϕ and z. In the 3-D Fourier transform, $P(\omega, k, \omega_z, \delta)$, ω is the radial frequency, k is the Fourier index, and ω_z is the axial frequency. The exact rebinning algorithm yields the following relation between the 3-D Fourier transforms of oblique and direct sinograms[2,3].

$$P(\omega,k,\omega_z,\delta) = \exp(-i\Delta\phi)P(\omega\chi,k,\omega_z 0)$$

In this relation, $\Delta\phi$ is the phase shift: $\Delta\phi = k\arctan\alpha$, and χ is the frequency scaling: $\chi = \sqrt{1+\alpha^2}$.

For the fast implementation, an approximation can be derived by considering the first-order truncation Taylor expansions in α of the phase shift and of the frequency scaling factor.

$$P(\omega,k,\omega_z,\delta) \cong \exp(-i\frac{k\delta}{\omega}\omega_z)P(\omega,k,\omega_z,0)$$

As the only dependence on the axial frequency ω_z is a linear phase shift, it is possible to calculate the inverse 1-D Fourier transform of $P(\omega,k,\omega_z,\delta)$ (with respect to ω_z,

$$P(\omega,k,z,\delta) \cong P(\omega,k,z-\frac{k\delta}{\omega},0)$$

This Fourier rebinning approximation relates the 2-D Fourier transform of an oblique sinogram (z, δ) to the 2-D Fourier transform of a slice shifted axially by a frequency-dependent offset $\Delta z = -k\delta/\omega$. The Fourier rebinning equation is considered as the frequency-distance relation stating that the value of P at the frequency (ω,k) receives contributions mainly from sources located at a fixed distance $t = -k/\omega$ along the lines of integration. Note that t represents the signed distance measured on the transaxial projection of line response (LOR) from the midpoint of the LOR. The Fourier rebinning does not require execution of an axial Fourier transform with respect to z. This property considerably simplifies the implementation not only because of the small number of Fourier transforms, but more importantly because the data need no longer be known for all values of z, and hence the truncated data do not need to be estimated[2].

After all projection data is rebinned to parallel slices on the frequency space, inverse 2-D Fourier transform is calculated to return sinogram $P_{2D}(s,\phi,z,0)$. Finally, 2-D image reconstruction is performed.

The new algorithm (the improvement of Median filter)

First, images reconstructed with the FORE algorithm were processed by a three-dimensional median filter in order to suppress noise. The median filter has two operation modes: New Median ver.1 and New Median ver.2. The first one uses a 3*3*3 matrix of filter size (27 voxel). The second one is a three-dimensional cross joint filter (7 voxel).

Second, the new algorithms are set up with the criterion to subtract the filtered image

from the non-filtered image in order to avoid removing small hot spots. This criterion decides each pixel value in the final image. The criterion is as follow: if the pixel values, in the matrix of cross joint (7 voxel), of subtraction image are positive number, the pixel value in the center of cross joint is returned to the value before filtering in order to recover the removed hot spots. The pixel value keeps with the value processed by the filter when there is at least one negative pixel value in the matrix of cross joint. This concept is originated from the difference between hot spot and noise. When we image a point source in the detector ring, the corresponding hot spot will be evenly spread on the neighbor pixels due to spatial resolution of detectors used in a PET scanner. On the other hand, the noise profile almost always shows a signal alternating with high and low values irrespective of the spatial resolution of detector. So, if the pixel values of subtraction image are positive numbers in a region, the criterion judges that hot spot is removed in this pixel. On the other hand, if not, noise is removed.

Experimental

The 3-D PET data were obtained with the Shimadzu SET-2400W scanner, which has the axial view of 20cm and 32 slices, in CYRIC. Commonly, a lot of data collected with this PET system is sent to SX4/44R super computer in the computer center of Tohoku University. However, in this experiment, image reconstruction was performed using workstation (AlphaStation XP1000) in CYRIC for the purpose of estimating reconstruction time without super computer. Both the 3D-FBP and the FORE algorithms used in this experiment were implemented in the Shimadzu SET-2400W.

In the first experiment, mainly designed to evaluate image quality, the radioisotope injected in the pool-phantom (20cm of the diameter, 25cm of height) was F-18 and the total counts for scan time were about $1.7*10^9$ counts. The new algorithms were applied for the image reconstructed with the FORE algorithm and 2D-FBP.

In the second experiment, the new algorithms were applied for clinical data of a cancer patient to evaluate the quantification checking hot spots smaller than filter size were removed. Data were acquired for 3 minutes after 1 hour from injection of FDG.

Result and Discussion

Processing time

Table 1 shows the time required for image reconstruction and filter processing. The time required for reconstruction in the FORE+2DFBP algorithm was found to be ten times less than that in 3D-FBP. In addition to this, the new algorithm does not lengthen the time of image reconstruction, because it is a simple algorithm.

Evaluation for image quality (for the pool-phantom experiment)

Figure 2 shows standard deviation for pixel value of the plane phantom in a 3- cm

circular region of interest (ROI). While the standard deviation of the FORE+2DFBP is higher than that of the 3D-FBP in all slices, that of the New Median ver.2 is almost same as that of 3D-FBP in the region of ± 23 slices (about 73% of all slices) from the center slice No.32 in the cylindrical scanner of SET-2400W. For the New Median ver.1, the standard deviation of almost all slices is lower than that of 3D-FBP. From these results, the quality of image is best improved when the New Median ver.1 was applied. This is caused by the size of Median filter. If Median filter of large size is applied, you can get an image of good quality, but if you will have a problem of removing small hot spots, as discussed below.

Evaluation of Quantification (for the clinical data)

Figures 3 and 4 are reconstructed images of clinical data. The former is at the slice No.30 and the latter is at the slice No.7. Comparing the images processed by New Median ver.1 and ver.2 with those processed by FORE+2DFBP, we can clearly see that many streak artifacts are removed by New Median filter processing. In addition to this, a comparison with the image processed by 3D-FBP let us to notice that hot spots are kept by New Median filtering. As shown in Fig. 4, the image of FORE+2DFBP is very noisy and cannot clearly reveal a hot spot. However, the hot spot can be distinguished from background if the new developed algorithms are applied.

Figures 5 and 6 show profile across small hot spots in the middle slice No.30 and the edge slice No.7 respectively. As shown in Fig. 5, while two hot spots are distinguished, a small hot spot of about 3 pixel (6mm) size are removed for a portion of 1 pixel. But such hot spot removal was not observed for the New Median ver.2. Fig.6 shows that both new algorithms suppress the noise and keep the value of relatively large hot spots even in the edge slice.

Removing hot spot is not a serious problem for this experiment, but it will be a big problem if better spatial resolution and quantification are required. So, we will study further noise reduction and quantification in filter processing of images reconstructed with FORE+2DFBP, and improve the algorithm of filter processing.

References

1) Tanaka E., RADIOISOTOPES, **46** (1997) 33.
2) Kitamura K., Tanaka K., Satoh T. and Amano M., SHIMADZU REVIEW, **55** (1998) 199.
3) Michel Defrise., P. E. Kinahan et al., IEEE Trans. Med. Imag., **15** (1997) 145.

Table 1. Processing time for 63 slices

Algorithm	Processing time
3D-FBP	4 hours
FORE+2DFBP	20 minutes
New Median ver.1 or ver.2	Less than 1 minute

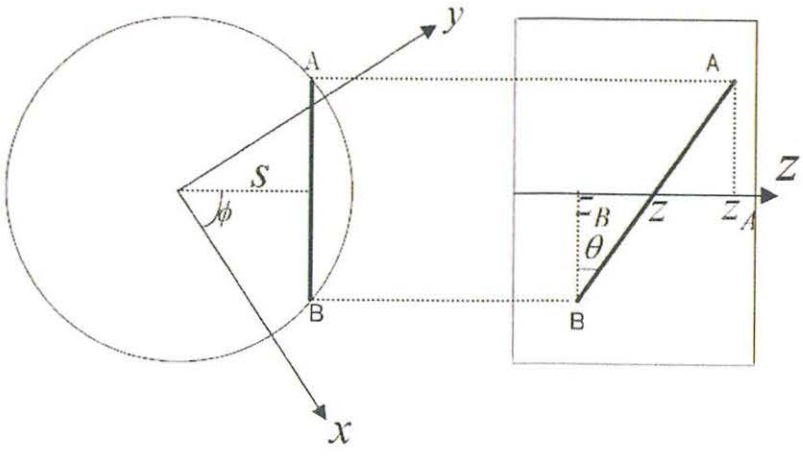

Fig. 1. Variables used in FORE.

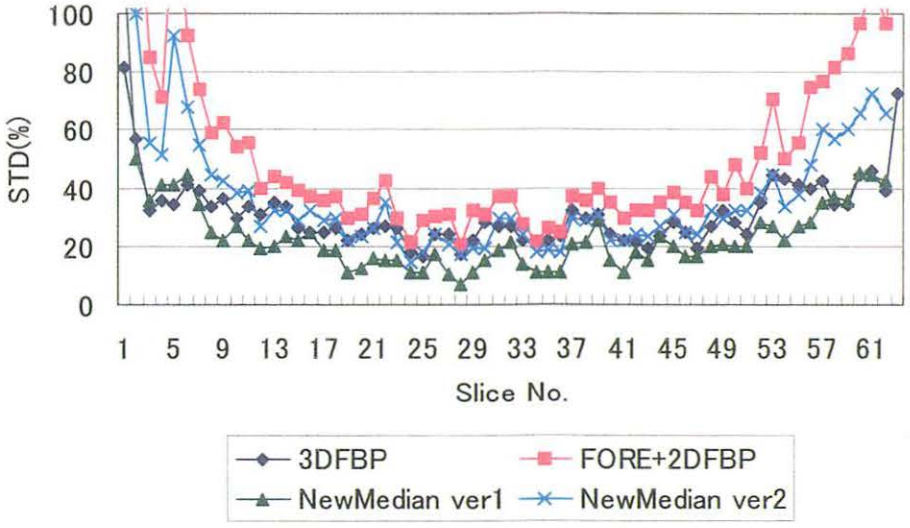

Fig. 2. Standard deviation in ROI of each slice.

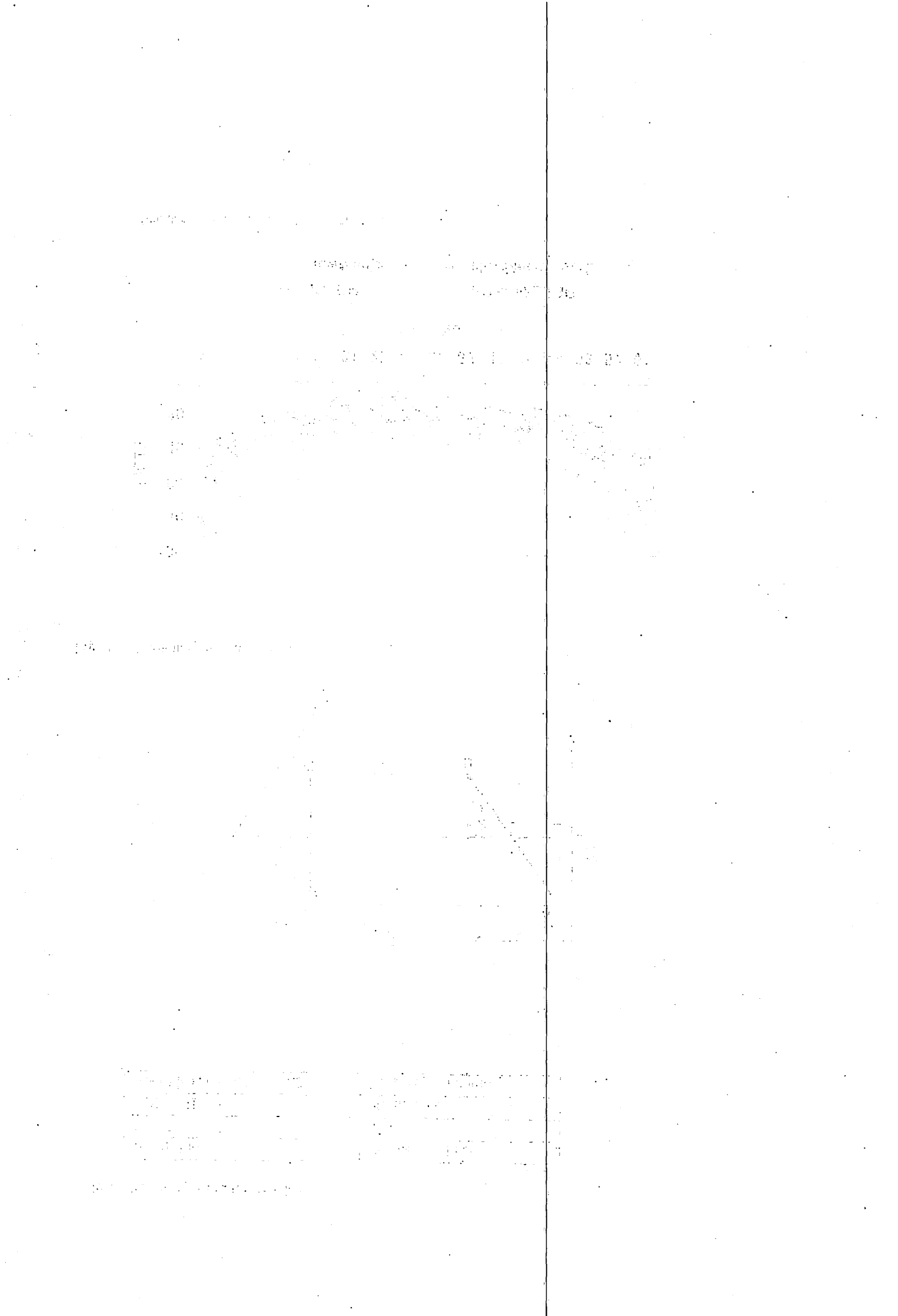

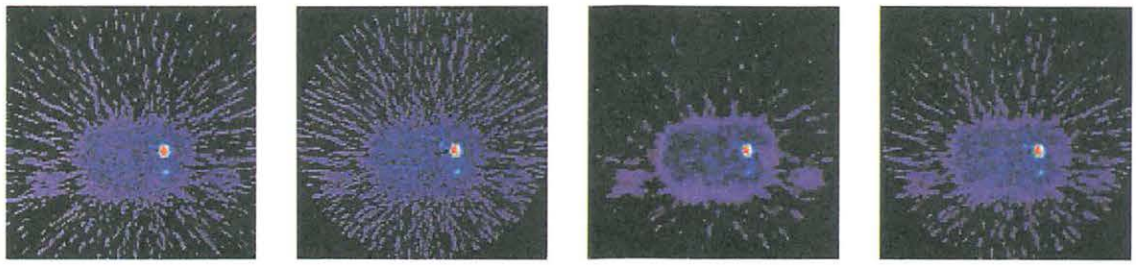

Fig. 3. Images (at slice No.30) reconstructed with 3D-FBP(left) and FORE+2DFBP(mid-left) and processed by New Median ver.1(mid-right) and New Median ver.2(right).

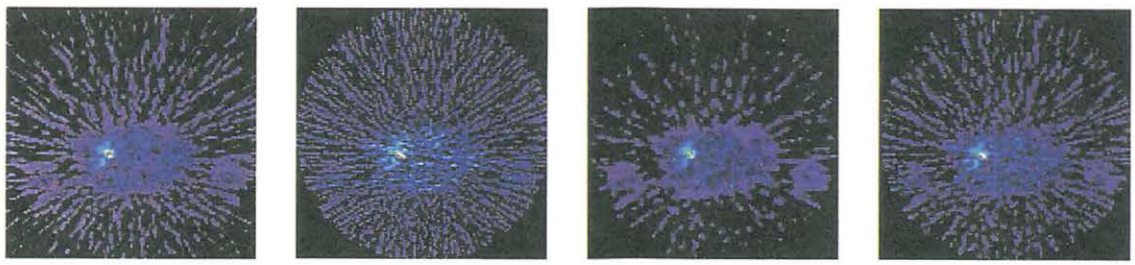

Fig. 4. Images (at slice No.7) reconstructed with 3D-FBP(left) and FORE+2DFBP(mid-left) and processed by New Median ver.1(mid-right) and New Median ver.2(right).

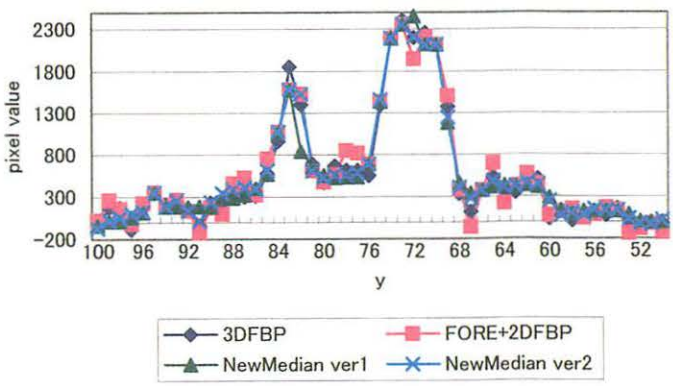

Fig. 5. Hot spot profile at slice No.30.

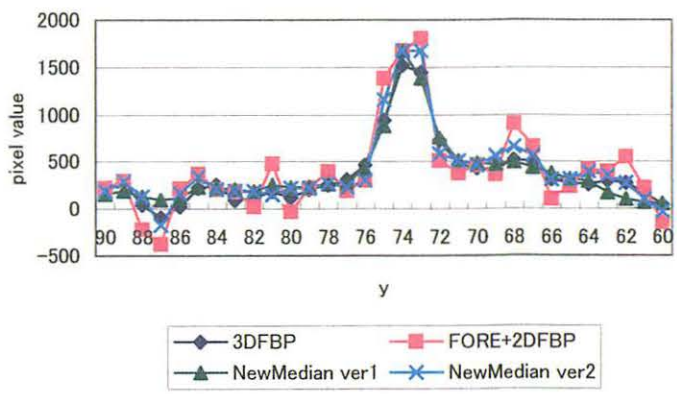

Fig. 6. Hot spot profile at slice No.7.

V. RADIATION PROTECTION AND TRAINING OF SAFE HANDLING

V. 1. Measurement of Thick Target Neutron Yields and Neutron Induced Activation Cross Sections for Ten's of MeV Protons and Neutrons

Aoki T., Hagiwara M., Baba M., Yashima H., Yonai S., Miura T., Kawata N., and Yamadera A.

Cyclotron and Radioisotope Center, Tohoku University

Introduction

Recently, applications of accelerators are extending to various fields from basic sciences to applied purposes. For the design of radiation shielding and safety system for modern high energy and high current accelerator systems, various nuclear data are required with high precision. However, little experimental nuclear data are available above 20 MeV because of lacks of appropriate accelerator facilities. We have started experiments for 1) thick target neutron yields and 2) neutron induced activation cross sections using the new 930 cyclotron on CYRIC.

Thick target neutron yields from the (p,n) and (d,n) reactions provide source term in the shielding calculation. Therefore, it is important to know angle-dependent secondary neutron spectra. Their data are required too for the choice of neutron sources. In the present experiments, we obtained the data for the C, Al and Ta(p,n) reactions at 50 MeV and the Li and Be(d,n) at 25 MeV. Aluminum and carbon are elements for beam-lines and beam-dumps in accelerators. Tantalum is often used for the target of the spallation neutron source as well as lead, owing to a soft neutron spectrum that is advantageous for moderated neutron fields for neutron capture therapy (NCT) and so on. The ^{7}Li(d,n) neutron source will be employed in the International Fusion Materials Irradiation Facility (IFMIF)[1]. For estimation of neutron irradiation effects, therefore, it is important to know the neutron flux and spectra, especially in high-energy parts. The data of the Be(d,n) reaction is of interest for intense neutron source based on the Be(d,n) reaction and for the comparison with the Li(d,n) spectra.

Activation cross sections are required to estimate radioactivity induced in the structural materials af accelerators. In this study, we measured the neutron activation cross sections of the ^{12}C(n,2n)^{11}C, ^{27}Al(n,p)^{27}Mg, ^{27}Al(n,α)^{24}Na and ^{nat}Cu(n,3n)^{61}Cu reactions by using quasi-monoenergetic p-^{7}Li neutrons for proton energy of 35, 50 and 70 MeV.

Thick Target Neutron Yields

Experiment

Measurements were carried out at the 5-th target room with the beam-swinger system. The thickness of the target was 15 mm (C), 10 mm (Al), 3.0 mm (Ta), 7.5 mm (Li) and 3.0 mm (Be). Each target and an aluminum-oxide beam monitor were placed on a stainless steel target holder in a target chamber. The holder was controllable remotely without stopping a beam and insulated from the ground to serve as a Faraday cup. The target chamber and the beam dump (carbon or aluminum) were shielded with iron bars and 1 m thick concrete walls to reduce neutron and g-ray backgrounds. Emitted neutrons were collimated by iron collimators (10-cm-diam and 1 m long), and detected by NE213 scintillation detectors, 14- cm-diam x 10-cm-thick or 2-inch-diam x 2-inch-thick which were placed around 11 m or 3.5 m from the target, respectively. Data were acquired for three parameters, TOF, pulse-height and pulse-shape event by event using NIM type multi-parameter data acquisition system.

Data reduction

Neutron TOF spectra gated by a pulse-shape signal and lower pulse-height bias were converted into energy spectra. In this measurement, there was serious frame-overlap where low energy neutrons were passed over by high-energy neutrons in a succeeding pulse because the beam chopping system was not available yet. To reduce the influence of flame-overlap, data was processed for various soft bias level higher than the maximum light output for each TOF region. In this way, we tried to obtain low energy neutron data from overlapping parts by setting multistage bias and interpolating the non-overlap regions. The data were deduced down to 8 MeV or so with this techniques but the lower region will be measured again using a beam chopper. The efficiency vs. energy curves of detectors were obtained by calculations using the Monte Carlo code SCINFUL[2)] that was verified within ±5% up to 80 MeV by Meigo[3)]. Then, the spectra were divided by the efficiency and the solid angle and converted into differential yields. All yields were normalized by the integrated beam charge.

Activation cross sections

Experiment

The irradiation was done with quasi-monoenergetic neutrons by the ^{7}Li(p,n) reaction at the 5-th fifth target-room. In this experiment, a proton beam of 35, 50 and 70 MeV bombarded lithium targets whose thickness was 2.70, 4.46 and 8.71mm respectively. The emitted neutrons were collimated by a 10-cm-diam×1-m-long iron collimator. The irradiation samples were placed about 2.5 m away from the ^{7}Li target and ~10 cm away from the collimator entrance. The size of sample was 4.0-cm-diam×1.0-cm-long expect for the ^{12}C sample for 70 MeV. The irradiation time was from 32- to 81 minutes, the proton beam

current was several ten's to hundreds of nanoamperes.

The neutron fluence was measured with the TOF method using a 14-cm-diam×10-cm-long NE213 liquid scintillation detector that was placed around 11 m from the ^{7}Li target. This detector was used also for monitoring the fluctuation of beam currents with a multi-channel scaler (MCS). The absolute detector efficiency was calculated with the Monte Carlo code, SCINFUL[2,3]. Figure 1 shows the neutron spectra for 35, 50, 70 MeV proton incidences.

Gamma-rays emitted from the irradiated samples were measured by a Ge detector (EURISYS MESURES EGPC50-195-R (relative efficiency 48.0 %)) with a multi-channel analyzer. Measurements were carried out immediately after irradiations by putting the sample in contact with the surface of Ge detector to increase the geometrical efficiency. The absolute efficiency of the Ge detector was determined using the electron-photon cascade Monte Carlo code, EGS4[4]. We confirmed the calculated values from the agreement of experimental values for standard gamma-ray sources at distance 15 cm away from the surface of the Ge detector.

Data reduction

The intensities of radioisotopes were determined from the peak counts of gamma-ray spectra. The counts were corrected for the decay, the peak efficiency of Ge detector, the self-absorption effect in the samples and the beam current fluctuation during irradiation. The data of the gamma-ray energies, the branching ratios and half-lives of produced radioisotopes were obtained from Ref. [5]. The fluctuation of neutron flux during irradiation was recorded by MCS with dwelling time of 60 seconds. The ratio was stable enough in series of irradiation experiments.

The activation cross section was obtained by dividing the reaction rate by the neutron fluence. However, the reaction rate R includes the contribution of the continuums of neutrons in the ^{7}Li (p,n) source. The reaction rate R is decomposed to that by peak neutrons and continuums neutrons as follows:

$$R = \int_{E_{th}}^{E_{max}} \sigma_{act}(E)\cdot\phi(E)dE = \int_{E_{th}}^{E_{min}} \sigma_{act}(E)\cdot\phi(E)dE + \int_{E_{min}}^{E_{max}} \sigma_{act}(E)\cdot\phi(E)dE \qquad (1)$$

where E_{th} = threshold energy, E_{max} = maximum energy of the peak neutrons, E_{min}= minimum energy of peak neutrons. Therefore, to obtain the reaction rate for the peak neutrons, it is necessary to eliminate the contributions of continuum neutrons. For the reason, it is desirable to obtain cross section data in self-consistent manner by taking data step by step from low incident energy. However, at present, data points are still a few (30, 45 and 65 MeV). Therefore, the contribution of the low-energy neutron continuum was removed using calculated data for activation cross sections and the measured neutron flux. Therefore, the present values are still preliminary, because they include uncertainty due to low energy

continuum contribution. The cross section $\sigma_{act}(E_{peak})$ are obtained by eq. (2).

$$\sigma_{act}(E_{peak}) = \frac{R}{\phi(E_{peak})} \times \frac{\int_{E_{min}}^{E_{max}} \sigma_{act}(E)\cdot\phi(E)dE}{\int_{E_{th}}^{E_{min}} \sigma_{act}(E)\cdot\phi(E)dE + \int_{E_{min}}^{E_{max}} \sigma_{act}(E)\cdot\phi(E)dE} \qquad (2)$$

Result and discussion

The results are shown in fig.2 ((p,n),) fig.3 ((d,n)), fig.4 ($^{12}C(n,2n)^{11}C$), Fig.5 ($^{27}Al(n,p)$, (n,α)) and Fig.6 ($^{nat}Cu(n,x)^{61}Cu$ reaction). For comparison, the Pb(p,n) data of LA-150[6], activation cross section data of ENDF/B-VI and other calculated or experimental data are also shown. In the fig.2 and fig.3, the error bars represent the uncertainties due to counting statistics alone. The absolute value is preliminary because the present data contains the uncertainty in absolute values due to secondary electron emission. Thus, we discuss only shapes of the spectra.

First, the experimental spectra are consistent with the Q values of the reactions: -18.1 MeV, -3.00 MeV, -5.59 MeV and -0.970 MeV for the $^{12}C(p,n)$, $^{13}C(p,n)$, $^{27}Al(p,n)$ and $^{181}Ta(p,n)$ reactions, respectively, and if the energy of incident protons is 50 MeV and the emission angle is 15 deg, the maximum energy of emitted neutron is 31.5 MeV, 46.7 MeV, 44.3 MeV and 49.0 MeV, respectively. From the results, it can be said that carbon is superior to other nuclides as a elements for beam dump owing to lower secondary neutrons yields.

The spectrum from the Ta(p,n) reaction is consistent with LA-150[6]. However, below 25 MeV, experimental yields for Ta is higher than the calculated spectrum for lead. The spectrum of tantalum is softer than for aluminum because of many low energy neutrons through the (p,2n), (p,3n) and (p,4n) reactions.

The above argument is true also for the case of (d,n) reactions. These experimental spectra are consistent with the the Q values 3.38 MeV, 15.03 MeV and 4.36 MeV, respectively for the $^{6}Li(d,n)$, $^{7}Li(d,n)$ and $^{9}Be(d,n)$ reactions. If the energy of incident deuterons is 25 MeV and the emission angle is 0 deg, the maximum of emitted neutron energy is 27.9 MeV, 39.4 MeV and 29.1 MeV respectively. The Be(d,n) yields simply decrease with the neutron energy, while the Li(d,n) spectra have high-energy edge caused by $^{7}Li(d,n_{0,1})^{8}Be$ components with high Q value.

The intensity of high-energy tail takes maximum around 20 deg and the total neutron yields are maximum around 4 deg. It can be said that to reduce the influence of high-energy neutrons and obtain high intensity irradiation field, neutrons to forward-angles close to zero-deg may be preferable. Later, lower energy neutron yields should be measured with a beam chopping system.

In the activation cross sections shown in Fig.4, the ratio of the peak contribution in eq.(2) was obtained using ENDF/B-VI data. The present values are different from THO

(98) data by Kim et. al.[7] but closer to the ENDF/B-VI data. At 30 MeV the present data is in good agreement with other data. Further, in higher energy, the present data are close to decreasing feature with energy of ENDF/B-VI, while THO(98) data by Kim et.al. are rather flat. In the case of $^{12}C(p,pn)^{11}C$ reaction, the cross section seems flat in corresponding energy. However, in the case of the $^{12}C(n,2n)^{11}C$ reaction the decrease of cross sections with energy looks more reasonable because of competition with (n,3n) reaction in high energy region. Nevertheless, our experimental data are not final yet, and it is important to obtain the self-consistent experimental data by using experimental data alone.

In Fig.5, our experimental data are much larger than expected from the evaluated values in lower energy region. The probable reason of high values is the contribution of scattered neutrons because of low threshold energies of the reactions. It is possible that the contribution of low energy neutrons due to scattering around collimators is much larger than assumed in eq.(2). The data will be cheeked again using improved geometry.
In fig.6, the present data show energy dependence similar with the calculation but are smaller markedly than both data. The contribution of neutron continuum was subtracted using Fukahori's calculation. The obtained data will be required more examinations and corrections for increasing the certainty.

Summary

In the present measurements, thick target neutron yields from C(p,n), Al(p,n) and Ta(p,n) reactions at 50 MeV and Li(d,n) and Be(d,n) reactions at 25 MeV and neutron induced activation cross sections of $^{12}C(n,2n)^{11}C$, $^{27}Al(n,p)^{27}Mg$ and $^{27}Al(n,\alpha)^{24}Na$ and $^{nat}Cu(n,x)^{61}Cu$ reactions for 30, 45 and 65 MeV neutrons were obtained.

In the measurements of thick target neutron yields, we obtained reasonable results down to ~10 MeV by making correction for the flame–overlap effect due to lack of a beam chopping system and the multistage biasing technique. Measurement will be extended to lower energy neutrons with the beam chopping system and to higher precision absolute value. In addition, measurements in other incident energy and backward angle will be carried out.

In the measurements of activation cross section, the measured cross sections are compared with other experimental data and calculated data. The shape of the measured cross section curve is in fair agreement with the calculated data of ENDF/B-VI data files and Fukahori's calculation using the ALICE code. The measured data are rather smaller than other experimental data and calculated data for $^{12}C(n,2n)^{11}C$ and $^{nat}Cu(n,x)^{61}Cu$ reactions but higher for $^{27}Al(n,p)^{27}Mg$ and $^{27}Al(n,\alpha)^{24}Na$. These data are preliminary and more examinations and corrections will be done. It is desirable to obtain these data in finer energy step and to obtain self-consistent data.

References

1) IFMIF CDATEAM, IFMIF Conceptual Design Activity Final Report edited by Marcello Martone, Report 96.11, Enea, Dipartimento Energia, Frascati (1996).
2) Dickens J. K., ORNL-6436, Oak Ridge National Laboratory, 1988.
3) Meigo S., Nucl. Instrum. Methods in Physics Research **A 401** (1997) 365.
4) Nelson W. R., Hirayama H., Rogers D. W. O.: EGS4 code system, SLAC –265 (Stanford Linear Accelerator Laboratory, 1985).
5) Table of Isotopes, 8th ed., FIRESTONE R. B. and SHIRLEY V. S., Eds., John Wiley and Sons, New York (1996).
6) Cadwick M. B. et al., Necl. Sci. Eng., **1331**, (1999) 293.
7) Kim E. J. et al, Nucl. Sci. Eng., **129** (1998) 209.

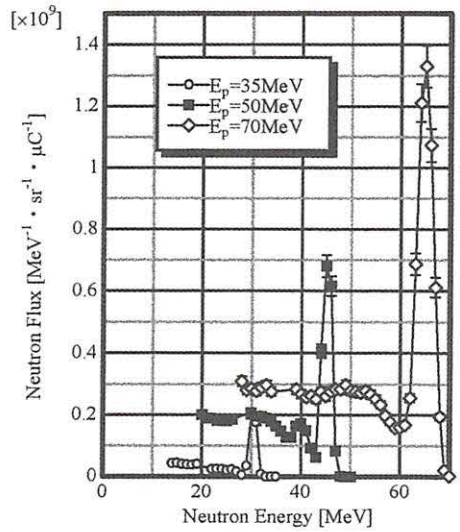

Fig. 1. ^{7}Li(p,n) spectrum.

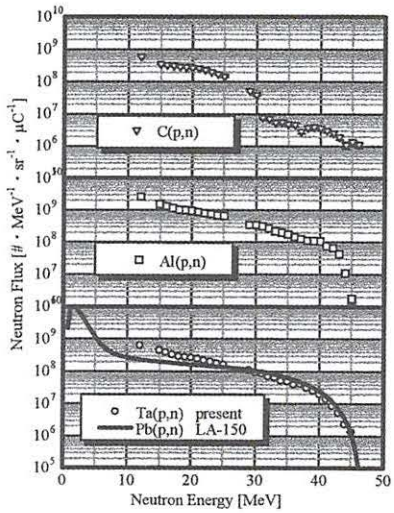

Fig. 2. Thick(p,n) spectra and Pb(p,n) data of LA-150.

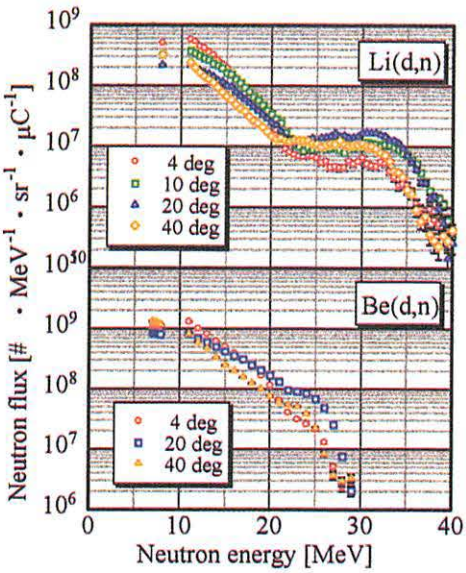

Fig. 3. Li(d,n) and Be(d,n) spectra.

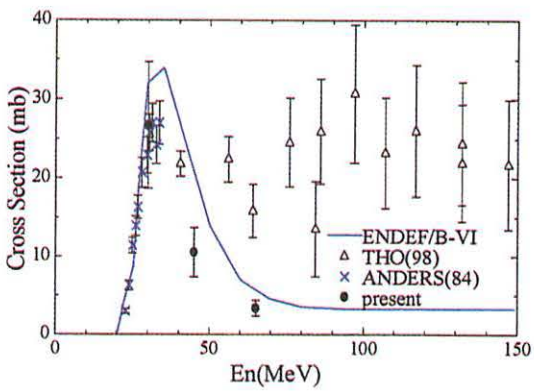

Fig. 4. ^{12}C(n,2n)^{11}C reaction.

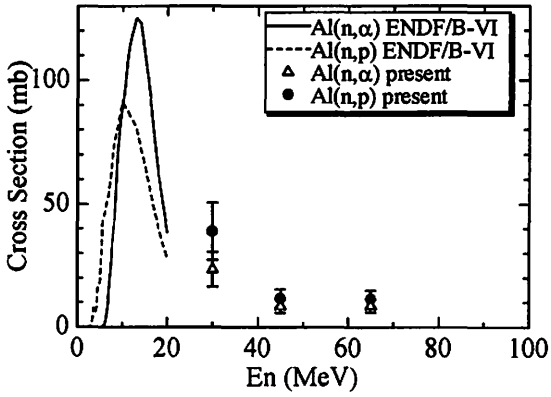

Fig. 5. $^{27}Al(n,p)$, (n,α) reaction.

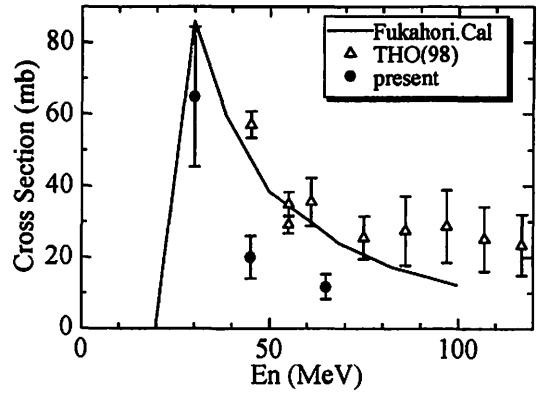

Fig. 6. $^{nat}Cu(n,x)^{61}Cu$ reaction.

V. 2. Measurment of Newtron Spatial Distribution by Using Activation Foils and Imaging Plate

Hagiwara M., Aoki T., YamaderaA., and Baba M.**

Quantum Science and Energy Engineering, Tohoku University
*Cyclotron and Radioisotope Center, Tohoku University**

Introduction

The imaging plate (IP) is a radiation sensor[1,2] consisting of photostimulable phosphor layer of BaFBr(Eu) which was originally developed by Fuji Film Co., Ltd. to measure the two-dimensional radioactivity distribution as a digital image. It has a sensitivity more than 100 times higher than that of the X-ray film. Its well-known superior characteristics are described in other papers[1-3].

On the other hand, the IP has a drawback not to separate the type and the energy of the incident radiation. For neutron measurement, the IP containing gadolinium has been developed. Cross section of gadolinium for thermal neutron is very large. It has a high sensitivity for thermal neutrons and has been used for neutron diffraction experiments, but has a high sensitivity for gamma rays too. Therefore it can not be applied for the fields with high induced activities such as in accelerator vaults.

Thermal neutron measuring method by using activation foils and the IP was proposed[4]. By this method, we can measure many samples at the same time and consequently we can take very long measuring period. We applied this method to the measurement of thermal, epithermal and fast neutron spatial distributions[5]. This method has been used in high gamma-ray fields, such as cyclotron vault and medical linac facilities.

Experiment

A thin sheet of gold (0.1 mm thick, 10 mm in diameter, 143 mg by weight) was used as an activation foil. A pair of activation foil was prepared; one was covered with aluminum foil and the other with a 1mm-thick cadmium foil. The 48 pairs of them were set 1.5 m apart from each others and 1.5 m high from floor level in the TR1. The HM-12AVF cyclotron was operated at the condition of the incident proton energy of 12 MeV, beam current of about 27 μA, irradiation time of 2 hours and the target material of water ($H_2{}^{18}O$).

One day after the cyclotron operation, all gold foils were put on the IP (BAS-IIIs, white plate of 20 cm×40 cm), and left for 24 hours in a lead-shield box which reduces the

natural gamma rays to a 1/10 level. The stored image was read out by the BAS-1000 analyzer (Fuji Film Co., Ltd.). The BAS-1000 has the pixel size of 100μ m and it takes about 3.5 minutes to read out one image.

Some of the foils were measured with pure a Ge gamma-ray analyzer system to identify induced radioisotopes and to calculate the yields of ^{196}Au and ^{198}Au. The former is produced with fast neutrons by the ^{197}Au(n,2n)^{196}Au reaction and the later with thermal and epithermal neutrons by the ^{197}Au (n, γ) ^{198}Au reaction.

Suitable thickness of gold foil was determined by using ^{252}Cf neutron sources. Figure 1 shows the relation between a thickness and a PSL density of irradiated gold foils. In the region less than 0.2 mm in thickness, the curve inclines sharp and over the 0.2 mm, the curve reaches almost flat. The curve indicates the suitable thickness is around 0.05 mm for measuring PSL, but this thickness is too thin to prepare samples and has not enough activities for measuring gamma rays with a Ge detector. Therefore we settled the thickness of gold foils to be 0.1 mm.

Results and discussion

The detection efficiency and the detection limit of IPs for ^{252}Cf neutrons were calculated to be 1.26×10^{-6}PSL/n.cm^2 and 3.4×10^{7}n/cm^2, respectively.

Figures 2 and 3 show a thermal neutron spatial distribution measured with aluminum covered gold foils and a epithermal-neutron spatial distribution measured with cadmium covered gold foils, respectively, at 1.5 m high over the floor the level. These distribution maps are not so accurate and not so fine. By sampling with smaller meshes, we can take more accurate and finer map.

Figure 4 shows a neutron distribution at the center of the downstairs. The PSL density decreases exponentially from the top of stair (2m) to the underground floor (9m) and the thermal neutron flux in the underground floor was as low as a detection limit. Comparing two curves, the slope of epithermal neutrons is larger than thermal ones, because of epithermal neutrons are thermalized abruptly in a short pass.

The activities in the underground floor were too weak to measure by using conventional GM counter systems. In the usual activation foil method, a Ge detector is often used, but in case of very weak activated samples and a large number of ones, this method is very time consuming and tedious, and we conclude that our method is preferable.

Conclusion

We developed a neutron spatial distribution measuring method by using activation foils and imaging plates (IPs). It has high sensitivity for neutrons and no sensitivity for gamma rays.

Two kinds of 0.1 mm-thick gold foils were prepared; one was covered with an aluminum foil and the other was covered with a 1 mm-thick cadmium foil. Many pairs of

activation foils were placed in the neutron field for 2 hour and were contacted on IP (BAS-III s) for 1 day. The stored image of the IP was readout by BAS-1000 (Fuji Film Co., Ltd.). By using a ^{252}Cf neutron source, the detection efficiency and detection limit were calculated to be 1.26×10^{-6} PSL/n.cm^2 and 3.4×10^{7}n/cm^2, respectively. The cadmium ratios were changed from 1.7 to 2.8, depending on the location in the accelerator vault.

References

1) Sonoda M., Takano M., Miyahara J. and Kato H., Radiology **148** (1983) 833.
2) Amemiya Y. and Miyahara J., Nature(London), **339** (1993) 89.
3) Miyahara J., Chemistry Today **223** (1989) 29.
4) Toyoda A., Eda K., Ishihara T. and Masumoto K., KEK Proceedings 2000-**13,15** (2000).
5) Hagiwara M., Aoki T., Yamadera A. and Baba M., The 13th International Conference on Solid State Dosimetry (2001), Athens.

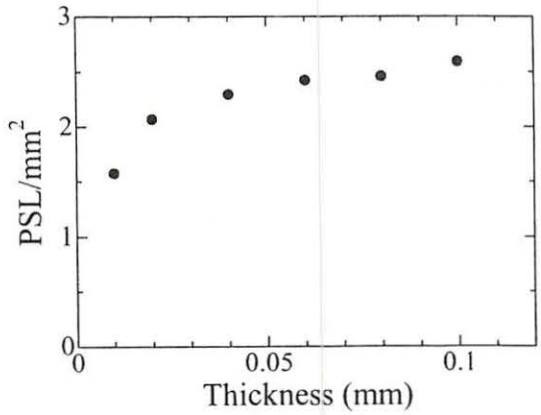

Fig. 1. Relation between thickness and PSL density of irradiated gold foil.

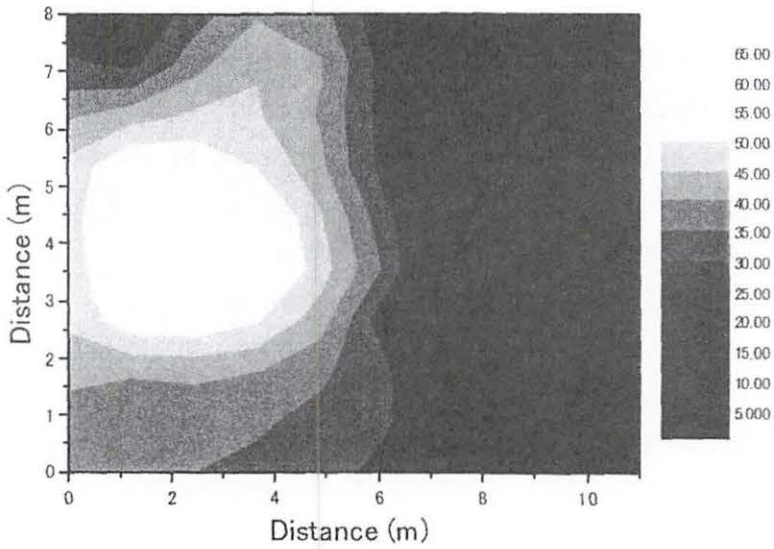

Fig. 2. Thermal neutron spatial distribution measured with aluminum covered gold foils at 1.5m high over floor level.

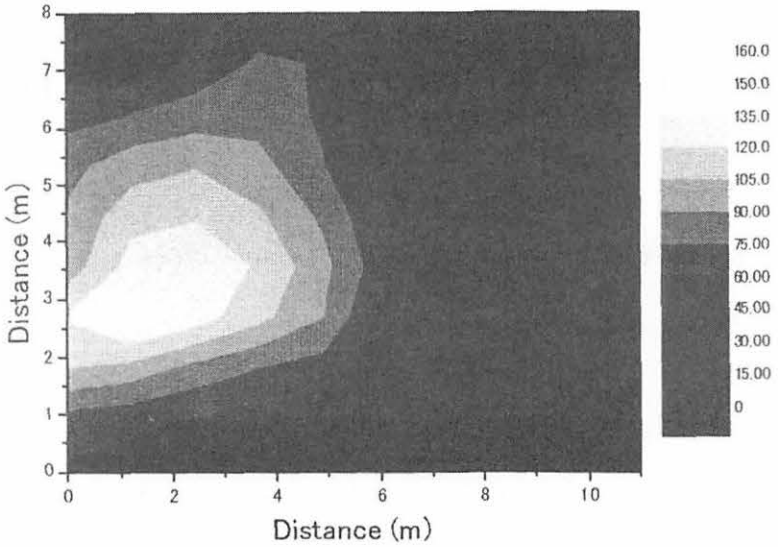

Fig. 3. Epithermal-neutron spatial distribution measured with cadmium covered gold foils at 1.5m high over floor level.

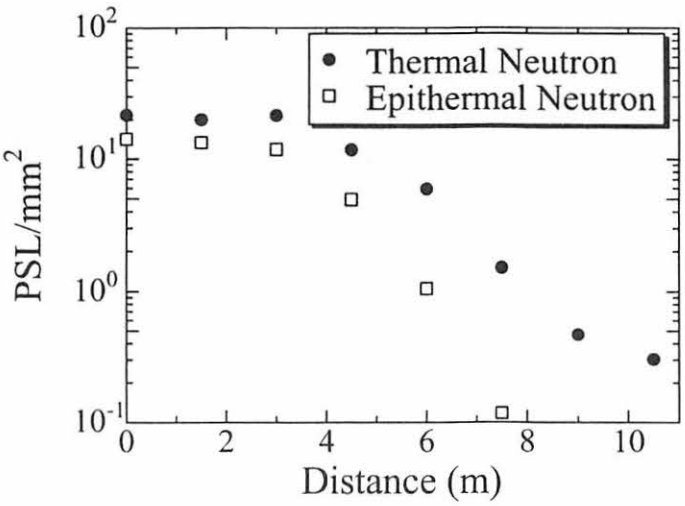

Fig. 4. Thermal and epithermal neutron distributions at the center of downstairs.
(-○-) : Thermal neutron. (-●-) : Epithermal neutron.

V. 3. Development of Position-Sensitive Proton Recoil Telescope (PSPRT)

Miura T., Baba M., Kawata N., Aoki T., Hagiwara M.

Cyclotron and Radioisotope Center, Tohoku University

INTRODUCTION

Fast neutron spectra measurement is important in the area of radiation safety. As a fast neutron spectrometer, a proton recoil counter telescope (PRT) detector[1] is widely used. The PRT can deduce the neutron energy (E_n) by using a recoil proton energy (E_p) and a recoil angle (θ);

$$E_p = E_n \cos^2\theta , \quad (1)$$

$$\Delta E_p = E_n \sin 2\theta \, \Delta\theta . \quad (2)$$

The equation (2) expresses the uncertainty of the proton energy for the angular spread $\Delta\theta$, and it indicates that the uncertainty at forward angles is smaller than in backward angles. In the PRT, θ is determined by the geometry in the experimental setup, and only E_p is measured. In conventional design, the detection efficiency must be lower to achieve good energy resolution, because a thin radiator and a small angular spread of recoil protons are required.

In order to achieve high resolution as well as high efficiency concurrently, we have developed a position-sensitive proton recoil telescope (PSPRT) which employs a position-sensitive photomultiplier (PS-PMT) and a scintillator for both a radiator and a proton-detector. This system enables to obtain the information not only on E_p but also θ from the position data for both detectors. Therefore the PSPRT can be used under a large solid angle, without deterioration in the energy resolution.

For example, if protons within 5 degree recoil angle are collected with radiator-detector distance of 5 cm, in the case of a conventional PRT, the sizes of the radiator and the detector should be smaller than 4.4 mm in diameter. On the other hand, in the PSPRT, both detectors are allowed to be as large as 50 mm in diameter corresponding to an effective area of PS-PMT (Hamamatsu R2486) for the same energy resolution as the former case. Therefore, roughly speaking, the efficiency of the PSPRT is more than one hundred times as high as the conventional one with the same energy resolution.

Further, a thick radiator can be used in the PSPRT, because the information of energy loss in the radiator can be obtained from the light output from the radiator scintillator. The PSPRT, therefore, is expected to achieve both of good energy resolution and high detection efficiency concurrently with a compact and solid composition. We expect that the PSPRT contributes to the measurements of neutron spectrum behind shields in accelerator facilities and the spectrum of cosmic neutrons, and fusion neutrons for the plasma diagnostics.

STRUCTURE OF THE SPECTROMETER

As shown in Fig.1, the PSPRT consists of two position sensitive detectors (PS-DET), a radiator-detector (PS-DET1) and a proton-detector (PS-DET2), placed facing each other. The PS-DET1 consists of an NE102A plastic scintillator and a PS-PMT (Hamamatsu R2486), and the PS-DET2 is essentially the same as PS-DET1. The R2486 photomultiplier is of cross-anode type with an effective area of 50 mm in diameter. A neutron enters from backward of the PS-DET1 and ejects a proton, which is stopped in the PS-DET2. Signals are taken in coincidence between two PS-PMTs in order to decrease background events. *En* is determined by using eq.(1). E_p is obtained from the pulse heights from PS-DET1 and PS-DET2, and θ is deduced by the position-information in x-y coordinates of both detectors.

PS-PMT outputs four signals, *x1, x2, y1* and *y2*. A scintillating point (x,y) is provided by the method of charge-division;

$$x = x2 / (x1 + x2), \tag{3}$$

$$y = y2 / (y1 + y2). \tag{4}$$

The pulse height is obtained by $(x1+x2+y1+y2)$. The position resolution of PS-PMT itself is better than 1 mm (FWHM ~0.3 mm) from the result of position calibration using a LED. However, the sensitivity of PS-PMT is not uniform enough, and the maximum difference is about 40 % even in the center part. To obtain pulse height information, therefore, the correction for the non-uniformity is necessary.

MEASUREMENT OF RESPONSE FOR 14.1 MEV NEUTRONS

(a) EXPERIMENTAL SETUP

The response of the PSPRT was measured at the Tohoku University 4.5 MV Dynamitron facility for 14.1 MeV mono-energetic neutrons produced by the T(d,n)α reaction. The experimental setup is shown in Fig.1. The neutrons at emergent angle of 90° were used to reduce the energy spread of neutrons less than 100 keV. The distance between the neutron source and radiator was taken longer than 100 cm to reduce divergence of the neutron incident angle to the radiator. In this experiment, NE102A plastic scintillators, 1 mm and 3 mm-thick, were employed for the PS-DET1 and PS-DET2, respectively. The distance between the scintillators was 5 cm. To prevent a crosstalk of lights between scintillators, a 0.03 mm-thick black polypropylene foil was placed on the surface of PS-DET2.

Four anode signals from each PS-PMT, eight signals in total were collected using CAMAC electronics. At first, the anode signal was divided into two signals in a linear fan-out, one is input into a charge-sensitive ADC and collected as a pulse height signal, and the other one is used for logic signal to take coincidence and make a gate-signal.

(b) DATA REDUCTION

The position information was deduced by using eq.(2),(3). Since the PS-PMT is cylindrical and difficult to align against rotation in the experimental setup, a position calibration was performed by scanning x and y axes with a LED to determine a relation between the signal height and the position. Therefore, position data was adjusted to make consistent the position data of both detectors.

The validity of position calibration of both detectors was confirmed experimentally by shadowing protons with a cadmium plate placed vertically and horizontally between detectors as shown in Fig.3(a). Cadmium was selected as a non-proton emitting element due to high Z. As an example, the result for the horizontal scale is shown in Fig.3(b). Neutrons are cut in the upper half and it confirmed the consistency of axis-calibration for both detectors.

The scattering angle was obtained by the following equation,

$$\cos\theta = \frac{\vec{A} \cdot \vec{B}}{|A||B|}, \qquad (5)$$

where $\vec{A}$ and $\vec{B}$ are the vectors describing the position of PS-DET1 and PS-DET2, respectively.

The proton energy was determined by taking a sum of pulse heights PH1 and PH2 from the PS-DET1 and PS-DET2, respectively. The gain of pulse height was adjusted to satisfy the following equation,

$$\mathrm{PH1}(\theta) + \mathrm{PH2}(\theta) = \mathrm{Ep}(\theta) = (\text{constant}). \qquad (6)$$

Finally, neutron energy was deduced by using eq.(1).

RESULTS AND DISCUSSION

In this measurement, the effective area of PS-PMT was limited within 20 mm in diameter due to problems in light-collection for events in outer regions of one PS-PMT.

Figure 4 shows a scatter plot for pulse height of PS-DET1 vs. PS-DET2. The gains were adjusted to satisfy the eq.(6). The high energy events around the solid line in Fig.4 correspond to forward scattering. The range of 14 MeV protons in the NE102A plastic scintillator is ~2.19 mm, then the recoil proton can stop in the PS-DET2. In the PS-DET1, proton goes out from the radiator of 1mm-thick, and a portion of the energy was lost

there.

Figure 5 shows a scatter plot for the proton energy E_p vs. the recoil angle θ. In this figure, two groups are observed. The group in the higher energy region is due to proton events, and this should be on a curve of eq.(1). The other group, which locates in the lower energy region and corresponds to a large number of events around 0 channel in fig.4, is caused by gamma ray. This identification was done by the following facts; (a) when a lead plate inserted between PS-DET1 and PS-DET2, proton events disappeared, but no change for the low energy group, (b) when the neutron beam was stopped, both groups diminished.

Figure 6 shows the comparison of the neutron spectra for events with $\theta < 10$ deg. and all events corresponding to the result of the conventional PRT.
The energy resolution of PSPRT was ~7.7 % by a Gaussian fitting, and this is much better than the conventional PRT in the same geometry. The present resolution is expected to be improved significantly by performing the correction for non-uniformity of the sensitivity in the PS-PMT and proton energy-loss through the air and the polypropylene foil. Now the sensitivity measurement for the device is in progress for the former correction.

CONCLUSION

Position sensitive proton recoil telescope (PSPRT) has been developed. The PSPRT consists of two detectors using position-sensitive photomultipliers (PS-PMT) and scintillators, and achieves much higher detection efficiency than a conventional proton recoil telescope without losing energy resolution so much, because information can be obtained on (1) scattering-angles, (2) proton energy and (3) energy-loss in the radiator scintillator.

The response of the PSPRT was measured for 14.1 MeV neutrons, and the validity of position calibration was confirmed. The energy resolution, however, was not good enough, 7~8 %. Correction for (a) non-uniformity of sensitivity in the PS-PMT and (b) a proton energy-loss through the air and the thin polypropylene foil will improve the resolution markedly. Furthermore, improvement of energy resolution can be expected by employing scintillators producing higher light output than NE102A for the proton detector.

The PSPRT is expected to detect the high energy neutron (tens of MeV) by improving the design of scintillators. For detection of high energy protons, thick scintillator and particle identification are necessary. In order to prevent divergence of light and to keep the position information, we plan to employ a stack of long and narrow scintillators with light shield. A CsI(Tl) crystal is expected as a scintillator for proton detector, because its pulse shape differs according to particle type and the CsI(Tl) is one of scintillators with the biggest light output. The test for tens of MeV neutrons is in progress in CYRIC.

Reference

1) Glenn F. Knoll, Radiation Detection and Measurement, John Wiley & Sons, Inc.

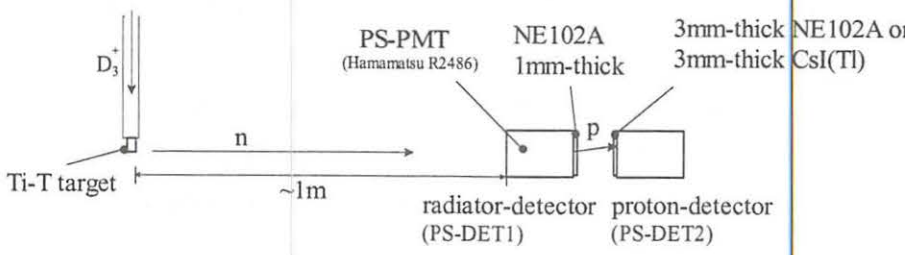

Fig.1. Structure of the PSPRT and the experimental setup.

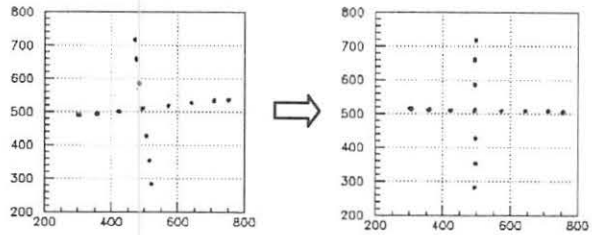

Fig.2. Result of position calibration to obtain the relation between position data from PS-PMT and real one.

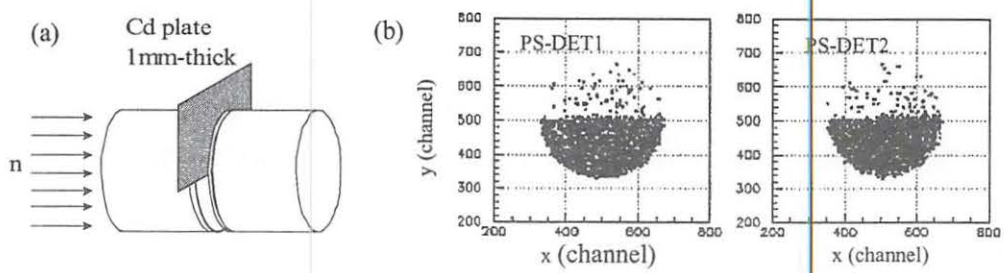

Fig.3. Experimental confirmation of coordinate axes between PS-DET1 and PS-DET2 (a) experimental setup (b) results of position data.

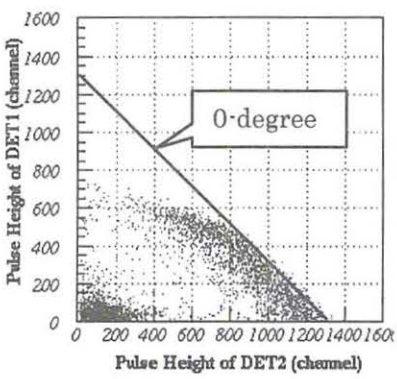

Fig.4. Scatter plot for pulse height of PS-DET1 vs. PS-DET2.

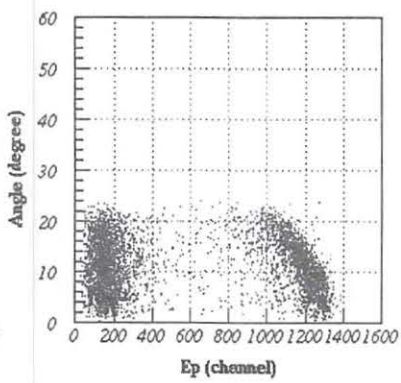

Fig.5. Scatter plot for *Ep* vs. recoil angle θ.

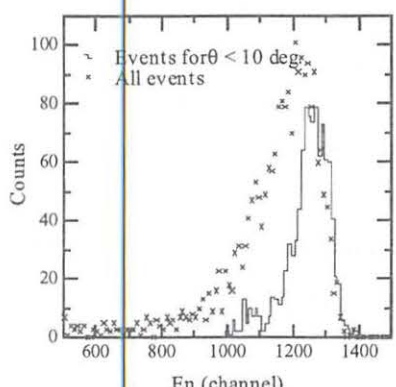

Fig.6. Neutron spectra.

V. 4. Dependence on the Radiations and their Energies for Fading Functional Equation of Imaging Plate

*Ohuchi H., and Yamadera A.**

Graduate School of Pharmaceutical Sciences, Tohoku University,
*Cyclotron and Radioisotope Center, Tohoku University**

Introduction

For utilization of an imaging plate (IP) ,made of BaFBr:Eu^{2+} phosphor, for an integral type detector, the estimation of fading is very important especially around ambient temperatures. We have been continuing our study[1-3] of measuring fading characteristics and developed functional equations expressing the fading effect in the following equation, which is the sum of several components, as functions of elapsed time (t) and absolute temperature (K);

$$(PSL)_{t,k}/(PSL)_{0,k} = A_1 \cdot \exp\{-a \cdot t \cdot \exp(-E_a/(R \cdot K))\} + A_2 \cdot \exp\{-b \cdot t \cdot \exp(-E_b/(R \cdot K))\} ,\ldots, + A_n \cdot \exp\{-n \cdot t \cdot \exp(-E_n/(R \cdot K))\}$$

where $(PSL)_{t,k}$ and $(PSL)_{0,k}$ refer to the photo-stimulated luminescence (PSL) of elapsed time t and 0 after irradiation, respectively, A_n the component amplitude, E_n the activation energy, R the gas constant, and K the absolute temperature.

We developed a universal functional equation which showed excellent agreement at all temperatures ranging from 0 to 60°C and over all time periods from 0.03 to approximately 500 hours after irradiation with a ^{244}Cm source between the experiment data and calculated results using IPs; BAS-UR and BAS-TR[3].

In this study, our objective is to investigate the dependence on the radiations of alpha, beta, and gamma -rays and their energies for fading effect and to make functional equations to correct the fading at practical radiation fields.

Experimental

The commercially available IP (Fuji Film Co.) BAS-TR, BAS-UR, and BAS-MS were used. The difference on the structure among three types of IPs is listed in Table 1. The IP was irradiated with the alpha or beta-ray source by placing the source directly on the IP ,which was kept in an aluminium IP cassette inside an incubator having a temperature controlled to ± 1°C during irradiation and the time elapsed prior to reading the latent image.

The IP set in an aluminium IP cassette was irradiated with the gamma-ray source 0.5m to 1.5m apart, then, the IPs were kept inside an incubator until the reading. A ^{244}Cm planchet source (specific radioactivity of 2.9 KBq) as an alpha-ray source, ^{14}C, ^{32}P, ^{36}Cl source (radioactivity of 740.0, 11.7, and 4.0 KBq and maximum beta energy of 0.156,1.711, and 0.709 MeV, respectively) as a beta-ray source, and ^{60}Co and ^{137}Cs point source (0.5136 and 0.280 mGy/hour at 1m on Jan.16 2001, respectively and gamma emission energy of 0.173 and 1.333 MeV from ^{60}Co source and 0.662 MeV from ^{137}Cs source) as a gamma-ray source were used. Irradiation period was fixed for 15 minutes. The fading characteristics were measured at temperatures of 10, 30, and 50°C and for time periods from 0.03 to approximately 100 hours after irradiation. The IP was then read by the image reader (Fuji Film Co.) BAS-1000 for BAS-TR and BAS-UR and BAS-5000 for BAS-MS, respectively.

Results

Dependence on the energies of β and γ particles

The temperature dependence of the fading effect of the latent image after irradiation with each beta-ray source using BAS-TR is shown in Fig.1. There is no difference on fading curves at each temperature between three beta-ray sources having different maximum beta energy. The temperature dependence of the fading effect with each gamma-ray source using BAS-TR is shown in Fig.2. There also seems no difference between two gamma-ray sources. The same results were found when BAS-UR and BAS-MS were used.

These facts mean that the fading effect is independent of the energies incident of beta and gamma particles in any type of IPs used in this experiment.

Dependence on the type of radiation

Fig.3 shows the fading curves after irradiation with alpha, beta, or gamma-ray source using BAS-TR. It is clearly shown that there is no difference between them except the first component which fades out in very short elapsed time after irradiation with alpha-ray source. This means the fading effect is independent of the type of radiation except the first component by irradiation with alpha-ray source.

The same results were obtained when BAS-UR and BAS-MS were used ,however, the ratio of the first component, which is owing to alpha rays, to other components seems apparently smaller on BAS-UR and BAS-MS than on BAS-TR. Actually, the ratio is getting smaller in order of BAS-TR, BAS-UR, and BAS-MS. This difference is considered to be from the difference of the protective layer thickness. As shown in Table 1, BAS-TR lacks a protective surface layer although BAS-UR and BAS-MS have a 6 and 9 μ m thick protective layer, respectively. The contribution of alpha rays should be reduced by attenuation of the alpha rays through the protective layer.

Functional equations

The measured PSLs were analyzed by a method described in a previous paper[1]. A functional fading equation after irradiation with the ^{244}Cm source using BAS-TR could be written as

$$\begin{aligned}(PSL)_{t,k}/(PSL)_{0,k} = {} & 0.461\exp\{-2.19\times10^{8}\cdot t\cdot\exp(-6.14\times10^{3}/K)\} \\ & +0.277\exp\{-1.60\times10^{13}\cdot t\cdot\exp(-1.02\times10^{4}/K)\} \\ & +0.230\exp\{-7.98\times10^{12}\cdot t\cdot\exp(-1.05\times10^{4}/K)\} \\ & +0.030\exp\{-1.99\times10^{12}\cdot t\cdot\exp(-1.05\times10^{4}/K)\} \\ & +0.002\exp\{-4.96\times10^{10}\cdot t\cdot\exp(-1.05\times10^{4}/K)\} \qquad (1)\end{aligned}$$

A functional fading equation after irradiation with beta or gamma -ray source using BAS-TR could also be written as

$$\begin{aligned}(PSL)_{t,k}/(PSL)_{0,k} = {} & 0.177\exp\{-2.19\times10^{8}\cdot t\cdot\exp(-6.14\times10^{3}/K)\} \\ & +0.426\exp\{-1.60\times10^{13}\cdot t\cdot\exp(-1.02\times10^{4}/K)\} \\ & +0.355\exp\{-7.98\times10^{12}\cdot t\cdot\exp(-1.05\times10^{4}/K)\} \\ & +0.042\exp\{-1.99\times10^{12}\cdot t\cdot\exp(-1.05\times10^{4}/K)\} \qquad (2)\end{aligned}$$

Comparing Eqs.(1) and (2), it is found that the values in the brackets of every terms, which means the half-lives of the components, are same. It is also found that relative ratio of the component amplitude of the second term, the third one, to the forth one ; (0.52:0.43:0.05) is the same in both equations. On the other hand, the ratio of the component amplitude of the first term to other components is larger in Eq.(1) than in Eq.(2). This means the contribution by alpha rays from the ^{244}Cm source is large in the first component. The fifth component in Eq.(1) has considerably small in magnitude, so that in Eq.(2), it could not be measured because of an inadequate radioactivity of the beta or gamma -ray source.

In the same way, a functional fading equation after irradiation with the ^{244}Cm source using BAS-UR could be written as

$$\begin{aligned}(PSL)_{t,k}/(PSL)_{0,k} = {} & 0.582\exp\{-6.93\times10^{11}\cdot t\cdot\exp(-8.11\times10^{3}/K)\} \\ & +0.378\exp\{-2.95\times10^{10}\cdot t\cdot\exp(-8.71\times10^{3}/K)\} \\ & +0.038\exp\{-1.59\times10^{11}\cdot t\cdot\exp(-9.85\times10^{3}/K)\} \\ & +0.002\exp\{-6.75\times10^{9}\cdot t\cdot\exp(-9.97\times10^{3}/K)\} \qquad (3)\end{aligned}$$

A functional fading equation after irradiation with beta or gamma -ray source using BAS-UR could also be written as

$$\begin{aligned}(PSL)_{t,k}/(PSL)_{0,k} = {} & 0.521\exp\{-6.93\times10^{11}\cdot t\cdot\exp(-8.11\times10^{3}/K)\} \\ & +0.433\exp\{-2.95\times10^{10}\cdot t\cdot\exp(-8.71\times10^{3}/K)\} \\ & +0.043\exp\{-1.59\times10^{11}\cdot t\cdot\exp(-9.85\times10^{3}/K)\} \\ & +0.003\exp\{-6.75\times10^{9}\cdot t\cdot\exp(-9.97\times10^{3}/K)\} \qquad (4)\end{aligned}$$

Similar to BAS-TR, the values in the brackets of every terms are found to be same and the relative ratio of the component amplitude of the second term, the third one, to the forth one is the same (0.90:0.09:0.005) in both equations. The ratio of the component amplitude of the first term, which is owing to alpha rays from the ^{244}Cm source, is larger in Eq.(3) than in Eq.(4). Comparing Eqs.(1) and (3), the ratio of the component amplitude of the first term is apparently smaller on BAS-UR than on BAS-TR because alpha rays are attenuated through the protective layer.

Discussion

The IP has a lot of excellent propaties as a detector of two-dimensional images[4-6], however, it has a defect of having a large fading effect that results in a serious hindrance of quantitative measurements. We developed a novel functional equation to correct fading[3]. In this paper, we've clearly shown that the fading effect is independent of the energies of beta and gamma-rays and is independent of the type of radiation, either, except the first component irradiated with alpha-ray source. These results make the fading correction simple at practical radiation fields and lead us to the possibility of quantitative measurements using the IP.

References

1) Ohuchi H.,Yamadera A. and Nakamura T., Nucl. Instrum. & Methods, **A450** (2000) 343-352.
2) Ohuchi H.,Yamadera A. and Nakamura T., KEK Proceedings of the 14th Workshop Radiation Detectors and Their Uses,**14** (2000) 72-82.
3) Ohuchi H. and Yamadera A., Rad. Meas. to be sumitted.
4) Sonoda M., Takano M., Miyahara J. and Kato H., Radiology **148** (1983) 833-838.
5) Amemiya Y., Wakabayashi K., Tanaka H., Ueno Y. and Miyahara J., Science **237** (1987) 164-168.
6) Amemiya Y. and Miyahara J., Nature **336** (1988) 89-90.

Table 1. Structure of three types of IPs.

type of IP	BAS-TR	BAS-UR	BAS-MS
size(cm)	20x40	12.7x12.7	20x25
thickness of protective layer (μm)	0	6	9
thickness of phosphor layer (μm)	50	130	115
thickness of base (μm)	250	188	188
thickness of ferrite layer (μm)	160	0	160

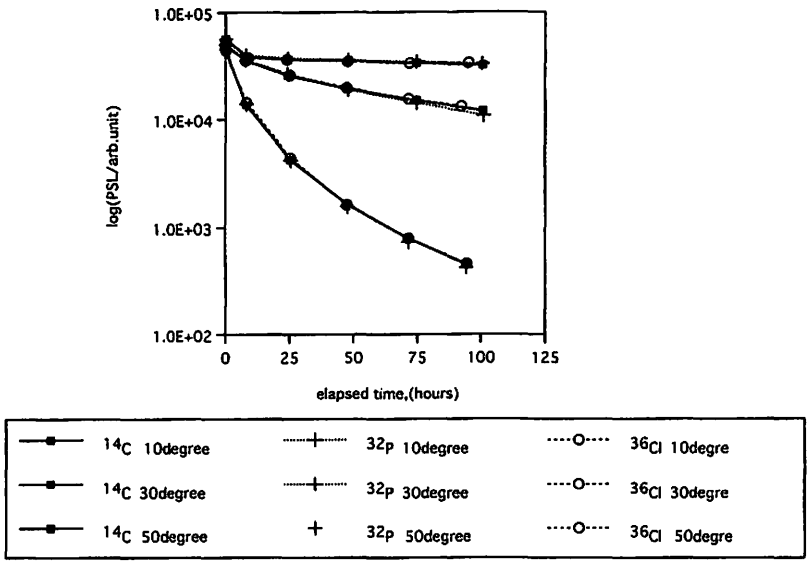

Fig. 1. Temperature dependence of the fading effect of the latent image after irradiation with each beta-ray source using BAS-TR.

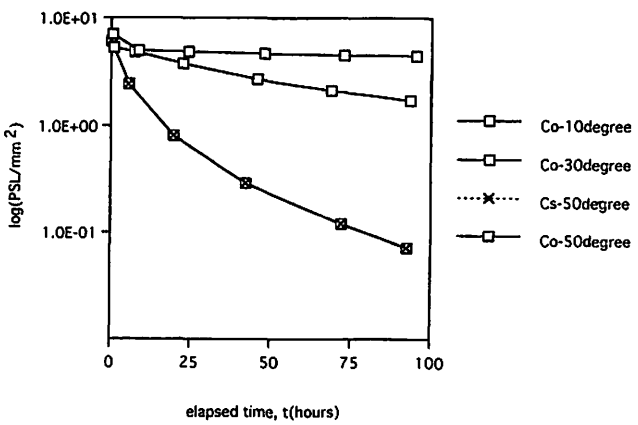

Fig. 2. Temperature dependence of the fading effect of the latent image after irradiation with each gamma-ray source using BAS-TR.

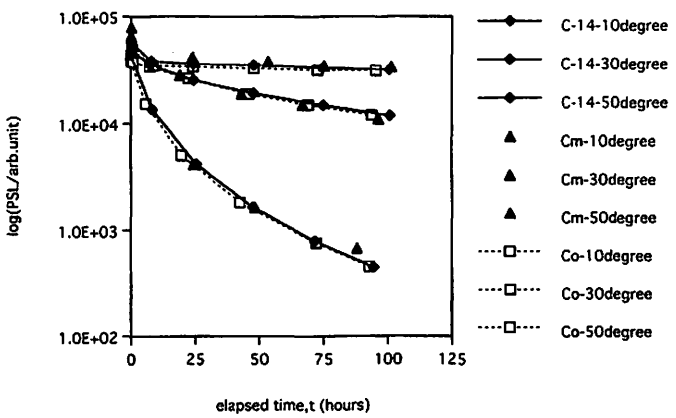

Fig. 3. Temperature dependence of the fading effect of the latent image after irradiation with alpha, beta, or gamma-ray source using BAS-TR.

V. 5. Training for Safehandling of Radiation and Radioisotopes and X-Ray Machines for Beginners in Tohoku University

Baba M., Yamadera A., Miyata T. and Nakamura T.

Cyclotron and Radioisotope Center, Tohoku University

Training for safehandling of radiation and radioisotopes for beginners has been conducted twice a year from 1977 in Tohoku University. The contents of lectures and practices are shown in Table 1. In 2000 the training was performed for 539 persons. The departments to which they belong are given in Table 2.

Training for safehandling of X-ray machines and electron microscopes began from the end of 1983. The training is scheduled to be held twice a year at the same time as the safehandling of radiation and radioisotopes. Only lectures are given and not practices. The contents of the lectures and the distributions of trainees are shown in Tables 3 and 4, respectively.

Training for safehandling of synchrotron radiation began from the end of 1995. The contents of the lectures are the same as safehandling of radiation and radioisotopes for beginners and not practices. In 2000 the training was performed for 60 persons.

Table 1. Contents of lectures and practices for safehandling of radiation and radioisotopes in 2000.

Lectures (one day)	
Radiation physics and measurements	1.5 (h)
Chemistry of radioisotopes	1.0
Radiological protection ordinance	1.5
Effects of radiation on man	1.0
Safehandling of radioisotopes	1.5

Practices (one day)	
Treatment of unsealed radioactive solution	4.0 (h)
Measurements of surface contamination and decontamination	1.0
Measurements of gamma rays and beta rays	2.0

Table 2. Distribution of trainees for safehandling of radiation and radioisotopes in 2000.

Department	Staff	Student	Total
Medicine	8	87	95
Dentistry	3	22	25
Pharmacy	2	66	68
Science	3	74	77
Engineering	2	98	100
Agriculture	0	95	95
Research Institutes	12	49	61
The others	2	16	18
Total	32	507	539

Table 3. Contents of lectures for safehandling of X-ray machines and electron microscopes in 2000.

Safehandling of X-ray machines	1.5 (h)
Radiological protection ordinance	1.0
VTR for safehandling of radiation and radioisotopes	1.0

Table 4. Distribution of trainees for safehandling of X-ray machines and electron microscopes in 2000.

Department	Staff	Student	Total
Science	2	25	27
Engineering	17	113	130
Research Institutes	19	103	122
The others	0	0	0
Total	38	241	279

Table 5. Distribution of trainees for synchrotron radiation in 2000.

Department	Staff	Student	Total
Science	1	14	15
Engineering	0	24	24
Research Institutes	2	19	21
Total	3	57	60

V. 6. Radiation Protection and Management

*Miyata T., Yamadera A., Baba M., Nakamura T. and Watanabe N.**

Cyclotron and Radioisotope Center, Tohoku University
*Japan Radiation Protection Co., Ltd.**

(1) Unsealed radionuclides used in the center

The kinds and activities of unsealed radionuclides handled in the center in 2000 are shown in Table 1. The table includes the isotopes produced by the cyclotron, purchased from the Japan Isotope Association and took over from another RI institutes.

(2) Individual monitoring

The exposure doses of the workers in the center in 2000 is given in Table 2. They were less than the permissible doses.

(3) Monitoring of the workplace

Radiation dose rates inside and outside of the controlled areas were monitored periodically and as needed. They were below the legal permissible levels. Surface contamination levels of the floors inside the controlled areas were measured by smear method and with survey meters periodically and as needed. They also cleared under the legal regulation levels.

(4) Wastes management

The radioactive wastes delivered to the Japan Radioisotope Association in 2000 are shown in Table 3. The concentration of radioisotopes in the air released after filtration from the stack was monitored with stack gas monitors. The levels were less than the legalregulation levels. The radioactive water was storaged at the tanks at least for 3 days and then released to the sewerage after confirming that the concentration was less than permissible levels.

The treated volume of radioactive waste of organic scintillator was 480 l by the incinerator made by Fujikogyo Co., Ltd.

Table 1. Unsealed radionuclides used in the center in 2000.

(a) Cyclotron Building(kBq)

group 1,2		group 3		group 4	
^{252}Cf	658.340	^{11}C	687,859,600.000	^{14}C	2,220.000
		^{15}O	5,180,000.000	^{18}F	667,876,100.000
		^{32}P	2,652.620	^{3}H	1,812.000
total	658.340	total	693,042,252.620	total	667,880,132.000

(b) RI Building(kBq)

group 1,2		group 3		group 4	
^{90}Sr	300.000	^{11}C	259,000.000	^{3}H	82,972.860
^{60}Co	2,866.140	^{32}P	1,204,108.287	^{14}C	15,821.200
^{68}Ge	11,525.000	^{33}P	18,557.150	^{18}F	224,366,710.000
^{125}I	30.000	^{35}S	26,233.712	^{201}Tl	144,300,000
^{137}Cs	15,103.300				
total	29,824.440	total	1,507,899.149	total	224,609,804.060

Research Building(kBq)

group 1,2		group 3		group 4	
		^{11}C	407,000.000		
		^{15}O	51,060,000.000		
total	0.000	total	51,467,000.000	total	0.000

Table 2. Occupational radiation exposures at the center in 2000

Dose range (mSv)	Number ofindividuals
No measurable exposure	48
Measurable exposure less than 1.0	12
1.0 to 2.0	1
Total persons monitored	61

Table 3. Radioactive wastes delivered to the Japan Radioisotope Association in 2000

Wastes Container		Number
solids		
Combustible Type I	50 l drum	12
Combustible Type I	50 l drum	8
Incombustibles(for press)	50 l drum	3
// not for press)	50 l drum	3
Annimal carcasses	50 l drum	2
Filters	1 l /unit	0
liquids		
inorganic liquids	25 l PE bottle	8

Type I: Cloth and Paper made of natural cellulose.

Type II: Combustible Plastics such as Polyethylene and Polypropy

VI. PUBLICATION

VI. PUBLICATIONS

(January 2000 ~ December 2000)

A

1. Isovector part of optical potentials studied through analog transitions in the (p,n) reaction at 35 MeV
G. C. Jon, H. Orihara, C. C. Yun, A. Terakawa, K. Itoh, A. Yamamoto, H. Suzuki, H. Mizuno, G. Kamurai, K. Ishii, and H. Ohnuma,
PHYSICAL REVIEW C **62**, 044609-1-5(2000)

2. Anew convenient method for the preparation of 4-[^{18}F] fluorobenzyl halides
R. Iwata, C. Pascali, A. Bogni, G. Horvath, Z. Kovacs, K. Yanai, T. Ido
Applied Radiation Isotopes **52** (2000) 87-92

3. Synthesis of 1-[18F]Fluoro-1-(hycroxymethyl)-ethoxy]methyl-2 nitroimidazole([18F]FENI),a potential Agent for Imaging Hypoxic Tissues by PET
Hiroaki Wada, Ren Iwata Tatsuo Ido Yoshihiro Takai
Journal of Compounds and Radiopharmaceuticals **43**,785-793(2000)

4. Synthesis of 3-[1H-imidazol-4-yl]propyl 4[^{18}F]fluorobenzyl ether ([18F]fluoroproxyfan) : Apotential radioligand for imaging histamine H3 receptors
Ren Iwata, Geza Horvath, Claudio Pascali, ABogni, Kazuhiko Yanai Zoltan Kovacs, Tatsuo Ido
Journal of Compounds and Radiopharmaceuticals **43**, 873-882 (2000)

5. [F-18]Labeling of 1,2-Diacylglycerols
Toshihiro Takahashi, Tatsuo Ido, Shinji Nagata, Ren Iwta
Journal of Compounds and Radiopharmaceuticals **43**, 943-969 (2000)

6. Synthesis of 11-*O*-(8-[^{18}F]fluorooctanoyl)-2-*O*-palmitoyl-*rac*-glycerol for Imaging Intracellular Signal Transduction
Shozo Furumoto, Ren Iwata Tatsuo Ido
Journal of Labelled Compound and Radiopharmaceuticals **43**,11159-1172(2000)

7. Imaging Findings of the Brain After Performing Yoga: APET study
Laxmi Narayan SINGH, Masatoshi. ENDO, Keeiichiro YAMAGUCHI
Masayasu MIYAKE, Shoich WATANUKI, Myeong Gi JEONG, Masatoshi ITOH
Journal of International Society of Life Information Science **18**, (2000)

8. REPRODUCIBILITY OF PET BRAIN MAPPING OF CANCER PATIENTS
MANABU TASHIRO, FREIMUT D. JUENGLING, MICHAEL J, REINHARDT, INGO BRINK, STEFAN HOEGERLE, MICHAEL MIX, KAZUO KUBOTA, KEIICHIRO YAMAGUCHI, MASATOSHI ITOH, HIDETADA SASAKI, ERNST MOSER, EGBERT U. NITZSCHE
Psycho-Oncology **9**, 157 (2000)

9. Glucose uptake by individual skeletal muscles during running using whole-body positron emission tomography
Toshihiko Fujimoto, Masatoshi Itoh, Manabu Tashiro, Keiichiro Yamaguchi,

Kazuo Kubota, Hiroaki Ohmori
Eur. J. Appl. Physiol. **83** (2000)297-302

B

10. Retention of words in long-term memory: a functional neuroanatomical study with PET
Jiro Okuda, Tshikatsu Fujii, Atsushi Yamadori, Ryuta Kawamura, Takashi Tsukiura, Hiroya Ohtake, Reiko Fukatsu, Kyoko Suzuki, Masatoshi Itoh, and Hiroshi Fukuda
COGNITIVE NEUROSCIENCE AND NEUROPSYCHOLOGY **11**,323 (2000)

11. Regional and Temporal Profiles of Phorbol 12,13-Dibutyrate binding After Myocardial Infarction in Effects of Captopril treatment
Shigeto Namiuchi, Yutaka Kagaya, Masanobu Chida, Yuriko Yamane, Chikako Takahashi, Mitsumasa Fukuchi, Fumiaki Tezuka, Jun Watanabe, Tastuo Ido, and Kunio Shirato
Journal of Cardiovascular Pharmacology **35**, 353(2000)

12. Sequential changes of [^{3}H]forskolin,[^{3}H]cyclohexyladenosine and [^{3}H]PN200-110 binding sites in the brain of 6-hydroxydopamine-lesioned rats
T. ARAKI, H. TANJI, H. KATO, Y. IMAI, M. MIZUGAKI,Y. ITOYAMA
Acta Physiol Scand **169**, 71-78(2000)

13. Long-Term Right Ventricular Volume Overload Increases Myocardial Fluorodeoxyglucose Uptake in the Interventricular Septum in Patients With Atrial Septal Defect
Hiroki Otani, MD; Yutaka Kagaya,MD; Yriko Yamane, MD; Masanobu Chida MD; Kenta Ito, MD; Shigeto Namiuchi, MD; Nobuyuki Shiba, MD; Yoshito Koseki, MD; Mototsugu Ninomiya, MD; Jun Ikeda, MD; Haruo Saito,MD; Shin Maruoka, MD; Takehiko Fujiwara, MD; Tatsuo Ido, PhD; Nobumasa Ishide, MD; Kunio Shirato, MD
Circulation **101**, 1686-1692(2000)

14. Sequential changes of cholinergic and dopaminergic receptors in brains after 6-hydroxydopamine lesions of the medial forebrain bundle in rats
T. Araki, H. Tanji, K. Fujihara, H. Kato, Y. Imai, M. Mizugaki, Y. Itoyama
J Neural Transm **107**, 873-884 (2000)

15. Temporal changes of dopaminergic and glutamatergic receptors in 6-hydroxydopamiine-treated rat brain
Tsutomu Araki, Hiroaki Tanji, Hiroyuki Kato, Yutaka Imai, Michnao Mizugaki , Yasuto Itoyama
European Neuropsychopharmacology **10** (2000) 365-375

16. Comparison of Intratumoral Distribution of 99mTc-MIBI and Deoxyglucose in Mouse Breast Cancer Models
Hromchi Ohira, Kazuo Kubota, Noriaki Ohuchi, Yukou Harada, Hiroshi Fukuuda, Susumu Satomi
THE JOURRNAL OF NUCLEAR MEDICINE **41**, 1561-1568 (2000)

17. HISTAMNE H_1 RECEPTRS IN PATIENTS WITH ALZHEIMER' S DISEASE ASSESSED BYPOSITRON EMISSION TOMOGRAPHY
M. HICUCHI, K. YANAI, N. OKAMURA, K. MMECURO, H. ARAI, M. ITOH, R. IWATA, T. IDO, T. WATANABE, H. SASAKI
Neuroscience **99**,.721-729 (2000)

18. Relationship Between Effects of Alcoohol on Psychomotor Performances and Blood Alcohol Concentrations
Masaaki Tagawa, Michiko Kano Nobuyuki Okamura, Masatoshi Itoh, Eiko Sakurai,

Takehiko Watanabe, Kazuhiko Yanai
Jpn.. J. *Pharmacol.* **83**, 253-2600 (2000)

19. Functional neuroimaging of cognition impaired by a classical antihistamine, *d*-chlorpheniramine
Nobuyuki Okamura, Kazuhikoo Yanai, Makoto Higuchi, Jun Sakai, Ren Iwata, Tatsuo Ido, Hidetada Sasaki, Takehiko Watanabe, Masatoshi Itoh
British Journal of Pharmacology **129**, 115-123 (2000)

20. ^{18}F-fluorodopa PET study of striatal dopamine uptake in the diagnosis of dementia with Lewy bodies
N Okamura, H. Arai, M. Higuchi, T. Matsui M. Tashiro, M. Shinkawa, M. Itoh, T. Ido, H. Sasaki
NEUROLOGY **55**, 1575-1576 (2000)

VII. MEMBERS OF COMMITTEE

VII. Members of Committees (as of Jan. 1, 2001)

General

(Chairman)	Hikonojo	Orihara	(CYRIC)
	Osamu	Hashimoto	(Graduate School of Science)
	Hiroshi	Kudo	(Graduate School of Science)
	Akira	Takahashi	(Graduate School, Division of Medicine)
	Haruhiko	Takada	(Graduate School, Division of Dentistry)
	Yasushi	Ohizumi	(Faculty of Pharmaceutical Sciences)
	Katsunori	Abe	(Graduate School of Engineering)
	Teruo	Miyazawa	(Draduate School of Agricultural Science)
	Isamu	Sato	(Institute for Materials Research)
	Minoru	Issiki	(Institute for Advanced Materials Processing)
	Hiroshi	Fukuda	(Institute for Development, Aging and Cancer)
	Jirohta	Kasagi	(Laboratory of Nuclear Science)
	Syogo	Yamada	(University Hospital)
	Tsutomu	Shinozuka	(CYRIC)
	Tatsuo	Ido	(CYRIC)
	Mamoru	Baba	(CYRIC)
	Masatoshi	Itoh	(CYRIC)
	Takashi	Nakamura	(Graduate School of Engineering)
	Akira	Yamadera	(CYRIC)
	Keizo	Ishii	(Graduate School of Engineering)
	Tadao	Saitou	(Draduate School of Agricultural Science)
	Makoto	Watanabe	(Research Institute of Scientific Measurements)
	Tanetoshi	Koyama	(Institute for Chemical Reaction Science)

Research Program

(Chairman)	Takashi	Nakamura	(Graduate School of Engineering)
	Osamu	Hashimoto	(Graduate School of Science)
	Tsutomu	Sekine	(Graduate School of Science)
	Akira	Takahashi	(Graduate School, Division of Medicine)
	Kazuhiko	Yanai	(Graduate School, Division of Medicine)
	Hidetada	Sasaki	(Graduate School, Division of Medicine)
	Katsunori	Abe	(Graduate School of Engineering)

	Keizo	Ishii	(Graduate School of Engineering)
	Ren	Iwata	(Graduate School of Engineering)
	Isamu	Sato	(Institute for Materials Research)
	Hiroshi	Fukuda	(Institute for Development, Aging and Cancer)
	Tsutomu	Shinozuka	(CYRIC)
	Tatsuo	Ido	(CYRIC)
	Masatoshi	Itoh	(CYRIC)

Cyclotron

(Chairman)	Osamu	Hashimoto	(Graduate School of Science)
	Toshio	Kobayashi	(Graduate School of Science)
	Satoru	Kunii	(Graduate School of Science)
	Tsutom	Sekine	(Graduate School of Science)
	Hirokazu	Tamura	(Graduate School of Science)
	Kazushige	Maeda	(Graduate School of Science)
	Keizo	Ishii	(Graduate School of Engineering)
	Akira	Hasegawa	(Graduate School of Engineering)
	Isamu	Sato	(Institute for Materials Research)
	Minoru	Issiki	(Institute for Advanced Materials Processing)
	Takashi	Nakamura	(Graduate School of Engineering)
	Ren	Iwata	(Graduate School of Engineering)
	Tatsuo	Ido	(CYRIC)
	Masatoshi	Itoh	(CYRIC)
	Tsutomu	Shinozuka	(CYRIC)
	Astuki	Terakawa	(CYRIC)

Radiation Protection and Training of Safe Handling

(Chairman)	Takashi	Nakamura	(Graduate School of Engineering)
	Yoshiaki	Fujii	(Graduate School of Science)
	Hiroshi	Kudo	(Graduate School of Science)
	Yoshihiko	Uehara	(School of Medicine)
	Yoshihiro	Takai	(University Hospital)
	Yasushi	Yamazoe	(Graduate School, Division of Pharmaceutical Sciences)
	Keizo	Ishii	(Graduate School of Engineering)
	Toshiyasu	Yamaguchi	(Graduate School of Agricultural Science)
	Masayuki	Hasegawa	(Institute for Materials Research)
	Hiroshi	Fukuda	(Institute for Development, Aging and Cancer)

	Tatsuo	Ido	(CYRIC)
	Mamoru	Baba	(CYRIC)
	Akira	Yamadera	(CYRIC)
	Tanetoshi	Koyama	(Institute for Chemical Reaction Science)

Life Science

(Chairman)	Tatsuo	Ido	(CYRIC)
	Kazuo	Yamamoto	(Graduate School of Science)
	Yasuhito	Itoyama	(Graduate School, Division of Medicine)
	Kazuie	Iinuma	(Graduate School, Division of Medicine)
	Syogo	Yamada	(Graduate School, Division of Medicine)
	Reizo	Shirane	(Graduate School, Division of Medicine)
	Masahiko	Yamamoto	(Graduate School, Division of Medicine)
	Michinao	Mizugaki	(University Hospital)
	Makoto	Watanabe	(Graduate School, Division of Dentistry)
	Yasushi	Yamazoe	(Graduate School, Division of Pharmaceutical Sciences)
	Keizo	Ishii	(Graduate School of Engineering)
	Satoshi	Yokota	(Graduate School of Agricultural Science)
	Hiroshi	Fukuda	(Institute for Development, Aging and Cancer)
	Kazuo	Kubota	(Institute for Development, Aging and Cancer)
	Shin	Maruoka	(College of Medical Sciences)
	Takashi	Nakamura	(Graduate School of Engineering)
	Masatoshi	Itoh	(CYRIC)
	Kei-ichiro	Yamaguchi	(CYRIC)
	Yoshihito	Funaki	(CYRIC)

Prevention of Radiation Hazards

(Chairman)	Takashi	Nakamura	(Graduate School of Engineering)
	Osamu	Hashimoto	(Graduate School of Science)
	Tsutomu	Sekine	(Graduate School of Science)
	Keizou	Ishii	(Graduate School of Engineering)
	Tatsuo	Ido	(CYRIC)
	Manoru	Baba	(CYRIC)
	Tsutomu	Shinozuka	(CYRIC)
	Akira	Yamadera	(CYRIC)
	Sadayuki	Sasaki	(CYRIC)
	Takamoto	Miyata	(CYRIC)

VIII. PERSONNEL

VIII. Personnel (as of Jan. 1, 2001)

Director Hikonojo Orihara

Division of Accelerator

Osamu	Hashimoto[1)]
Tsutomu	Shinozuka
Akiyoshi	Yamazaki
Masahiro	Fujita
Eiji	Tanaka
Shizuo	Kan[6)]
Shizuo	Chiba[6)]
Yasushi	Ohmiya[6)]
Naoto	Takahashi[6)]

Division of Instrumentations

	Hikonojo	Orihara
—	Keizo	Ishii[2)]
	Astuki	Terakawa
	Toshiyuki	Misu
—	Sho-ichi	Watanuki
—	Tsutomu	Ichikawa
	Yukihiro	Oishi

Division of Radiopharmaceutical Chemistry

Tatsuo	Ido
Ren	Iwata[2)]
Yoshihito	Funaki
Masahiro	Yu-ki
Atsuko	Abe
Hideo	Takahashi
Yo-ichi	Ishikawa[7)]

Division of Cyclotron Nuclear Medicine

Masatoshi	Itoh
Kazuhiko	Yanai[4)]
Keiichiro	Yamaguchi
Kaoru	Ozaki
Takashi	Rikimaru
Masayasu	Miyake

Division of Radiation Protection and Safety Control

Mamoru	Baba
Takashi	Nakamura[2)]
Akira	Yamadera
Takamoto	Miyata
Noboru	Watanabe[7)]

Graduate Student and Researcher

Tetsu	Sonoda	(Graduate School of Science)
Takehiko	Suzuki	(Graduate School of Science)
Tatsuaki	Oshima	(Graduate School of Science)
Hiroshi	Suzuki	(Graduate School of Science)
Kazuaki	Kumagai	(Graduate School of Science)
Yasuo	Saito	(Graduate School of Science)
Yu-ji	Kikuchi	(Graduate School of Science)
Takeo	Uekusa	(Graduate School of Science)
Hiroaki	Fujisawa	(Graduate School of Science)
Takashi	Uemori	(Graduate School of Science)
Syozou	Furumoto	(Graduate School, Division of Pharmaceutical Sciences)
Tania G.	Valdes	(Graduate School, Division of Pharmaceutical Sciences)
Toshihiko	Kumagai	(Graduate School, Division of Pharmaceutical Sciences)
Sachiko	Tanaka	(Graduate School, Division of Pharmaceutical Sciences)
Megumi	Akasaka	(Graduate School, Division of Pharmaceutical Sciences)
Kyouka	Takashima	(Graduate School, Division of Pharmaceutical Sciences)
Manabu	Tashiro	(Graduate School, Division of Medicine)
Md. Mehedi	Masud	(Graduate School, Division of Medicine)
Koya	Fujiwara	(Graduate School, Division of Medicine)
Mejia Aurelio		(Graduate School, Division of Medicine)
Jeong Myeong Gi		(Graduate School, Division of Medicine)

Mastoshi	Endo	(Graduate School, Division of Medicine)
Laxmi N.	Singh	(Graduate School, Division of Medicine)
Takako	Miura	(Graduate School of Engineering)
Tsutomu	Hiroi	(Graduate School of Engineering)
Takao	Aoki	(Graduate School of Engineering)
Michiya	Sasaki	(Graduate School of Engineering)
Daniel A. H	Rasolonjatovo	(Graduate School of Engineering)
Hiroshi	Iwase	(Graduate School of Engineering)
Hiroshi	Yashima	(Graduate School of Engineering)
Hisaki	Satoh	(Graduate School of Engineering)
Syunsuke	Yonai	(Graduate School of Engineering)
Takashi	Katoh	(Graduate School of Engineering)
Masatane	Akiyama	(Researcher)

Office Staff

Hiroshi	Hara
Sadayuki	Sasaki
Yukinori	Mitobe
Kyoko	Fujisawa
Junko	Matsuno
Fumiko	Mayama
Mitsuko	Endo
Yu-ko	Yamashita
Kietu	Takahashi
Yuri	Okumura
Noriko	Suzuki
Kimiko	Abe
Keietsu	Aizawa
Toshiyuki	Watanabe[7)]

1) Graduate School of Science
2) Graduate School of Engineering
3) Institute for Materials Research
4) Graduate School, Division of Medicine
5) Institute for Development, Aging and Cancer
6) SUMI-JU Accelerator Service Ltd.
7) Japan Radiation Protection Co., Ltd.